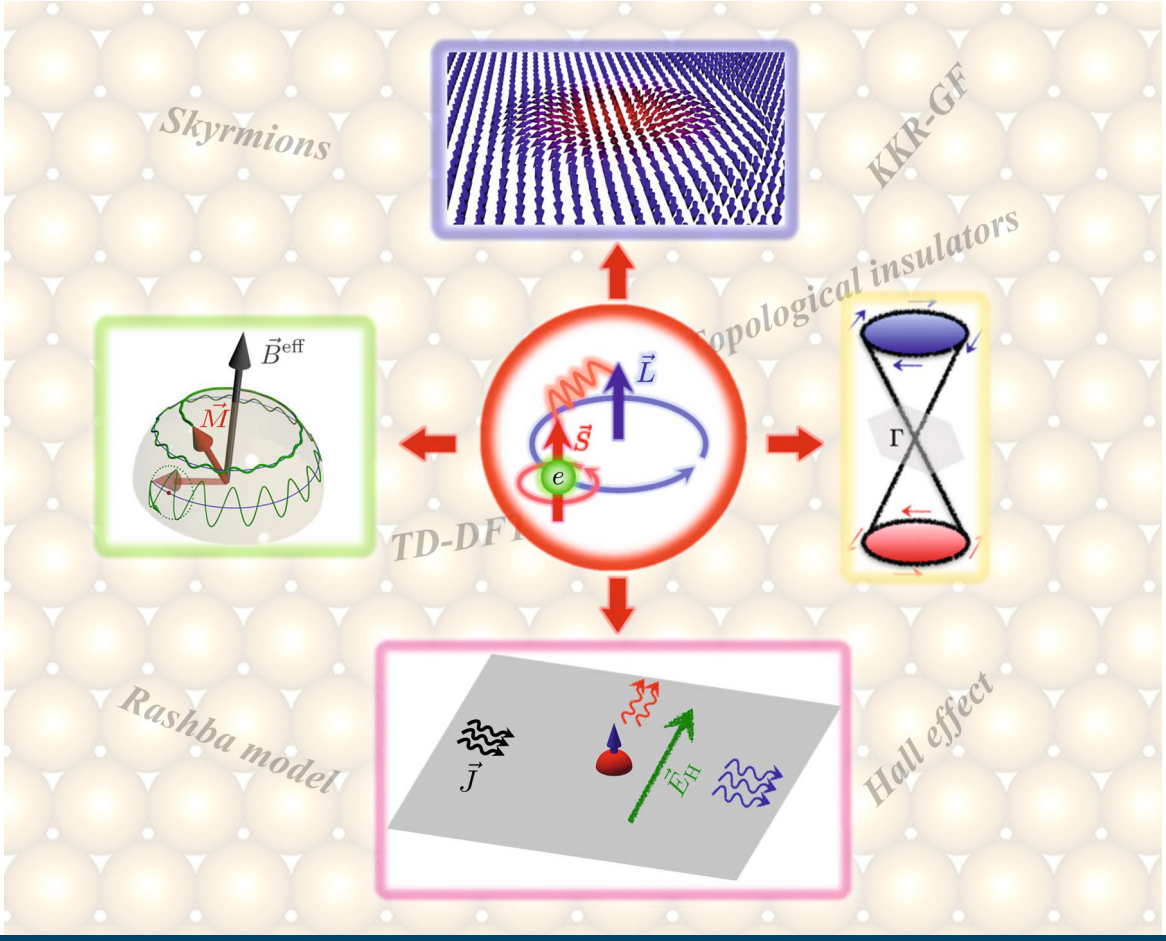

Spin-orbitronics at the nanoscale: From analytical models to real materials

Juba Bouaziz

Schlüsseltechnologien / Key Technologies
Band / Volume 204
ISBN 978-3-95806-429-4

Mitglied der Helmholtz-Gemeinschaft

JÜLICH
Forschungszentrum

Schriften des Forschungszentrums Jülich
Reihe Schlüsseltechnologien / Key Technologies Band / Volume 204

Forschungszentrum Jülich GmbH
Peter Grünberg Institut (PGI)
Quanten-Theorie der Materialien (PGI-1/IAS-1)

Spin-orbitronics at the nanoscale: From analytical models to real materials

Juba Bouaziz

Schriften des Forschungszentrums Jülich
Reihe Schlüsseltechnologien / Key Technologies Band / Volume 204

ISSN 1866-1807 ISBN 978-3-95806-429-4

Bibliografische Information der Deutschen Nationalbibliothek.
Die Deutsche Nationalbibliothek verzeichnet diese Publikation in der
Deutschen Nationalbibliografie; detaillierte Bibliografische Daten
sind im Internet über http://dnb.d-nb.de abrufbar.

Herausgeber und Vertrieb:	Forschungszentrum Jülich GmbH Zentralbibliothek, Verlag 52425 Jülich Tel.: +49 2461 61-5368 Fax: +49 2461 61-6103 zb-publikation@fz-juelich.de www.fz-juelich.de/zb
Umschlaggestaltung:	Grafische Medien, Forschungszentrum Jülich GmbH
Druck:	Grafische Medien, Forschungszentrum Jülich GmbH
Copyright:	Forschungszentrum Jülich 2019

Schriften des Forschungszentrums Jülich
Reihe Schlüsseltechnologien / Key Technologies, Band / Volume 204

D 82 (Diss. RWTH Aachen University, 2019)

ISSN 1866-1807
ISBN 978-3-95806-429-4

Vollständig frei verfügbar über das Publikationsportal des Forschungszentrums Jülich (JuSER)
unter www.fz-juelich.de/zb/openaccess.

Abstract

This thesis provides a theoretical description of magnetic nanostructures in inversion-asymmetric environments with strong spin-orbit interaction (SOI). The theoretical concepts introduced here can be applied in the field of spin-orbitronics, which consists of exploiting the SOI to manipulate the electron spin without external magnetic fields. The investigated systems display a plethora of interesting phenomena ranging from chiral magnetic interactions to gapped magnetic excitations. In practice, we adopt two different approaches: First, a model-based one relying on the Rashba Hamiltonian, which is employed to demystify and understand magnetic and transport properties of magnetic nanostructures embedded in a Rashba electron gas. Second, we use a first-principles approach within the framework of the Korringa-Kohn-Rostoker (KKR) Green function method to investigate the ground state properties of magnetic impurities in topologically insulating hosts. This method is suitable to simulate nanostructures in real space. Then, we employed our newly developed code based on time-dependent density functional theory to compute the spin excitation spectra of these magnetic nanostructures embedded in topological insulators. Moreover, the KKR Green function method was used to simulate the electronic structure and ground state properties of large magnetic nanostructures, namely magnetic Skyrmions.

In the first part, the analytical Rashba Green function and the scattering matrices modeling the magnetic impurities in the s-wave approximation are employed for the computation of the magnetic interaction tensor which contains: isotropic exchange, Dzyaloshinskii-Moriya (DM) and pseudo-dipolar interactions. The competition between these interactions leads to a rich phase diagram depending on the distance between the magnetic impurities. Next, we consider an external perturbing electric field and investigate the transport properties by computing the residual resistivity tensor within linear response theory. The contribution of SOI is explored. The investigation of arbitrary orientations of the impurity magnetic moment allowed a detailed analysis of contributions from the anisotropic magnetoresistance and planar Hall effect. Moreover, we calculate the impurity induced bound currents in the Rashba electron gas, which are used to compute the induced orbital magnetization. For a trimer of impurities with a non-vanishing spin chirality (SC) a finite orbital magnetization is observed when SOI is turned off. Since it emerges from the SC, it was named chiral orbital magnetization.

In the second part, we investigate the doping of topological insulators with magnetic impurities, which breaks time-reversal symmetry, leading to the prediction of a gap opening at the Dirac point when the magnetic moments are oriented in the perpendicular direction with respect to the surface of the topological insulator. This could potentially functionalize the topological surface states by enabling the control of the quantum anomalous Hall effect and dissipationless transport. Several experimental investigations obtained conflicting results, generating a lot of controversy on this point. Since the orientation of the magnetic moments depends on their magnetic anisotropy energy, we use the KKR Green function method to investigate isolated $3d$ and $4d$ transition metal impurities on the surfaces and in the bulk of Bi_2Te_3 and Bi_2Se_3. We explore the impact of impurity induced

in-gap states on the orientation of the magnetic moments, their dynamical spin-excitations and on the zero-point spin-fluctuations affecting the magnetic stability. We propose to use scanning tunneling spectroscopy in the inelastic mode to verify our predictions.

In the third part, we focus on magnetic Skyrmions which are topologically protected spin textures. These magnetic entities can be stabilized by the DM interaction. Relying on the KKR method we access the electronic structure of sub-5 nm Skyrmions and propose the spin mixing tunneling magnetoresistance (TXMR) for an all-electrical detection of Skyrmions in devices. Furthermore, we suggest to use X-ray magnetic circular dichroism (XMCD) as a magnetic microscopy technique for optical detection of non-collinear spin-textures such as Skyrmions. This can be achieved due to a chiral contribution to the orbital moments, driven by the non-collinear spin texture, and acquiring a topological nature for large skyrmions.

Table of Contents

Chapter 1

Introduction

Information technology (IT) consists of storing, manipulating and studying large amounts of data. In our modern society, IT has become of major importance since most devices used in our daily lives (such as laptops, smartphones, and even cars) rely on it. A huge progress has been made in this area since the 1950's: Computers evolved from wardrobe-sized machines with storage capacities in the order of MB to tiny gadgets capable of storing a few TBs. These improvements have been facilitated with the development of spintronics, which embodies the study of the electron spin (additionally to its charge) in solid-state systems and its usage in devices. One of the most prominent achievements of spintronics was the discovery of the giant magneto-resistance (GMR) effect [1, 2] by Albert Fert and Peter Grünberg, for which they were awarded the physics Nobel prize in 2007. The setup needed to observe the GMR effect consists of a system containing two magnetic layers separated by a nonmagnetic spacer. When the two magnetic layers are coupled antiferromagnetically, a drastic increase in the resistance is observed compared to the ferromagnetic configuration. The GMR effect was exploited to build magnetic field sensors used in hard disk drives, biosensors, etc.

Despite the recent progress in the field of spintronics, faster, smaller and more affordable devices are still needed. The ever-increasing need for higher storage density oriented research (or applications) towards the miniaturization of magnetic memories. However, this miniaturization is constricted by the superparamagnetic limit [3]: when the magnetic units used to store the information are too small, they become unstable regarding thermal fluctuations, which may change the orientation of the magnetization resulting in loss of the information. The construction of reliable smaller magnetic bits requires the use of materials that display a high magnetic anisotropy energy (*i.e.* a high barrier between the different magnetic alignments). The magnetic anisotropy originates from a relativistic effect called the spin-orbit interaction. In theory, the smallest unit that can potentially be used to store information is a single magnetic atom, for which the quantum mechanical nature must be taken into account. Therefore, the development of novel high-density storage devices requires a deep understanding of fundamental concepts such as: the spin-orbit interaction, magnetic anisotropy energy and other magnetic properties at the nanoscale.

In practice, the current technology faces other limitations as well. The present electronic devices are based on silicon and relies on the transport, manipulation, and storage of the electronic charge. However, due to heat dissipation (Joule effect), their operating speed is limited [4]. Thus, alternative technologies, such as the spintronic-based devices, are required. In this case, the energy dissipated during a switching event (most significant contribution to the dissipation) can be smaller than $k_{\mathrm{B}}T$ (k_{B} is the Boltzmann constant and T is the temperature) for coherently operating spin systems driven out of thermal equilibrium [5]. The processing speed of spintronic computing unit has been found comparable to the existing electronic ones [6]. Another appealing alternative is the use of dissipationless spin currents [7]. The existence of such non-dissipative and reversible spin currents induced by an electric current is allowed according to the generalized Ohm's law [7]. These spin currents can be manipulated by magnetic fields for example. Recently, a new spin current control mechanism that takes advantage of the intrinsic spin-orbit interaction and external electric fields in semiconductors has been predicted [8, 9, 10]. This is known as the spin Hall effect which was first observed experimentally in GaAs and InGaAs thin films [11]. The discovery of the spin Hall effect and the interplay between charge and spin degrees of freedom (relying on the SOI) in nonmagnetic materials opened a new road in spintronics, called spin-orbitronics.

A very promising class of materials of potential use in spin-orbitronics are topological insulators. Their bulk band structure is topologically non-trivial due to the spin-orbit interaction. They can be observed in two dimensional (2D) or three dimensional (3D) systems [12, 13]. Topological insulators are insulating in the bulk while hosting conducting states on the surface. The edge states are topologically protected from backscattering due to spin-momentum locking and time reversal symmetry. The spin-momentum locking confines the electrons spin in the surface plane and time reversal symmetry enforces the spins at $\vec{k}$ and $-\vec{k}$ to point in opposite directions.

Topological insulators provide an experimental realization of the quantum spin Hall effect [14, 12], where the edges host intrinsic spin currents which have the potential to remodel information processing. In 3D topological insulators, backscattering can be allowed when the Fermi surface has warping (when the Fermi surface is anisotropic). The spin-momentum locking makes the spin rotate as an electron moves around the Fermi surface. When that happens, the electronic wave function acquires a global non-trivial phase, known as Berry phase [15]. The presence of a non-zero Berry phase (in this case equal to π [16]) has a significant impact on the electrical conductivity, leading, for example, to a weak antilocalization in presence of disorder [17]. More exotic effects can be observed in topological insulators. One of the most appealing is the Majorana zero modes, which are predicted to occur when a topological insulator is interfaced with a superconductor. The experimental realization of Majorana fermions is predicted to be used in fault-tolerant quantum computing [18]. The Bi_2Se_3 compound is a good prototype for 3D topological insulators since its topological surface state remains at room temperature [16]. Bi_2Se_3 thin films display a lot of interesting properties. For instance, when an electric current is injected into the material, it generates a spin polarization due to the spin-momentum locking [19]. The strong spin-orbit interaction in Bi_2Se_3 also offers an adequate playground for the observation of spin-orbit torques (SOT). When an in-plane electric current is injected into a Cr-doped Bi_2Se_3 bilayer, a giant SOT leads to a switching of the magnetization [20].

This current-induced magnetization switching may be used in future spin-orbitronics applications to create low power dissipation devices.

The breaking of time reversal symmetry in topological insulators can be a source of other numerous interesting effects. As an example, the doping of 3D topological insulators (Bi_2Te_3 and Sb_2Te_3) with high concentrations of Cr magnetic impurities allowed the experimental realization of the quantum anomalous Hall effect (QAHE) at low temperatures [21]. The observation of the QAHE is a signature of a gap opening at the Dirac point, which is still a topic subjected to controversy: While some experimental investigations reported the presence of a gap [22, 23, 24], others did not observe it [25, 26, 27, 28, 29]. Several mechanisms can lead to a gap opening. For instance, the formation of impurity bands hybridizing with the topological surface states [30, 31, 32], or the creation of a ferromagnetic order combined with an out-of-plane magnetic anisotropy (favors a perpendicular orientation of the magnetic moments with respect to the surface) are two examples. For the latter case, the magnetic anisotropy plays an important role, therefore, it attracted a lot of attention. It was explored by means of X-ray magnetic circular dichroism (XMCD), spin-polarized scanning tunneling microscopy (SP-STM), as well as first principles calculations using density functional theory (DFT) [27, 33, 34, 35, 32, 36]. It was shown that the nature (donor or acceptor of electrons), the concentration and deposition site of the magnetic dopant play crucial roles in the determination of the magnetic anisotropy.

The magnetic anisotropy can also be extracted from the transversal spin excitations spectra of the magnetic impurities. These spin excitations are observed using inelastic scanning tunneling spectroscopy (ISTS) [37]. They create additional tunneling channels that induce a variation in the conductance at the magnetic excitation energies. The magnetization dynamics can be accessed theoretically from first principles using time-dependent density functional theory (TD-DFT). The central quantity in TD-DFT is the transverse dynamical magnetic susceptibility or response function [38, 39]. This quantity describes the excitations of the system, giving its energy (from the position of the peak) and lifetime (from the line-width of the peaks). In recent years, the transverse magnetic susceptibilities of adatoms deposited on metallic surfaces were calculated from first principles [40]. This allowed a quantitative comparison and prediction of experimental data [40, 37, 41]. The knowledge of the dynamical magnetic susceptibility also allows the determination of the zero-point spin-fluctuations (ZPSF), which quantifies the deviations of the magnetic moments from their equilibrium direction. These deviations can be relatively large for adatoms on metallic surfaces [42]. These fluctuations can also reduce considerably the magnetic anisotropy, making the moment unstable regarding external perturbations.

Besides being important for topological insulators, the spin-orbit interaction is a source of interest in semiconductors as well. When the inversion symmetry is broken, the spin-orbit interaction splits the energy bands. This was initially predicted for noncentrosymmetric wurtzite semiconductors by Dresselhaus [43] and Rashba [44]. When the spin splitting in momentum occurs at interfaces, it is called the Rashba effect which displays a spin-momentum locking similarly to topological insulators. In this case, however, the energy bands are topologically trivial. The Rashba effect leads to several interesting phenomena such as the spin Hall effect, spin interference, spin galvanic effect, magnetoelectric effects and non-collinear magnetism [45]. A giant Rashba spin splitting can be engineered by depositing a monolayer of Bi on a Si(111) surface [46]. The Rashba ef-

fect has also been detected on metallic surfaces. The first observation has been made on a Au(111) surface using ARPES [47]. Afterwards, several clean surfaces also displayed the same effect [48, 49]. In presence of magnetic impurities, the interplay between the Rashba effect and magnetism gives rise to various interesting effects. The Dzyaloshinskii-Moriya (DM) interaction [50, 51] is a typical example. It leads to the formation of non-collinear magnetic spin textures and fixes their chirality as observed in 2D spin spirals [52, 53, 54] or unidimensional systems [55, 56]. The DM interaction is defined by the DM vector which obeys the Moriya rules [50]. More recently, it was reinterpreted in terms of a Doppler shift induced by an intrinsic spin current [57]. In the long range limit, the DM interaction is mediated by conduction electrons [58, 59] and displays similarities with the Ruderman-Kittel-Kasuya-Yosida (RKKY) interactions [60, 61, 62]. In this limit, it has been observed experimentally using STM that the DM vector length oscillates while changing direction [63]. When external perturbations such as electric fields are present, the combination of Rashba effect and magnetism can be a source of magnetoelectric effects. Indeed, the magnetization direction has a deep impact on the transport properties of the system due to the spin-orbit interaction. In the transverse direction, contributions from the anomalous Hall effect (AHE), involving the out-of-plane component of the magnetization, are expected. They can be related to the topology of the electronic structure and the Berry phase acquired by the electrons [64]. Moreover, in the longitudinal response, the anisotropic magnetoresistance (AMR) is observed. It has a quadratic dependence on the spin-orbit strength (Rashba parameter) and is always a positive quantity. AMR gives rise to a transverse contribution which is independent from AHE called the planar Hall effect (PHE) [65, 66]. Even in absence of external electric fields, the Rashba spin-orbit interaction in conjunction with a finite magnetization (breaking time reversal symmetry) can give rise to a non-vanishing bound charge current. In the classical picture, these finite bound currents produce an orbital magnetization. More recently, we observed that an orbital magnetization can arise due to non-collinear magnetic structures without any relativistic contribution. We refer to it as chiral orbital magnetization (COM) [67].

As discussed before, the topology of the band structure allows the appearance of a topological insulating phase with conducting edge states. Analogously, complex topologies of the magnetic structure are expected to lead to interesting properties in magnetic systems. For instance, the presence of the spin-orbit interaction in a magnetic inversion-asymmetric environment generates the DM interaction that can stabilize topological magnetic objects such as magnetic Skyrmions — particle-like swirling spin textures [68]. The magnetic moments forming a Skyrmion rotate progressively from one orientation at the edges to the opposite orientation at the core, with a fixed chirality. Depending on this chirality, there are two main kinds of magnetic Skyrmions: Néel-type and Bloch-type [69]. Each Skyrmion type conforms with the symmetries of the interactions among the magnetic moments. These symmetries are fixed by the crystal structure. Skyrmions were first observed in magnetic compounds, where the crystal structure is non-centrosymmetric [70, 71]. They were also found in magnetic thin films deposited on heavy metals. The heavy metal substrate produces a strong DM interaction due to its large spin-orbit interaction. The first systems studied were Fe/Ir(111) and Pd/Fe/Ir(111) [72]. The sizes of the Skyrmions found in these systems are typically small (a few nanometers wide). Nonetheless, large magnetic fields and low temperatures are required to stabilize a Skyrmion lattice or single

Skyrmions [73].

Skyrmions can be characterized by their topological charge $\mathcal{Q}$, an integer quantity that measures the winding of the magnetization. For that reason, $\mathcal{Q}$ is also referred as "winding number". For topologically trivial magnetic textures such as ferromagnets or spin spirals, $\mathcal{Q}$ is zero. However, Skyrmions have a finite integer $\mathcal{Q}$ and are topologically non-trivial. This provides Skyrmions with intriguing characteristics such as the topological protection, *i.e.* a Skyrmion cannot be continuously deformed into another magnetic texture with a different $\mathcal{Q}$. This means that Skyrmions are stabilized by a topological barrier [74]. Furthermore, it is essential to mention that Skyrmions possess a solitonic nature, meaning that they have a finite extension that grants them a particle-like motion and interaction. This makes them attractive for future spintronics devices [69]. Magnetic Skyrmions are also appealing since the energy cost required for their motion or excitation is low. The current densities required to create a Skyrmion motion are orders of magnitude lower in comparison to the ones used to move magnetic domain walls [75, 76]. The topological magnetic structure of Skyrmions also revealed to be a source of other interesting effects. For instance, the non-collinear spin texture gives rise to emergent electromagnetic fields [77]. These fields generate a topological Hall effect (THE) that provides an electric signature of magnetic Skyrmions [78, 79].

In order to unravel and connect the physics of topological insulators, Rashba effect and Skyrmions, in this thesis we investigate the interplay between magnetism and spin-orbit interaction. On the one hand, we study magnetic doping of a 2D Rashba electron gas. We use a simple two band Rashba model to build a bottom up approach in order to understand and demystify the multitude of phenomena generated by the scattering of Rashba electrons off magnetic impurities. On the other hand, we use DFT to have a material specific and accurate description of magnetic impurities embedded in topological insulators thin films and bulk. Furthermore, we employ TD-DFT to access the dynamical properties of these magnetic impurities under time-dependent external magnetic fields. Finally, we investigate larger magnetic nanostructures, Skyrmions, fully from first principles and examine their electronic structure, as well as their spin and orbital magnetic properties. The different concepts explored in this thesis represent a collection of theoretical advances in the field of spin-orbitronics. The thesis is structured as follows:

Chapter 2 consists of a theoretical introduction. The basics of DFT and its spin-polarized extension are presented, followed by a solution of the Kohn-Sham equations within the framework of multiple scattering theory using the Korringa-Kohn-Rostoker (KKR) Green function method. We then discuss the magnetic anisotropy and its computation from DFT using different methods: band energy differences and the torque method. Afterwards, an extension to TD-DFT is presented allowing the computation of spin excitations. In the zero-frequency limit, the phenomenological Landau-Lifshitz-Gilbert (LLG) model is used to help interpret the spin excitation spectra and extract information about the magnetic anisotropy, damping and nutation of the magnetization. This chapter is closed by connecting the zero-point spin-fluctuations to the dynamical magnetic susceptibility.

Chapter 3 focuses on the scattering of the Rashba electrons on magnetic impurities and the related emerging phenomena. By means of scattering theory, the Rashba Green function is computed analytically. The transition matrices characterizing the magnetic impurities are derived within the s-wave approximation. Relying on the infinitesimal rota-

tion method [80], the magnetic exchange interaction tensor is calculated. Afterwards, we perform numerical calculations to determine the ground state orientation of the magnetic moments of the impurities. Furthermore, we apply an external perturbing electric field and investigate the magnetoelectric properties resulting from the magnetic impurities. The residual resistivity tensor is calculated using linear response theory, the AMR and PHE were observed. Moreover, we explore the orbital degree of freedom of a magnetically doped Rashba electrons by calculating the bound currents. A multiple scattering expansion of the Green function was performed to establish a link between the orbital magnetization and the chiral magnetic texture of the impurities. The model system used consists of Fe impurities deposited on a Au(111) surface state that display a Rashba splitting [47].

In chapter 4, we employ the real space KKR Green function method to investigate magnetic impurities embedded in topological insulators. When the magnetic moment of the impurity is perpendicular to the surface of the topological insulator, a gap opening at the Dirac point was predicted [81, 16]. Therefore, we computed the ground state properties of $3d$ and $4d$ transition metal magnetic impurities embedded in Bi_2Te_3 and Bi_2Se_3 thin films and bulk (prototypes of 3D topological insulators). Impurity induced in-gap states are observed in the LDOS, which may fill the band gap. These calculations allowed to highlight the importance of the bulk states on the electronic structure of the impurities. We then compute the magnetic anisotropy energy, and show that it can reach rather large values — up to 6 meV for Co in Bi_2Te_3 with an out-of-plane orientation. The magnetic anisotropy is computed using three different methods: band energy differences, torque method and the static magnetic susceptibility. The strengths and limitations of each method are highlighted. In addition to that, we investigate the magnetic excitation spectrum of $3d$ and $4d$ impurities embedded in these topologically insulating hosts. For that, we used our freshly implemented code which computes consistently the spin excitations spectra for magnetic atoms embedded in hosts with strong spin-orbit interaction. We also discussed the magnetization dynamics in terms of the extracted the LLG parameters. Finally, relying of the fluctuation-dissipation theorem, the magnetic susceptibility is used to compute ZPSF, which are employed to estimate the reduction of the magnetic anisotropy barrier.

In chapter 5, the real space KKR Green function method is used to simulate larger magnetic structures, Skyrmions, that are created in a magnetic layer deposited on a heavy metal with strong spin-orbit interaction. We simulate a single magnetic Skyrmion embedded in the Fe layer of a Pd/Fe/Ir(111) heterostructure. Three different Skyrmion sizes have been considered. Once more, a multiple scattering expansion of the Green function leads to an interpretation of the spin splittings observed in the LDOS of the magnetic elements. The change in the splitting of the LDOS gives rise to the tunneling spin mixing magnetoresistance (TXMR). These observations are corroborated using a generalized Alexander-Anderson model. Moreover, we investigated the orbital magnetization for the considered Skyrmions. The non-vanishing chirality of their spin structure gives birth to a COM, which can be observed by comparing their orbital magnetization with and without spin-orbit interaction. Finally, we show that for large magnetic Skyrmions, the COM is quantized and becomes a topological orbital magnetization (TOM), which is invariant under continuous deformations of the Skyrmion.

We then conclude the work, summarizing the results and providing a short outlook on future interesting research directions.

Chapter 2

Theoretical foundations

Solids are ordered arrangements of atoms, which consist of nuclei and a cloud of electrons surrounding them. Using the Born-Oppenheimer approximation [82], the nuclear motion can be decoupled from the electronic one, we then are left with the electronic many-body problem, which is described in the non-relativistic case by the static Schrödinger equation given in Eq. (2.1). The exact solution of this equation requires a huge computational effort and is impossible for systems containing a large number of interacting electrons. In order to circumvent this problem Hohenberg, Kohn and Sham introduced density functional theory (DFT) [83, 84], which allows to access the ground state properties of interacting systems.

This chapter is structured as follows: First, we discuss the basics of DFT and the main approximations used to solve its central object, the Kohn-Sham equations. Second, we review a solution of these equations in the framework of multiple scattering theory using the Korringa-Kohn-Rostoker (KKR) Green function method [85, 86, 87]. This method is a very powerful technique which allows the computation of periodic systems and defects (using a real space embedding scheme). It consists of two steps:

- Solve the Kohn-Sham equations for each atom separately.
- Connect the atomic sites to each other using multiple scattering theory.

Third, we discuss the computation of magnetic anisotropy using DFT. This anisotropy fixes the direction of the magnetization according to the crystal structure. Fourth, we review the extension of DFT to time-dependent systems (TD-DFT) including a linear response formulation of the problem. The linear response approach is used when the system is subjected to small time-dependent perturbations. TD-DFT will be used to study the dynamical magnetic excitations of magnetic impurities embedded in topological insulators. Finally, we briefly summarize the technical aspects of the codes used in the thesis, and the required developments to generate some of the results shown in the thesis.

2.1 The many-body problem

A system containing N interacting electrons is described in non-relativistic quantum mechanics by the many-body Schrödinger equation:

$$\hat{H}\,\psi_i(\vec{r}_1\,\sigma_1, \vec{r}_2\,\sigma_2, ..., \vec{r}_N\,\sigma_N) = \varepsilon_i\,\psi_i(\vec{r}_1\,\sigma_1, \vec{r}_2\,\sigma_2, ..., \vec{r}_N\,\sigma_N) \quad , \tag{2.1}$$

$\hat{H}$ is the Hamiltonian of the system. $\psi_i(\vec{r}_1\,\sigma_1, \vec{r}_2\,\sigma_2, ..., \vec{r}_N\,\sigma_N)$ is the antisymmetric many-body wave function and eigenfunction of $\hat{H}$ with the eigenvalue ε_i. $\{\vec{r}_i\,\sigma_i\}$ represent the real-space position and spin of the ith electron. $\hat{H}$ can be decomposed into three parts:

$$\begin{cases} \hat{H} = \hat{T} + \hat{V} + \hat{W} & , \\ \hat{T} = \sum_{i=1}^{N} -\vec{\nabla}^2_{\vec{r}_i} & , \\ \hat{V} = \sum_{i=1}^{N} v(\vec{r}_i) & , \\ \hat{W} = \frac{1}{2}\sum_{i\neq j}^{N} \frac{2}{|\vec{r}_i - \vec{r}_j|} & . \end{cases} \tag{2.2}$$

$\hat{T}$ is the kinetic energy operator and $\vec{\nabla}_{\vec{r}_i}$ is the gradient according to $\vec{r}_i$. $\hat{V}$ is an external potential that includes the interaction with nuclei or with, for example, an external field. $\hat{W}$ is the Coulomb electron-electron interaction. $\hat{H}$ from Eq. (2.2) is given in Rydberg atomic units ($\hbar = 1, e = \sqrt{2}, m_e = \frac{1}{2}$). The solution of the many-body problem consists of finding $\psi_i(\vec{r}_1\,\sigma_1, \vec{r}_2\,\sigma_2, ..., \vec{r}_N\,\sigma_N)$. However, this task is very hard to achieve due to the electron-electron interaction which does not allow a factorization of the wave function. The complexity of the problem grows exponentially with the number of particles (N). As an example we consider an Fe atom, it contains 26 electrons, in three-dimensions we have $3 \times 26 = 78$ degrees of freedom, and if we try to solve Eq. (2.1) on a real space grid with 10 points in each dimension, one needs to store 10^{78} numbers which is approximately the number of atoms in the universe. Considering that systems in solids contains thousands of atoms, we clearly see that it is impossible to store such amount of data. Therefore, a better method for treating solids using a quantum mechanical description of the electron is needed. This is possible using DFT which will be discussed in detail in the next section.

2.2 Density functional theory (DFT)

One possible way to circumvent the problem is to focus on the single-particle probability density instead of computing the many-body wave function. For a system constituted of N interacting electrons described by $\hat{H}$ of Eq. (2.1), the ground state single-particle probability density reads:

$$n_0(\vec{r}) = \sum_{\sigma_i} \int \mathrm{d}\vec{r}_2 ... \,\mathrm{d}\vec{r}_i\, |\psi_i(\vec{r}\,\sigma_1, \vec{r}_2\,\sigma_2, ..., \vec{r}_N\,\sigma_N)|^2 \quad , \tag{2.3}$$

where $n_0(\vec{r})$ is computed from the wave function, which obeys the Schrödinger equation. Thus, it is straightforward to see that $n_0(\vec{r})$ is a functional of the external potential $v(\vec{r})$ (*i.e.* $n_0[v](\vec{r})$). The converse relation which states that the potential is a functional of the density is contained in the first Hohenberg-Kohn theorem [83]: "*The ground state density*

$n_0(\vec{r})$ *uniquely determines the potential* $v(\vec{r})$*, up to a constant*". The second theorem states that: "*The total energy functional is minimized by the ground state density*". The remaining task is to find the ground state density. This was achieved by Kohn and Sham [84], they introduced an auxiliary system (Kohn-Sham system) containing non-interacting particles with same ground state density as the interacting one. The non-interacting particles are subject to a Kohn-Sham potential $v_{\mathrm{KS}}(\vec{r})$, the latter one is divided into a dominant part which is known analytically and a small unknown contribution which has to be approximated. The Hamiltonian describing the Kohn-Sham system is:

$$H_{\mathrm{KS}} = \sum_{i=1}^{N} -\vec{\nabla}^2_{\vec{r}_i} + v_{\mathrm{KS}}(\vec{r}_i) \quad . \tag{2.4}$$

H_{KS} is the so-called Kohn-Sham Hamiltonian. The many-body wave function for the non-interacting system is given by a Slater determinant of single-particle orbitals $\phi_i(\vec{r})$ (Kohn-Sham orbitals) which fulfill the following Schrödinger equation:

$$\left(-\vec{\nabla}^2_{\vec{r}} + v_{\mathrm{KS}}(\vec{r})\right)\, \phi_i(\vec{r}) = \varepsilon_i\, \phi_i(\vec{r}) \quad . \tag{2.5}$$

ε_i represent the single-particle energies and the ground state density is:

$$n_{\mathrm{KS}}(\vec{r}) = \sum_{i=1}^{N} \left|\phi_i(\vec{r})\right|^2 \quad . \tag{2.6}$$

Coming back to the interacting many-body problem, we express the total energy functional of the system as

$$E[n] = T[n] + W[n] + \int \mathrm{d}\vec{r}\, n(\vec{r})\, v(\vec{r}) \quad , \tag{2.7}$$

where $T[n]$ and $W[n]$ represent the kinetic and electron-electron interaction energies, respectively. We now write $E[n]$ using the quantities of the non-interacting system defined by Eq. (2.4):

$$E[n] = T_{\mathrm{KS}}[n] + \int \mathrm{d}\vec{r}\, n(\vec{r})\, v(\vec{r}) + \int \mathrm{d}\vec{r} \int \mathrm{d}\vec{r}\,' \, \frac{n(\vec{r})\, n(\vec{r}\,')}{|\vec{r} - \vec{r}\,'|} + E_{\mathrm{xc}}[n] \quad . \tag{2.8}$$

$T_{\mathrm{KS}}[n]$ is the kinetic energy of the non-interacting particles, the second term is the energy due the external potential $v(\vec{r})$, the third term is the classical Coulomb energy and the last one is called exchange-correlation energy, which can be written as:

$$E_{\mathrm{xc}}[n] = T[n] - T_{\mathrm{KS}}[n] + W[n] - \int \mathrm{d}\vec{r} \int \mathrm{d}\vec{r}\,' \, \frac{n(\vec{r})\, n(\vec{r}\,')}{|\vec{r} - \vec{r}\,'|} \quad . \tag{2.9}$$

Assuming that $n_{\mathrm{KS}}(\vec{r}) = n_0(\vec{r})$ and using the second Hohenberg-Kohn theorem in Eq. (2.8) (minimum energy condition) for a fixed number of particles N, we obtain the expression of the Kohn-Sham potential:

$$v_{\mathrm{KS}}(\vec{r}) = v(\vec{r}) + \int \mathrm{d}\vec{r}\,' \, \frac{2n_0(\vec{r}\,')}{|\vec{r} - \vec{r}\,'|} + v_{\mathrm{xc}}[n_0](\vec{r}) \quad . \tag{2.10}$$

The previous equation shows that knowledge of $v_{\mathrm{KS}}(\vec{r})$ gives the exact ground state density for the interacting many-body problem. However, the exchange-correlation contribution $v_{\mathrm{xc}}[n_0](\vec{r}) = \frac{\delta E_{\mathrm{xc}}}{\delta n(\vec{r})}\Big|_{n_0}$ is unknown, therefore, one needs approximations for this term. In practice, several approximations for the exchange-correlation energy are used such as the local density approximation (LDA) which is discussed in the next section.

2.2.1 Approximations to the exchange-correlation energy functional

The first approximation for the exchange-correlation energy was the LDA introduced by Kohn and Sham. In this approximation the exchange-correlation energy has a local dependence on the density:

$$E_{\mathrm{xc}}^{\mathrm{LDA}}[n] = \int \mathrm{d}\vec{r}\, n(\vec{r})\, \varepsilon_{\mathrm{xc}}(n(\vec{r})) \quad . \tag{2.11}$$

$\varepsilon_{\mathrm{xc}}(n(\vec{r}))$ is the exchange-correlation energy density of the homogeneous electron gas. The LDA is expected to provide accurate results for systems with densities that vary slowly in space. However, it also provides good results for inhomogeneous systems, since the LDA fulfills exact constraints leading to correct physical results. $\varepsilon_{\mathrm{xc}}(n(\vec{r}))$ can be decomposed into two parts:

$$\varepsilon_{\mathrm{xc}}(n(\vec{r})) = \varepsilon_{\mathrm{x}}(n(\vec{r})) + \varepsilon_{\mathrm{c}}(n(\vec{r})) \quad . \tag{2.12}$$

The first term in the previous equation, represents the exchange contribution which can be calculated using the Hartree-Fock method for the homogeneous electron gas [88] and is given by: $\varepsilon_{\mathrm{x}}(n(\vec{r})) = -\frac{3}{2}\left(\frac{3}{\pi} n(\vec{r})\right)^{\frac{1}{3}}$. The second term in Eq. (2.12) is the correlation contribution, it can be obtained numerically for example using the Quantum Monte Carlo method [89]. More elaborate approximations for the exchange-correlation energy functional were introduced afterwards. For example, the generalized gradient approximation (GGA), which takes into account the gradient of the density [90]. In this thesis, we use the LDA with a parametrization provided by Vosko, Wilk, and Nusair [91].

2.2.2 DFT for spin-polarized systems

Previously, we omitted the spin degree of freedom. The Kohn-Sham formalism was extended to spin-polarized systems by von Barth and Hedin [92]. The Kohn-Sham orbitals are replaced by spinors:

$$\underline{\phi}_i(\vec{r}) = \begin{pmatrix} \phi_i^{\uparrow}(\vec{r}) \\ \phi_i^{\downarrow}(\vec{r}) \end{pmatrix} = \sum_{\sigma=\uparrow,\downarrow} \phi_i^{\sigma}(\vec{r})\, \boldsymbol{\chi}^{\sigma} \quad . \tag{2.13}$$

$\boldsymbol{\chi}^{\sigma}$ represent the basis vectors in spin space with respect to some chosen quantization axis:

$$\boldsymbol{\chi}^{\uparrow} = \begin{pmatrix} 1 \\ 0 \end{pmatrix} \quad ; \quad \boldsymbol{\chi}^{\downarrow} = \begin{pmatrix} 0 \\ 1 \end{pmatrix} \quad . \tag{2.14}$$

The exchange-correlation energy is now a functional of the ground state particle density $n_0(\vec{r})$ and spin density $\vec{m}_0(\vec{r})$ *i.e.* $E_{\mathrm{xc}} = E_{\mathrm{xc}}[n, \vec{m}]$, the central quantities in the spin-dependent Kohn-Sham formalism namely $n_0(\vec{r})$ and $\vec{m}_0(\vec{r})$ are related to the Kohn-Sham

spinors via:

$$n_0(\vec{r}) = \sum_{i=1}^{N_{\text{occ}}} \underline{\phi}_i^{\dagger}(\vec{r})\, \mathbb{1}_2\, \underline{\phi}_i(\vec{r}) \quad ; \quad \vec{m}_0(\vec{r}) = \sum_{i=1}^{N_{\text{occ}}} \underline{\phi}_i^{\dagger}(\vec{r})\, \vec{\boldsymbol{\sigma}}\, \underline{\phi}_i(\vec{r}) \quad . \tag{2.15}$$

$\mathbb{1}_2$ is the 2×2 identity matrix and $\vec{\boldsymbol{\sigma}}$ is the Pauli vector which contains the Pauli matrices defined as:

$$\boldsymbol{\sigma}_x = \begin{pmatrix} 0 & 1 \\ 1 & 0 \end{pmatrix} \quad ; \quad \boldsymbol{\sigma}_y = \begin{pmatrix} 0 & -\mathrm{i} \\ \mathrm{i} & 0 \end{pmatrix} \quad ; \quad \boldsymbol{\sigma}_z = \begin{pmatrix} 1 & 0 \\ 0 & -1 \end{pmatrix} \quad . \tag{2.16}$$

The Kohn-Sham equation given in Eq. (2.5) is rewritten to include the exchange-correlation magnetic field $\vec{B}_{\text{xc}}(\vec{r})$, which is due to the finite spin polarization of the system:

$$\left[\left(-\vec{\nabla}_{\vec{r}}^{\,2} + v_{\text{KS}}(\vec{r})\right)\, \mathbb{1}_2 + \vec{B}_{\text{xc}}(\vec{r}) \cdot \vec{\boldsymbol{\sigma}}\right]\, \underline{\phi}_i(\vec{r}) = \varepsilon_i\, \underline{\phi}_i(\vec{r}) \quad . \tag{2.17}$$

The previous equation shows that the non-interacting particles of the Kohn-Sham system are not only subjected to a potential $v_{\text{KS}}(\vec{r})$ but also coupled to the exchange-correlation magnetic field $\vec{B}_{\text{xc}}(\vec{r})$, which is related to $E_{\text{xc}}[n, \vec{m}]$ via:

$$\vec{B}_{\text{xc}}(\vec{r}) = \left.\frac{\delta E_{\text{xc}}[n, \vec{m}]}{\delta \vec{m}(\vec{r})}\right|_{n_0, \vec{m}_0} \quad . \tag{2.18}$$

$\vec{B}_{\text{xc}}(\vec{r})$ is a functional of n_0 and $\vec{m}_0$. Similarly to $v_{xc}[n]$, $\vec{B}_{\text{xc}}(\vec{r})$ is approximated in practice. In the local spin density approximation (LSDA) $\vec{B}_{\text{xc}}(\vec{r})$ always points in the same direction as $\vec{m}_0(\vec{r})$. From Eq. (2.17) one can see that $\phi_i^{\sigma}(\vec{r})$ are coupled. Nonetheless, for collinear magnetic systems $\vec{\boldsymbol{\sigma}}$ can be replaced by $\boldsymbol{\sigma}_z$, when a suitable choice of the quantization axis is made, thus, the component of $\underline{\phi}_i(\vec{r})$ decouples allowing to solve Eq. (2.17) for each component separately.

2.3 Green functions and embedding technique

In practice, we want to use DFT to compute material-specific magnetic properties of nanostructures deposited on surfaces. Most DFT codes are based on wave function methods which rely on periodic boundary conditions. Therefore, in order to simulate a defect embedded in a pristine crystalline host, one needs to use a large supercell to avoid interactions between the defect and its periodic copies. We follow a different route and use a Green function based method which consists of two steps: first, the Green function of the periodic host is computed. Second, assuming that the perturbation in the potential is localized around the defect, we consider a real space cluster in which the impurity (we call impurity any finite nanostructure placed in an otherwise periodic system) is embedded using a Dyson equation [93, 94].

We define the single-particle Green function as the solution of the inhomogeneous counterpart of the single-particle Kohn-Sham equation given Eq. (2.5):

$$(\varepsilon + \mathrm{i}\eta - H_{\text{KS}}(\vec{r}))\; G(\vec{r}, \vec{r}', \varepsilon) = \delta(\vec{r} - \vec{r}') \quad . \tag{2.19}$$

Here η is a positive real number for the retarded Green function used through the thesis. We may take the limit $\eta \to 0^+$ at the end of the calculation. Using the eigenvalues ε_i and eigenfunctions $\phi_i(\vec{r})$ of the homogeneous counterpart of Eq. (2.19), the Green function $G(\vec{r}, \vec{r}', \varepsilon + \mathrm{i}\eta)$ can be written as sum over all eigenstates. This is called the spectral or Lehmann-representation of the Green function:

$$G(\vec{r}, \vec{r}', \varepsilon + \mathrm{i}\eta) = \sum_i \frac{\phi_i(\vec{r})\, \phi_i^*(\vec{r}')}{\varepsilon + \mathrm{i}\eta - \varepsilon_i} \quad . \tag{2.20}$$

The previous equation shows that the Green function has poles at ε_i which are the eigenenergies of $H_{\mathrm{KS}}(\vec{r})$. In the limit $\eta \to 0^+$, $G(\vec{r}, \vec{r}', \varepsilon + \mathrm{i}\eta)$ describes the propagation of an outgoing wave at a point $\vec{r}$, created from a source at a position $\vec{r}'$. This can be easily seen when considering the time-dependent Green function defined as the Fourier transform of $G(\vec{r}, \vec{r}', \varepsilon + \mathrm{i}\eta)$:

$$G(\vec{r}, \vec{r}', t - t') = \int_{-\infty}^{+\infty} \frac{\mathrm{d}\varepsilon}{2\pi}\, G(\vec{r}, \vec{r}', \varepsilon + \mathrm{i}\eta)\, e^{-\mathrm{i}\varepsilon(t-t')} \quad . \tag{2.21}$$

For an electron subjected to a time-independent potential, the wave function $\psi(\vec{r}, t)$ at a point $\vec{r}$ and time t can be written as [94]:

$$\psi(\vec{r}, t) = \int \mathrm{d}\vec{r}'\, G(\vec{r}, \vec{r}', t - t_0)\, \psi(\vec{r}', t_0) \quad . \tag{2.22}$$

where $t_0 < t$ since $G(\vec{r}, \vec{r}', t - t_0)$ propagates the wave function forward in time, therefore, the Green function is also referred to as a propagator.

The Green function for the periodic system is computed in the framework of multiple scattering theory described in Sec. 2.4. The impurity is embedded via a Dyson equation [94, 95]:

$$\begin{aligned} G^{\mathrm{I}}(\varepsilon) &= G^{\mathrm{H}}(\varepsilon) + G^{\mathrm{H}}(\varepsilon)\, (V^{\mathrm{I}} - V^{\mathrm{H}})\, G^{\mathrm{I}}(\varepsilon) \quad , \\ &= G^{\mathrm{H}}(\varepsilon) + G^{\mathrm{H}}(\varepsilon)\, \Delta V\, G^{\mathrm{I}}(\varepsilon) \quad . \end{aligned} \tag{2.23}$$

For simplicity, we have omitted the position dependence in the potentials and the Green function $G(\varepsilon)$. Eq. (2.23) is solved in a finite region surrounding the impurity, since the perturbation it causes is localized in space. V^{I} and V^{H} represent the potentials in the region disturbed by the impurity, with and without the defect, respectively. $G^{\mathrm{I}}(\varepsilon)$ defines the Green function of the system in presence of the impurity, $G^{\mathrm{H}}(\varepsilon)$ is the Green function of the undisturbed host. The previous Dyson equation given in Eq. (2.23) can be understood in terms of multiple scattering events due to the perturbing potential ΔV. When expanding $G^{\mathrm{I}}(\varepsilon)$ in the right hand side we obtain:

$$G^{\mathrm{I}}(\varepsilon) = G^{\mathrm{H}}(\varepsilon) + G^{\mathrm{H}}(\varepsilon)\, \Delta V\, G^{\mathrm{H}}(\varepsilon) + G^{\mathrm{H}}(\varepsilon)\, \Delta V\, G^{\mathrm{H}}(\varepsilon)\, \Delta V\, G^{\mathrm{H}}(\varepsilon) + \ldots \quad . \tag{2.24}$$

The previous equation represents the expansion of the Green function into Born series.

2.3.1 Ground state expectation value of an observable from the Green function

Using the spectral representation of the Green function given by Eq. (2.20) combined with the following identity,

$$\lim_{\eta\to 0^+} \frac{1}{\varepsilon \pm \mathrm{i}\eta - \varepsilon_i} = \mathcal{P}\left(\frac{1}{\varepsilon - \varepsilon_i}\right) \mp \mathrm{i}\pi\delta(\varepsilon - \varepsilon_i) \quad , \tag{2.25}$$

where $\mathcal{P}$ is the principal value, we can easily show that the ground state expectation value of any observable represented by a single-particle operator $\hat{\mathcal{O}}$ at zero temperature is expressed through the Green function as:

$$\langle\hat{\mathcal{O}}\rangle = -\frac{1}{\pi}\mathrm{Im}\int_{-\infty}^{\varepsilon_\mathrm{F}} \mathrm{d}\varepsilon\, \mathrm{Tr}\,\hat{\mathcal{O}}\, G(\varepsilon) \quad . \tag{2.26}$$

ε_F is the Fermi energy of the system. The trace is taken over all degrees of freedom, namely: position, orbitals and spin. The electron density, which is the central quantity in DFT as discussed in Sec. 2.2 can be easily computed in the position representation via:

$$n(\vec{r}) = -\frac{1}{\pi}\mathrm{Im}\int_{-\infty}^{\varepsilon_\mathrm{F}} \mathrm{d}\varepsilon\, \mathrm{Tr}\, G(\vec{r},\vec{r},\varepsilon) \quad . \tag{2.27}$$

For spin-polarized systems discussed in Sec. 2.2.2, the Kohn-Sham orbitals are replaced by spinors. Therefore, the Green function acquires a spin structure and is defined as:

$$\boldsymbol{G}(\vec{r},\vec{r}',\varepsilon+\mathrm{i}\eta) = \begin{pmatrix} G^{\uparrow\uparrow}(\vec{r},\vec{r}',\varepsilon+\mathrm{i}\eta) & G^{\downarrow\uparrow}(\vec{r},\vec{r}',\varepsilon+\mathrm{i}\eta) \\ G^{\uparrow\downarrow}(\vec{r},\vec{r}',\varepsilon+\mathrm{i}\eta) & G^{\downarrow\downarrow}(\vec{r},\vec{r}',\varepsilon+\mathrm{i}\eta) \end{pmatrix} \quad . \tag{2.28}$$

The bold symbol is used to indicate that the Green function is a matrix in spin space. The spin magnetization density $\vec{m}(\vec{r})$ is also a quantity of interest and is simply given by:

$$\vec{m}(\vec{r}) = -\frac{1}{\pi}\mathrm{Im}\int_{-\infty}^{\varepsilon_\mathrm{F}} \mathrm{d}\varepsilon\, \mathrm{Tr}\,\vec{\boldsymbol{\sigma}}\,\boldsymbol{G}(\vec{r},\vec{r},\varepsilon) \quad . \tag{2.29}$$

We have briefly discussed the utility of Green functions for treating defects embedded in periodic solids. We defined the single particle Green function, and related it to the ground state expectation value of observables used in density functional theory. In the next section, we explain how the Green function is computed in practice in the framework of multiple scattering theory.

2.4 The Korringa-Kohn-Rostoker Green function method

The Green function is obtained in practice using the Korringa-Kohn-Rostoker (KKR) method, initially proposed by Korringa, Kohn and Rostoker [85, 86]. This method consists of dividing the space into Voronoi cells, each cell is constituted of a scattering center and its neighboring points in space. The scattering centers usually represent atoms in a solid. In our description of the method we limit ourselves to the atomic sphere approximation

(ASA), where the Voronoi cell is a sphere and the scattering potential is radially symmetric (*i.e.* $V(\vec{r}) = V(r)$), and we include the full charge density. A general discussion including a full-potential treatment can be found in Ref. [96]. For the magnetic case we introduce the rigid spin approximation (*i.e.* $\vec{B}^i_{\text{xc}}(\vec{r})$ is parallel to $\vec{e}_i$ which represents the average magnetization direction within each cell i). The electronic structure is obtained within two steps. First, each atomic region is considered separately as a single atom. This single-site problem is solved by expanding the electronic wave function in a spherical harmonics basis, then solving the radial Schrödinger equation numerically in presence of the atomic potential. The boundary conditions are specified in the second step, which consists in connecting the atomic sites to each other, using multiple scattering theory. When an electron is scattered by the potential of an atomic region, the outgoing electronic wave can be represented by the incoming wave and a transition matrix (t-matrix). The intercell electron propagation is described by the structural Green function defined in Sec. 2.4.3, it consists of a free electron Green function renormalized by the presence of atomic potentials via the t-matrix. The latter ensures that an electron wave coming into a cell is a superposition of the outgoing waves from the rest of the cells forming the solid. Therefore, the Green function in the KKR representation is a sum of two contributions: an onsite and a non-local one.

2.4.1 Free electrons

Before discussing the KKR formalism applied for real crystals, we first apply it to the simple case of a three-dimensional free electron gas (*i.e.* $V(\vec{r}) = 0$). The electronic wave function $\psi_{\vec{k}}(\vec{r})$ is a plane wave and is expanded in the real spherical harmonics basis $Y_L(\hat{r}) = Y_L(\theta_r, \phi_r)$ and $\vec{r}$ is expressed as $\vec{r} = (r\cos\phi_r \sin\theta_r, r\sin\phi_r \sin\theta_r, r\cos\theta_r)$ in Cartesian coordinates. L is a combined index for the orbital angular moment quantum numbers (l, m):

$$\begin{aligned} \psi_{\vec{k}}(\vec{r}) &= e^{\mathrm{i}\vec{k}\cdot\vec{r}} \quad , \\ &= \sum_L 4\pi \mathrm{i}^l j_l(kr)\, Y_L(\hat{r})\, Y_L(\hat{k}) \quad . \end{aligned} \tag{2.30}$$

The wave vector $\vec{k}$ is related to the energy ε via $k = |\vec{k}| = \sqrt{\varepsilon}$, and $r = |\vec{r}|$. $j_l(kr)$ is the spherical Bessel function of first kind. The Green function connecting a point located at a position $\vec{r}$ in space to a point located at $\vec{r}\,'$ in a three-dimensional free electron gas, for an energy ε is given by:

$$g(\vec{r}, \vec{r}\,', \varepsilon) = -\frac{1}{4\pi} \frac{e^{\mathrm{i}k|\vec{r}-\vec{r}\,'|}}{|\vec{r}-\vec{r}\,'|} \quad . \tag{2.31}$$

$g(\vec{r}, \vec{r}\,', \varepsilon)$ is expanded in its turn in a real spherical harmonics basis:

$$\begin{aligned} g(\vec{r}, \vec{r}\,', \varepsilon) &= -\mathrm{i}k \sum_L Y_L(\hat{r})\, g_l(r, r\,', \varepsilon)\, Y_L(\hat{r}\,') \quad , \\ &= -\mathrm{i}k \sum_L Y_L(\hat{r})\, j_l(kr_<)\, h_l(kr_>)\, Y_L(\hat{r}\,') \quad . \end{aligned} \tag{2.32}$$

$g_l(r, r', \varepsilon)$ are the expansion coefficients, $r_{<(>)}$ is the smaller (larger) of the radii r and r', respectively. $j_l(kr)$ and $h_l(kr')$ represent the spherical Bessel and Hankel functions of first kind, respectively. In the limit $r \to 0$, $j_l(kr)$ is finite while $h_l(kr)$ diverges. In the spirit of the KKR method, we now divide the space occupied by the three-dimensional free electron gas into cells, each cell is centered at a position $\vec{X}_i$ from the origin and define $\vec{x}$ as an incell position according to $\vec{X}_i$, therefore, $\vec{r} = \vec{X}_i + \vec{x}$. The Green function given in Eq. (2.32) is rewritten in the KKR representation as:

$$\begin{aligned} g(\vec{x} + \vec{X}_i, \vec{x}' + \vec{X}_j, \varepsilon) = -\mathrm{i}k \sum_L Y_L(\hat{x})\, j_l(kx_<)\, h_l(kx_>)\, Y_L(\hat{x}')\, \delta_{ij} \\ + \sum_{LL'} Y_L(\hat{x})\, j_l(kx)\, g^{ij}_{LL'}(\varepsilon)\, j_{l'}(kx')\, Y_{L'}(\hat{x}') \quad . \end{aligned} \tag{2.33}$$

$g^{ij}_{LL'}(\varepsilon)$ are called structural Green functions or structure constants, they can be computed as follows:

$$g^{ij}_{LL'}(\varepsilon) = -4\pi\mathrm{i}k\,(1-\delta_{ij}) \sum_{L''}^{l+l'} \mathrm{i}^{l-l'+l''} C_{LL'L''}\, h_{L''}(k|\vec{X}_i - \vec{X}_j|)\, Y_{L''}(\hat{X}_i - \hat{X}_j) \quad . \tag{2.34}$$

The coefficients $C_{LL'L''}$ are the Gaunt coefficients:

$$C_{LL'L''} = \int\int \mathrm{d}\phi_x\, \mathrm{d}\theta_x\, \sin\theta_x\, Y_L(\hat{x})\, Y_{L'}(\hat{x})\, Y_{L''}(\hat{x}) \quad . \tag{2.35}$$

θ_x and ϕ_x are the polar and azimuthal angles in spherical coordinates, respectively. $\vec{x}$ can be expressed as: $\vec{x} = (x\cos\phi_x \sin\theta_x, x\sin\phi_x \sin\theta_x, x\cos\theta_x)$ in the Cartesian basis.

2.4.2 Single site problem

We now consider the presence of a finite potential $V^i(\vec{x})$ within each cell i and solve the Schrödinger equation to determine the electronic wave function $\psi^i_{\vec{k}}(\vec{x})$. Similarly to Eq. (2.30) the electronic wave function is expanded in a real spherical harmonics basis:

$$\psi^i_{\vec{k}}(\vec{x}) = \sum_L 4\pi\mathrm{i}^l R^i_{LL'}(x,\varepsilon)\, Y_{L'}(\hat{x})\, Y_L(\hat{k}) \quad . \tag{2.36}$$

Assuming a spherically symmetric potential (*i.e.* $V(\vec{x}) = V(x)$), there is no mixing between the angular momentum channels of $R^i_{LL'}(x,\varepsilon)$. Thus, $R^i_{LL'}(x,\varepsilon)$ is diagonal in the L-subspace and Eq. (2.36) is simply written as:

$$\psi^i_{\vec{k}}(\vec{x}) = \sum_L 4\pi\mathrm{i}^l R^i_l(x,\varepsilon)\, Y_L(\hat{x})\, Y_L(\hat{k}) \quad . \tag{2.37}$$

For simplicity, we consider a non spin-polarized system and the radial Schrödinger equation reads:

$$\left[-\frac{1}{x}\frac{\partial^2}{\partial x^2}x + \frac{l(l+1)}{x^2} + V^i(x) - \varepsilon\right] R^i_l(x,\varepsilon) = 0 \quad , \tag{2.38}$$

The formal solution of Eq. (2.38) is given by the Lippman-Schwinger equation:

$$R_l^i(x,\varepsilon) = j_l(kx) + \int_0^{x_\mathrm{m}} \mathrm{d}x' x'^2 \, g_l(x,x',\varepsilon)\, V^i(x')\, R_l^i(x',\varepsilon) \quad . \tag{2.39}$$

The previous equation describes the propagation of an incident partial wave $j_l(kx)$ eigenstate of the three-dimensional free electron gas (see Eq. (2.30)) scattering at a potential $V^i(x)$. x_m is the radius of the atomic sphere. $R_l^i(x,\varepsilon)$ is called the regular solution of the Schrödinger equation, as it remains finite for $x \to 0$. When $V^i(x)$ vanishes, $R_l^i(x,\varepsilon)$ is simply given by $j_l(kx)$. Considering $x > x_\mathrm{m}$ and the definition of $g_l(x,x',\varepsilon)$ given in Eq. (2.32), we can introduce the t-matrix as:

$$t_l^i(\varepsilon) = \int_0^{x_\mathrm{m}} \mathrm{d}x' x'^2 \, j_l(kx')\, V^i(x')\, R_l^i(x',\varepsilon) \quad . \tag{2.40}$$

$t_l^i(\varepsilon)$ contains the information about the scattering phase shifts $\delta_l^i(\varepsilon)$ which are discussed in details in Sec. 3.3 for a two dimensional electron gas. The t-matrix will be used in the next section on multiple scattering to compute the structural Green function. Eq. (2.38) also has an irregular solution $H_l^i(x,\varepsilon)$ which diverges when $x \to 0$, it is given by:

$$H_l^i(x,\varepsilon) = h_l(kx)\, \beta_l^i + \int_0^{x_\mathrm{m}} \mathrm{d}x' x'^2 \, g_l(x,x',\varepsilon)\, V^i(x')\, H_l^i(x',\varepsilon) \quad . \tag{2.41}$$

The coefficient β_l^i defines the boundary condition and ensures that $H_l^i(x,\varepsilon) = h_l(kx)$ for $x > x_m$. The former is defined as:

$$\beta_l^i = 1 + \mathrm{i}k \int_0^{x_\mathrm{m}} \mathrm{d}x' x'^2 \; j_l(kx')\, V^i(x')\, H_l^i(x',\varepsilon) \quad . \tag{2.42}$$

In analogy to the first term in Eq. (2.33), when a spherical scattering potential $V^i(x)$ is present in the cell i, the single site Green function is given as a sum over L of products of regular and irregular solutions:

$$\begin{aligned} G^{\mathrm{s},i}(\vec{x},\vec{x}',\varepsilon) &= -\mathrm{i}k \sum_L Y_L(\hat{x})\, R_l^i(x_<,\varepsilon)\, H_l^i(x_>,\varepsilon)\, Y_L(\hat{x}') \quad , \\ &= \sum_L Y_L(\hat{x})\, G_l^{\mathrm{s},i}(x,x',\varepsilon)\, Y_L(\hat{x}') \quad . \end{aligned} \tag{2.43}$$

$G^{\mathrm{s},i}(\vec{x},\vec{x}',\varepsilon)$ is the single site ASA Green function. This form is valid for real energies. However, for complex energies which are used in practice to reduce the numerical effort (see discussion below), one must distinguish between the right and left solutions. In presence of non-collinear magnetism or spin-orbit interaction the right and left solutions are not equivalent anymore, and the left must computed explicitly as discussed in Sec. 2.4.5.

The Green function has poles at the eigenenergies ε_i (see Eq. (2.20)). Therefore, the evaluation of the energy integral given in Eq. (2.27) translates into summing up delta functions numerically, this is very inconvenient and cannot be achieved. In order to overcome this issue the energy integral must be extended to a contour integral in the upper half ($\mathrm{Im}\,\varepsilon > 0$) of the complex plane [97]. This extension is possible since the retarded Green

function given in Eq. (2.20) is analytical in the upper complex plane (because for $\eta \to 0^+$ the poles of the Green function are shifted to lower half with $\mathrm{Im}\,\varepsilon < 0$). Due to the imaginary part in the energy, the poles are broadened and fewer points are needed to perform the energy integration (typically $40 - 50$ energy points). The drawback when using complex energies is that the operator which defines the regular (or irregular) solutions $(\varepsilon - H)$ becomes non-Hermitian, thus, we must distinguish between the right and left solutions. Nonetheless, in ASA and in absence of spin-orbit interaction or non-collinear magnetism the left and right solutions are equivalent [96].

2.4.3 Multiple scattering problem

After solving the single site problem, we consider a collection of scattering centers. The position of each scattering center is given by a lattice vector $\vec{X}_i$. First, we assume that the KKR Green function can be decomposed into an onsite and a multiple scattering part. Second, we impose that the KKR Green function obeys the following Dyson equation:

$$\begin{aligned} G(\vec{x}+\vec{X}_i,\vec{x}'+\vec{X}_j,\varepsilon) =& g(\vec{x}+\vec{X}_i,\vec{x}'+\vec{X}_j,\varepsilon) + \sum_k \int \mathrm{d}\vec{x}'' g(\vec{x}+\vec{X}_i,\vec{x}''+\vec{X}_k,\varepsilon) \\ & \times V^k(x''+\vec{X}_k)\, G(\vec{x}''+\vec{X}_k,\vec{x}'+\vec{X}_j,\varepsilon) \quad , \end{aligned} \tag{2.44}$$

where the sum on k includes all lattice positions. We can derive a Dyson equation for the structural Green function $G^{ij}_{LL'}(\varepsilon)$, which involves the structure constant $g^{ij}_{LL'}(\varepsilon)$ and the single site scattering matrices $t^i_l(\varepsilon)$:

$$G^{ij}_{LL'}(\varepsilon) = g^{ij}_{LL'}(\varepsilon) + \sum_k \sum_{L''} g^{ik}_{LL''}(\varepsilon)\, t^k_{l''}(\varepsilon)\, G^{kj}_{L''L'}(\varepsilon) \quad . \tag{2.45}$$

The physical interpretation of Eq. (2.45) can be obtained when expanding the second term on the right side into Born series. This shows that Eq. (2.45) describes a free particle which encounters multiple scattering events at each cell i in presence of a potential $V^i(x)$, where the information of the single site scattering is encoded in the $t^i_l(\varepsilon)$ matrices. In practice, the algebraic Dyson equation is solved by exploiting the translation symmetry of the system. Assuming that the unit cell contains N_{uc} atoms, each atomic position in the crystal is given by:

$$\vec{X}_{i\mu} = \vec{X}_i + \vec{X}_\mu \quad . \tag{2.46}$$

$\vec{X}_i$ being the lattice vector and $\vec{X}_\mu$ the vector connecting the basis atom to the lattice position. The Fourier transform of Eq. (2.45) to k-space is performed:

$$G^{\mu\nu}_{LL'}(\vec{k},\varepsilon) = \sum_j G^{ij,\mu\nu}_{LL'}(\varepsilon)\, e^{-\mathrm{i}\vec{k}\cdot(\vec{X}_i - \vec{X}_j)} \quad . \tag{2.47}$$

The choice of i is arbitrary in Eq. (2.47) since the system is periodic. The sum on j includes all lattice positions. However, the introduction of repulsive potentials reduces the spatial extension of $G^{ij,\mu\nu}_{LL'}(\varepsilon)$ as discussed in Ref. [98]. $G^{\mu\nu}_{LL'}(\vec{k},\varepsilon)$ is computed using a

matrix inversion and Fourier transformed back to obtain $G^{ij,\mu\nu}_{LL'}(\varepsilon)$:

$$G^{ij,\mu\nu}_{LL'}(\varepsilon) = \frac{1}{V_{\mathrm{BZ}}} \int \mathrm{d}\vec{k} \left[\left(1 - \boldsymbol{t}(\varepsilon)\, \boldsymbol{g}(\vec{k},\varepsilon) \right)^{-1} \boldsymbol{g}(\vec{k},\varepsilon) \right]^{\mu\nu}_{LL'} e^{\mathrm{i}\vec{k}\cdot(\vec{X}_i - \vec{X}_j)} \quad . \tag{2.48}$$

V_{BZ} is the volume of the Brillouin zone. $\boldsymbol{g}(\vec{k},\varepsilon)$ is a matrix in (L, L') and (μ,ν) subspaces, it represents the Fourier transform of the structure constant, while $\boldsymbol{t}(\varepsilon)$ is a matrix diagonal in (L, L') for spherical potentials and diagonal in (μ,ν) as well, since it is a site diagonal quantity. After computing the single site part of the Green function (see Sec. 2.4.2) and the structural Green function given by Eq. (2.48), the full KKR Green function – including the onsite and structural parts – is written similarly to the free electron case (see Eq. (2.33)) as:

$$\begin{aligned} G(\vec{x} + \vec{X}_i, \vec{x}\,' + \vec{X}_j, \varepsilon) = & \sum_{L} Y_L(\hat{x})\, G^{\mathrm{s},i}_{l}(x, x', \varepsilon)\, Y_L(\hat{x}\,')\, \delta_{ij} \\ & + \sum_{LL'} Y_L(\hat{x})\, R^i_l(x,\varepsilon)\, G^{ij}_{LL'}(\varepsilon)\, R^j_{l'}(x',\varepsilon)\, Y_{L'}(\hat{x}\,') \quad , \end{aligned} \tag{2.49}$$

where $R^i_l(x,\varepsilon)$ represents the regular solution of Eq. (2.38) in cell i.

2.4.4 Charge neutrality and Lloyd's formula

The electron density obtained from Eq. (2.27) using the KKR Green function fails to produce the electron charge equalizing the nuclear charge Q. This is due to the introduction of an $L_{\max}$ cutoff in the sums of Eq. (2.49) (without the L-truncation *i.e.* $L_{\max} \to \infty$, $n(\vec{r})$ is normalized to Q). In practice, a finite value for $L_{\max}$ is used which leads to a shift of the Fermi energy. This procedure is not problematic for metals, however, for gapped systems such as semiconductors, insulators or topological insulators, it can lead to a shift of ε_{F} into the valence or conduction band making these materials metals [99]. This issue can be solved using Lloyd's formula [100, 101]. When restricting ourselves to the non spin-polarized case, the integrated density of states (DOS), $N(\varepsilon)$, reads:

$$N(\varepsilon) = \int_{-\infty}^{\varepsilon} \mathrm{d}\varepsilon' n(\varepsilon') \quad , \tag{2.50}$$

it can also be rewritten using the LLoyd's formula as:

$$N(\varepsilon) = N^{\mathrm{F}}(\varepsilon) + \frac{2}{\pi} \mathrm{Im} \sum_i \mathrm{Tr} \ln \boldsymbol{\alpha}^i(\varepsilon) - \frac{2}{\pi} \mathrm{Im}\, \mathrm{Tr} \ln \boldsymbol{M}(\varepsilon) \quad . \tag{2.51}$$

The first term on the right hand side of Eq. (2.51) represents the integrated DOS of free electrons. The sum over i includes all the atoms contained in the system. The first trace is over the L-index while the second one is over L and the cell index i. The second term on the right hand is the contribution of the single site scattering to the integrated DOS, α^i is the so-called α-matrix, for spherical potentials it is given by:

$$\alpha^i_l(\varepsilon) = 1 - \mathrm{i}k \int_0^{x_{\mathrm{m}}} x'^2 \mathrm{d}x'\, h_l(kx')\, V^i(x')\, R^i_l(x',\varepsilon) \quad . \tag{2.52}$$

The last term on the right hand in Eq. (2.51) is the multiple scattering contribution to the integrated DOS, $\boldsymbol{M}(\varepsilon)$ is the KKR matrix and is computed using the structure constants and t-matrices:

$$\boldsymbol{M}^{ij}_{LL'}(\varepsilon) = \delta_{ij}\,\delta_{LL'} + g^{ij}_{LL'}(\varepsilon)\,t^{j}_{l'}(\varepsilon) \quad . \tag{2.53}$$

The Lloyd's formula provides the integrated DOS over all space, but the traces in Eq. (2.51) still requires an $L_{\max}$ cutoff. However, neglecting the matrix elements with $L > L_{\max}$ in Eq. (2.51) causes no problem, since this would mean replacing the potential by a projection potential acting in the subspace $L < L_{\max}$ [101]. Therefore, Eq. (2.51) procures the correct integrated DOS when using a finite $L_{\max}$. The remaining task is now to use the $N(\varepsilon)$ obtained from Lloyd's formula to renormalize the electron density computed from the truncated KKR Green function. On the one hand, the electron density calculated from the truncated Green function reads:

$$\tilde{n}(\vec{x}+\vec{X}_i) = -\frac{2}{\pi}\sum_n \mathrm{Im}\left[\omega_n\,\tilde{G}(\vec{x}+\vec{X}_i,\vec{x}+\vec{X}_i,\varepsilon_n)\right] \quad . \tag{2.54}$$

The factor 2 in the previous equation accounts for spin up and down. The sum over n represents the discretized integral over energy using a contour in the complex plane as discussed previously. ω_n represent the complex energy integration weight for the energies ε_n. Thus, the electronic charge obtained from the truncated Green function is then:

$$\begin{aligned}\tilde{Q} &= \sum_i \int \mathrm{d}\vec{x}\,\tilde{n}(\vec{x}+\vec{X}_i) \quad , \\ &= -\frac{2}{\pi}\sum_i \int \mathrm{d}\vec{x}\ \sum_n \mathrm{Im}\left[\omega_n\,\tilde{G}(\vec{x}+\ \vec{X}_i,\vec{x}+\vec{X}_i,\varepsilon_n)\right] \quad .\end{aligned} \tag{2.55}$$

On the other hand, the normalized charge Q is:

$$Q = \sum_n \mathrm{Im}\left[\omega_n\,n(\varepsilon_n)\right] \quad , \tag{2.56}$$

where $n(\varepsilon) = \frac{\mathrm{d}N(\varepsilon)}{\mathrm{d}\varepsilon}$ and $N(\varepsilon)$ is obtained using Eq. (2.51). Comparing Eq. (2.55) and Eq. (2.56) gives the condition to ensures charge neutrality (*i.e.* $\tilde{Q} = Q$) in the system:

$$-\frac{2}{\pi}\,\lambda_n \int_V \mathrm{d}\vec{x}\ \mathrm{Im}\left[\omega_n\,\tilde{G}(\vec{x}+\vec{X}_i,\vec{x}+\vec{X}_i,\varepsilon_n)\right] = \mathrm{Im}\left[\omega_n\,n(\varepsilon_n)\right] \quad , \tag{2.57}$$

where λ_n are coefficients introduced to renormalize the energy integration weights ω_n in order to agree with Lloyd's formula and ensure charge neutrality.

2.4.5 Spin-orbit interaction in KKR

We now discuss the spin-orbit interaction (SOI) which, combined with the breaking of inversion symmetry is at the core of most effects presented in this thesis, including the Dzyaloshinskii-Moriya interaction, the Rashba effect and the edge states observed in topological insulators. The SOI can be obtained from an expansion of the Dirac equation and

retaining terms up $\frac{v^2}{c^2}$ as shown in Ref. [102], v is the magnitude of the electron velocity and c is the speed of light. The SOI Hamiltonian is given by:

$$\boldsymbol{H}_{\text{SOI}} = -\frac{\alpha^2}{2}\,\vec{\boldsymbol{\sigma}}\cdot(e\vec{E}(\vec{x})\times\vec{p}) \quad . \tag{2.58}$$

$\alpha \sim \frac{1}{137}$ is the fine structure constant. Classically, the SOI can be viewed as an interaction between the electron spin and the magnetic field emerging in its rest frame as a result of its motion in an electric field $\vec{E}(\vec{x}) = -\frac{1}{e}\vec{\nabla}\,V(\vec{x})$. $\boldsymbol{H}_{\text{SOI}}$ is added to the left hand side of Eq. (2.38) within each atomic cell i. For spherically symmetric potentials, Eq. (2.58) can be simplified even further to show explicitly the orbital momentum $\vec{L}$ coupled to the spin:

$$\begin{aligned}\boldsymbol{H}_{\text{SOI}} &= \frac{\alpha^2}{2}\,\vec{\boldsymbol{\sigma}}\cdot\left(\frac{1}{x}\frac{\mathrm{d}V^i(x)}{\mathrm{d}x}\vec{x}\times\vec{p}\right) \quad , \\ &= \frac{\alpha^2}{2x}\frac{\mathrm{d}V^i(x)}{\mathrm{d}x}\,\vec{\boldsymbol{\sigma}}\cdot(\vec{x}\times\vec{p}) \quad , \\ &= \lambda(x)\,\vec{L}\cdot\vec{\boldsymbol{\sigma}} \quad .\end{aligned} \tag{2.59}$$

Where the prefactor $\lambda(x) = \frac{\alpha^2}{2x}\frac{\mathrm{d}V^i(x)}{\mathrm{d}x}$. When $\boldsymbol{H}_{\text{SOI}}$ is included into Eq. (2.38), the Lippman-Schwinger equation reads:

$$\begin{aligned}&\begin{pmatrix} R^{i,\uparrow\uparrow}_{lm}(x,\varepsilon) & R^{i,\uparrow\downarrow}_{lm}(x,\varepsilon) \\ R^{i,\downarrow\uparrow}_{lm}(x,\varepsilon) & R^{i,\downarrow\downarrow}_{lm}(x,\varepsilon)\end{pmatrix} = \begin{pmatrix} j_l(kx) & 0 \\ 0 & j_l(kx)\end{pmatrix} + \sum_{m'}\int \mathrm{d}x' x'^2\, g_l(x,x',\varepsilon) \\ &\begin{pmatrix} V(x') - \mathrm{i}m'\,\delta_{m,-m'}\lambda(x') & \alpha^-_{m,m'}\lambda(x') \\ \alpha^+_{m,m'}\lambda(x') & V(x') + \mathrm{i}m'\,\delta_{m,-m'}\lambda(x')\end{pmatrix}\begin{pmatrix} R^{i,\uparrow\uparrow}_{lm'}(x',\varepsilon) & R^{i,\uparrow\downarrow}_{lm'}(x',\varepsilon) \\ R^{i,\downarrow\uparrow}_{lm'}(x',\varepsilon) & R^{i,\downarrow\downarrow}_{lm'}(x',\varepsilon)\end{pmatrix} .\end{aligned} \tag{2.60}$$

In the previous equation the spin structure of $R^{i,\sigma\sigma'}_{lm}(x,\varepsilon)$ is shown explicitly. The regular solutions are no longer diagonal in spin space and depend on m due to the SOI, $\{\alpha^-_{m,m'}, \alpha^+_{m,m'}\}$ are coefficients that couple regular solutions with different m values (the expressions of these coefficients can be found in Ref. [103]). A possible solution to Eq. (2.60) is to expand it in a Born series and solve iteratively. This is a good approach for the regular solution, however, it fails for the irregular one since it diverges near the nucleus. Therefore, Eq. (2.60) must be solved exactly, in practice this is done using a Chebychev polynomial basis [96]. Another aspect that must be taken into account in presence of the SOI, is the left solutions which must be computed separately. Indeed, the right and left solutions are defined as:

$$\begin{cases}(\varepsilon - \boldsymbol{H})\,\boldsymbol{R} = 0 \quad , \\ \bar{\boldsymbol{R}}\,(\varepsilon - \boldsymbol{H}) = 0 \quad .\end{cases} \tag{2.61}$$

The dependences on $(r, l$ and $\varepsilon)$ were omitted for simplicity. $\boldsymbol{R}$ and $\bar{\boldsymbol{R}}$ are matrices in spin space denoting the right and left solutions, respectively. They can be expressed in terms of the Lippmann-Schwinger equation as:

$$\begin{cases}\boldsymbol{R} = j + g\,\boldsymbol{V}\,\boldsymbol{R} \quad , \\ \bar{\boldsymbol{R}} = j + \bar{\boldsymbol{R}}\,\boldsymbol{V}\,g \quad .\end{cases} \tag{2.62}$$

j is the spherical Bessel functions and g is the free electron Green function. Eq. (2.62) shows that when the potential $\boldsymbol{V}$ is diagonal in spin space the right and left solutions are equivalent, however, the presence of the SOI or non-collinear magnetism creates non-zero off-diagonal components in $\boldsymbol{V}$, thus, the left solution differs from the right one and must be explicitly computed.

As previously mentioned, in the presence of SOI, the left and right solutions are inequivalent, the single site Green function expansion in real spherical harmonics is non-diagonal in m, $\boldsymbol{G}^{\mathrm{s},i}_{lm,m'}(x,x',\varepsilon)$ in cell i is rewritten as [96]:

$$\begin{aligned}\boldsymbol{G}^{\mathrm{s},i}_{lm,m'}(x,x',\varepsilon) = -\mathrm{i}k \Big[&\Theta(x'-x)\,\boldsymbol{R}^i_{lm}(x,\varepsilon)\,\bar{\boldsymbol{H}}^i_{lm'}(x',\varepsilon) \\ &+\Theta(x-x')\,\boldsymbol{H}^i_{lm}(x,\varepsilon)\,\bar{\boldsymbol{R}}^i_{lm'}(x',\varepsilon)\Big] \quad .\end{aligned} \tag{2.63}$$

Where $\Theta(x)$ is the Heaviside step function and $\boldsymbol{G}^{\mathrm{s,i}}_{lm,m'}(x,x',\varepsilon)$ depends explicitly on the left and right solutions. Then, the full KKR Green function reads [96]:

$$\begin{aligned}\boldsymbol{G}(\vec{x}+\vec{X}_i,\vec{x}\,'+\vec{X}_j,\varepsilon) = &\sum_{LL'} Y_L(\hat{x})\,\boldsymbol{G}^{\mathrm{s},i}_{lm,m'}(x,x',\varepsilon)\,Y_{L'}(\hat{x}\,')\,\delta_{ij}\,\delta_{ll'} \\ &+\sum_{LL'} Y_L(\hat{x})\,\boldsymbol{R}^i_{lm}(x,\varepsilon)\,\boldsymbol{G}^{ij}_{LL'}(\varepsilon)\,\bar{\boldsymbol{R}}^j_{l'm'}(x',\varepsilon)\,Y_{L'}(\hat{x}\,') \quad .\end{aligned} \tag{2.64}$$

2.4.6 KKR in a projection basis

In the KKR method, the Green function is represented in a radial and energy dependent basis, namely the regular and irregular solutions of the radial Schrödinger equation $R_l^{i,\sigma\sigma'}(x,\varepsilon)$ and $H_l^{i,\sigma\sigma'}(x,\varepsilon)$. Nonetheless, the Green function can be written in an energy independent basis which reproduces the ground state properties with reliability. In practice, we build an energy independent radial basis starting from the normalized regular solutions, chosen at a set of energies ε_{b} in the valence band:

$$\phi^{\sigma}_{ilb}(x) = \frac{R_l^{i,\sigma\sigma}(x,\varepsilon_{\mathrm{b}})}{\sqrt{\int_0^{x_{\mathrm{m}}} \mathrm{d}x\, x^2\, R_l^{i,\sigma\sigma}(x,\varepsilon_{\mathrm{b}})}} \quad . \tag{2.65}$$

$\phi^{\sigma}_{ilb}(x)$ is the radial basis function for an atom i in absence of SOI with a value l of the angular momentum quantum number and with a spin σ. Then for each i, l and spin channel σ, we diagonalize separately the overlap matrix:

$$\mathcal{O}^{il}_{bb'} = \int_0^{x_{\mathrm{m}}} \mathrm{d}x\, x^2\, \phi^{\sigma}_{ilb}(x)\,\phi^{\sigma}_{ilb'}(x) \quad , \tag{2.66}$$

and keep the eigenvectors with the two largest eigenvalues, which define linear combinations of the respective input radial basis functions, and are used to define the basis function for atom i and angular momentum quantum number l. For our calculations, four energies

are enough to give an accurate description of the Green function [41]. In the new constructed basis, we now write the Green function as:

$$G^{\sigma\sigma'}(\vec{x}+\vec{X}_i,\vec{x}\,'+\vec{X}_j,\varepsilon)=\sum_{LL'}Y_L(\hat{x})\,G^{\sigma\sigma'}_{iL,jL'}(x,x',\varepsilon)\,Y_{L'}(\hat{x}\,') \quad , \tag{2.67}$$

with

$$G^{\sigma\sigma'}_{iL,jL'}(x,x',\varepsilon)=\sum_{bb'}\phi^{\sigma}_{ilb}(x)\,G^{\sigma\sigma'}_{iLb,jL'b'}(\varepsilon)\,\phi^{\sigma'}_{jl'b'}(x') \quad . \tag{2.68}$$

The spin dependence of the Green function is shown explicitly. The introduction of a projection basis to simplify the KKR Green function is a very useful technique which allows to separate between the radial and energy dependence of the Green function. This proves to be very useful when computing more complicated quantities such as the Kohn-Sham susceptibility discussed in Sec. 2.6.3 or electron-magnon self-energies [40, 104].

2.5 Magnetic anisotropy

In magnetic materials, the magnetization tends to align along a certain direction according to its structural axes. This is due to the magnetic anisotropy energy. The direction which minimizes the energy is called the easy-axis. The internal energy of the magnetic system can be expanded with respect to θ and ϕ, which represent the polar and azimuthal angles of the magnetization direction $\vec{M}$, respectively. Usually the expansion is performed in terms of the directional cosines $(\alpha_1,\alpha_2,\alpha_3)=(\sin\theta\cos\phi,\sin\theta\sin\phi,\cos\theta)$ of $\vec{M}$ according to the crystal axes. The crystal symmetry of the system imposes the form of the angular dependence. Hexagonal lattices for example possess a high symmetry axis (along the c-direction). For theses uniaxial systems, the internal energy is written as [105]:

$$\varepsilon_{\text{int}}=\varepsilon_0-\mathcal{K}\,\sin^2\theta-\mathcal{K}'\sin^4\theta-\ldots \quad . \tag{2.69}$$

ε_0 contains the isotropic energy contributions. $\mathcal{K}$ and $\mathcal{K}'$ are called magnetic anisotropy constants. The magnetic anisotropy in solids can have different origins, for example dipolar interactions [106], the latter one is important in bulk materials. Another interaction capable of generating a magnetic anisotropy is the SOI, it is called the magnetocrystalline anisotropy. The presence of SOI leads to a breaking of the spin rotational symmetry, thus, the spin magnetic moment favors a certain orientation in real-space.

In order to understand how the magnetocrystalline anisotropy originates from the SOI, we proceed to second order perturbation theory in λ (λ is the SOI constant). The change in the energy is given by [107]:

$$\Delta\varepsilon_i=\lambda\,\langle\psi_i|\,\vec{L}\cdot\vec{\boldsymbol{\sigma}}\,|\psi_i\rangle+\lambda^2\sum_{j\neq i}\frac{|\,\langle\psi_i|\,\vec{L}\cdot\vec{\boldsymbol{\sigma}}\,|\psi_j\rangle\,|^2}{\varepsilon_i-\varepsilon_j} \quad . \tag{2.70}$$

$|\psi_i\rangle$ and $|\psi_j\rangle$ represent the eigenstates of the unperturbed Hamiltonian associated with the eigenenergies ε_i and ε_j, respectively. $|\psi_i\rangle$ are the eigenstates of the unperturbed Hamiltonian without SOI, thus, the orbital moment is quenched and $\langle\psi_i|\,\vec{L}\,|\psi_i\rangle=0$ as discussed

in Ref. [108]. This makes the first order contribution of the SOI vanish. Thus, after summing up over energies of all occupied states, we obtain the second order contribution of the SOI to the total energy:

$$\Delta\varepsilon_{\mathrm{SOI}} = \lambda^2 \sum_{i\in\mathrm{occ}} \sum_{j\neq i} \frac{|\langle\psi_i|\,\vec{L}\cdot\vec{\boldsymbol{\sigma}}\,|\psi_j\rangle|^2}{\varepsilon_i - \varepsilon_j} \quad , \tag{2.71}$$

where the term inside the sum is odd when swapping indices i and j. Therefore, only the coupling between occupied and unoccupied states will contribute to $\Delta\varepsilon_{\mathrm{SOI}}$:

$$\Delta\varepsilon_{\mathrm{SOI}} = \lambda^2 \sum_{i\in\mathrm{occ}} \sum_{j\in\mathrm{unocc}} \frac{|\langle\psi_i|\,\vec{L}\cdot\vec{\boldsymbol{\sigma}}\,|\psi_j\rangle|^2}{\varepsilon_i - \varepsilon_j} \quad , \tag{2.72}$$

which gives important insights by relating the magnitude of the magnetic anisotropy energy (MAE), obviously it is proportional to λ^2, to the details of the band structure [107].

2.5.1 Magnetic force theorem

In practice, the MAE of a magnetic system can be determined using DFT. It is obtained from total energy differences. For a uniaxial system the internal energy is given by Eq. (2.69). When restricting ourselves to second order in θ in the expansion, the MAE reduces to the anisotropy constant $\mathcal{K}$ which is related to the total energy differences via:

$$\mathcal{K} = \varepsilon_{\mathrm{tot}}(\vec{M} \parallel z) - \varepsilon_{\mathrm{tot}}(\vec{M} \parallel x) \quad . \tag{2.73}$$

The MAE is typically in the meV energy range, therefore, one needs to compute the total energies with high accuracy. In practice, these calculations can be tedious since they require a very high amount of k-points. Adding to that, two self-consistent calculations must be performed (for $\vec{M} \parallel z$ and $\vec{M} \parallel x$). An alternative route is to use the so-called magnetic force theorem [109, 110, 111], it allows to compute $\mathcal{K}$ only using one self-consistent calculation. It states the following: if the change in the charge density $n(\vec{r})$ and spin magnetization density $\vec{m}(\vec{r})$ is small when rotating the spin magnetization (one shot calculation) from the z-axis to the x-axis, then $\mathcal{K}$ is given by the band energy difference between the two magnetic configurations:

$$\begin{aligned} \mathcal{K} &= \varepsilon_{\mathrm{band}}(\vec{M} \parallel z) - \varepsilon_{\mathrm{band}}(\vec{M} \parallel x) \quad , \\ &= \int_{-\infty}^{\varepsilon_{\mathrm{F}}} \mathrm{d}\varepsilon\,(\varepsilon - \varepsilon_{\mathrm{F}})\,(n_{\vec{M}\parallel z}(\varepsilon) - n_{\vec{M}\parallel x}(\varepsilon)) \quad . \end{aligned} \tag{2.74}$$

Where $n_{\vec{M}\parallel z}(\varepsilon)$ $(n_{\vec{M}\parallel x}(\varepsilon))$ represents the DOS of the system when the spin magnetic moment points along z-axis (x-axis). In this thesis, we compute the MAE for single magnetic impurities embedded in a real-space cluster containing nonmagnetic atoms, therefore, we can rewrite $\mathcal{K}$ as a sum over atomic cells:

$$\begin{aligned} \mathcal{K} &= \sum_i \int_{-\infty}^{\varepsilon_{\mathrm{F}}} \mathrm{d}\varepsilon\,(\varepsilon - \varepsilon_{\mathrm{F}})\,(n^i_{\vec{M}\parallel z}(\varepsilon) - n^i_{\vec{M}\parallel x}(\varepsilon)) \quad , \\ &= \mathcal{K}_{\mathrm{A}} + \mathcal{K}_{\mathrm{C}} \quad . \end{aligned} \tag{2.75}$$

The sum in Eq. (2.75) runs over all the atoms contained in the system with a local density of states (LDOS) $n^{k}_{\vec{M}}(\varepsilon)$. $\mathcal{K}_{\mathrm{A}}$ is the MAE at the impurity site, while $\mathcal{K}_{\mathrm{C}}$ is the MAE of remaining atoms in the system. Thus, the MAE is a non-local quantity for which the convergence regarding the cluster size must be achieved [112].

2.5.2 The torque method

As aforementioned, the MAE is typically in the meV range. When using band energy differences discussed previously, the band energies must be computed with a high precision. An alternative way to obtain the MAE within the framework of the magnetic force theorem is to compute the magnetic torque. The magnetic torque acting on the spin magnetic moment $\vec{m}_j$, which points along a direction $\vec{e}_j$ is given by:

$$\begin{aligned}\vec{T}_j &= \frac{\partial \varepsilon_{\text{band}}}{\partial \vec{e}_j} \quad , \\ &= -\frac{1}{\pi} \sum_i \operatorname{Im} \operatorname{Tr}_\sigma \int_{-\infty}^{\varepsilon_{\mathrm{F}}} \mathrm{d}\varepsilon \, (\varepsilon - \varepsilon_{\mathrm{F}}) \, \frac{\partial \boldsymbol{G}_{ii}(\varepsilon)}{\partial \vec{e}_j} \quad .\end{aligned} \tag{2.76}$$

Where $\boldsymbol{G}_{ii}(\varepsilon)$ is a matrix in spin-space, similar to the Green function given in Eq. (2.28) with the real space dependence within each cell i integrated out:

$$\boldsymbol{G}_{ii}(\varepsilon) = \int \mathrm{d}\vec{x} \; \boldsymbol{G}_{ii}(\vec{x}, \vec{x}, \varepsilon) \quad . \tag{2.77}$$

The expression for the torque can be simplified further using the properties of the Green function:

$$\frac{\partial \boldsymbol{G}_{ii}(\vec{x}, \vec{x}, \varepsilon)}{\partial \vec{e}_j} = \int \mathrm{d}\vec{x}' \boldsymbol{G}_{ij}(\vec{x}, \vec{x}', \varepsilon) \, \frac{\partial \boldsymbol{H}^{j}_{\mathrm{KS}}(\vec{x}')}{\partial \vec{e}_j} \, \boldsymbol{G}_{ji}(\vec{x}', \vec{x}, \varepsilon) \quad . \tag{2.78}$$

$\boldsymbol{H}^{j}_{\mathrm{KS}}(\vec{x})$ is the spin polarized Kohn-Sham Hamiltonian given in Eq. (2.17) for cell j. Combining Eq. (2.76) and Eq. (2.78) the torque $\vec{T}_j$ is given by:

$$\vec{T}_j = -\frac{1}{\pi} \sum_i \operatorname{Im} \operatorname{Tr}_\sigma \int_{-\infty}^{\varepsilon_{\mathrm{F}}} \mathrm{d}\varepsilon \int \mathrm{d}\vec{x} \int \mathrm{d}\vec{x}' (\varepsilon - \varepsilon_{\mathrm{F}}) \, \boldsymbol{G}_{ij}(\vec{x}, \vec{x}', \varepsilon) \, \frac{\partial \boldsymbol{H}^{j}_{\mathrm{KS}}(\vec{x}')}{\partial \vec{e}_j} \, \boldsymbol{G}_{ji}(\vec{x}', \vec{x}, \varepsilon) \quad . \tag{2.79}$$

The previous expression can simplified further, once more we can use another property of the Green function:

$$\frac{\partial \boldsymbol{G}_{jj}(\vec{x}', \vec{x}', \varepsilon)}{\partial \varepsilon} = -\sum_i \int \mathrm{d}\vec{x} \, \boldsymbol{G}_{ji}(\vec{x}', \vec{x}, \varepsilon) \, \boldsymbol{G}_{ij}(\vec{x}, \vec{x}', \varepsilon) \quad . \tag{2.80}$$

The preceding identity is used to derive the Lloyd's formula given in Eq. (2.51) as done in Ref. [95]. After substitution, the torque takes the following form:

$$\vec{T}_j = \frac{1}{\pi} \operatorname{Im} \operatorname{Tr}_\sigma \int_{-\infty}^{\varepsilon_{\mathrm{F}}} \mathrm{d}\varepsilon \int \mathrm{d}\vec{x} \, (\varepsilon - \varepsilon_{\mathrm{F}}) \, \frac{\partial \boldsymbol{G}_{jj}(\vec{x}, \vec{x}, \varepsilon)}{\partial \varepsilon} \, \frac{\partial \boldsymbol{H}^{j}_{\mathrm{KS}}(\vec{x})}{\partial \vec{e}_j} \quad . \tag{2.81}$$

Using partial integration and since $\boldsymbol{G}_{jj}(\vec{x},\vec{x},\varepsilon)$ vanishes when $\varepsilon \to -\infty$, the torque becomes:

$$\vec{T}_j = -\frac{1}{\pi}\mathrm{Im}\,\mathrm{Tr}_\sigma \int_{-\infty}^{\varepsilon_\mathrm{F}} \mathrm{d}\varepsilon \int \mathrm{d}\vec{x}\, \boldsymbol{G}_{jj}(\vec{x},\vec{x},\varepsilon)\, \frac{\partial \boldsymbol{H}^j_{\mathrm{KS}}(\vec{x})}{\partial \vec{e}_j} \quad . \tag{2.82}$$

From the previous equation, we can define the torque density at each point $\vec{x}$ in the cell i as:

$$\vec{t}_j(\vec{x}) = -\frac{1}{\pi}\mathrm{Im}\,\mathrm{Tr}_\sigma \int_{-\infty}^{\varepsilon_\mathrm{F}} \mathrm{d}\varepsilon\, \boldsymbol{G}_{jj}(\vec{x},\vec{x},\varepsilon)\, \frac{\partial \boldsymbol{H}^j_{\mathrm{KS}}(\vec{x})}{\partial \vec{e}_j} \quad . \tag{2.83}$$

Considering the form of $\boldsymbol{H}^j_{\mathrm{KS}}(\vec{x})$ given in Eq. (2.17) and assuming the rigid spin approximation *i.e.* $\vec{B}^j_{\mathrm{xc}}(\vec{x}) = B^j_{\mathrm{xc}}(\vec{x})\,\vec{e}_k$, the torque density reads:

$$\vec{t}_j(\vec{x}) = -\frac{1}{\pi}\,\mathrm{Im}\,\mathrm{Tr}_\sigma \int_{-\infty}^{\varepsilon_\mathrm{F}} \mathrm{d}\varepsilon\, B^j_{\mathrm{xc}}(\vec{x})\, \vec{\boldsymbol{\sigma}}\, \boldsymbol{G}_{jj}(\vec{x},\vec{x},\varepsilon) \quad . \tag{2.84}$$

Finally, the magnetic torque acting on the spin moment $\vec{M}_j$ is expressed in terms of $B^j_{\mathrm{xc}}(\vec{x})$ as:

$$\begin{aligned} \vec{T}_j &= \int \mathrm{d}\vec{x}\; \vec{t}_j(\vec{x}) \quad , \\ &= -\frac{1}{\pi}\,\mathrm{Im}\,\mathrm{Tr}_\sigma \int \mathrm{d}\vec{x} \int_{-\infty}^{\varepsilon_\mathrm{F}} \mathrm{d}\varepsilon\, B^j_{\mathrm{xc}}(\vec{x})\, \vec{\boldsymbol{\sigma}}\, \boldsymbol{G}_{jj}(\vec{x},\vec{x},\varepsilon) \quad . \end{aligned} \tag{2.85}$$

In equilibrium the spin moments point along a direction $\vec{e}_n$ (easy-axis). If we consider uniaxial systems, the phenomenological form for the internal energy expanded to second order in the magnetization reads [105]:

$$\varepsilon_{\mathrm{int}} = \varepsilon_0 + \frac{\mathcal{K}}{M^2}\,(\vec{M}\cdot\vec{e}_n)^2 + \ldots \quad . \tag{2.86}$$

When combining Eq. (2.86) and Eq. (2.76), we notice that the components of the torque contain the MAE $\mathcal{K}$. The torque $\vec{T}$ reads:

$$\vec{T} = \sum_i \vec{T}_i = 2\mathcal{K}\,(\vec{e}_M\cdot\vec{e}_n)\,\vec{e}_n \quad . \tag{2.87}$$

The sum includes all the atoms of the system. The transversal part of the torque $\vec{T}^{\mathrm{trans}}$ is written as:

$$\vec{T}^{\mathrm{trans}} = 2\mathcal{K}\left[(\vec{e}_M\cdot\vec{e}_n)\,\vec{e}_n - (\vec{e}_M\cdot\vec{e}_n)^2\,\vec{e}_M\right] \quad . \tag{2.88}$$

When the easy axis is along the z-direction, then $\vec{e}_n = \vec{e}_z$ and assuming a $45°$ rotation in the (xz)-plane away from the z-axis [105], the transversal part of the torque reads:

$$\vec{T}^{\mathrm{trans}} = (-\frac{\mathcal{K}}{\sqrt{2}}, 0, \frac{\mathcal{K}}{\sqrt{2}}) \quad , \tag{2.89}$$

where $\vec{e}_M = \frac{1}{\sqrt{2}}\vec{e}_x + \frac{1}{\sqrt{2}}\vec{e}_z$. Furthermore, the torque acting on $\vec{M}$ has components along x and z-axis but not along the y-axis. This is due to the fact that the easy-axis is along $\vec{e}_z$ (*i.e.* $m_y = 0$) and $\vec{m}$ is in the (xz)-plane (also $m_y = 0$) , thus, no torque along y-axis is expected.

2.6 Time-dependent density functional theory (TD-DFT)

Our aim is to compute the spin excitations spectrum of magnetic impurities embedded in periodic hosts. Thus, we include an external time-dependent potential $v(\vec{r},t)$ into the Hamiltonian, the system is then described by the time-dependent Schrödinger equation:

$$\mathrm{i}\frac{\partial}{\partial t}\psi(\vec{r}_1\,\sigma_1,\vec{r}_2\,\sigma_2,....,\vec{r}_N\,\sigma_N,t)=\hat{H}(t)\,\psi(\vec{r}_1\,\sigma_1,\vec{r}_2\,\sigma_2,....,\vec{r}_N\,\sigma_N,t) \quad , \tag{2.90}$$

where the many-body wave function is time-dependent, $\hat{H}(t)$ is a time-dependent Hamiltonian of the system similar to $\hat{H}$ from Eq. (2.2) with $v(\vec{r})$ is replaced by $v(\vec{r},t)$. The one-to-one correspondence between the external potential $v(\vec{r},t)$ and the time-dependent density was first proved by Runge and Gross [113]. The Runge-Gross theorem states the following:"*Two densities $n(\vec{r},t)$ and $n'(\vec{r},t)$ evolving from the same initial state $\psi(t_0)$ will differ at any time $t>t_0$ when evolving under two different Taylor expandable potentials $v'(\vec{r},t)\neq v(\vec{r},t)+C(t)$*". $C(t)$ is a purely time-dependent function. Therefore, we can compute the time-dependent density of the many-body interacting system by solving the time-dependent Kohn-Sham (TD-KS) equation:

$$\left(-\frac{1}{2}\vec{\nabla}^2_{\vec{r}}+v_{\mathrm{KS}}(\vec{r},t)\right)\,\phi_i(\vec{r},t)=\mathrm{i}\,\frac{\partial}{\partial t}\phi_i(\vec{r},t) \quad . \tag{2.91}$$

$\phi_i(\vec{r},t)$ are the time-dependent Kohn-Sham orbitals which gives access to the time-dependent density:

$$n(\vec{r},t)=\sum_{i=1}^{N}|\phi_i(\vec{r},t)|^2 \quad . \tag{2.92}$$

The time-dependent Kohn-Sham potential $v_{\mathrm{KS}}(\vec{r},t)$ is given similarly to the static one by:

$$v_{\mathrm{KS}}(\vec{r},t)=v(\vec{r},t)+\int \mathrm{d}\vec{r}'\,\frac{2n(\vec{r}',t)}{|\vec{r}-\vec{r}'|}+v_{\mathrm{xc}}[n](\vec{r},t) \quad . \tag{2.93}$$

The time-dependent Kohn-Sham formalism allows the exact computation of $n(\vec{r},t)$ for an interacting system starting from the ground state with a density $n_0(\vec{r})$. Once more, $v_{\mathrm{xc}}[n](\vec{r},t)$ is unknown and needs to be approximated, the most obvious approximation is to use the exchange-correlation functionals from static DFT and replace $n_0(\vec{r})$ with $n(\vec{r},t)$:

$$v^{\mathrm{A}}_{\mathrm{xc}}[n](\vec{r},t)=\left.v_{\mathrm{xc}}[n](\vec{r})\right|_{n(\vec{r},t)} \quad . \tag{2.94}$$

This is known as the adiabatic approximation, which is valid when the perturbation is "slowly" changing in time and the system stays in its instantaneous eigenstate then $v_{\mathrm{xc}}[n](\vec{r},t)$ depends only on the density at time t. In practice, the most used approximation is the adiabatic LDA (ALDA). For spin-polarized systems the time dependence affects the magnetic part of the exchange-correlation as well (*i.e.* $\vec{B}_{\mathrm{xc}}[n,\vec{m}](\vec{r},t)$) and in the adiabatic approximation it reads:

$$\vec{B}^{\mathrm{A}}_{\mathrm{xc}}[n,\vec{m}](\vec{r},t)=\left.\vec{B}_{\mathrm{xc}}[n,\vec{m}](\vec{r})\right|_{n(\vec{r},t),\vec{m}(\vec{r},t)} \quad . \tag{2.95}$$

Similarly to the static case (LSDA), in the adiabatic LSDA the exchange-correlation magnetic field points always in the direction of the magnetization $\vec{m}(\vec{r},t)$.

2.6.1 Linear response theory within TD-DFT

The dynamics of the electronic many-body system can described by the TD-KS equation as discussed previously. However, when the deviations from the ground state are small, the dynamics of our system can be captured using linear response theory. In the following we briefly discuss the basics of linear response theory. We consider a system described by the time-dependent Schrödinger equation:

$$\mathrm{i}\,\frac{\partial}{\partial t}\,|\psi(t)\rangle = \hat{H}(t)\;|\psi(t)\rangle \quad ; \quad \hat{H}(t) = \hat{H}_0 + \delta\hat{v}(t) \quad . \tag{2.96}$$

$\hat{H}_0$ is a time-independent Hamiltonian and $\delta\hat{v}(t)$ is a small external perturbation which is only non-zero for $t > t_0$, it couples to an operator $\hat{B}$ via:

$$\delta\hat{v}(t) = \hat{B}\,\delta\zeta(t) \quad . \tag{2.97}$$

$\delta\zeta(t)$ is a pure time-dependent function. The expectation value on an operator $\hat{A}$ is given by:

$$\langle\hat{A}\rangle(t) = \langle\psi(t)|\,\hat{A}\,|\psi(t)\rangle \quad . \tag{2.98}$$

$|\psi(t)\rangle$ is the solution of Eq. (2.96) and can be written as: $|\psi(t)\rangle = e^{-\mathrm{i}\hat{H}_0(t-t_0)}\,\mathcal{U}(t)\;|\psi(t_0)\rangle$. $|\psi(t_0)\rangle$ is the initial wave function at t_0 and $\mathcal{U}(t)$ is the time evolution operator which can be expanded to first order in $\delta\zeta(t)$ (small perturbation):

$$\mathcal{U}(t) \sim 1 - \mathrm{i}\int_{t_0}^{t} \mathrm{d}t'\;\hat{B}(t')\,\delta\zeta(t') + ... \quad . \tag{2.99}$$

Plugging back this expansion into Eq. (2.98) and keeping only linear terms in $\delta\zeta(t)$, we get for the expectation value of $\hat{A}$:

$$\langle\hat{A}\rangle(t) = \langle\psi(t_0)|\,\hat{A}(t)\,|\psi(t_0)\rangle - \mathrm{i}\int_{t_0}^{t} \mathrm{d}t'\;\langle\psi(t_0)|\,[\hat{A}(t),\hat{B}(t')]\,|\psi(t_0)\rangle\;\delta\zeta(t') \quad . \tag{2.100}$$

Where $\hat{A}(t) = e^{\mathrm{i}\hat{H}_0(t-t_0)}\,\hat{A}\,e^{-\mathrm{i}\hat{H}_0(t-t_0)}$ is the Heisenberg representation of the operator $\hat{A}$. The change in the expectation value of $\hat{A}$ due to $\delta\hat{v}(t)$ is:

$$\begin{aligned}
\delta\langle\hat{A}\rangle(t) &= \langle\hat{A}\rangle(t) - \langle\psi(t_0)|\,\hat{A}\,|\psi(t_0)\rangle \quad , \\
&= -\mathrm{i}\int \mathrm{d}t'\;\Theta(t-t')\;\langle\psi(t_0)|\,[\hat{A}(t),\hat{B}(t')]\,|\psi(t_0)\rangle\;\delta\zeta(t') \quad , \\
&= \int \mathrm{d}t'\chi_{AB}(t-t')\,\delta\zeta(t') \quad .
\end{aligned} \tag{2.101}$$

$\Theta(t)$ is the Heaviside step function and $\chi_{AB}(t-t')$ is the response function of the system to the external perturbation $\delta\zeta(t')$. We can also see that $\delta\langle\hat{A}\rangle(t)$ depends on all the $\delta\zeta(t')$ functions for $t' < t$. By taking the Fourier transform of Eq. (2.101) we simply get a convolution:

$$\delta\langle\hat{A}\rangle(\omega) = \chi_{AB}(\omega)\,\delta\zeta(\omega) \quad , \tag{2.102}$$

where the perturbation has a frequency ω. $\chi_{AB}(\omega)$ can be written using the complete eigenbasis ($\sum_n |\psi_n\rangle \langle\psi_n| = 1$) of $\hat{H}_0$ and its eigenvalues ($\hat{H}_0 |\psi_n\rangle = \varepsilon_n |\psi_n\rangle$):

$$\chi_{AB}(\omega + \mathrm{i}\eta) = \sum_{mn} \left[f(\varepsilon_n) - f(\varepsilon_m)\right] \frac{\hat{A}_{nm}\hat{B}_{mn}}{\omega - (\varepsilon_m - \varepsilon_n) + \mathrm{i}\eta} \quad . \tag{2.103}$$

The previous equation represents the Lehmann representation of $\chi_{AB}(\omega+\mathrm{i}\eta)$. η is a small positive quantity, $f(\varepsilon)$ is the Fermi-Dirac distribution and $\hat{A}_{mn} = \langle\psi_m| \hat{A} |\psi_n\rangle$. Using the spectral representation of the single-particle Green function given in Eq. (2.20) when A and B are local operators, the real-space representation of $\chi_{AB}(\omega + \mathrm{i}\eta)$ reads:

$$\begin{aligned}\chi_{AB}(\vec{r},\vec{r}',\omega+\mathrm{i}\eta) = &-\frac{1}{\pi}\int \mathrm{d}\varepsilon\, f(\varepsilon)\, \mathrm{Tr}\left(\hat{A}\, G(\vec{r},\vec{r}',\varepsilon+\omega+\mathrm{i}\eta)\, \hat{B}\, \mathrm{Im}\, G(\vec{r}',\vec{r},\varepsilon+\mathrm{i}0^+)\right) \\ &-\frac{1}{\pi}\int \mathrm{d}\varepsilon\, f(\varepsilon)\, \mathrm{Tr}\left(\hat{A}\, \mathrm{Im}\, G(\vec{r},\vec{r}',\varepsilon+\mathrm{i}0^+)\, \hat{B}\, G(\vec{r}',\vec{r},\varepsilon-\omega-\mathrm{i}\eta)\right) \quad .\end{aligned} \tag{2.104}$$

We now come back to the TD-DFT formulation of linear response theory. In the presence of a small time-dependent external electrostatic potential $\delta v_n(\vec{r},t)$ and external magnetic field $\delta\vec{B}(\vec{r},t)$, the central quantities in TD-DFT namely $n(\vec{r},t)$ and $\vec{m}(\vec{r},t)$ can be written as:

$$\begin{cases} n(\vec{r},t) = n_0(\vec{r}) + \delta n(\vec{r},t) \quad , \\ \vec{m}(\vec{r},t) = \vec{m}_0(\vec{r}) + \delta\vec{m}(\vec{r},t) \quad . \end{cases} \tag{2.105}$$

$n_0(\vec{r})$ and $\vec{m}_0(\vec{r})$ are the ground state electron and magnetization density. The Fourier transforms of $\delta n(\vec{r},t)$ and $\delta\vec{m}(\vec{r},t)$ in linear response are written as:

$$\begin{aligned} &\delta n_\alpha(\vec{r},\omega) = \sum_\beta \int \mathrm{d}\vec{r}'\, \chi^0_{\alpha\beta}(\vec{r},\vec{r}',\omega)\, \delta v_{\mathrm{eff},\beta}(\vec{r}',\omega) \quad , \\ &\{\alpha,\beta\} = \{x,y,z,n\} \quad . \end{aligned} \tag{2.106}$$

$\delta\vec{n}(\vec{r},t)$ and $\delta\vec{v}_{\mathrm{eff}}(\vec{r}',t')$ are column vectors defined as:

$$\delta\vec{n}(\vec{r},\omega) = \begin{pmatrix} \delta m_x(\vec{r},\omega) \\ \delta m_y(\vec{r},\omega) \\ \delta m_z(\vec{r},\omega) \\ \delta n(\vec{r},\omega) \end{pmatrix} \quad ; \quad \delta\vec{v}_{\mathrm{eff}}(\vec{r},\omega) = \begin{pmatrix} \delta B_{\mathrm{eff},x}(\vec{r},\omega) \\ \delta B_{\mathrm{eff},y}(\vec{r},\omega) \\ \delta B_{\mathrm{eff},z}(\vec{r},\omega) \\ \delta v_{\mathrm{eff},n}(\vec{r},\omega) \end{pmatrix} \tag{2.107}$$

and $\underline{\chi}^0(\vec{r},\vec{r}',t-t')$ is the Kohn-Sham response function given by a 4×4 tensor:

$$\underline{\chi}^0 = \begin{pmatrix} \chi^0_{xx} & \chi^0_{xy} & \chi^0_{xz} & \chi^0_{xn} \\ \chi^0_{yx} & \chi^0_{yy} & \chi^0_{yz} & \chi^0_{yn} \\ \chi^0_{zx} & \chi^0_{zy} & \chi^0_{zz} & \chi^0_{zn} \\ \chi^0_{nx} & \chi^0_{ny} & \chi^0_{nz} & \chi^0_{nn} \end{pmatrix} \quad . \tag{2.108}$$

We omitted the position $(\vec{r},\vec{r}')$ and the time dependences in $\underline{\chi}^0$ for simplicity. Its components are given by Eq. (2.104), where the operators $\{\hat{A},\hat{B}\}$ are replaced by $\{\hat{S}_\alpha,\hat{S}_\beta\}$ with

$\hat{S}_\alpha = \boldsymbol{\sigma}_\alpha$ for $\alpha \in \{x, y, z\}$ and $\hat{S}_n = \mathbb{1}_2$ for the electron density. Besides the external time-dependent perturbation $\delta\vec{v}_{\text{eff}}(\vec{r}, \omega)$ contains a many-body contribution accounting for the change of $v_{\text{xc}}(\vec{r}, \omega)$ and $\vec{B}_{\text{xc}}(\vec{r}, \omega)$:

$$\delta v_{\text{eff},\alpha}(\vec{r}, \omega) = \delta v_\alpha(\vec{r}, \omega) + \delta_{\alpha,n} \int \mathrm{d}\vec{r}\,' \frac{2\delta n(\vec{r}\,', \omega)}{|\vec{r} - \vec{r}\,'|} + \delta v_{\text{xc},\alpha}(\vec{r}, \omega) \quad , \tag{2.109}$$

where the first term represents the external contribution $\delta\vec{v}(\vec{r}, \omega) = \{\delta\vec{B}(\vec{r}, \omega), \delta v_n(\vec{r}, \omega)\}$. The second term from the previous equation is the Hartree response, while the last one represents the perturbation in the exchange-correlation potential:

$$\delta v_{\text{xc},\alpha}(\vec{r}, \omega) = \sum_\beta \int \mathrm{d}\vec{r}\,' \, K^{\text{xc}}_{\alpha\beta}(\vec{r}, \vec{r}\,', \omega) \, \delta n_\beta(\vec{r}\,', \omega) \quad . \tag{2.110}$$

$K^{\text{xc}}_{\alpha\beta}(\vec{r}, \vec{r}\,', \omega)$ is the Fourier transform of the exchange-correlation kernel which is determined by the ground state electron and magnetization density:

$$K^{\text{xc}}_{\alpha\beta}(\vec{r}, \vec{r}\,', \omega) = \left. \frac{\delta v_{\text{xc},\alpha}(\vec{r}, \omega)}{\delta n_\beta(\vec{r}\,', \omega)} \right|_{n_0, \vec{m}_0} \quad . \tag{2.111}$$

$\delta n_\alpha(\vec{r}, \omega)$ can also be related to the external perturbation $\delta\vec{v}(\vec{r}, \omega)$ using the enhanced susceptibility $\chi_{\alpha\beta}(\vec{r}, \vec{r}\,', \omega)$ via:

$$\delta n_\alpha(\vec{r}, \omega) = \sum_\beta \int \mathrm{d}\vec{r}\,' \, \chi_{\alpha\beta}(\vec{r}, \vec{r}\,', \omega) \, \delta v_\beta(\vec{r}\,', \omega) \quad . \tag{2.112}$$

$\chi_{\alpha\beta}(\vec{r}, \vec{r}\,', \omega)$ contains poles at the excitations energies of the interacting system. When combining Eq. (2.106), Eq. (2.112) and Eq. (2.109), one can show that $\chi_{\alpha\beta}(\vec{r}, \vec{r}\,', \omega)$ is related to $\chi^0_{\alpha\beta}(\vec{r}, \vec{r}\,', \omega)$ by a Dyson-like equation:

$$\begin{aligned} \chi_{\alpha\beta}(\vec{r}, \vec{r}\,', \omega) = \chi^0_{\alpha\beta}(\vec{r}, \vec{r}\,', \omega) + \\ \sum_{\gamma\mu} \int \mathrm{d}\vec{r}_1 \, \mathrm{d}\vec{r}_2 \, \chi^0_{\alpha\gamma}(\vec{r}, \vec{r}_1, \omega) \left(K^{\text{xc}}_{\gamma\mu}(\vec{r}_1, \vec{r}_2, \omega) + \frac{\delta_{\gamma n} \, \delta_{\mu n}}{|\vec{r}_1 - \vec{r}_2|} \right) \chi_{\mu\beta}(\vec{r}_2, \vec{r}\,', \omega) \quad . \end{aligned} \tag{2.113}$$

In presence of the SOI or magnetic non-collinearity, the longitudinal and transversal blocks of $\chi^0_{\alpha\beta}(\vec{r}, \vec{r}\,', \omega)$ are coupled (due to the spin structure of the Green function), therefore, one must solve Eq. (2.113) including all the components. Within the ALDA, $K^{\text{xc}}_{\alpha\beta}(\vec{r}, \vec{r}\,', \omega)$ is frequency-independent and local in space, and when the spin magnetization density is along the z-axis ($i.e.\ \vec{B}_{\text{xc}}(\vec{r}) = B_{\text{xc}}(\vec{r})\,\vec{e}_z$) the transverse part of the exchange-correlation kernel ($K^{\text{xc}}_\perp = K^{\text{xc}}_{xx} = K^{\text{xc}}_{yy}$) is simply written as:

$$\begin{aligned} K^{\text{xc}}_\perp(\vec{r}, \vec{r}\,', \omega) &= K^{\text{xc}}_\perp(\vec{r}) \, \delta(\vec{r} - \vec{r}\,') \quad , \\ &= \frac{2B_{\text{xc}}(\vec{r})}{m(\vec{r})} \, \delta(\vec{r} - \vec{r}\,') \quad . \end{aligned} \tag{2.114}$$

If the coupling between the longitudinal and the transversal part is small then one can solve Eq. (2.113) for each block separately. When $\vec{m}(\vec{r}) \parallel z$-axis, it is advantageous to introduce the $\{+,-\}$ basis using the ladder operators $\hat{S}_\pm = \frac{\hat{S}_x \pm \mathrm{i}\hat{S}_y}{2}$ instead of using the $\{x,y\}$ basis. The transverse Kohn-Sham response in the $\{+,-\}$ basis $\underline{\chi}^{0,\mathrm{T}}_{\{+,-\}}$ reads:

$$\begin{aligned} \underline{\chi}^{0,\mathrm{T}}_{\{+,-\}} &= \begin{pmatrix} \frac{1}{2} & \frac{\mathrm{i}}{2} \\ \frac{1}{2} & -\frac{\mathrm{i}}{2} \end{pmatrix} \begin{pmatrix} \chi^0_{xx} & \chi^0_{xy} \\ \chi^0_{yx} & \chi^0_{yy} \end{pmatrix} \begin{pmatrix} \frac{1}{2} & \frac{1}{2} \\ \frac{\mathrm{i}}{2} & -\frac{\mathrm{i}}{2} \end{pmatrix} \quad , \\ &= \begin{pmatrix} \chi^0_{++} & \chi^0_{+-} \\ \chi^0_{-+} & \chi^0_{--} \end{pmatrix} \quad . \end{aligned} \tag{2.115}$$

From the previous equation, the spin-flip Kohn-Sham response function $\chi^0_{+-}(\omega)$ is defined as:

$$\chi^0_{+-}(\omega) = \frac{1}{4}(\chi^0_{xx}(\omega) - \mathrm{i}\chi^0_{xy}(\omega) + \mathrm{i}\chi^0_{yx}(\omega) + \chi^0_{yy}(\omega)) \quad . \tag{2.116}$$

The radial dependencies were omitted for simplicity.

2.6.2 Spin splitting sum rule

In absence of SOI or an external magnetic field, the global SU(2) invariance leads to a Goldstone mode at zero frequency, *i.e.* since there are no anisotropies any transversal perturbation should lead to an infinite response $\chi_{+-}(\omega = 0) \to \infty$. Numerically small inaccuracies occur in $\chi^0_{+-}(\omega)$ and $K^{\mathrm{xc}}_{\perp}(\vec{r})$ shifting the pole of the susceptibility to a finite frequency in the meV range comparable to the gap opening due to SOI, and we must use a sum rule to fix this inconsistency [40, 41].

When the magnetization density is along the z-axis it connects to $B_{\mathrm{xc}}(\vec{r})$, SOI and external magnetic field via:

$$m_z(\vec{r}) = -\frac{1}{\pi}\,\mathrm{Im}\,\mathrm{Tr}_\sigma \int_{-\infty}^{\varepsilon_\mathrm{F}} \mathrm{d}\varepsilon \int \mathrm{d}\vec{r}_1 \int \mathrm{d}\vec{r}_2\, G_{\uparrow\uparrow}(\vec{r},\vec{r}_1,\varepsilon)\,\Delta(\vec{r}_1,\vec{r}_2,\varepsilon)\,G_{\downarrow\downarrow}(\vec{r}_2,\vec{r},\varepsilon) \quad . \tag{2.117}$$

$\Delta(\vec{r},\vec{r}\,',\varepsilon)$ is an energy-dependent splitting related to the Kohn-Sham Hamiltonian of Eq. (2.17) which in presence of SOI and an external magnetic field reads:

$$\boldsymbol{H}_{\mathrm{KS}}(\vec{r}) = \left(-\vec{\nabla}^2_{\vec{r}} + v_{\mathrm{KS}}(\vec{r})\right) \mathbb{1}_2 + \vec{B}_{\mathrm{xc}}(\vec{r}) \cdot \vec{\boldsymbol{\sigma}} + \lambda(r)\,\vec{L} \cdot \vec{\boldsymbol{\sigma}} + \vec{B}^{\mathrm{ext}} \cdot \vec{\boldsymbol{\sigma}} \quad . \tag{2.118}$$

$\Delta(\vec{r}_1,\vec{r}_2,\varepsilon)$ is given in terms of $\boldsymbol{H}_{\mathrm{KS}}(\vec{r})$ and $(\varepsilon - H^{\sigma\sigma}_{\mathrm{KS}}(\vec{r}))\,\tilde{G}_{\sigma\sigma}(\vec{r},\vec{r}\,',\varepsilon) = \delta(\vec{r}-\vec{r}\,')$ as:

$$\begin{aligned} \Delta(\vec{r},\vec{r}\,',\varepsilon) = &\left(H^{\uparrow\uparrow}_{\mathrm{KS}}(\vec{r}) - H^{\downarrow\downarrow}_{\mathrm{KS}}(\vec{r})\right)\delta(\vec{r}-\vec{r}\,') \\ &+ H^{\uparrow\downarrow}_{\mathrm{KS}}(\vec{r})\,\tilde{G}_{\downarrow\downarrow}(\vec{r},\vec{r}\,',\varepsilon)\,H^{\downarrow\uparrow}_{\mathrm{KS}}(\vec{r}\,') \\ &- H^{\downarrow\uparrow}_{\mathrm{KS}}(\vec{r})\,\tilde{G}_{\uparrow\uparrow}(\vec{r},\vec{r}\,',\varepsilon)\,H^{\uparrow\downarrow}_{\mathrm{KS}}(\vec{r}\,') \quad . \end{aligned} \tag{2.119}$$

Using Eq. (2.117) and Eq. (2.119), we can identify separately the different contributions to $m_z(\vec{r})$ from $B_{\mathrm{xc}}(\vec{r})$, SOI and the external magnetic field:

$$m_z(\vec{r}) = m^{\mathrm{xc}}_z(\vec{r}) + m^{\mathrm{SOI}}_z(\vec{r}) + m^{\mathrm{ext}}_z(\vec{r}) \quad . \tag{2.120}$$

The contribution of the exchange-correlation magnetic field to the magnetization $m_z^{\mathrm{xc}}(\vec{r})$ reads:

$$m_z^{\mathrm{xc}}(\vec{r}) = -\frac{2}{\pi}\,\mathrm{Im}\int_{-\infty}^{\varepsilon_{\mathrm{F}}} \mathrm{d}\varepsilon \int \mathrm{d}\vec{r}\,'\, G_{\uparrow\uparrow}(\vec{r},\vec{r}\,',\varepsilon)\, B_{\mathrm{xc}}(\vec{r}\,')\, G_{\downarrow\downarrow}(\vec{r}\,',\vec{r},\varepsilon) \quad , \tag{2.121}$$

which interestingly can be reformulated using the static spin-flip Kohn-Sham susceptibility $\chi^0_{+-} = \frac{1}{4}(\chi^0_{xx} - \mathrm{i}\chi^0_{xy} + \mathrm{i}\chi^0_{yx} + \chi^0_{yy})$ as:

$$\begin{aligned} m_z^{\mathrm{xc}}(\vec{r}) &= 2\int \mathrm{d}\vec{r}\,'\, \chi^0_{+-}(\vec{r},\vec{r}\,',\omega=0)\, B_{\mathrm{xc}}(\vec{r}\,') \quad . \\ &= \int \mathrm{d}\vec{r}\,'\, \chi^0_{+-}(\vec{r},\vec{r}\,',\omega=0)\, K_{\perp}^{\mathrm{xc}}(\vec{r}\,')\, m_z(\vec{r}\,') \quad . \end{aligned} \tag{2.122}$$

The previous equation represents the magnetization sum rule, in practice first $m^{\mathrm{xc}}(\vec{r})$ is computed using Eq. (2.121) then Eq. (2.122) is inverted to compute $K_{\perp}^{\mathrm{xc}}(\vec{r})$, this procedure enforces by construction the Goldstone mode at zero frequency in absence of SOI or external fields. In order to illustrate this, we omit the real-space dependence, Eq. (2.122) reads then:

$$K_{\perp}^{\mathrm{xc}} = \frac{\left(\chi^0_{+-}(\omega=0)\right)^{-1} m_z^{\mathrm{xc}}}{m_z^{\mathrm{xc}} + m_z^{\mathrm{SOI}} + m_z^{\mathrm{ext}}} \quad . \tag{2.123}$$

In absence of SOI and external magnetic fields, $K_{\perp}^{\mathrm{xc}}$ is simply given by:

$$K_{\perp}^{\mathrm{xc}} = \left(\chi^0_{+-}(\omega=0)\right)^{-1} \quad . \tag{2.124}$$

Furthermore, the transversal block in $\underline{\chi}(\omega)$ decouples from the rest of the elements and $\chi_{+-}(\omega)$ reads:

$$\chi_{+-}(\omega) = \frac{\chi^0_{+-}(\omega)}{1 - K_{\perp}^{\mathrm{xc}}\chi^0_{+-}(\omega)} \quad . \tag{2.125}$$

When plugging $K_{\perp}^{\mathrm{xc}}$ into the previous equation, we see clearly that $\chi_{+-}(\omega)$ diverges at $\omega = 0$.

2.6.3 Taylor expansion of the Kohn-Sham susceptibility

In practice $\chi^0_{\alpha\beta}(\vec{r},\vec{r}\,',\omega)$ is computed using Eq. (2.104) and the Kohn-Sham Green functions in the projection basis defined in Sec. 2.4.6. In this basis the Kohn-Sham response function reads:

$$\begin{aligned} \chi^0_{\alpha\beta}(\vec{r},\vec{r}\,',\omega) = \sum_{L_1 s_1 b_1 \ldots} & Y_{L_1}(\hat{r})\, Y_{L_2}(\hat{r})\, \phi^{s_1}_{il_1b_1}(r)\, \phi^{s_2}_{il_2b_2}(r) \\ & \times \chi^{0,s_1s_2s_3s_4}_{\alpha\beta,iL_1L_2b_1b_2,jL_3L_4b_3b_4}(\omega)\, \phi^{s_3}_{jl_3b_3}(r\,')\, \phi^{s_4}_{jl_4b_4}(r\,')\, Y_{L_3}(\hat{r}\,')\, Y_{L_4}(\hat{r}\,') \quad . \end{aligned} \tag{2.126}$$

$\chi^0_{\alpha\beta}(\vec{r},\vec{r}\,',\omega)$ requires the computation of the Kohn-Sham Green function for each frequency which can be very time-consuming. Nonetheless, for the frequency range of interest (meV) the Kohn-Sham susceptibility is almost linear in frequency, therefore, one can

perform a Taylor expansion for the projected Kohn-Sham Green function around $\omega = 0$:

$$G^{\sigma\sigma'}_{iLb,jL'b'}(\varepsilon+\omega+\mathrm{i}\eta) = G^{\sigma\sigma'}_{iLb,jL'b'}(\varepsilon+\mathrm{i}\eta) + \omega\frac{\mathrm{d}}{\mathrm{d}\varepsilon}G^{\sigma\sigma'}_{iLb,jL'b'}(\varepsilon+\mathrm{i}\eta) + \frac{\omega^2}{2}\frac{\mathrm{d}^2}{\mathrm{d}\varepsilon^2}G^{\sigma\sigma'}_{iLb,jL'b'}(\varepsilon+\mathrm{i}\eta) + \ldots \quad . \tag{2.127}$$

Plugging back the previous equation into Eq. (2.67), we obtain the Taylor expansion in frequency for the Kohn-Sham Green function $G(\vec{r},\vec{r}\,',\varepsilon+\omega+\mathrm{i}\eta)$. The latter one is then inserted to Eq. (2.104) providing a Taylor expansion for the Kohn-Sham susceptibility:

$$\chi^0_{\alpha\beta}(\vec{r},\vec{r}\,',\omega) = \chi^0_{\alpha\beta}(\vec{r},\vec{r}\,',0) + \omega\,\chi^{0,\prime}_{\alpha\beta}(\vec{r},\vec{r}\,') + \omega^2\,\chi^{0,\prime\prime}_{\alpha\beta}(\vec{r},\vec{r}\,') + \ldots \quad . \tag{2.128}$$

The first term on the right hand side is the static Kohn-Sham susceptibility. The second term gathers elements of the form $G(\varepsilon)\,\frac{\mathrm{d}}{\mathrm{d}\varepsilon}G(\varepsilon)$, while the last term gathers elements of the form $G(\varepsilon)\,\frac{\mathrm{d}^2}{\mathrm{d}\varepsilon^2}G(\varepsilon)$. All these terms are integrated over energy as well.

2.6.4 Mapping TD-DFT into the Landau-Lifshitz-Gilbert equation

In order to get more insights into the magnetization dynamics, we connect the magnetic susceptibility obtained within TD-DFT to the phenomenological Landau-Lifshitz-Gilbert (LLG) equation [114]. We use the generalized formulation of the LLG equation which includes a tensorial damping $\mathcal{G}$, the impact of the damping on the magnetization precession is shown in Fig. 2.1a, as well as nutation effects via the nutation tensor $\mathcal{I}$, which are shown in Fig. 2.1b. The nutation effects are important at high frequencies [115]. The equation governing the precession of the spin magnetic moment $\vec{M}$ is given by:

$$\frac{\mathrm{d}\vec{M}}{\mathrm{d}t} = -\gamma\,\vec{M}\times\left(\vec{B}^{\mathrm{eff}} + \mathcal{G}\cdot\frac{\mathrm{d}\vec{M}}{\mathrm{d}t} + \mathcal{I}\cdot\frac{\mathrm{d}^2\vec{M}}{\mathrm{d}t^2}\right) \quad , \tag{2.129}$$

$\vec{M}$ is the spin magnetic moment obtained after integrating the spin magnetization density $\vec{m}(\vec{r})$ given in Eq. (2.29) over the cell containing the magnetic atom:

$$\vec{M} = \int \mathrm{d}\vec{r}\;\vec{m}(\vec{r}) \quad . \tag{2.130}$$

γ is the gyromagnetic ratio ($\gamma = 2$ in atomic units) and $\vec{B}^{\mathrm{eff}}$ is the effective field acting on the magnetization. It contains two contributions, external and internal, the latter one is arising from the MAE:

$$\vec{B}^{\mathrm{eff}} = \vec{B}^{\mathrm{ext}} + \vec{B}^{\mathrm{a}} \quad , \quad \vec{B}^{\mathrm{a}} = -\frac{\partial\varepsilon_{\mathrm{int}}}{\partial\vec{M}} = -\frac{2\mathcal{K}}{M^2}\,(\vec{M}\cdot\vec{e}_n)\,\vec{e}_n \quad . \tag{2.131}$$

$\vec{e}_n$ is the easy axis of $\vec{M}$ and $\varepsilon_{\mathrm{int}}$ is the phenomenological form for the internal energy given in Eq. (2.86). We now consider that the magnetic moment points along the z-axis (*i.e.* $\vec{e}_n = \vec{e}_z$) and that $\vec{B}^{\mathrm{ext}}$ is a small time-dependent transverse magnetic field:

$$\vec{B}^{\mathrm{ext}}(t) = b_x(t)\,\vec{e}_x + b_y(t)\,\vec{e}_y \quad ;\ \text{with}\ \{b_x(t), b_y(t)\} \ll |\vec{B}^{\mathrm{a}}| \quad . \tag{2.132}$$

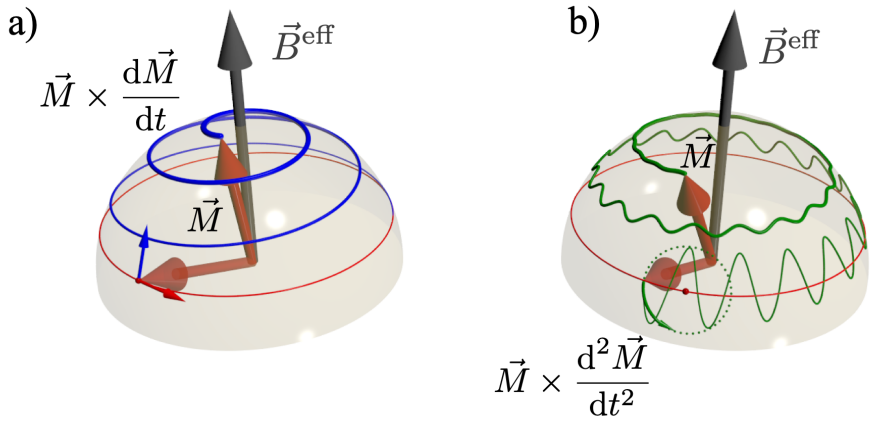

Figure 2.1: Precession of the spin magnetic moment $\vec{M}$ around the effective field $\vec{B}^{\mathrm{eff}}$. a) Damping of the precession. b) Nutation of the spin magnetic moment.

Therefore, $\vec{M}(t)$ acquires small transverse components:

$$\vec{M}(t) = M_x(t)\,\vec{e}_x + M_y(t)\,\vec{e}_y + M\,\vec{e}_z \tag{2.133}$$

Plugging Eq. (2.132) and Eq. (2.133) into Eq (2.129) under the following assumptions:

- $\{M_x, M_y\} \ll M$ allowing the linearization of Eq. (2.129).
- In the ground state the torque between the effective field and the magnetization must be zero: $\left(M\vec{e}_z \times \vec{B}^{\mathrm{a}}\right) = 0$.

One can show that the Fourier transform of Eq. (2.129) for the transverse components of the magnetization can be written as:

$$\sum_{\beta=x,y} \left(\frac{B_z^{\mathrm{a}}}{M}\delta_{\alpha\beta} + \frac{\mathrm{i}\omega}{\gamma M}\sum_{\mu}\epsilon_{\alpha\beta\mu} + \mathrm{i}\omega\,\mathcal{G}_{\alpha\beta} + \omega^2\,\mathcal{I}_{\alpha\beta} \right) M_\beta(\omega) = b_\alpha(\omega) \quad . \tag{2.134}$$

$\epsilon_{\alpha\beta\mu}$ is the Levi-Civita tensor. The previous equations allow a connection between the linearized LLG equation and the transverse magnetic susceptibility obtained from Eq. (2.113) with the $\vec{r}$-dependencies integrated out.

$$\sum_{\beta=x,y} \left(\chi^{\mathrm{LLG}}_{\alpha\beta}(\omega)\right)^{-1} M_\beta(\omega) = b_\alpha(\omega) \quad , \tag{2.135}$$

where $\chi^{\mathrm{LLG}}_{\alpha\beta}(\omega)$ is the magnetic susceptibility in the LLG model. The damping and nutation are rank-2 tensors that can be decomposed into a symmetric part (labeled with the superscript s) and an anti-symmetric part (labeled with the superscript a). For systems

with uniaxial symmetry (such as C_{3v}), the damping tensor has the following form:

$$\mathcal{G}^s = -\frac{1}{\gamma M}\begin{pmatrix} \mathcal{G}^s_\parallel & 0 & 0 \\ 0 & \mathcal{G}^s_\parallel & 0 \\ 0 & 0 & \mathcal{G}^s_\perp \end{pmatrix} \quad ; \quad \mathcal{G}^a = \frac{1}{\gamma M}\begin{pmatrix} 0 & \mathcal{G}^a_\perp & -\mathcal{G}^a_\parallel \\ -\mathcal{G}^a_\perp & 0 & \mathcal{G}^a_\parallel \\ \mathcal{G}^a_\parallel & -\mathcal{G}^a_\parallel & 0 \end{pmatrix} \quad . \tag{2.136}$$

And similarly for the nutation tensor:

$$\mathcal{I}^s = -\frac{1}{\gamma M}\begin{pmatrix} \mathcal{I}^s_\parallel & 0 & 0 \\ 0 & \mathcal{I}^s_\parallel & 0 \\ 0 & 0 & \mathcal{I}^s_\perp \end{pmatrix} \quad ; \quad \mathcal{I}^a = \frac{1}{\gamma M}\begin{pmatrix} 0 & \mathcal{I}^a_\perp & -\mathcal{I}^a_\parallel \\ -\mathcal{I}^a_\perp & 0 & \mathcal{I}^a_\parallel \\ \mathcal{I}^a_\parallel & -\mathcal{I}^a_\parallel & 0 \end{pmatrix} \quad . \tag{2.137}$$

A similar decomposition is done for the magnetic interactions tensor discussed in Sec. 3.5.1. Combining Eq. (2.134) and Eq. (2.135), the transverse components of the damping and nutation tensors can be extract from the transverse dynamical magnetic susceptibility computed within TD-DFT:

$$\begin{cases} \left(\chi^{\mathrm{LLG}}_{xx}(\omega)\right)^{-1} = -\frac{2\mathcal{K}}{M^2} - \frac{\mathrm{i}\omega}{\gamma M}\mathcal{G}^s_\parallel - \frac{\omega^2}{\gamma M}\mathcal{I}^s_\parallel & . \\ \left(\chi^{\mathrm{LLG}}_{xy}(\omega)\right)^{-1} = \frac{\mathrm{i}\omega}{\gamma M}(1+\mathcal{G}^a_\perp) + \frac{\omega^2}{\gamma M}\mathcal{I}^a_\perp & . \end{cases} \tag{2.138}$$

The spin-flip magnetic susceptibility in the LLG model $\chi^{\mathrm{LLG}}_{+-}(\omega)$ is given in terms of the MAE, damping and nutation transverse components as:

$$\chi^{\mathrm{LLG}}_{+-}(\omega) = \frac{1}{2}\frac{M\gamma}{-\frac{2\mathcal{K}\gamma}{M} - (1+\mathcal{G}^a_\perp + \mathrm{i}\mathcal{G}^s_\parallel)\,\omega + (-\mathcal{I}^s_\parallel + \mathrm{i}\mathcal{I}^a_\perp)\,\omega^2} \quad . \tag{2.139}$$

Note that the sign convention chosen in LLG for the perturbation Hamiltonian is different compared to the one used in TD-DFT, therefore, $\chi^{\mathrm{LLG}}_{\alpha\beta}(\omega) = -\chi_{\alpha\beta}(\omega)$.

2.6.5 Zero-point spin-fluctuations

Previously, we have discussed the transverse dynamical magnetic susceptibility. It turns out that the knowledge of the later one gives access to the so-called zero-point spin-fluctuations (ZPSF) , which are quantum fluctuations present at zero temperature capable of altering the magnetic properties of the system. There is an analogy with the quantum harmonic oscillator where the vibrational energy is $\varepsilon_\nu = \omega_0\left(\nu + \frac{1}{2}\right)$. ν is an integer number labeling the quantized energy levels and ω_0 is the vibration frequency. At zero temperature (ground state) $\nu = 0$, the remaining energy $\varepsilon_0 = \frac{\omega_0}{2}$ is attributed to these zero-point fluctuations. For the quantum harmonic oscillator, ZPSF are present because the momentum operator $\vec{p}$ and the position operator $\vec{x}$ do not commute. This is a consequence of the Heisenberg uncertainty principle. The fluctuations of an observable $\hat{A}$ from equilibrium are contained in the dynamical structure factor:

$$\begin{aligned} \mathcal{S}_{\hat{A}\hat{A}^\dagger}(\omega) &= \frac{1}{2\pi}\int \mathrm{d}t\, \langle \hat{A}(t)\hat{A}^\dagger\rangle\, e^{\mathrm{i}\omega t} \quad , \\ &= \langle\hat{A}\rangle^2\,\delta(\omega) + \frac{1}{2\pi}\int \mathrm{d}t\, \langle \delta\hat{A}(t)\,\delta\hat{A}^\dagger\rangle\, e^{\mathrm{i}\omega t} \quad . \end{aligned} \tag{2.140}$$

$\delta\hat{A}$ represents the amount of fluctuations of the observable $\hat{A}$ (*i.e.* $\hat{A} = \langle\hat{A}\rangle + \delta\hat{A}$). $\mathcal{S}_{\hat{A}\hat{A}^\dagger}(\omega)$ is related to the dissipative part of the response function $\mathrm{Im}\chi_{\hat{A}\hat{A}^\dagger}(\omega)$ by the so-called fluctuation-dissipation theorem [116], which at zero temperature reads:

$$\mathcal{S}_{\hat{A}\hat{A}^\dagger}(\omega) = -\frac{1}{\pi}\mathrm{Im}\chi_{\hat{A}\hat{A}^\dagger}(\omega) \quad . \tag{2.141}$$

We consider only the transverse spin-fluctuations since it has been shown for several magnetic adatoms on metallic surfaces in Ref. [42] that the longitudinal fluctuations are one order of magnitude smaller than the former ones. The transverse dynamical structure factor is defined as:

$$\mathcal{S}_\perp(\omega) = -\frac{1}{\pi}\left(\mathrm{Im}\chi_{xx}(\omega) + \mathrm{Im}\chi_{yy}(\omega)\right) \quad . \tag{2.142}$$

Assuming that the spin moment is along the z-axis, $\langle\hat{S}_x\rangle = \langle\hat{S}_y\rangle = 0$. Then, the variance of the transversal spin-fluctuations in equilibrium $\xi_\perp^2$ is given by the integral over all frequencies of $\mathcal{S}_\perp(\omega)$:

$$\begin{aligned}\xi_\perp^2 &= -\frac{1}{\pi}\int_0^{+\infty} \mathrm{d}\omega \left(\mathrm{Im}\chi_{xx}(\omega) + \mathrm{Im}\chi_{yy}(\omega)\right) \quad , \\ &= -\frac{1}{\pi}\int_0^{+\infty} \mathrm{d}\omega\, \mathrm{Im}\chi_\perp(\omega) \quad ,\end{aligned} \tag{2.143}$$

where $\mathrm{Im}\chi_\perp(\omega) = \mathrm{Im}\chi_{xx}(\omega) + \mathrm{Im}\chi_{yy}(\omega)$ defines a form of the transverse response function which is important for ZPSF (note that it is different from $\chi_{+-}(\omega)$). The frequency integral in Eq. (2.143) goes up to $+\infty$, for large frequencies $\omega \gg \omega_{\max}$, $\mathrm{Im}\chi_\perp(\omega) \propto \frac{1}{\omega^2}$ where $\omega_{\max}$ represents the resonance frequency (see Sec. 4.7.2). This allows to introduce a cutoff frequency, ω_c, considering that with TD-DFT one has access only to a finite range of frequencies. For $\omega > \omega_c$, we assume the following for the imaginary part of the transversal response function:

$$\mathrm{Im}\chi_\perp(\omega) = \frac{\omega_c^2}{\omega^2}\,\mathrm{Im}\chi_\perp(\omega_c) \quad . \tag{2.144}$$

$\xi_\perp^2$ is then given by a sum of two terms, the main contribution coming from the resonance in $\mathrm{Im}\chi_\perp(\omega)$ and a smaller contribution originating from the tail of $\mathrm{Im}\chi_\perp(\omega)$ at high frequencies.

2.6.6 Renormalization of the magnetic anisotropy energy

It has been shown that the ZPSF introduced previously are important for magnetic impurities [42]. These ZPSF make the magnetic moments less stable regarding external perturbations, this leads to a lowering of the MAE barrier. In order to estimate this reduction, we consider a magnetization $\vec{M}(\vec{r})$ with an easy axis in an arbitrary direction $\vec{e}_n$ and apply similar principles than those used in the spin-fluctuation theory of Moriya [117]. The magnetization is expressed as

$$\vec{M}(\vec{r}) = \vec{M}_{\mathrm{eq}} + \delta\vec{M}(\vec{r}) \quad , \tag{2.145}$$

where $\vec{M}_{\text{eq}}$ is the equilibrium magnetization and $\delta\vec{M}(\vec{r})$ represents the local fluctuations of $\vec{M}(\vec{r})$ at each point $\vec{r}$. By symmetry considerations one can postulate [118]:

$$\int_{V_{\text{m}}} \mathrm{d}\vec{r}\,\left(\delta\vec{M}(\vec{r})\right)^n = \begin{cases} \langle \delta\vec{M}^n \rangle & \text{for } n \text{ even} \quad , \\ 0 & \text{for } n \text{ odd} \quad . \end{cases} \tag{2.146}$$

We are interested in the influence of spin fluctuations on the magnetic anisotropy, which involves the square of the magnetization:

$$\langle \vec{M}^2 \rangle = \langle \left(\vec{M}_{\text{eq}} + \delta\vec{M}\right)^2 \rangle = \vec{M}_{\text{eq}}^2 + \langle \delta\vec{M}^2 \rangle \quad . \tag{2.147}$$

We now include the contribution of the ZPSF into the phenomenological form of the internal energy and Eq. (2.86) is rewritten as:

$$\varepsilon_{\text{sf}} = \varepsilon_0 + \frac{\mathcal{K}}{M^2} \langle (\vec{M} \cdot \vec{e}_n)^2 \rangle + \ldots \quad . \tag{2.148}$$

ε_{sf} is the internal energy in presence of ZPSF. Furthermore, we separate the longitudinal and transversal contributions of $\delta\vec{M}$, therefore, we introduce $\delta M_i'$ as its components in the local frame of the magnetization $\vec{M}$ which points in an arbitrary direction $\vec{e}_M$ in the (xz)-plane with an angle θ away from z-axis:

$$\begin{aligned} \delta\vec{M} &= \sum_{i=x,y,z} \delta M_i' \, \vec{e}_i \quad , \\ &= \delta M_x' (\cos\theta \, \vec{e}_x - \sin\theta \, \vec{e}_z) + \delta M_y' \, \vec{e}_y + \delta M_z' (\sin\theta \, \vec{e}_x + \cos\theta \, \vec{e}_z) \quad . \end{aligned} \tag{2.149}$$

$\vec{e}_i'$ are the basis vectors in the rotated frame of the magnetization. $\{\delta M_x', \delta M_y'\}$ represent the transversal fluctuations, while, $\delta M_z'$ account for the longitudinal ones within the local spin frame of reference. Assuming that the easy axis of $\vec{M}$ is along the z-direction and using Eq. (2.149), the internal energy can be written as:

$$\begin{aligned} \varepsilon_{\text{sf}}(\theta) &= \varepsilon_0 + \frac{\mathcal{K}}{M^2} \langle (\vec{M} \cdot \vec{e}_z)^2 \rangle \quad , \\ &= \varepsilon_0 + \frac{\mathcal{K}}{\vec{M}_{\text{eq}}^2 + \sum_i \delta M_i'^2} \left((\vec{M}_{\text{eq}}^2 + \delta M_z'^2) \cos^2\theta + \delta M_x'^2 \sin^2\theta \right) \quad . \end{aligned} \tag{2.150}$$

The renormalized MAE anisotropy due to ZPSF, $\mathcal{K}_{\text{sf}}$, is given by the difference between the internal energy when $\vec{M} \parallel \vec{e}_z$ and $\vec{M} \parallel \vec{e}_x$, respectively:

$$\begin{aligned} \mathcal{K}_{\text{sf}} &= \varepsilon_{\text{sf}}(0) - \varepsilon_{\text{sf}}(\pi/2) \quad , \\ &= \mathcal{K} \left(1 - \frac{2\delta M_x'^2 + \delta M_y'^2}{\vec{M}_{\text{eq}}^2 + \sum_i \delta M_i'^2} \right) \quad . \end{aligned} \tag{2.151}$$

For systems without in-plane anisotropy, $\delta M_x' = \delta M_y' = \delta M_\perp'$ and considering that the longitudinal fluctuations are one order of magnitude smaller than the transversal ones:

$$\mathcal{K}_{\text{sf}} = \mathcal{K} \left(1 - \frac{3\delta M_\perp'^2}{\vec{M}_{\text{eq}}^2 + 2\delta M_\perp'^2} \right) \quad . \tag{2.152}$$

The presence of the fluctuations leads to a reduction of the MAE barrier since $\delta M_\perp'^2 > 0$ affecting the magnetic stability of the system.

2.7 Technical aspects of the KKR codes and new implementations

2.7.1 KKR codes available in Jülich

In practice, we use the KKR codes available in Jülich. In order to describe the periodic host systems discussed in the thesis, we used the KKR-Jülich-Münich code (KKR-JM). The program starts from atomic potentials embedded in a free electron gas. The atomic potentials and the geometrical construction of the system are created using a utility called the Voronoi code. The KKR-JM code includes the spin-orbit interaction (SOI) self-consistently in the atomic sphere approximation and in the full potential (FP) approach. It solves the Lippmann-Schwinger equation exactly by performing an inversion in a Chebychev polynomial basis [96]. The KKR-JM code is parallelized over energies and atoms for the solution of the single site problem (see Eq. (2.39)). The multiple scattering problem is also solved in parallel over energies and k-points (see Eq. (2.48)). The code uses different levels of parallelization (MPI, OpenMP and hybrid).

Once the host system is generated self-consistently, we use the KKR-impurity code to perform real space calculations. The impurity code employs a set of Green functions and t-matrices computed from the host system within a finite region in space called impurity cluster. The latter one contains all the atoms affected by the embedded defect. The KKR-impurity code uses the Dyson equation shown in Eq. (2.23) to embed impurities (or clusters of impurities) self-consistently and compute their ground state properties (charge, spin moment, orbital moment and density of states). The impurity code has an MPI parallelization over the energies.

To access the dynamical properties of the system an extension to TD-DFT is required. There is a separate code available which grants access to the magnetic response functions to external time-dependent magnetic fields (using linear response TD-DFT), it received the appellation KKR-susc code. It is attached to the KKR-impurity code and uses its inputs. The KKR-susc code introduces the projection basis discussed in Sec. 2.4.6. However, the available version of the KKR-susc code was interfaced with an older version of the impurity code which does not include the SOI from the host. The SOI is introduced self-consistently in the impurity cluster within the projection basis scheme. This approach is not suitable to treat system with large SOI where the details of the band structure are of crucial importance, this is the case for topological insulators which are materials of interest in this thesis.

2.7.2 New implementations in the KKR-impurity and KKR-susc codes

One of the main goals of the thesis was to compute the response of magnetic impurities subjected to external time-dependent magnetic fields. These impurities are embedded in topological insulators where the SOI is strong. Therefore, it has to be included in the host system self-consistently, then in the impurity cluster using the KKR-impurity code and finally in the KKR-susc code. In order to fulfill these requirements, several changes had to be made on the KKR-impurity code as well as on the KKR-susc code. The task consisted of writing a new interface. The essential new implementations are listed in the following:

Generalization of the Radial meshes

As mentioned previously, the old version of the KKR-susc code was interfaced with an older KKR-impurity code. This old version had only one radial mesh panel within the ASA approximation. However, the most recent version of the KKR-JM code and impurity code requires a more general radial mesh with different panels. These are needed because this recent version has a full potential extension, where at edges of the atomic cell the charge density presents kinks and sharp features that need to be integrated over different panels. First, we transmitted the information on the panels from the KKR-impurity code to the KKR-susc code and created new variables to handle the panels. Second, we generalized the integration routines in the KKR-susc code to include more than one panel. Third, every routine in the code where a real space integration or derivation is performed was updated to include more than a single panel.

Handling off-diagonal elements

In practice, the regular solutions and the onsite Green function are the quantities that are projected on the basis defined in Sec. 2.4.6. The old version of the impurity code does not include SOI and also does not handle non-collinear magnetism, the regular solutions and the onsite Green function are diagonal in spin space. Thus, only the spin diagonal components were projected and transmitted to the KKR-susc code. In presence of SOI from the host, several changes must be made. First, due to the presence of SOI from the host, the regular solutions and the onsite Green function acquire off-diagonal elements in spin ($R_{lm}^{\sigma\sigma'}(r) \neq 0$), second, they also depend on m as can be seen from Eq. (2.60). Third, the left solutions discussed previously are not equivalent to the right ones in presence of SOI. Therefore, new projection routines that includes spin off-diagonal elements, m-dependent projection coefficients, left solutions have been implemented. In presence of non-collinear magnetism and SOI from the host further changes are required, since the KKR-impurity code computes the regular solutions and onsite Green function in the local frame of the magnetization, thus, the projection coefficients are obtained in the local frame. Nonetheless, the projection coefficients are assembled together with the structural Green function which is in the global frame. Thus, new routines transforming the regular solutions (right and left) and the onsite Green function from the local spin frame of reference to the global one had been implemented. Furthermore, in the old version of the KKR-JM code the structural Green function was generated for collinear systems without SOI, therefore, once more only the spin diagonal elements where required in the KKR-susc code. For the new version of the code, new routines handling and transmitting the structural Green function with the spin off-diagonal elements were implemented as well.

Energy parallelization of the KKR-susc code

The new solver that includes SOI interaction from the host and in the impurity code is very accurate. However, in practice it solves the Lippmann Schwinger equation given by Eq. (2.60) in a Chebychev polynomial basis, which is numerically expensive, therefore, the KKR-impurity code is parallel over energies. We made use of the existing energy parallelization in the KKR-impurity code to perform the projections in parallel. Nonethe-

less, the parallel energy distributions do not conform with the energy integrals used in the KKR-susc code to compute the magnetic susceptibility (see Eq. (2.104)). In oder to overcome this issue, the code was splitted into two parts: first the projection is done in parallel, then the magnetic response function is computed in serial. This requires several changes: First, the different arrays namely: the regular solutions, onsite Green function, structural Green function and t-matrix are all energy dependent quantities, therefore, they have been allocated dynamically on each MPI process within the KKR-susc code. Second, after performing the projection for each energy in parallel, all the arrays are gathered into the main process. We implemented new routines that perform this task. The main process is then used to write to disc: the projection coefficients, the projected onsite Green function, the structural Green function and the t-matrix into separate files. This required the implementation of new routines that handle the write/read (I/O) of these quantities. Finally, a restart mode was implemented into the KKR-susc code, which runs in serial, shortcuts the projection and reads the needed data from the projection files. Several consistency checks were made to ensure the compatibility between the sum rule, the dynamical magnetic susceptibility and new implementations.

All these implementations are compatible with the previous version of the code and are not in conflict with other functionalities included in the KKR-susc code:

- External magnetic fields.
- LDA + U (The Hubbard U is a correction that accounts for the Coulomb repulsion between electrons on the same atom).
- Magnetic interactions (computes the magnetic interaction tensor discussed in Sec. 3.5).
- Time-dependent magnetic susceptibility within linear response TD-DFT.
- Ground state charge and spin currents.

The new version of the code was used to generate all the results shown in Chapter 4. In Fig. 2.2, we show a schematic comparison between the old and the new version of the code. The new implementations add an essential feature: the inclusion of the SOI from the host, which is necessary when dealing with magnetically doped topological insulators.

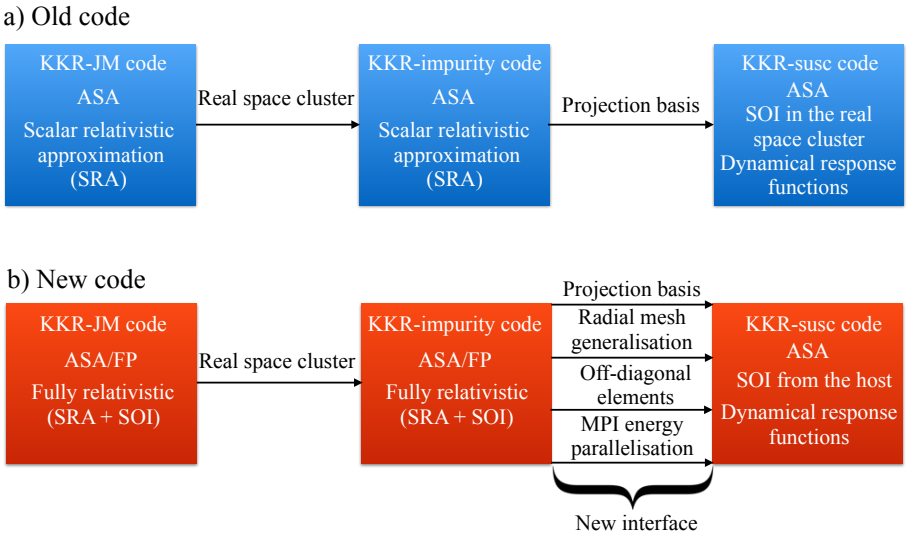

Figure 2.2: Comparison between: a) The old version of the KKR-JM/KKR-impurity/KKR-susc codes and b) The new version of these codes. The recent developments required to compute dynamical magnetic susceptibility with SOI included from the host system are also highlighted.

Chapter 3

Scattering of Rashba electrons off magnetic impurities

The absence of spatial inversion symmetry combined with the spin-orbit interaction lead to a spin-splitting of the energy bands in non-magnetic materials. At surfaces with high-symmetry, these spin-splittings are well described by the so-called Rashba Hamiltonian given in Eq. (3.1). The Rashba spin-splitting at metallic surfaces was first observed for the two-dimensional (2D) Shockley surface state of the Au(111) surface [47, 119]. It was then investigated for a number of clean [48, 49] and alloyed surfaces [120, 121], and surfaces of semiconductors in contact with heavy metals [46]. Recently, large spin-splittings were observed in ferroelectrics as well [122, 123].

On possible way of studying the spin-splitting of the surface states is by the deposition of magnetic impurities. Indeed, when a defect is present on the surface, the Rashba electrons scatter-off that defect and this induces oscillations in the charge density of the 2D surface states, which are called Friedel oscillations [124]. However, no signature of the spin-splitting was observed theoretically in the Friedel oscillations for the charge density [125]. More recently, Lounis *et al.* showed that a signature of the spin-splitting can be observed in the Friedel oscillations of the spin magnetization density [126]. Besides Friedel oscillations a multitude of rich phenomena can occur due to the scattering of Rashba electrons on magnetic impurities.

In this thesis we address three examples of the manifestation of such scattering processes. The first example is due to the multiple scattering of Rashba electrons at magnetic impurities, that leads to an indirect exchange mechanism known as the Ruderman-Kittel-Kasuya-Yosida (RKKY) interaction [60, 62, 61]. In addition to the isotropic exchange, magnetic impurities deposited on surfaces with spin-orbit interaction give rise to the so-called Dzyaloshinskii-Moriya (DM) interaction [51, 50], which favors non-collinear magnetic structures. The second example is the impact on magnetotransport properties. In particular, we expect contributions to the planar Hall effect (PHE) as well as the anisotropic magnetoresistance (AMR). The anomalous Hall effect (AHE) is expected to be absent if no external magnetic fields are applied [64]. Both the PHE and AHE are observed as

a voltage transverse to the applied current [64, 127], in contrast to the AMR, which is measured in the longitudinal geometry. The third example is the presence of bound state charge current swirling around the magnetic impurities. They give rise to a finite orbital magnetization. For chiral magnetic structures, the orbital magnetization is non-vanishing even without spin-orbit interaction [67].

This chapter covers a wide variety of phenomena and consists of three main parts. The first part introduces the Rashba Hamiltonian and the basic quantities used in scattering theory such as the t-matrix. This is followed by an analysis of Friedel oscillations for the charge and spin magnetization density for Fe atoms deposited on Au(111), which is the system considered throughout this chapter. Then we discuss the magnetic interactions between impurities, we track the origin of the DM interaction and of the not much investigated pseudo-dipolar interaction. At long distances, we have access to a rich phase diagram not addressed in the usual bulk or 2D materials. Moreover, we consider dimers and complex magnetic nanostructures.

The second part is about the scattering off impurities of Rashba electrons in presence of external electric fields. We introduce a wave function formulation of the scattering problem in two dimensions, and perform an expansion of the Rashba Green function in a cylindrical basis (similar to the expansion done in Sec. 2.4.1 for the 3D electron gas Green function). Then within linear response theory we compute the residual resistivity tensor (an identical approach is used for the magnetic susceptibility within TD-DFT in Sec. 2.4.1). We also analyze the dependence of the residual resistivity tensor on the direction of the spin moment, and discuss the AMR effect in the diagonal part, while PHE is observed in the off-diagonal components.

In the third part, we discuss the induced bound currents in the Rashba electron gas due to a single magnetic impurity, afterwards, we solve a Poisson equation using the bound currents to access the orbital magnetization. Then we consider a dimer coupled antiferromagnetically in presence of the DM interaction. Finally, we examine a trimer with a non-vanishing scalar chirality in presence and in absence of the spin-orbit interaction, respectively.

The part of this chapter discussing magnetic interactions has been published in Ref. [128]. The section dedicated to the residual resistivity tensor was published in Ref. [66]. Finally, the last part addressing the impurity induced orbital magnetization was published in Ref. [129].

3.1 Rashba Hamiltonian

As discussed previously, the spin-orbit interaction (SOI) leads in a structure-asymmetric environment (such as a surface or interface) to a spin-splitting of the otherwise two-fold degenerate eigenstates of a two-dimensional electron gas. The model of Bychkov and Rashba [44, 130] describes this splitting by adding to the kinetic energy of the free electrons a linear term in momentum. The Rashba Hamiltonian is given by:

$$\boldsymbol{H}_{\mathrm{R}} = \frac{p_x^2 + p_y^2}{2m^*}\,\mathbb{1}_2 - \frac{\alpha_{\mathrm{so}}}{\hbar}(\boldsymbol{\sigma}_x p_y - \boldsymbol{\sigma}_y p_x) \quad , \tag{3.1}$$

where p_γ, $\gamma \in \{x, y\}$, are the components of the momentum operator $\vec{p}$ in a Cartesian coordinate system with x, y coordinates in the surface plane whose surface normal points along $\vec{e}_z$. m^* is the effective mass of the electron. $\boldsymbol{\sigma}_\gamma$ are the Pauli matrices and $\mathbb{1}_2$ is the unit matrix in spin-space with a global spin frame of reference where the spin z-direction is aligned parallel to $\vec{e}_z$. α_{so} is the Rashba parameter, a measure of the strength of the SOI and the parameter that controls the degree of Rashba spin-splitting. The eigenstates corresponding to this Hamiltonian are written as a product of a plane wave in real space and a two-component spinor

$$\psi_{\vec{k}\pm}(\vec{r}) = \frac{1}{\sqrt{2}} e^{\mathrm{i}\vec{k}\cdot\vec{r}} \begin{pmatrix} 1 \\ \pm \mathrm{i} e^{\mathrm{i}\phi_{\vec{k}}} \end{pmatrix} \text{ with } \phi_{\vec{k}} = \arctan\left(\frac{k_y}{k_x}\right) \quad , \tag{3.2}$$

i.e. they can be considered as a superposition of spin-up and down-states when measured with respect to the surface normal. The orientation of the local spin-quantization axis is given by the expectation value $\vec{n}_\pm(\vec{k})$:

$$\begin{aligned} \vec{n}_\pm(\vec{k}) &= \langle \psi_{\pm\vec{k}} | \vec{\boldsymbol{\sigma}} | \psi_{\pm\vec{k}} \rangle \quad , \\ &= \pm(-\sin\phi_{\vec{k}}, \cos\phi_{\vec{k}}, 0) \quad , \\ &= \pm\vec{e}_\phi \quad . \end{aligned} \tag{3.3}$$

It lies in the surface plane and is perpendicular to the wave vector $\vec{k} = k\,(\cos\phi_{\vec{k}}, \sin\phi_{\vec{k}}, 0)$ $= k\,\vec{e}_k$. We find that the quantization axis is independent of the magnitude k and depends only on the direction $\vec{e}_k$ of the wave vector $\vec{k}$. With respect to this quantization axis that is parallel to $\vec{e}_\phi$ in a cylindrical coordinate system, $\psi_{\vec{k}\pm}(\vec{r})$ are spin pure eigenstates and we can associate $\psi_{\vec{k}\pm}(\vec{r})$ for $\alpha = +(-)$ as spin-up (-down) state. The energy dispersion is characterized by the k-linear splitting of the free-electron parabolic band dispersion as denoted:

$$\varepsilon_\pm(k) = \frac{\hbar^2 k^2}{2m^*} \pm \alpha_{\mathrm{so}} k = \frac{\hbar^2}{2m^*}\left[(k \pm k_{\mathrm{so}})^2 - k_{\mathrm{so}}^2\right]. \tag{3.4}$$

Due to the z-inversion broken symmetry and the presence of the SOI, the minima of the spin-up and -down parabolas are shifted by the Rashba or the spin-orbit wave vector, respectively, $k_{\mathrm{so}} = \frac{m^* \alpha_{\mathrm{so}}}{\hbar^2}$. The wave number for each band is defined by:

$$\begin{cases} k_\pm = k_{\mathrm{M}} \mp k_{\mathrm{so}} \quad , \\ \text{with } k_{\mathrm{M}} = \left[\frac{2m^*\varepsilon}{\hbar^2} + k_{\mathrm{so}}^2\right]^{1/2} , \end{cases}$$

so that $k_+ - k_- = -2\,k_{\mathrm{so}}$ holds irrespective of the value of $\varepsilon(> 0)$. For a constant energy cut, the spin structure is shown in Fig. 3.1.

3.2 Rashba Green function

The Green function is one of the central quantities needed to study the scattering of Rashba electron off magnetic impurities. It allows to use an embedding technique via the Dyson equation given in Eq. (2.23). Thus, we connect the Green function describing the Rashba electrons in presence of magnetic impurities $\boldsymbol{G}(\vec{r}, \vec{r}\,', \varepsilon)$ and the unperturbed Rashba Green

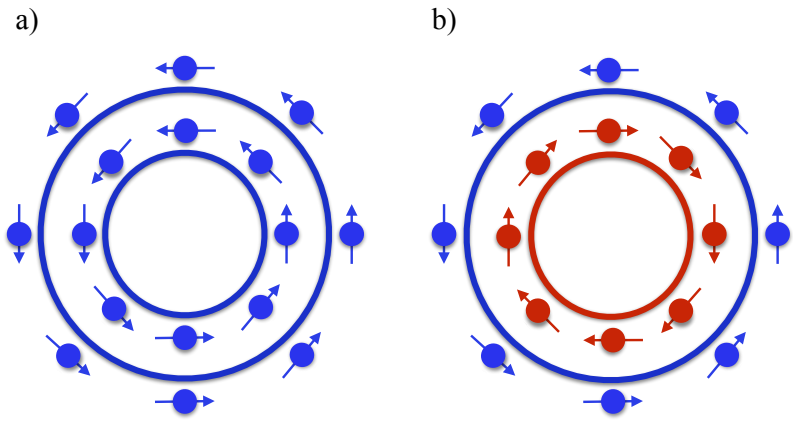

Figure 3.1: Spin texture in the reciprocal space for a Rashba electron gas. a) For negative energies located under the crossing of the Rashba bands. b) For positive energies located above the band crossing.

function $\boldsymbol{G}^{\mathrm{R}}(\vec{r},\vec{r}\,',\varepsilon)$. The Rashba Green function is computed analytically using the spectral representation given in Eq. (2.20). Where the Kohn-Sham orbitals are replaced by $\psi_{\vec{k}\alpha}(\vec{r})$ (eigenstates of $\boldsymbol{H}_{\mathrm{R}}$) and the Kohn-Sham eigenenergies by $\varepsilon_\alpha(\vec{k})$ (eigenvalues of $\boldsymbol{H}_{\mathrm{R}}$):

$$\boldsymbol{G}^{\mathrm{R}}(\vec{r},\vec{r}\,',\varepsilon+\mathrm{i}\eta)=\sum_{\vec{k}\alpha}\frac{\psi_{\vec{k}\alpha}(\vec{r})\,\psi^{\dagger}_{\vec{k}\alpha}(\vec{r}\,')}{\varepsilon-\varepsilon_\alpha(\vec{k})+\mathrm{i}\eta}\quad , \tag{3.5}$$

η is real and positive to ensure convergence. The Rashba Green function has translational invariance: $\boldsymbol{G}^{\mathrm{R}}(\vec{r},\vec{r}\,',\varepsilon)=\boldsymbol{G}^{\mathrm{R}}(\vec{R},\varepsilon)$, with $\vec{R}=\vec{r}-\vec{r}\,'$. After performing the sums over $\vec{k}$ and α, The Rashba Green function is given by a matrix in spin space:

$$\boldsymbol{G}^{\mathrm{R}}(\vec{R},\varepsilon)=\begin{pmatrix} G_{\mathrm{D}} & -G_{\mathrm{ND}}\,e^{-\mathrm{i}\beta} \\ G_{\mathrm{ND}}\,e^{\mathrm{i}\beta} & G_{\mathrm{D}} \end{pmatrix}\quad , \tag{3.6}$$

β is the angle between $\vec{R}$ and the x-axis. The diagonal and off diagonal elements of the Rashba Green function in spin space are defined as:

$$G_{\mathrm{D}}(R,\varepsilon)=-\frac{\mathrm{i}m^*}{2\hbar^2(k_++k_-)}\Big[k_-\,H_0^{(1)}(k_-R)+k_+\,H_0^{(1)}(k_+R)\Big]\quad , \tag{3.7}$$

$$G_{\mathrm{ND}}(R,\varepsilon)=-\frac{\mathrm{i}m^*}{2\hbar^2(k_++k_-)}\Big[k_-\,H_1^{(1)}(k_-R)-k_+\,H_1^{(1)}(k_+R)\Big]\quad . \tag{3.8}$$

$H_n^{(1)}(x)$ is a cylindrical Hankel function of the first kind for the n-order.

3.3 Transition matrix

Here, we derive an approximation for the transition matrix (t-matrix) introduced previously in Sec. 2.4.2. It describes the scattering of an electron due to the presence of a single potential $\boldsymbol{v}(\vec{r})$, where $\boldsymbol{v}(\vec{r})$ is a 2×2 matrix in spin space. The Dyson equation characterizing this scattering process reads in real space:

$$\boldsymbol{G}(\vec{r},\vec{r}\,',\varepsilon) = \boldsymbol{G}^{\mathrm{R}}(\vec{r},\vec{r}\,',\varepsilon) + \int \mathrm{d}\vec{r}\,''\, \boldsymbol{G}^{\mathrm{R}}(\vec{r},\vec{r}\,'',\varepsilon)\, \boldsymbol{v}(\vec{r}\,'')\, \boldsymbol{G}(\vec{r}\,'',\vec{r}\,',\varepsilon) \quad . \tag{3.9}$$

The previous equation can be reformulated in terms of the t-matrix, which is related to the scattering potential via:

$$\boldsymbol{t}(\vec{r},\vec{r}\,',\varepsilon) = \boldsymbol{v}(\vec{r})\, \delta(\vec{r}-\vec{r}\,') + \int \mathrm{d}\vec{r}\,''\, \boldsymbol{v}(\vec{r})\, \boldsymbol{G}^{\mathrm{R}}(\vec{r},\vec{r}\,'',\varepsilon)\, \boldsymbol{t}(\vec{r}\,'',\vec{r}\,',\varepsilon) \quad . \tag{3.10}$$

Thus, when using the t-matrix Eq. (3.9) reads:

$$\begin{aligned} \boldsymbol{G}(\vec{r},\vec{r}\,',\varepsilon) &= \boldsymbol{G}^{\mathrm{R}}(\vec{r},\vec{r}\,',\varepsilon) \\ &+ \int \mathrm{d}\vec{r}\,''\mathrm{d}\vec{r}\,'''\, \boldsymbol{G}^{\mathrm{R}}(\vec{r},\vec{r}\,'',\varepsilon)\, \boldsymbol{t}(\vec{r}\,'',\vec{r}\,''',\varepsilon)\, \boldsymbol{G}^{\mathrm{R}}(\vec{r}\,''',\vec{r}\,',\varepsilon) \quad . \end{aligned} \tag{3.11}$$

The formulation of the scattering problem in terms of t-matrix in Eq. (3.11) is more convenient since it allows to make approximations at the t-matrix level. For the considered systems, when Rashba electrons scatter off an impurity whose spatial extent is much smaller than the Fermi wave length λ_{F}, we can proceed within the s-wave approximation [131, 126]. For such a scatterer, the spatial dependency of the t-matrix can be approximated with a δ-function. Furthermore, neglecting the spin-orbit interaction at the level of the impurity is justified considering that for the studied impurities it is rather small (Fe impurities). In this case, and when the magnetic moment of the impurity is pointing along the z-axis (*i.e.* perpendicular to surface plane), the t-matrix is diagonal in spin space and reads:

$$\boldsymbol{t}(\vec{r},\vec{r}\,',\varepsilon) = \begin{pmatrix} t^{\uparrow\uparrow}(\varepsilon) & 0 \\ 0 & t^{\downarrow\downarrow}(\varepsilon) \end{pmatrix} \delta(\vec{r})\, \delta(\vec{r}\,') \quad . \tag{3.12}$$

The diagonal spin components of the t-matrix are given by:

$$\begin{aligned} t^{\sigma\sigma}(\vec{r},\vec{r}\,',\varepsilon) &= t^{\sigma\sigma}(\varepsilon)\, \delta(\vec{r})\, \delta(\vec{r}\,') \quad , \\ &= \frac{\mathrm{i}\hbar^2}{m^*} \left(e^{2\mathrm{i}\delta_0^{\sigma\sigma}(\varepsilon)} - 1\right) \delta(\vec{r})\, \delta(\vec{r}\,') \quad . \end{aligned} \tag{3.13}$$

$\delta_0^{\sigma\sigma}(\varepsilon)$ is the phase shift between the scattered wave function at the impurity and the unscattered wave function for the orbital quantum number $m = 0$ (in two dimension). The analytical form of $t^{\sigma\sigma}(\varepsilon)$ was derived in Appendix A for a magnetic impurity in a two dimensional electron gas without spin-orbit interaction.

The s-wave approximation has been used numerous times for the interpretation of STM based experiments [131, 132, 133, 134]. It was employed in the context of standing waves on a Cu(111) surface [135] or a Au(111) surface [136], as well as for confined electronic

states in corrals of Fe or Co adatoms deposited on a Cu(111) surface [137, 138]. For Fe adatoms on a Cu(111) surface, good fits to the experimental features were obtained with a phase shift of $\pi/2$ but a better agreement was found with a phase shift of $\mathrm{i}\infty$, which would correspond to maximally absorbing adatoms (*i.e.* black dots) [138]. In the latter case, the overall scattering amplitude reduces by a factor of 2 compared to the situation where a phase shift of $\pi/2$ is considered.

$\delta_0^{\sigma\sigma}(\varepsilon)$ can be traced back to the local density of states (LDOS) at the impurity site using the so-called Friedel sum rule [124]:

$$Z = \frac{1}{\pi} \sum_{\sigma} \sum_{m=-\infty}^{\infty} \delta_m^{\sigma\sigma}(\varepsilon_\mathrm{F}) \quad , \tag{3.14}$$

where Z is the charge of the impurity. Using Eq. (3.14), one can derive the following relation between the spin-polarized LDOS at the impurity site and the scattering phase shift:

$$\rho^{\sigma\sigma}(\varepsilon) = \frac{1}{\pi} \sum_{m=-\infty}^{\infty} \frac{\mathrm{d}\delta_m^{\sigma\sigma}(\varepsilon)}{\mathrm{d}\varepsilon} \quad . \tag{3.15}$$

In order to access the phase shift $\delta_m^{\sigma\sigma}(\varepsilon)$, we computed the density of states of an Fe adatom deposited on Au(111) surface from first principles using the KKR Green function method discussed in Sec. 2.4. We considered both non-magnetic and magnetic Fe adatoms, for which the easy axis points out-of-plane (along the z-direction). We fitted the obtained impurity LDOS with Lorentzian functional forms. The result of the fit is shown in Fig. 3.2. In the s-wave approximation, the scattering phase shift can be computed analytically by integrating Eq. (3.15) and we obtain:

$$\delta_0^{\sigma\sigma}(\varepsilon) = \frac{\pi}{2} + \mathrm{atan}\left(\frac{\varepsilon - \varepsilon_\sigma}{\Gamma_\sigma}\right) \quad . \tag{3.16}$$

For magnetic Fe adatoms, $\varepsilon_\downarrow = 0.05\,\mathrm{eV}$ is the position of the resonance for the minority-spin channel slightly higher than the Fermi level ε_F located at zero energy and $\Gamma_\downarrow = 0.4\,\mathrm{eV}$ is the resonance width. For the majority-spin channel $\varepsilon_\uparrow = \varepsilon_\downarrow - 2.8\,\mathrm{eV}$ due to the exchange splitting and $\Gamma_\uparrow = 0.6\,\mathrm{eV}$. For the non-magnetic configuration $\varepsilon_\downarrow = \varepsilon_\uparrow = -0.21\,\mathrm{eV}$ and $\Gamma_\downarrow = \Gamma_\uparrow = 0.6\,\mathrm{eV}$.

The procedure displayed previously allows and an analytical description of the t-matrix using scattering phase shifts, which can accessed from first principles. It provides a reasonably accurate description of the scattered electronic waves at the impurities.

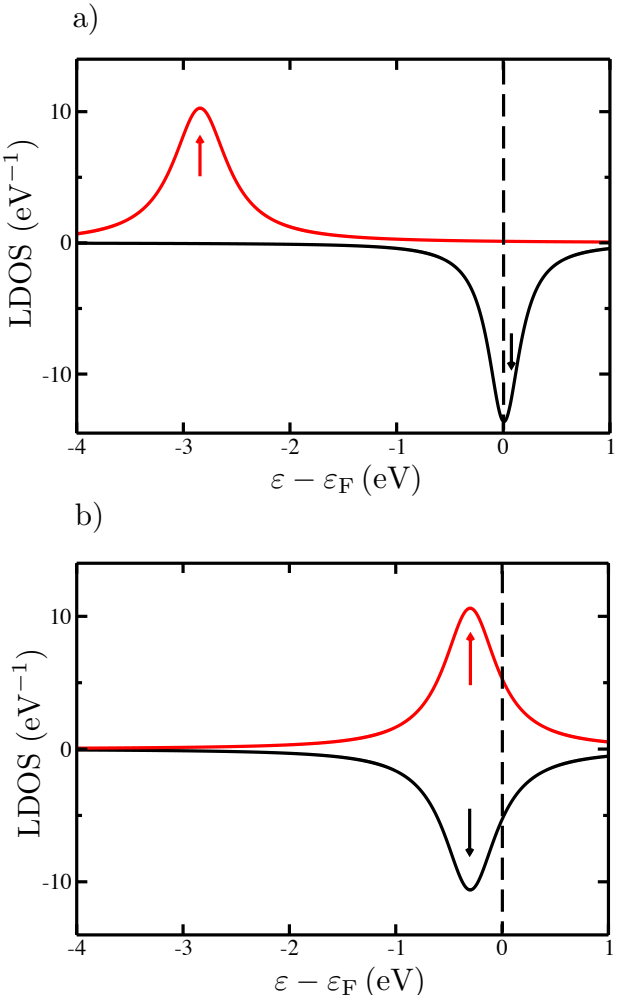

Figure 3.2: Local density of states of an Fe adatom deposited on a Au(111) surface described by a Lorentzian model wherein the broadening is induced by hybridization effects among the electronic states of the impurity with those of the substrate. Two cases are considered, a magnetic (a) versus a non magnetic impurity (b). After defining the phase shifts at the Fermi energy in the magnetic case, the phase shifts in the non-magnetic case are derived considering the same charge for both type of impurities.

3.4 Friedel oscillations

The Friedel oscillations introduced previously result from the screening of defects present in metallic systems [124]. The shape of the oscillations corresponds to the real space imaging of the Fermi surface, *i.e.* a two dimensional free electron gas with a cylindrically

symmetric Fermi surface displays cylindrical oscillations around defects. In a two dimensional electron gas without spin-orbit interaction, the Friedel oscillations in the charge density at a large distance from the scatterer are given by:

$$\delta n(r) = \frac{\sin(2k_{\mathrm{F}}r + \delta)}{r^2} \quad . \tag{3.17}$$

$\delta n(r)$ is the induced change in the charge density around the impurity, r is distance away from the impurity. k_{F} is the Fermi wave vector and δ is the scattering phase shift describing the impurity given in Eq. (3.16). The Friedel oscillations can be visualized experimentally using scanning tunneling microscopy (STM). One of the most outstanding experiments was done by Crommie *et al.* in Ref. [137], where they deposited corrals of Fe atoms on a Cu(111) surface. They observed that within the corral the surface states are localized and form a collection of resonant states.

3.4.1 Friedel oscillations in the induced charge density

As aforementioned, we now analyze the Friedel oscillations arising when a single magnetic impurity is deposited on a Rashba electron gas. The set up is parametrized for an Fe impurity on a Au(111) surface. The Fe impurity is introduced by solving the Dyson equation given in Eq. (3.11). It is described by the t-matrix in the s-wave approximation discussed in Sec. 3.3. The induced charge density at a distance r from the Fe impurity and an energy ε is computed from the Green function. For an Fe impurity located at the origin it reads:

$$\delta n(\vec{r}, \varepsilon) = -\frac{1}{\pi} \operatorname{Im} \operatorname{Tr}_{\sigma} \left(\boldsymbol{G}^{\mathrm{R}}(\vec{r}, 0, \varepsilon)\, \boldsymbol{t}(\varepsilon)\, \boldsymbol{G}^{\mathrm{R}}(0, \vec{r}, \varepsilon) \right) \quad . \tag{3.18}$$

Considering that the magnetic moment of the Fe impurity is along the z-direction (out-of-plane) [126], assuming that the SOI on the Fe impurity site is small and using the analytical form of the Rashba Green function given in Eq. (3.6), we obtain the following expression for $\delta n(\vec{r}, \varepsilon)$:

$$\delta n(\vec{r}, \varepsilon) = -\frac{1}{\pi} \operatorname{Im} \left[(G_{\mathrm{D}}\, G_{\mathrm{D}} + G_{\mathrm{ND}}\, G_{\mathrm{ND}}) \left(t^{\uparrow\uparrow}(\varepsilon) + t^{\downarrow\downarrow}(\varepsilon) \right) \right] \quad . \tag{3.19}$$

At large distances (*i.e.* $r \to \infty$), the Rashba Green function is given by its asymptotic form (see Appendix C) and the induced charge density is written as:

$$n(\vec{r}, \varepsilon) \propto \frac{4m^*}{\pi^2 \hbar^2 (k_+ + k_-)^2 r} \sqrt{k_- k_+}\, \cos((k_- + k_+) r) \quad . \tag{3.20}$$

When replacing the two wave vectors $k_{\pm} = k_{\mathrm{M}} \mp k_{\mathrm{so}}$ (describing the two Rashba bands), the induced charge simply reads:

$$n(\vec{r}, \varepsilon) \propto \frac{m^*}{\pi^2 \hbar^2 k_{\mathrm{M}}^2 r} \left(\frac{2m^* \varepsilon}{\hbar^2} \right) \cos(2k_{\mathrm{M}} r) \quad , \tag{3.21}$$

The previous equation shows the absence of interference due to the spin-orbit interaction (*i.e.* k_{so}) in the Friedel oscillations. Thus, one cannot observe the signature of the Rashba spin-splitting in the oscillations of the charge density.

3.4.2 Friedel oscillations in the induced spin magnetization density

The introduction of a magnetic impurity into the Rashba electron gas breaks time reversal symmetry (*i.e* $t^{\uparrow\uparrow}(\varepsilon) \neq t^{\downarrow\downarrow}(\varepsilon)$). This induces Friedel oscillations in the spin magnetization density within the Rashba electron gas [126]. Thus, we investigate the possibility of observing a signature of the spin-orbit interaction in the induced spin magnetization density given by:

$$\vec{m}(\vec{r},\varepsilon) = -\frac{1}{\pi}\,\mathrm{Im}\,\mathrm{Tr}_\sigma\left(\vec{\boldsymbol{\sigma}}\,\boldsymbol{G}^{\mathrm{R}}(\vec{r},0,\varepsilon)\,\boldsymbol{t}(\varepsilon)\,\boldsymbol{G}^{\mathrm{R}}(0,\vec{r},\varepsilon)\right) \quad . \tag{3.22}$$

$\vec{\boldsymbol{\sigma}}$ is the Pauli vector, the presence of the spin-orbit interaction within in the Rashba electron gas gives rise to in-plane components for the magnetization besides the out-of-plane component:

$$m_x(\vec{r},\varepsilon) = m_{xy}(\vec{r},\varepsilon)\,\cos\beta \quad , \tag{3.23}$$

$$m_y(\vec{r},\varepsilon) = m_{xy}(\vec{r},\varepsilon)\,\sin\beta \quad , \tag{3.24}$$

$$m_{xy}(\vec{r},\varepsilon) = -\frac{2}{\pi}\,\mathrm{Im}\left[G_{\mathrm{D}}\,G_{\mathrm{ND}}\,(t^{\uparrow\uparrow}(\varepsilon) - t^{\downarrow\downarrow}(\varepsilon))\right] \quad , \tag{3.25}$$

$$m_z(\vec{r},\varepsilon) = -\frac{1}{\pi}\,\mathrm{Im}\left[(G_{\mathrm{D}}\,G_{\mathrm{D}} - G_{\mathrm{ND}}\,G_{\mathrm{ND}})\,(t^{\uparrow\uparrow}(\varepsilon) - t^{\downarrow\downarrow}(\varepsilon)\right] \quad , \tag{3.26}$$

where $m_{xy}(\vec{r},\varepsilon)$ is the in-plane magnetization and β is the angle between $\vec{r}$ and the x-axis introduced in Eq. (3.6). The asymptotic form of $\vec{m}(\vec{r},\varepsilon)$ at large distances is given by:

$$\begin{aligned}
m_x(\vec{r},\varepsilon) &\propto \frac{m^*}{\pi^2\hbar^2 k_{\mathrm{M}}^2 r}\,(k_-\sin(2k_-r) - k_+\sin(2k_+r)\cos\beta \quad , \\
m_y(\vec{r},\varepsilon) &\propto \frac{m^*}{\pi^2\hbar^2 k_{\mathrm{M}}^2 r}\,(k_-\sin(2k_-r) - k_+\sin(2k_+r))\sin\beta \quad , \\
m_z(\vec{r},\varepsilon) &\propto \frac{m^*}{\pi^2\hbar^2 k_{\mathrm{M}}^2 r}\,(k_-\cos(2k_-r) + k_+\sin(2k_+r)) \quad .
\end{aligned} \tag{3.27}$$

The induced magnetization density is given by a linear combination of two wave vectors $k_\pm$ due to the spin-orbit interaction, which leads to interferences that can be measured using SP-STM. In particular one can notice a beating of the oscillations in $m_z(\vec{r},\varepsilon)$ at a distance $r_{\mathrm{so}} = \frac{\pi}{4k_{\mathrm{so}}} \approx 60\,\text{Å}$ for an Fe impurity on a Au(111) surface. A more detailed analysis shows that the magnetization density is given by a linear combination of two Skyrmionic waves. One wave propagates with k_+ while the other one propagates with k_- [126].

3.5 Interactions among magnetic impurities deposited on a Rashba electron gas

After studying the impact of a single magnetic impurity deposited on a two dimensional electron gas with Rashba spin-orbit interaction, we now consider systems with several

magnetic impurities interacting via Rashba electrons. The presence of the spin-orbit interaction and the lack of inversion symmetry generate the Dzyaloshinskii-Moriya (DM) interaction [51, 50], a key ingredient for non-collinear magnetism, which is at the heart of chiral magnetism. The DM interaction defines the rotation sense of the magnetization, rotating clockwise or counter clockwise along a given axis of a magnetic material. This is the case of spin-spirals in two-dimensional [52, 53, 54] or one-dimensional systems [55, 56] down to zero-dimensional non-collinear metallic magnets [63, 139, 140]. The ever-increasing interest in understanding the properties of the DM interaction and the corresponding vector is, thus, not surprising. Although the symmetry aspects of these interactions were discussed in the seminal work of Moriya [50], the ingredients affecting the magnitude and the particular orientation of a DM vector are not that explored but are certainly related to the details of the electronic structure.

In the context of long-range interactions mediated by conduction electrons, the DM interaction was addressed by Smith [59] and Fert and Levy [58]. They found a strong analogy with the RKKY interactions [60, 62, 61]. Indeed, the long-range DM vector oscillates in magnitude and changes its orientation as function of distance, which was recently confirmed experimentally with scanning tunneling microscopy (STM) and theoretically with ab-initio simulations based on density functional theory [63]. We note that today, besides theory, state-of-the-art STM experiments can be used to learn about the magnitude, oscillatory behavior and decay of the RKKY interactions as demonstrated in Refs. [141, 142, 143]. The information about all the magnetic interactions is contained in the magnetic exchange tensor $\boldsymbol{J}_{ij}$ which will be discussed in detail in the next sections.

3.5.1 Extended Heisenberg model

The generalization of the isotropic Heisenberg model to include anti-symmetric and anisotropic interactions is given in Ref. [144]. The elements of the magnetic exchange tensor, $\boldsymbol{J}_{ij}$, can be extracted by differentiating H_m according to $\vec{e}_i$ and $\vec{e}_j$:

$$H_\mathrm{m} = \frac{1}{2}\sum_{i,j} \vec{e}_i\, \boldsymbol{J}_{ij}\, \vec{e}_j \quad , \quad J_{ij}^{\alpha\beta} = \frac{\partial^2 H_\mathrm{m}}{\partial e_i^\alpha \partial e_j^\beta} \quad , \tag{3.28}$$

with $\{\alpha, \beta\} = \{x, y, z\}$ and $\vec{e}_i$ being the unit vector of the magnetic moment at site i. The exchange tensor is decomposed into three contributions:

$$\boldsymbol{J}_{ij} = \frac{1}{3}\left(\mathrm{Tr}\,\boldsymbol{J}_{ij}\right)\mathbb{1}_3 + \boldsymbol{J}_{ij}^\mathrm{A} + \boldsymbol{J}_{ij}^\mathrm{S} \quad . \tag{3.29}$$

In the right-hand side of the previous equation, the first term is the isotropic exchange and we define $J_{ij} = \frac{1}{3}\left(\mathrm{Tr}\,\boldsymbol{J}_{ij}\right)$, while $\mathbf{J}_{ij}^\mathrm{A}$ is the anti-symmetric part:

$$\boldsymbol{J}_{ij}^\mathrm{A} = \frac{\boldsymbol{J}_{ij} - \boldsymbol{J}_{ij}^\mathrm{T}}{2} \quad , \tag{3.30}$$

which is connected to the Dzyaloshinskii-Moriya vector components via:

$$\boldsymbol{J}_{ij}^\mathrm{A} = \begin{pmatrix} 0 & D_{ij}^z & -D_{ij}^y \\ -D_{ij}^z & 0 & D_{ij}^x \\ D_{ij}^y & -D_{ij}^x & 0 \end{pmatrix} \quad . \tag{3.31}$$

The last term of Eq. (3.29), $\boldsymbol{J}_{ij}^{\mathrm{S}}$, is the symmetric part that describes pseudo-dipolar interactions:

$$\boldsymbol{J}_{ij}^{\mathrm{S}} = \frac{\boldsymbol{J}_{ij} + \boldsymbol{J}_{ij}^{\mathrm{T}}}{2} - \frac{1}{3}\,\mathrm{Tr}\,\{\boldsymbol{J}_{ij}\}\,\mathbb{1}_3 \quad . \tag{3.32}$$

For the Rashba model, we will see that there is a more natural way of decomposing the tensor which is given in Eq. (3.42). The Hamiltonian H_{m} can be written in terms of the Dzyaloshinskii-Moriya vector as:

$$H_{\mathrm{m}} = \frac{1}{2}\sum_{ij} J_{ij}\,\vec{e}_i \cdot \vec{e}_j + \frac{1}{2}\sum_{ij} \vec{D}_{ij} \cdot (\vec{e}_i \times \vec{e}_j) + \frac{1}{2}\sum_{ij} \vec{e}_i\,\boldsymbol{J}_{ij}^{\mathrm{S}}\,\vec{e}_j \quad . \tag{3.33}$$

3.5.2 Mapping procedure

The strategy is to consider the Hamiltonian describing the electronic structure of the nanostructures and perform the same type of differentiation as in Eq. (3.28) in order to identify the tensor of magnetic exchange interactions. We use Lloyd's formula [100], which permits the evaluation of the energy variation due to an infinitesimal rotation of the magnetic moments, starting from a collinear configuration [80, 145, 144]. In general, the contribution to the band energy (single-particle energy) after embedding the nanostructure is given by:

$$\varepsilon_{\mathrm{band}} = \frac{1}{\pi}\,\mathrm{Im}\int_{\varepsilon_{\mathrm{R}}}^{\varepsilon_{\mathrm{F}}} \mathrm{d}\varepsilon\,\mathrm{Tr}\ln \boldsymbol{T}(\varepsilon)^{-1} \quad , \tag{3.34}$$

where ε_{F} is the Fermi energy, $\varepsilon_{\mathrm{R}} = -\frac{\hbar^2 k_{\mathrm{so}}^2}{2m^*}$ is the bottom of the Rashba energy bands and Tr is the trace over impurity position- and spin-indices. $\boldsymbol{T}(\varepsilon)$ is the full scattering matrix given by a Dyson equation:

$$\boldsymbol{T}_{ij}^{-1}(\varepsilon) = \boldsymbol{t}_i^{-1}(\varepsilon)\,\delta_{ij} - \boldsymbol{G}_{ij}^{\mathrm{R}}(\varepsilon) \quad , \tag{3.35}$$

$\boldsymbol{T}_{ij}(\varepsilon)$ is the full scattering matrix connecting the sites i and j. In practice, we use the s-wave approximation as in Eq. (3.13). The Green function describing the magnetic nanostructures is given by a Dyson equation similar to Eq. (3.9). However, $\boldsymbol{t}_i(\varepsilon)$ is replaced by $\boldsymbol{T}_{ij}(\varepsilon)$ to include the multiple scattering effects:

$$\boldsymbol{G}_{ij}(\varepsilon) = \boldsymbol{G}_{ij}^{\mathrm{R}}(\varepsilon) + \sum_{km} \boldsymbol{G}_{ik}^{\mathrm{R}}(\varepsilon)\,\boldsymbol{T}_{km}(\varepsilon)\,\boldsymbol{G}_{mj}^{\mathrm{R}}(\varepsilon) \quad . \tag{3.36}$$

The elements of the tensor of exchange interaction are then given by:

$$J_{ij}^{\alpha\beta} = \frac{\partial^2}{\partial e_i^\alpha \partial e_j^\beta}\varepsilon_{\mathrm{band}} = -\frac{1}{\pi}\,\mathrm{Im}\int_{\varepsilon_{\mathrm{R}}}^{\varepsilon_{\mathrm{F}}} \mathrm{d}\varepsilon\,\mathrm{Tr}\,\frac{\partial^2}{\partial e_i^\alpha \partial e_j^\beta}\ln \boldsymbol{T}(\varepsilon) \quad . \tag{3.37}$$

Using Eq. (3.35), we evaluate the required second derivative and find for the elements of the tensor of exchange interactions:

$$J_{ij}^{\alpha\beta} = -\frac{1}{\pi}\,\mathrm{Im}\int_{\varepsilon_{\mathrm{R}}}^{\varepsilon_{\mathrm{F}}} \mathrm{d}\varepsilon\,\mathrm{Tr}\,\boldsymbol{t}_i^\alpha(\varepsilon)\,\boldsymbol{G}_{ij}(\varepsilon)\,\boldsymbol{t}_j^\beta(\varepsilon)\,\boldsymbol{G}_{ji}(\varepsilon) \quad , \tag{3.38}$$

the trace is taken over the spin-index, and $\boldsymbol{t}_i^{\alpha}(\varepsilon)$ is simply the derivative of $\boldsymbol{t}_i(\varepsilon)$ with respect to e_i^{α}. Since the t-matrix can be written as:

$$\boldsymbol{t}_i(\varepsilon) = \frac{t_i^{\uparrow\uparrow}(\varepsilon) + t_i^{\downarrow\downarrow}(\varepsilon)}{2}\,\mathbb{1}_2 + \frac{t_i^{\uparrow\uparrow}(\varepsilon) - t_i^{\downarrow\downarrow}(\varepsilon)}{2}\,\vec{\boldsymbol{\sigma}}\cdot\vec{e}_i \quad , \tag{3.39}$$

we find that $\boldsymbol{t}_i^{\alpha}(\varepsilon) = \frac{\partial \boldsymbol{t}_i(\varepsilon)}{\partial e_i^{\alpha}} = \Delta_i(\varepsilon)\,\boldsymbol{\sigma}_{\alpha}$, with $\Delta_i(\varepsilon) = \frac{t_i^{\uparrow\uparrow}(\varepsilon) - t_i^{\downarrow\downarrow}(\varepsilon)}{2}$. The final form of the tensor of magnetic exchange interactions is then finally given by:

$$J_{ij}^{\alpha\beta} = -\frac{1}{\pi}\,\mathrm{Im}\int_{\varepsilon_{\mathrm{R}}}^{\varepsilon_{\mathrm{F}}} \mathrm{d}\varepsilon\,\Delta_i(\varepsilon)\,\Delta_j(\varepsilon)\,\mathrm{Tr}\,\boldsymbol{\sigma}_{\alpha}\,\boldsymbol{G}_{ij}(\varepsilon)\,\boldsymbol{\sigma}_{\beta}\,\boldsymbol{G}_{ji}(\varepsilon) \quad . \tag{3.40}$$

We see that Eq. (3.40) depends on the magnetic structure of the impurity cluster, since it involves the renormalized Green function which depends on the orientation of the magnetic moments of the impurities via Eq. (3.36). In practice, we consider three different ferromagnetic configurations, aligned along the x, y and z-axes, compute the respective exchange tensors and keep the transverse blocks (e.g. for the ferromagnetic configuration along z, we keep the xy-block); elements that occur repeatedly are averaged.

3.6 Magnetic properties of dimers

Before studying the magnetic interactions between magnetic adatoms for complicated nanostructures, we first compute the magnetic interaction tensor for two adatoms, relying on two approaches: first using the RKKY-approximation, expected from second order perturbation theory and used for example by Ref. [146]; second by solving numerically the Dyson equation given in Eq. (3.36).

3.6.1 RKKY-approximation

The magnetic interactions given in Eq. (3.40) can be computed analytically, by considering the unrenormalized Green functions, $\boldsymbol{G}_{ij}^{\mathrm{R}}(\varepsilon)$, instead of $\boldsymbol{G}_{ij}(\varepsilon)$. In the particular case of a two-dimensional Rashba electron gas, the Rashba Green function can be expressed using Pauli matrices:

$$\boldsymbol{G}_{ij}^{\mathrm{R}}(\varepsilon) = G_{\mathrm{D}}\,\mathbb{1}_2 - \mathrm{i}\,G_{\mathrm{ND}}\,(\cos\beta\,\boldsymbol{\sigma}_y - \sin\beta\,\boldsymbol{\sigma}_x) \quad . \tag{3.41}$$

β is the angle between the vector connecting the impurities i, j and the x-axis (see Sec. 3.2). Surprisingly, we found anisotropies in the diagonal part of the exchange tensor that are generally neglected in the literature. The physical meaning of these anisotropies can be traced back to the extended Heisenberg model defined by the tensor of magnetic exchange interactions. In fact, by defining the x-axis as the line connecting the two sites i and j, we show in Appendix B that the extended Heisenberg Hamiltonian describing the corresponding magnetic coupling can be written as:

$$H_{\mathrm{m}} = J(r)\,\vec{e}_i\cdot\vec{e}_j + D(r)\,(\vec{e}_i\times\vec{e}_j)_y + I(r)\,e_i^y\,e_j^y \quad , \tag{3.42}$$

where the exchange constants ($J(r)$, $D(r)$ and $I(r)$) are related to the Rashba Green function by:

$$J(r) = -\frac{2}{\pi}\,\mathrm{Im}\int_{\varepsilon_R}^{\varepsilon_F} \mathrm{d}\varepsilon\,\Delta_i(\varepsilon)\,\Delta_j(\varepsilon)\,(G_D^2 - G_{ND}^2) \quad , \tag{3.43}$$

$$D(r) = \frac{4}{\pi}\,\mathrm{Im}\int_{\varepsilon_R}^{\varepsilon_F} \mathrm{d}\varepsilon\,\Delta_i(\varepsilon)\,\Delta_j(\varepsilon)\,G_D\,G_{ND} \quad , \tag{3.44}$$

$$I(r) = -\frac{4}{\pi}\,\mathrm{Im}\int_{\varepsilon_R}^{\varepsilon_F} \mathrm{d}\varepsilon\,\Delta_i(\varepsilon)\,\Delta_j(\varepsilon)\,G_{ND}^2 \quad . \tag{3.45}$$

$J(r)$ is the isotropic exchange interaction and r is the distance between two impurities i and j, defined in this particular case (dimer along the x-axis) as $J(r) = J_{ij}^{xx} = J_{ij}^{zz}$, which if positive favors an antiferromagnetic coupling in our convention, otherwise it favors a ferromagnetic coupling. $D(r)$ is the y component of the DM vector, which is by symmetry the only nonzero component (Third rule of Moriya [50]). This favors chiral magnetic textures lying in the (xz) plane. $I(r)$ is the pseudo-dipolar term, a two-ion anisotropy term, coming from the symmetric part of the exchange tensor. It leads to an anisotropy in the diagonal-part of the tensor of exchange interaction, for instance $J_{ij}^{xx} = J_{ij}^{zz} \neq J_{ij}^{yy}$. Considering the impurities along the x-axis, $I(r)$ is given by $J_{ij}^{yy} - J_{ij}^{zz}$. This anisotropy is finite because of the two-dimensional nature of the Rashba electrons, so the x- and y-directions are non-equivalent to the z-direction. Here, $I(r)$ favors a collinear magnetic structure along the y-axis and counteracts the DM interaction.

The analytical forms of the magnetic exchange interactions allow us to understand their origin in terms of the magnetic Friedel oscillations generated by single atoms [126]. These oscillations carry a complex magnetic texture that can be interpreted in terms of Skyrmionic-like waves. Within the RKKY-approximation and neglecting the energy dependence of $\Delta_i(\varepsilon)$, the isotropic interaction, $J(r)$, connecting two impurities at site i and j, is proportional to the z-component of magnetization generated at site j by a single impurity at site i. In other words, the impurity at site j feels the effective magnetic field generated by the magnetization at that site but induced by the adatom at site i ($J(r) \propto \int \mathrm{d}\varepsilon\, m_z(r,\varepsilon)$). $D(r)$, however, is defined by the in-plane component of the induced magnetization ($D(r) \propto \int \mathrm{d}\varepsilon\, m_{xy}(r,\varepsilon)$). Here, the corresponding magnetic field acting over the second impurity has an in-plane component and naturally leads to a non-collinear magnetic behavior, *i.e.* the natural impact of the DM vector. $I(r)$ does not have a simple interpretation, but it can be related to the anisotropy (difference) of the induced magnetization parallel to the impurity moment upon its rotation from out of plane to in plane.

Analytical evaluation of the isotropic exchange interaction $J(r)$

In order to derive analytically the exchange interactions, we use an approximation for the t-matrices. We assume that they are energy independent (resonant scattering for the minority-spin channel, *i.e.* $\delta^{\downarrow\downarrow}(\varepsilon) = \frac{\pi}{2}$, and no scattering for the majority-spin channel, *i.e.* $\delta^{\uparrow\uparrow}(\varepsilon) = \pi$), which allows us to write $\Delta_i(\varepsilon) = -\frac{2i\hbar^2}{m^*}$. This approximation used in Ref. [126] is reasonable for an adatom like Fe deposited on Au(111) surface. Then, we

find the asymptotic behavior of G_{D} and G_{ND} for large distances r (see Appendix C). The isotropic exchange constant can be expressed as:

$$\begin{aligned} J(r) &= \frac{2}{\pi^2 r}\,\mathrm{Im}\int_{\varepsilon_{\mathrm{R}}}^{\varepsilon_{\mathrm{F}}} \mathrm{d}\varepsilon\, \frac{\mathrm{i}}{(k_- + k_+)^2}\,(k_-\, e^{2\mathrm{i}k_- r} + k_+\, e^{2\mathrm{i}k_+ r}) \quad , \\ &= \frac{\hbar^2}{m^* \pi^2 r}\left[\frac{1}{2r}\sin(2k_{\mathrm{F}}r)\cos(2k_{\mathrm{so}}r) - k_{\mathrm{so}}\sin(2k_{\mathrm{so}}r)\;\mathrm{SI}(2k_{\mathrm{F}}r)\right] \quad . \end{aligned} \tag{3.46}$$

$\mathrm{SI}(x)$ is the sine-integrated function of x. $J(r)$ is found to be the sum of two functions. The first one evolves as a function of $\frac{1}{r^2}$, as expected for regular two-dimensional systems but the second function decays like $\frac{1}{r}$, which has been neglected in the work of Ref. [146]. The $\frac{1}{r}$ decay leads to a slower decay of $J(r)$ than what is known for a regular two-dimensional electron gas. The origin of this term is the Van Hove singularity at the bottom of the two bands; the density of states of the Rashba electron gas resembles that of a one -dimensional electron gas between ε_{R} and $\varepsilon = 0$, where the two bands cross. At very large distances, $\mathrm{SI}(x)$ converges to a constant ($\frac{\pi}{2}$) and $J(r)$ is behaving like $\frac{1}{r}\sin(2k_{\mathrm{so}}r)$. Naturally, when k_{so} is set to zero, we recover the classical form of the RKKY interaction without spin-orbit interaction for a free electron gas in two-dimensions, *i.e.* $J(r)$ evolves then like $\frac{1}{r^2}\sin(2k_{\mathrm{F}}r)$.

Analytical evaluation of the y component of the DM vector $D(r)$

Considering the same approximations used to compute the isotropic part of the exchange interaction tensor, we find the y-component of the DM vector $(D(r))$ simply given by:

$$\begin{aligned} D(r) &= -\frac{4}{\pi^2 r}\,\mathrm{Im}\int_{\varepsilon_{\mathrm{R}}}^{\varepsilon_{\mathrm{F}}} \mathrm{d}\varepsilon\, \frac{1}{2(k_- + k_+)^2}\,[\,k_-\, e^{2\mathrm{i}k_- r} - k_+\, e^{2\mathrm{i}k_+ r}\,] \quad , \\ &= -\frac{\hbar^2}{m^* \pi^2 r}\left[\frac{1}{2r}\sin(2k_{\mathrm{F}}r)\sin(2k_{\mathrm{so}}r) + k_{\mathrm{so}}\;\cos(2k_{\mathrm{so}}r)\,\mathrm{SI}(2k_{\mathrm{F}}r)\right] \quad . \end{aligned} \tag{3.47}$$

Like the isotropic exchange constant, $D(r)$ is a sum of two terms. The first term decays as $\frac{1}{r^2}$, while the second as $\frac{1}{r}$. A perturbative development of $D(r)$ in terms of k_{so} shows that $D(r)$ is first order in spin-orbit interaction. At very large distances $D(r)$ evolves like $\frac{1}{r}\cos(2k_{\mathrm{so}}r)$.

Analytical evaluation of the pseudo-dipolar term $I(r)$

The last quantity that is left to be determined is the pseudo-dipolar term $I(r)$. Following a similar approach as for calculating $J(r)$ and $D(r)$, we show in Appendix C that $I(r)$ is a sum of two integrals over the energy because of a branch cut in the Hankel functions. The first integral, denoted $I_1(r)$, goes from ε_{R} to zero and the second, $I_2(r)$, goes from zero to

$\varepsilon_{\rm F}$:

$$I_1(r) = -\frac{4}{\pi^2 r}\,\mathrm{Im}\int_{\varepsilon_{\rm R}}^{0}\mathrm{d}\varepsilon\,\frac{1}{2(k_- + k_+)^2}[\mathrm{i}\,(k_-\,e^{2\mathrm{i}k_- r} + k_+\,e^{2\mathrm{i}k_+ r})] + 2\sqrt{|k_-|k_+}\,e^{\mathrm{i}(k_+ - |k_-|)r}] \quad ,$$
$$I_2(r) = -\frac{4}{\pi^2 r}\,\mathrm{Im}\int_{0}^{\varepsilon_{\rm F}}\mathrm{d}\varepsilon\,\frac{\mathrm{i}}{2(k_- + k_+)^2}[k_-\,e^{2\mathrm{i}k_- r} + k_+\,e^{2\mathrm{i}k_+ r}\; - 2\sqrt{k_- k_+}\,e^{\mathrm{i}(k_- + k_+)r}] \quad . \tag{3.48}$$

If we sum up the two terms $I_1(r) + I_2(r)$:

$$I(r) = -J(r) + \frac{\hbar^2}{m^* \pi^2 r}\left[\int_{|k_{\rm so}|}^{k_{\rm F}}\mathrm{d}k\,\sqrt{1 - \frac{k_{\rm so}^2}{k^2}}\,\cos(2kr) - \int_0^{|k_{\rm so}|}\mathrm{d}k\,\sqrt{\frac{k_{\rm so}^2}{k^2} - 1}\,\sin(2kr)\right] \quad . \tag{3.49}$$

The integral involving $\cos(2kr)$ is important at short distances since it competes with one of the terms defining $-J(r)$. In fact, it has the opposite sign of $-\frac{1}{2r}\sin(2k_{\rm F}r)\cos(2k_{\rm so}r)$ (see Eq. (3.46)). This reduces considerably the value of I comparing to $J(r)$. The second integral involves $\sin(2kr)$ and therefore it leads to a small contribution for low values of $k_{\rm so}$. A perturbative development of $I(r)$ in terms of $k_{\rm so}$ shows that $I(r)$ is second order in spin-orbit interaction ($\propto k_{\rm so}^2$).

Comparison and evolution of the exchange interactions as a function of the distance

In Fig. 3.3, we plot the magnetic exchange interactions $J(r), D(r)$ and $I(r)$ as function of the distance between two magnetic adatoms deposited on a Au(111) surface. The parameters used for these simulations are given in Sec. 3.3. The black curve depicts $J(r)$, which at short distances is characterized by a wavelength $\lambda = \frac{\pi}{k_{\rm F}} \approx 18.5\,$Å. We see in Fig. 3.3 a beating of the oscillations, which can be understood by looking at the first term in Eq. (3.46). Writing it as $\frac{1}{4r}(\sin(2k_- r) + \sin(2k_+ r))$, with $k_\pm = k_{\rm F} \mp k_{\rm so}$, the superposition of these two wave vectors causes a beating effect at $r_{\rm so} = \frac{\pi}{4k_{\rm so}} \approx 60\,$Å . The finite value of $J(r)$ at $r_{\rm so}$ is due to the second term in Eq. (3.46), since $\mathrm{SI}(2k_{\rm F}r) \approx \frac{\pi}{2}$ and $\sin(2k_{\rm so}r) \approx 1$. One notices that for a large range of distances ($r > 40\,$Å) the magnetic interactions do not oscillate around the $y = 0$ axis, which is due to the $\mathrm{SI}(x)$ term present in Eqs. (3.46) and (3.47) for $J(r)$ and $D(r)$, while for $I(r)$, the shift comes from the last term in Eq. (3.49). All these terms originate from the Van Hove singularity at the bottom of the bands. Similarly to $J(r)$, $D(r)$ is negative for distances larger than $25\,$Å, which means within the RKKY-approximation, the chirality defined by the sign of the DM interaction changes only for dimers separated by rather small distances.

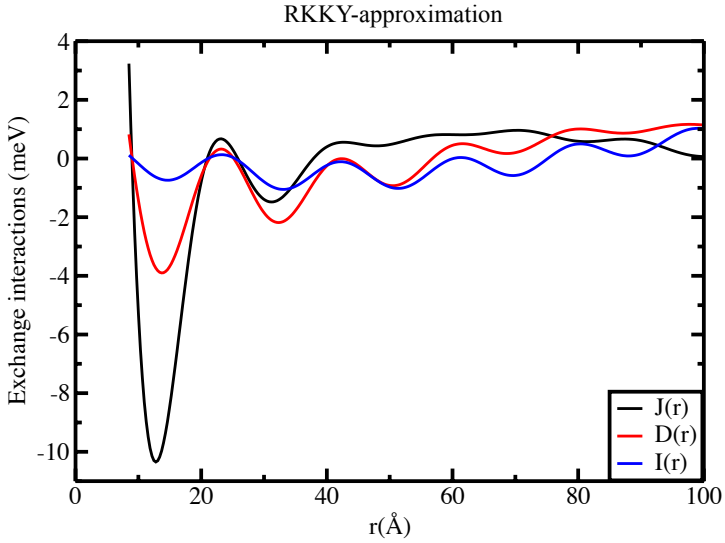

Figure 3.3: Evolution of the magnetic interactions $J(r)$, $D(r)$, $I(r)$ (see Eq. (3.28)) as a function of the distance, for $\alpha_{\rm so} = -0.4$ eV Å and $m^* = 0.26\ m_{\rm e}$ (parameters for Au(111) surface [147] used in Eq. (3.1)). We use the RKKY-approximation (see Eqs. (3.43), (3.44), 3.45) and assume a maximal scattering cross section for the minority spin channel ($\delta_\downarrow = \frac{\pi}{2}$) and no contribution for the majority spin channel ($\delta_\uparrow = \pi$).

3.6.2 Beyond the RKKY-approximation

The deposited magnetic impurities naturally renormalize the electronic properties of the Rashba electrons. We can now prove that the contributions of the sine integral to the magnetic interactions are artifacts of the RKKY approximation. When the energy approaches the Van Hove singularity, $\varepsilon \to \varepsilon_{\rm R} = -\frac{\hbar^2 k_{\rm so}^2}{2m^*}$, the multiple scattering series cannot be truncated, and the RKKY approximation cannot be made. The Green function connecting two impurities i and j is given by:

$$\begin{aligned} \boldsymbol{G}_{ij}(\varepsilon) &= (1 - \boldsymbol{G}^{\rm R}_{ij}(\varepsilon)\, \boldsymbol{t}_j(\varepsilon)\, \boldsymbol{G}^{\rm R}_{ji}(\varepsilon)\, \boldsymbol{t}_i(\varepsilon))^{-1}\, \boldsymbol{G}^{\rm R}_{ij}(\varepsilon) \\ &= \boldsymbol{G}^{\rm R}_{ij}(\varepsilon) + \boldsymbol{G}^{\rm R}_{ij}(\varepsilon)\, \boldsymbol{t}_j(\varepsilon)\, \boldsymbol{G}^{\rm R}_{ji}(\varepsilon)\, \boldsymbol{t}_i(\varepsilon)\, \boldsymbol{G}^{\rm R}_{ij}(\varepsilon) + \dots \quad , \end{aligned} \tag{3.50}$$

where the second equality corresponds to the multiple scattering, or Born series. When $\varepsilon \to \varepsilon_{\rm R}$, the Rashba Green function $\boldsymbol{G}^{\rm R}_{ij}(\varepsilon) \to \infty$. However, from the first equality in Eq. (3.50), we have $\boldsymbol{G}_{ij}(\varepsilon) \to 0$ for $\varepsilon \to \varepsilon_{\rm R}$, therefore, the Van Hove singularity will not contribute to the exchange interactions computed from Eq. (3.40) and the contribution from $\mathrm{SI}(x)$ vanishes.

In order to quantify the impact of the renormalization on the electronic states mediating the magnetic exchange interactions, we numerically compute $\boldsymbol{G}_{ij}(\varepsilon)$, by considering consistently the multiple scattering effects. This is done first via considering an energy dependence in the t-matrix assuming that they correspond to a Lorentzian in the electronic

structure of the impurities (see Sec. 3.4.1). Then we use Eq. (3.35) for computing $\boldsymbol{T}(\varepsilon)$. Afterwards we solve the Dyson equation (Eq. (3.36)) giving $\boldsymbol{G}(\varepsilon)$. The evolution of the three exchange interactions after renormalizing the Green function is given in Fig. 3.4. As expected, we note the disappearance of the RKKY-approximation artifact leading to the apparent offset of the oscillations beyond $r = 40$ Å (see Fig. 3.4). The beating effect in $J(r)$ occurs at the same distance as in the RKKY-approximation because it is an intrinsic property of the Rashba electron gas. At large distances the intensities of $J(r)$ and $D(r)$ are decreasing quickly, but $I(r)$ keeps oscillating up to a distance of $\approx$ 200 Å where it decreases quickly to zero.

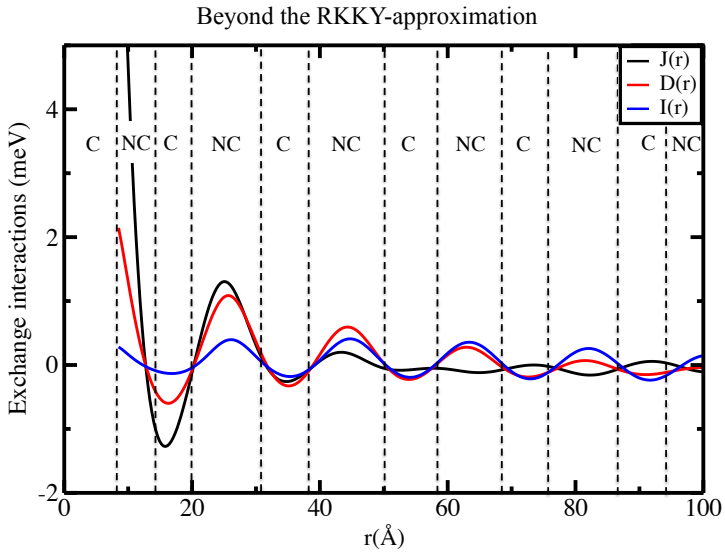

Figure 3.4: Beyond the RKKY-approximation and using the electronic structure renormalized by the presence of two impurities (Eqs. (3.36) and (3.40)). The vertical lines define a magnetic phase diagram indicating the nature of the orientation of the two magnetic moments as function of their separation. C indicates the collinear phase of the magnetic moments and NC the non-collinear phase.

3.6.3 Connecting the different parts of the exchange interaction tensor

Before discussing the magnetic phases emerging from the competition due to the different interactions present in our magnetic Hamiltonian H_m from Eq. (3.28), it is interesting to analyze the possibility of connecting $J(r)$ to $D(r)$ within our model. Recently, it was demonstrated that, in the context of a micromagnetic model, the spin stiffness $A \sim \sum_j r_j^2 J(r_j)$, the micromagnetic counterpart of $J(r)$, and $L = \sum_j r_j D(r_j)$, the counterpart of $D(r)$ called the Lifshitz invariant can be related to each other for low SOI [148]:

$$L \sim -2k_{\mathrm{so}}A \quad . \tag{3.51}$$

The sum over sites j is limited by the size of the nanostructure but it can be infinite, e.g. if dealing with a monolayer or an infinite wire. We checked the validity of the previous relation utilizing the analytical forms of $J(r)$ and $D(r)$ obtained in the RKKY-approximation, *i.e.* Eqs. (3.46) and (3.47), and found that Eq. (3.51) can be recovered for $k_{\rm so}r \ll 1$ but the error is proportional to the term involving the sine integral $\mathrm{SI}(2k_{\rm F}r)$. So if one neglects the contribution of the Van Hove singularity of the Rashba electron gas, one arrives at the formula of Kim *et al.* [148].

However, we proved that the multiple scattering precisely cancels this extra contribution, so we propose the following relation to hold:

$$D(r) = \frac{1}{2r}\frac{\partial J(r)}{\partial k_{\rm so}} \quad . \tag{3.52}$$

First, we compare the RKKY expressions in Fig. 3.5a, inserting the result of Eq. (3.46) in Eq. (3.52), and then the RKKY expression for $D(r)$ given in Eq. (3.47). The agreement is very poor, as expected. Second, in Fig. 3.5b we extract $J(r)$ from Eq. (3.40) and numerically evaluate Eq. (3.52), and then compare with $D(r)$ given also by Eq. (3.40). So for the more realistic case (using the renormalized electronic structure) we find that Eq. (3.52) is a very good approximation.

The intriguing implication of Eq. (3.52) is that it gives an interpretation for the origin of the chirality being left– or right–handed according to the sign of $D(r)$. For a given distance r, $D(r)$ can be of the same (opposite) sign of $J(r)$ if the latter's magnitude increases (decreases) with the spin-orbit interaction.

3.6.4 Magnetic configurations of dimers

Having established the behavior of the tensor of magnetic exchange interactions as a function of distance, we investigate now the magnetic ground state of different nanostructures characterized by different geometries and different sizes. After getting the magnetic interactions with the mapping procedure described in Sec. 3.5.2, we minimize the extended Heisenberg Hamiltonian with respect to the spherical angles, (θ_i, ϕ_i), defining the orientation of every magnetic moment:

$$\vec{e}_i = (\cos\phi_i \sin\theta_i, \sin\phi_i \sin\theta_i, \cos\theta_i) \quad . \tag{3.53}$$

In order to check the stability of the magnetic ground state, we often add to the extended Heisenberg Hamiltonian the term $K\sum_i (e_i^z)^2$, where K is a single-ion magnetic anisotropy energy favoring an out-of-plane orientation of the magnetic moment as it is the case for an Fe adatom on Au(111). We choose as a typical value $K = -6$ meV for all the investigated nanostructures [149].

For the particular case of the dimer, an analytical solution is achievable by noticing that two magnetic states are possible: collinear (C) and non-collinear (NC). This is counter-intuitive, since the presence of the DM interaction leads usually to a non-collinear ground state. The presence of the pseudo-dipolar term $I(r)$ makes the physics richer and stabilizes collinear magnetic states. Once more, because of the particular symmetry provided by the Rashba electron gas, within the non-collinear phase, the only finite component of the DM vector, $D_y(r)$, enforces the two magnetic moments to lie in (xz)-plane perpendicular to

the DM vector. Within the collinear phase, $I(r)$ enforces the moments to point along the y-axis.

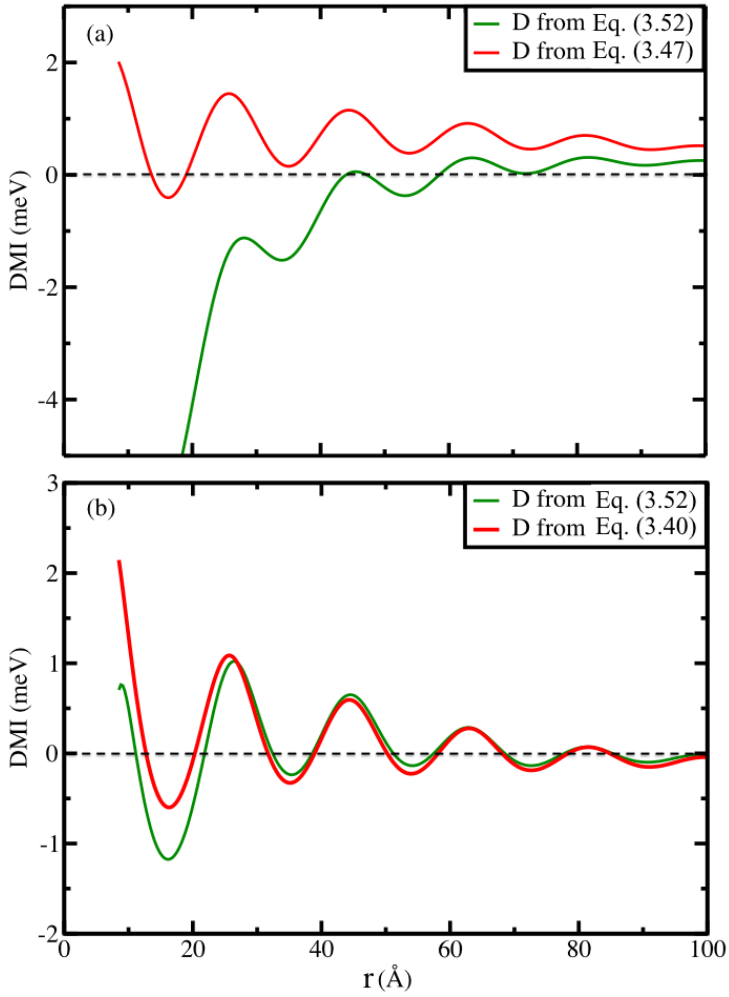

Figure 3.5: (a) Comparison between $D(r)$ computed from the RKKY-approximation, Eq. (3.47), and from Eq. (3.52). (b) The comparison involves $D(r)$ computed from the renormalized Green functions Eq. (3.40), *i.e.* beyond the RKKY-approximation, and from Eq. (3.52). As explained in the main text, the contribution from the Van Hove singularity that leads to the discrepancy seen in panel (a) is spurious.

Non-collinear phase

Here, the magnetic moments lie in the (xz)-plane and the pseudo-dipolar term does not contribute to the ground state energy. The ground state is then defined by the angle,

$\theta_0(r) = \text{atan}\frac{D(r)}{J(r)}$, between the two magnetic moments at sites i and j. The energy corresponding to this state is $-|J(r)|\sqrt{1+\frac{D^2(r)}{J^2(r)}}$. With the single-ion anisotropy, K, the ground state angle becomes $\theta_0 = \text{atan}\,(\frac{D(r)}{J(r)+K})$. As an example, we consider two adatoms separated by $d = 10.42$ Å which corresponds to the seventh nearest neighbors distance on Au(111) surface. In this case $J = 3.45$ meV and $D = 0.96$ meV and the ground state angle (θ_0) is $164°$ ($K = 0\,\text{meV}$) or $171°$ ($K = -6\,\text{meV}$).

Collinear phase

$D(r)$ does not contribute to the ground state configuration. When $J(r)$ and $I(r)$ are both negative the magnetic moments are parallel and point along the y-axis with the energy $J(r) + I(r)$, while for positive $J(r)$ and $I(r)$ the magnetic moments are anti-parallel and point along the y axis too, with the energy $-(J(r)+I(r))$. If $J(r)$ and $I(r)$ have opposite signs, for $J(r) > 0$ the magnetic moments are anti-parallel in the (xz)–plane with the energy $-J(r)$, while for $J(r) < 0$ the magnetic moments are parallel in the (xz)–plane with the energy $J(r)$. However, these last two solutions will not occur, since the NC phase is lower in energy.

Competing phases

There is competition between the collinear phase C and the non-collinear phase NC, which depends on the involved magnetic interactions. Without $I(r)$, Fig. 3.4 will consist of one single phase, the NC phase. The presence of the pseudo-dipolar interaction $I(r)$ provides an alternation of the two phases depending on the inter-adatom distance. The magnetic anisotropy K favours an out-of-plane orientation of the moments and tends to decrease the spatial range of the collinear phase where the moments point along the y-axis.

Magnetic phase diagram

We drop the r dependence of the magnetic interactions (J, D and I) and study the phase diagram of the dimers ($K = 0\,\text{meV}$) as seen in Fig. 3.6. The color scale shows the energy difference ΔE between the ground states found in the NC phase and C phase normalized by $|J|$. A negative (positive) energy difference corresponds to a NC (C) ground state. Thus the blue region corresponds to a C phase and the red region to a NC phase:

$$\begin{cases} \Delta E = \frac{E_{NC}-E_C}{|J|} = -\sqrt{1+\frac{D^2}{J^2}}+1 & \text{for } J \text{ and } I \text{ with an opposite sign,} \\ \Delta E = \frac{E_{NC}-E_C}{|J|} = -\sqrt{1+\frac{D^2}{J^2}}+(1+\frac{I}{J}) & \text{for } J \text{ and } I \text{ with the same sign.} \end{cases} \tag{3.54}$$

For small ratios $\frac{D}{J}$, if $\frac{I}{J} < 0$ then $\frac{\Delta E}{|J|}$ simplifies to $-\frac{D^2}{2J^2}$ and if $\frac{I}{J} > 0$ it simplifies to $-\frac{D^2}{2J^2}+\frac{I}{J}$, which define the magnetic phases plotted in Fig. 3.6. We notice that when I and J are of the same sign, the dimers are mostly characterized by a C ground state. The corresponding C phase is separated from the NC phase by a parabola as expected from the term $-\frac{D^2}{2J^2}$. Moreover, we note that even within the NC phase, a transition occurs when the sign of $\frac{I}{J}$ changes. This is related to the nature of the NC phase that changes by switching

the sign of $\frac{I}{J}$, which leads to an additional, $\frac{I}{J}$, term in the energy difference. As mentioned earlier, if $\frac{I}{J}$ is positive the moments are in plane and align (parallel or anti-parallel) along the y direction, while a negative $\frac{I}{J}$ leads to an alignment in the (xz) plane. For negative $\frac{I}{J}$, one notices that when $\frac{D}{J}$ goes to zero, the plotted energy difference goes to zero, which does not mean that the C and NC phases are degenerate but it is the signature that the rotation angle of the moments goes to zero. Thus, at $\frac{D}{J} = 0$, we have only a C phase.

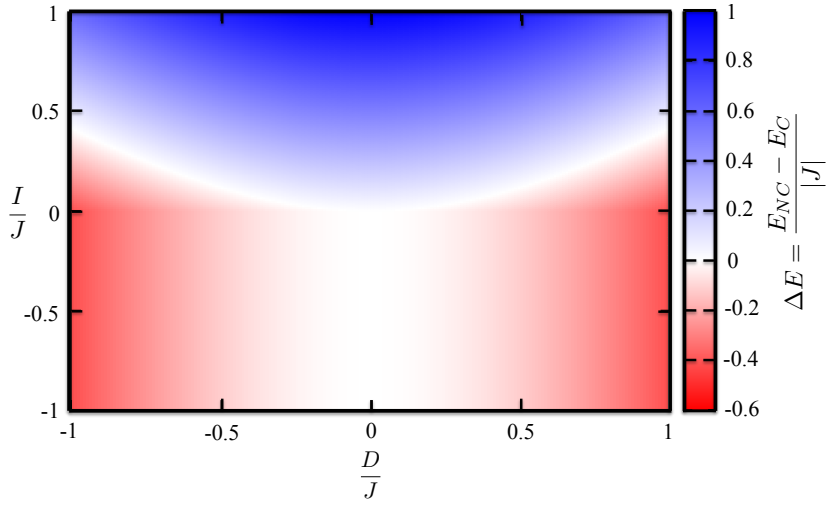

Figure 3.6: Phase diagram for the magnetic ground states of dimers. The color scale represents the energy difference normalized by $|J|$ between the non-collinear (red colour) and collinear states (blue colour) as function of the parameters $\{\frac{D}{J}, \frac{I}{J}\}$ (see Eq. (3.54)).

3.7 Magnetic properties of complex nanostructures

After studying the properties of magnetic dimers, we build more complex nanostructures of different sizes and shapes made of Fe adatoms deposited on Au(111) according to the parameters given in Sec. 3.6.2. The distance between the first nearest neighbors is chosen to be $d = 10.42$ Å for all structures, corresponding to the seventh nearest neighbors distance on the Au(111) surface (lattice parameter $a = 2.87$ Å). This is very close to what is accessible experimentally [150].

We compute the magnetic interactions for the considered nanostructures. For the chosen inter-adatom distance to build the magnetic nanostructures, interactions beyond nearest neighbors play no significant role. For that reason, we report in Table 3.1 only the average nearest-neighbor interactions, although all interactions are taken into account when determining the magnetic ground states numerically. The z component of the DM vector is two orders of magnitude smaller than the in-plane components for all the considered nanostructures, therefore, it will be omitted when discussing the magnetic ground states.

A summary of the obtained average magnetic interactions between nearest neighbors is provided in Table 3.1.

Structures	J (meV)	D (meV)	I (meV)	$\theta(^\circ)$
Chain	6.90	2.00	0.26	110
Trimer	3.51	1.00	0.13	117
Hexagon	5.64	1.67	0.23	164
Heptamer	4.69 (4.62)	1.37 (1.36)	0.18 (0.12)	120 (142)

Table 3.1: Summary of the average magnetic interactions between nearest neighbours for the calculated magnetic nanostructures. The values between parenthesis for the heptamer are for the nearest neighbors on the outer ring.

3.7.1 Magnetism of linear chains

We investigated several linear chains of different sizes. All of them presented the same characteristics. Here we discuss the example of a wire made of 14 adatoms. In this case, the isotropic exchange interaction between the nearest-neighbors is antiferromagnetic. On average it is equal to 6.90 meV, *i.e.* the double of the isotropic interaction obtained for the dimer, which highlights the impact of the nanostructure in renormalizing the electronic structure of the system. Within the RKKY-approximation, the magnetic interactions would be independent from the nature, shape, size of the deposited nanostructures. Due to the Moriya rules, the DM vector lies along the y-direction within the surface plane similar to the dimer case. It is thus perpendicular to the x-axis defined by the chain axis. The DM interaction is around 2 meV between nearest neighbors, *i.e.* once more the double of the value obtained for the dimer.

The magnetic ground state is a spiral contained in the (xz) plane with an average rotation angle of 110° between two nearest neighboring magnetic moments (see Fig. 3.7). Interestingly, this angle is much smaller than the one found for the dimer (164°) but similar to that found for intermediate chain sizes. The pseudo-dipolar term is around $I = 0.26$ meV, and it has no impact on the ground state. This situation is equivalent to the NC phase of the dimer. Of course, choosing an inter-atomic distance with a large pseudo-dipolar term for the dimers, leads generally to stable collinear magnetic wires (not shown here). We noticed that the effect of the magnetic anisotropy energy ($K = -6$ meV) is mainly on the edge atoms. Indeed, the rotation angles between adjacent inner-moments remain around 110° while at the edges, the magnetic moments are pointing more along the z-direction. The rotation angle between the magnetic moment at the edge and the z-axis is reduced to 25°.

3.7.2 Trimer

We studied a trimer forming an equilateral triangle. The isotropic exchange constant J is equal to 3.51 meV favoring antiferromagnetic coupling, a value close to the one found for the dimer. The frustration is large in this case leading to a non-collinear ground state even without SOI [151, 152]. The magnetic moments lie in the same plane, e.g. the surface

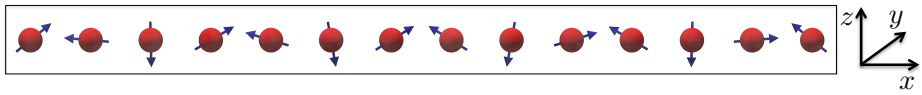

Figure 3.7: Magnetic ground state of a wire made of 14 adatoms. The interadatom distance is $d = 10.42$ Å, while the average nearest-neighbor isotropic exchange interaction is $J = 6.90$ meV and the nearest-neighbors DM vector points along the y-axis with an average intensity $D = 2$ meV. The magnetic anisotropy $K = 0$ meV. The spiral is characterized by an average rotation angle of 110° between nearest neighboring magnetic moments.

plane, with an angle of 120° between two magnetic moments. This state has continuous degeneracy, since rotating each magnetic moment in the same way leaves the energy invariant. If we now consider the DM interaction, we find that $\vec{D}$, with a magnitude of 1.0 meV (similar to the dimer's value), lies in the xy plane and perpendicular to the axis connecting two adatoms (see Fig. 3.8c). This interaction lifts the degeneracy present without D, stabilizing the magnetic structure shown in Fig. 3.8a and b. The pseudo-dipolar term I is equal to 0.13 meV and is small compared to J and D therefore the non-collinear phase is more stable. The isotropic interaction keeps the angle between the in-plane projections of the moment at 120°, while the DM interaction generates a slight upward tilting (81° instead of 90°). In fact, every DM vector connecting two sites favors the non-collinearity of the related magnetic moments by keeping them in the plane perpendicular to the surface and containing the two sites. This is however impossible to satisfy at the same time for the three pairs of atoms forming the trimer, which leads to the compromise shown in Fig. 3.8a and b. The magnetic anisotropy reduces ($K = -6$ meV) considerably the non-collinearity and the three moments are enforced to point almost-parallel to the z-axis. Two of the magnetic moments are characterized by an angle of 10° instead of 81° with respect to the z-axis, while the angle of the third moment is 173° as shown in Fig. 3.8d. This is an interesting outcome compared to the behavior of the wire, which is characterized by a large averaged DM interaction in comparison to the trimer. Obviously the shape of the nanostructure is important in stabilizing non-collinear magnetism.

3.7.3 Hexagon

We consider now a system of six atoms forming a hexagonal shape with the same interatomic distance as the one considered earlier. The magnetic ground state configuration is non-collinear as shown in Figs. 3.9 (a) and (b). The isotropic magnetic exchange interaction, J, between nearest neighbors is of antiferromagnetic type similarly to the value obtained for the other nanostructures studied so far. J reaches a value of 5.64 meV, which is rather close to the interaction found for the wire. In fact one could consider this hexagonal structure as a closed wire. The magnitude of the DM vector connecting two nearest neighbors is large, 1.67 meV, but not as large as the one of the wire. The non-collinear state is better appreciated when plotting the projection of the moments unit vectors on the surface plane in Fig. 3.9c and along the z-axis in Fig. 3.9d. The polar angle is either 16° or 164°, according to the antiferromagnetic nature of the interactions. The azimuthal angle follows the symmetry of the hexagon, leading to an azimuthal angle difference of

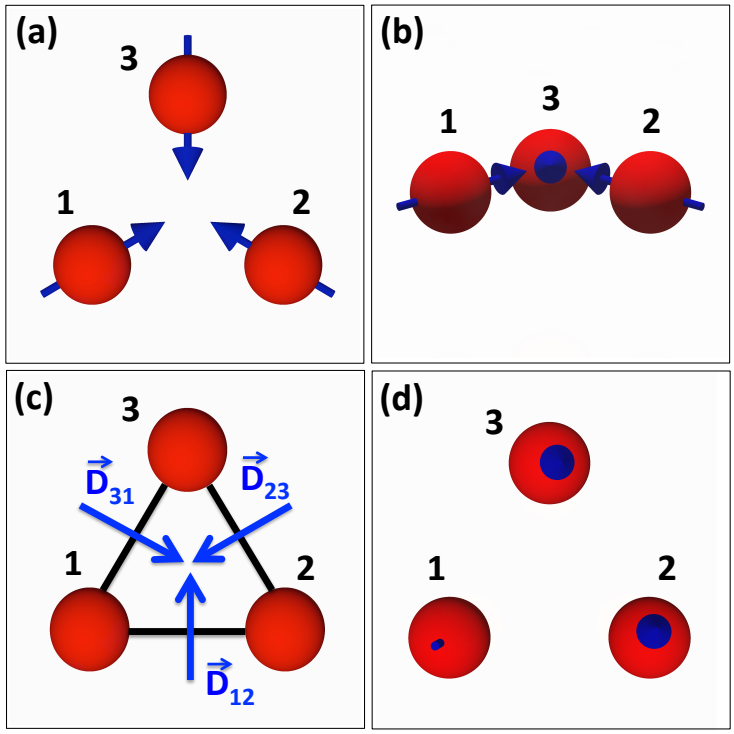

Figure 3.8: Non-collinear magnetic configuration for a trimer on an equilateral triangle shown from the top view (a) and side view (b). The interadatom distance $d = 10.42$ Å, while the isotropic exchange interaction is $J = 3.51$ meV and the intensity of DM vector is $D = 1$ meV (for $K = 0$ meV). The antiferromagnetic J leads to the 120° configuration and the DM interaction induces a slight upward tilting of the magnetic moments. The corresponding DM vectors are plotted in (c). (d) Top view for the magnetic ground state of the trimer with $K = -6$ meV.

120° between adjacent moments. The magnetic texture is a compromise involving the antiferromagnetic J and the DM vectors (plotted in Fig.3.9e). While J tries to make the moments anti-parallel to each other, the DM vector tends to make them lie in the plane perpendicular to the surface and containing at the same time the two pairs of atoms (similar to the dimer configuration). However, the magnetic moment has to satisfy the DM vectors arising from its nearest neighbors and therefore, the moment compromises and lies in the plane perpendicular to the surface and containing the atom of interest and the center of the hexagon. This is similar to what was found for the compact trimer. To test the stability of the non-collinear structure, we add the magnetic anisotropy energy and the polar angles become either 9° or 171°, *i.e.* a change of $\approx 5^\circ$, which shows that K has a smaller impact on the hexagon than on the trimer.

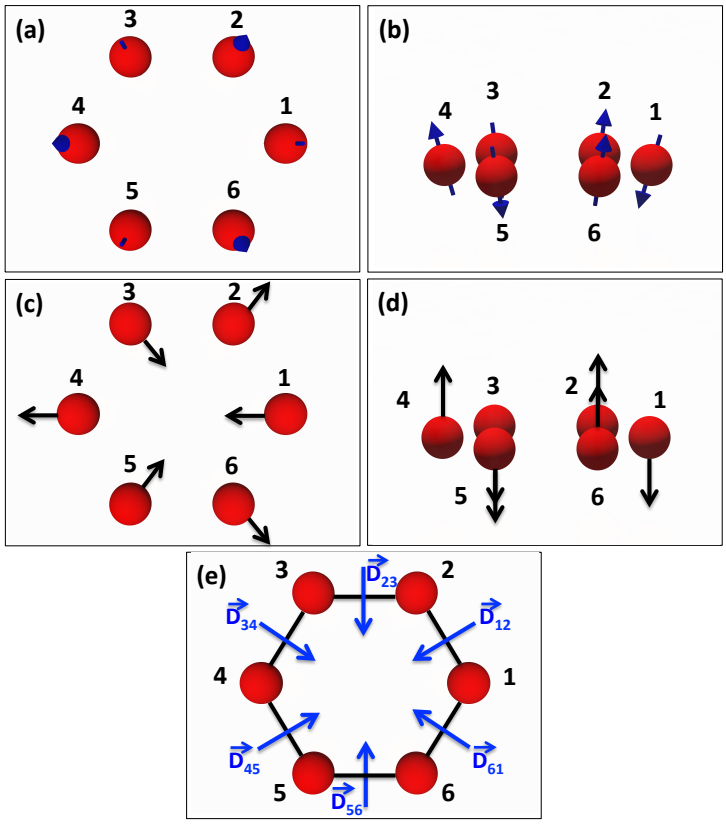

Figure 3.9: Top (a) and side (b) view of the magnetic ground state configuration for a hexagon made of six atoms. The interadatom distance is $d = 10.42$ Å, the nearest-neighbors isotropic exchange interaction is $J = 5.64$ meV and the intensity of the nearest-neighbors DM vector is $D = 1.67$ meV, while magnetic the anisotropy $K = 0$ meV. The projection of the unit vectors of the magnetic moments on the surface plane is given in (c) and the projection along the z-axis in (d). The corresponding DM vectors between the nearest neighbors are plotted in (e).

3.7.4 Heptamer

We add to the previous structure an atom in the center of the hexagon. Contrary to the other atoms this central atom has six neighbors and the magnetic ground state is profoundly affected by this addition as shown in Fig. 3.10a-b. The nearest neighbor isotropic exchange constant J, 4.69 meV, decreases slightly in comparison to the value found for the open structure. The obtained magnetic texture can be explained from the nearest neighboring DM interaction (1.37 meV) with the corresponding vectors plotted in Fig. 3.10e. The addition of the central atom creates frustration similar to the trimer case. Ideally, every pair of nearest neighboring moments have to lie in the same plane. Thus, the central magnetic moment has to lie within one of the three planes orthogonal to the surface and

passing by two of the outer atoms and the central one. In this configuration, the three atoms are satisfied and the 4 atoms left have the direction of their moments adjusted, which leads to the final spin-texture. Fig. 3.10c and d show respectively the projection of the magnetic moment along the z-axis and in the surface plane. Interestingly, when the single-ion magnetic anisotropy is added only the central moment is affected. It experiences a switch from the in-plane configuration to a quasi out-of-plane orientation. A side view is shown in Fig. 3.10f. This is another nice example showing how the stability of the non-collinear behavior is intimately related to the nature, shape, and size of the nanostructure.

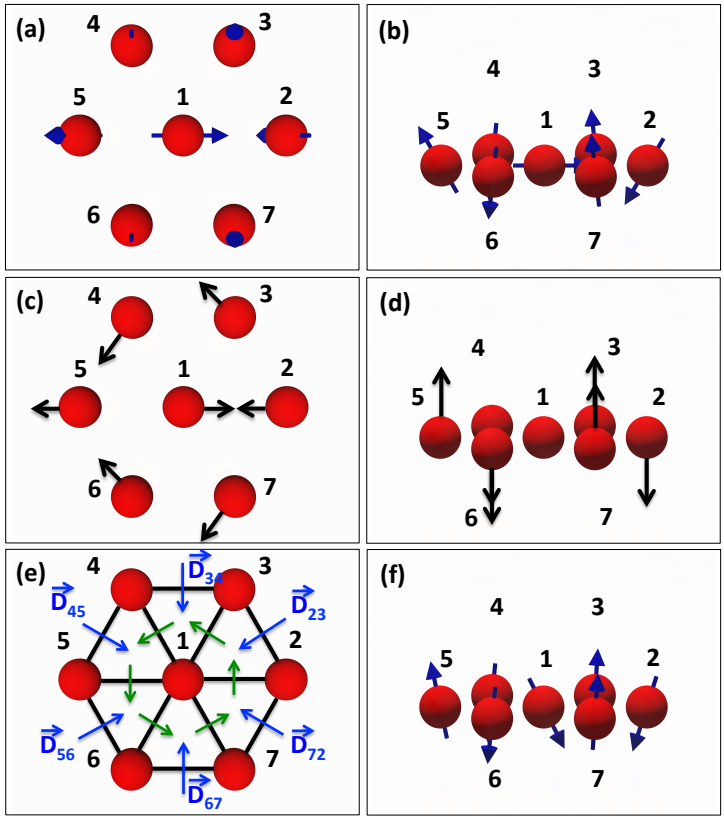

Figure 3.10: Non-collinear magnetic ground state found for the heptamer with an interadatom distance $d = 10.42$ Å, the nearest-neighbors isotropic exchange interaction is $J = 4.69\,(4.62)$ meV and the intensity of the nearest-neighbors DM vector is $D = 1.37\,(1.36)$ meV (the values between parenthesis are for the nearest neighbors on the outer ring), while the magnetic anisotropy $K = 0$ meV. (a) is the top view and (b) is the side view. The projection of the unit vectors of the magnetic moments on the surface plane is given in (c) and along the z-axis in (d). The corresponding DM vectors between the nearest neighbors are plotted in (e). In (f) the side view of the ground state after adding a single-ion magnetic anisotropy, K, of -6 meV.

3.8 Transport properties of Rashba electrons

In the previous section, we have seen that the scattering of Rashba electrons at magnetic impurities results in exchange interactions. This scattering can also be the source of magnetotransport properties. In particular, we expect contributions to the planar Hall effect (PHE), the anomalous Hall effect (AHE), as well as the anisotropic magnetoresistance (AMR). Both the PHE and AHE are observed as a voltage transverse to the applied current [64, 127], while AMR is measured in the longitudinal geometry with respect to the applied current. Consequently, PHE and AHE are characterized by the transverse resistivity ρ_{xy}, while the AMR is characterized by the longitudinal one, ρ_{xx}. For PHE, the in-plane component of the magnetization $M_{\parallel}$ with respect to the interface plane matters, while the AHE depends on the out-of-plane component M_z. Although the AMR has been known since 1856 [153], the PHE was not discovered until more than a century later [154]. Only recently it was established that the PHE can originate from the AMR without contributions from the AHE [65]. In absence of the SOI and of the magnetism at the impurity, the diagonal contributions of the resistivity tensor ρ_{xx} ($\rho_{xx} = \rho_{yy}$) induced by a single adatom can be expressed in terms of scattering phase shifts just alike the well-known expression by Friedel [124]:

$$\rho_{xx} = A_{\mathrm{F}} \sum_{l} (l+1)\, \sin^2[\delta_{l+1}(\varepsilon_{\mathrm{F}}) - [\delta_l(\varepsilon_{\mathrm{F}})] \quad , \tag{3.55}$$

where the residual resistivity ρ_{xx}, at $T = 0\,K$, induced by a nonmagnetic impurity with a spherical potential in a 3D degenerate free electron gas is related to the momentum transfer cross section of electrons at the Fermi surface given by a sum over the orbital momentum quantum numbers l. Here, A_{F} is a constant prefactor proportional to the inverse of the Fermi wave vector k_{F}. Similarly to the magnetic interactions, we considered an Fe impurity on the Au(111) surface, both nonmagnetic and magnetic, with perpendicular and arbitrary direction of the impurity moment with respect to the surface plane. If the impurity moment has a component parallel to the surface plane, the transition matrix as well as the transverse components of the resistivity tensor are nonzero, even when the perturbing potential $\boldsymbol{v}(\vec{r})$ has cylindrical symmetry, and a PHE is found. We follow the longitudinal resistivity and the AMR as a function of the spin-orbit strength and the transverse resistivity and the PHE as a function of the orientation of the magnetic impurity moment with respect to the surface plane. The AHE is absent since we consider a non spin polarized 2D Rashba electron gas [64, 127]. Also, we provide a phenomenological functional form for the different components of the residual resistivity as a function of the orientation of the magnetic moment.

3.8.1 Scattering States

Another alternative to study the scattering of the Rashba electrons at a single magnetic impurity is to consider the wave functions instead of the Green functions as in Eq. (3.9). In order to calculate the scattered wave functions, we exploit the cylindrical symmetry of the Rashba electron gas. Thus, we introduce the cylindrical coordinates (r, ϕ) with a radius r and azimuth ϕ between the vector $\vec{r}$ and the x-axis, and place the impurity at the origin of the coordinate system. For this purpose it is more convenient to expand the eigenfunctions

of the Rashba Hamiltonian (3.1) in terms of the cylindrical Bessel functions rather than plane waves as:

$$\psi_{\vec{k}\pm}(\vec{r}) = \sum_{m=-\infty}^{+\infty} \mathrm{i}^m \, e^{\frac{2m+1}{4}\mathrm{i}\pi} \, \psi_{\varepsilon m\pm}(\vec{r}) \quad . \tag{3.56}$$

Here

$$\psi_{\varepsilon m\pm}(\vec{r}) = \frac{e^{-\frac{2m+1}{4}\pi\mathrm{i}}}{\sqrt{2}} \begin{pmatrix} J_m(k_\pm r)e^{\mathrm{i}m\phi} \\ \mp J_{m+1}(k_\pm r)e^{\mathrm{i}(m+1)\phi} \end{pmatrix} \quad , \tag{3.57}$$

for an electron with an energy ε, located in one of the Rashba bands $\alpha = \pm$, and m is the orbital angular quantum number, $m \in \mathbb{Z}$, rather than the wave vector $\vec{k}$ or $(k, \phi_{\vec{k}})$. We note that $\psi_{\varepsilon m\alpha}(\vec{r})$ is an eigenvector for the z component of the total angular momentum operator $\mathbf{j}_z = \mathbf{l}_z + \frac{\hbar}{2}\boldsymbol{\sigma}_z$ with an eigenvalue $j_z = \hbar(m + \frac{1}{2})$ and $\mathbf{l}_z$ is the orbital angular momentum operator. $\psi_{\varepsilon m\alpha}(\vec{r})$ can be decomposed into an incident and an outgoing wave: $\psi_{\varepsilon m\alpha}(\vec{r}) = \psi^{\mathrm{in}}_{\varepsilon m\alpha}(\vec{r}) + e^{-(m+\frac{1}{2})\pi\mathrm{i}}\psi^{\mathrm{out}}_{\varepsilon m\alpha}(\vec{r})$. For each band component, the incoming and outgoing wave functions are respectively cylindrical Hankel functions of second kind (see Ref. [155] for a similar derivation),

$$\psi^{\mathrm{in}}_{\varepsilon m\pm}(\vec{r}) = \frac{e^{-\frac{2m+1}{4}\pi\mathrm{i}}}{2\sqrt{2}} \begin{pmatrix} H^{(2)}_m(k_\pm r)e^{\mathrm{i}m\phi} \\ \mp H^{(2)}_{m+1}(k_\pm r)e^{\mathrm{i}(m+1)\phi} \end{pmatrix} \quad , \tag{3.58}$$

and first kind,

$$\psi^{\mathrm{out}}_{\varepsilon m\pm}(\vec{r}) = \frac{e^{\frac{2m+1}{4}\pi\mathrm{i}}}{2\sqrt{2}} \begin{pmatrix} H^{(1)}_m(k_\pm r)e^{\mathrm{i}m\phi} \\ \mp H^{(1)}_{m+1}(k_\pm r)e^{\mathrm{i}(m+1)\phi} \end{pmatrix} \quad . \tag{3.59}$$

Their phase factors are chosen such that at large distances ($r \to \infty$) we can express them as:

$$\psi^{\mathrm{in}}_{\varepsilon m\pm}(\vec{r}) = \frac{1}{\sqrt{4\pi k_\pm r}} e^{-\mathrm{i}k_\pm r} e^{\mathrm{i}m\phi} \begin{pmatrix} 1 \\ \mp\mathrm{i}e^{\mathrm{i}\phi} \end{pmatrix} \quad , \tag{3.60}$$

$$\psi^{\mathrm{out}}_{\varepsilon m\pm}(\vec{r}) = \frac{1}{\sqrt{4\pi k_\pm r}} e^{\mathrm{i}k_\pm r} e^{\mathrm{i}m\phi} \begin{pmatrix} 1 \\ \pm\mathrm{i}e^{\mathrm{i}\phi} \end{pmatrix} \quad , \tag{3.61}$$

with $\psi^{\mathrm{in}}_{\varepsilon m\pm}(\vec{r})$ and $\psi^{\mathrm{out}}_{\varepsilon m\pm}(\vec{r})$ describing 2D cylindrical waves incoming toward and outgoing from the origin of the coordinate system, respectively. They are related by

$$\hat{T}\,\psi^{\mathrm{in}}_{\varepsilon m\pm}(\vec{r}) = \mp\mathrm{i}\,\psi^{\mathrm{out}}_{\varepsilon,\,-(m+1),\,\pm}(\vec{r}) \quad ,$$

where $\hat{T}$ denotes the time reversal operator. We then introduce a localized impurity for convenience placed at the origin of the cylindrical coordinate system of the 2D electron gas. We describe the elastic scattering of the wave function $\psi_{\varepsilon m\pm}(\vec{r})$ from the impurity with the Lippmann-Schwinger equation involving real and spin space coordinates:

$$\varphi_{\varepsilon m\alpha}(\vec{r}) = \psi_{\varepsilon m\alpha}(\vec{r}) + \int \mathrm{d}\vec{r}'\mathrm{d}\vec{r}''\; \boldsymbol{G}^{\mathrm{R}}(\vec{r},\vec{r}',\varepsilon)\,\boldsymbol{t}(\vec{r}',\vec{r}'',\varepsilon)\,\psi_{\varepsilon m\alpha}(\vec{r}'') \quad , \tag{3.62}$$

where $\boldsymbol{G}^{\mathrm{R}}(\vec{r},\vec{r}',\varepsilon)$ and $\boldsymbol{t}(\vec{r},\vec{r}',\varepsilon)$ are respectively the Rashba Green function and the transition matrix introduced previously. In the asymptotic region where the impurity potential

$\boldsymbol{v}(\vec{r})$ vanishes, Eq. (3.62) can be written in a simpler form by using scattering coefficients $C(m\alpha, m'\alpha')$. Then, the wave function of an incident electron with quantum state (ε, m, α) scattering elastically from a non-cylindrical impurity potential placed at the origin is expressed as

$$\varphi_{\varepsilon m\alpha}(\vec{r}) = \psi^{\rm in}_{\varepsilon m\alpha}(\vec{r}) + \sum_{m',\alpha'} \sqrt{\frac{k_{\alpha'}}{k_\alpha}}\, C(m\alpha, m'\alpha')\psi^{\rm out}_{\varepsilon m'\alpha'}(\vec{r}) \quad . \tag{3.63}$$

where the factor $\sqrt{k_{\alpha'}/k_\alpha}$ accounts for the fact that the incoming and outgoing waves, $\psi^{\rm in}_{\varepsilon m\alpha}$ and $\psi^{\rm out}_{\varepsilon m\alpha}$, carry electron current k_M/k_α rather than unity due to the relativistic correction of the velocity operator which will be discussed below. Here, the scattering coefficients fulfil the unitary condition,

$$\sum_{m_1\alpha_1} C(m\alpha, m_1\alpha_1)\, C^*(m'\alpha', m_1\alpha_1) = \delta_{mm'}\delta_{\alpha\alpha'} \quad , \tag{3.64}$$

Specifically, the diagonal elements of the above equation with $m = m'$ and $\alpha = \alpha'$,

$$\sum_{m_1\alpha_1} |C(m\alpha, m_1\alpha_1)|^2 = 1 \quad , \tag{3.65}$$

ensure a current conservation. For $\alpha \neq \alpha'$ the coefficients give weight to the inter-band transition during the scattering. For $m \neq m'$, the direction of $\vec{k}$ and thus the total angular momentum component of the Rashba electrons changes during the scattering process, and the scattering coefficients refer to the amplitude of the intra-band scattering. When $\boldsymbol{v}(\vec{r})$ has a cylindrical symmetry, *i.e.* $\boldsymbol{v}(\vec{r}) = \boldsymbol{v}(r)$, the orbital quantum number m is conserved and $C(m\alpha, m'\alpha')$ simplifies to $C(m\alpha, m\alpha')\,\delta_{m,m'}$. The scattered wave function will be a linear combination of the spin-splitted eigenstates denoted by the $+$ and $-$ bands. This mixing is due to the spin-flip inter-band transitions whose origin is the off-diagonal part of the Rashba Green $\boldsymbol{G}^{\rm R}(\vec{r}, \vec{r}', \varepsilon)$ function coming from the spin-orbit interaction.

3.8.2 Cylindrical expansion of the Green function and the t-matrix

We present the relation between the scattering coefficients $C(m\alpha, m\alpha')$ and the t-matrix $\boldsymbol{t}(\vec{r}, \vec{r}', \varepsilon)$ elements in the orbital momentum representation. For this purpose, it is convenient to express the Rashba Green function in terms of solutions of the Rashba Hamiltonian (3.1) in the cylindrical coordinate system presented in Sec. 3.8.1. In order to derive the Green function, we fix $\vec{r}'$ and consider $\boldsymbol{G}^{\rm R}(\vec{r}, \vec{r}', \varepsilon)$ to be a function of $\vec{r}$. Then, $\boldsymbol{G}^{\rm R}(\vec{r}, \vec{r}', \varepsilon)$ are found to be a linear combination of the solutions given by Eq. (3.57) and the out-going solutions (so-called irregular solutions) given by Eq. (3.59). Furthermore, by taking account of the cusp condition of the Green function at $r = r'$, it is easy to derive,

$$\begin{aligned} \boldsymbol{G}^{\rm R}(\vec{r}, \vec{r}', \varepsilon) \quad &= \frac{2}{{\rm i}\,(k_+ + k_-)} \\ \times \quad &\left\{ \begin{array}{ll} \sum_{m\alpha} k_\alpha\, \psi^{\rm out}_{\varepsilon m\alpha}(\vec{r})\, \psi^\dagger_{\varepsilon m\alpha}(\vec{r}')\, e^{-{\rm i}(m+\frac{1}{2})\pi} & \text{for } r > r' \quad , \\ \sum_{m\alpha} k_\alpha\, \psi_{\varepsilon m\alpha}(\vec{r})\, (\psi^{\rm out}_{\varepsilon m\alpha}(\vec{r}'))^\dagger\, e^{{\rm i}(m+\frac{1}{2})\pi} & \text{for } r < r' \quad . \end{array} \right. \end{aligned} \tag{3.66}$$

Using Eqs. (3.66) and (3.62), one arrives at this general expression for the scattering coefficients:

$$C(m\alpha, m'\alpha') = \Bigg[\delta_{mm'}\delta_{\alpha\alpha'} + \frac{2k_{\alpha'}}{\mathrm{i}(k_+ + k_-)} \times \langle\psi_{\varepsilon m'\alpha'}|\, \boldsymbol{t}(\varepsilon)\, |\psi_{\varepsilon m\alpha}\rangle\Bigg] \sqrt{\frac{k_\alpha}{k_{\alpha'}}} e^{-\mathrm{i}(m'+\frac{1}{2})\pi} \quad . \tag{3.67}$$

When the magnetic moment of the impurity is along the z-axis, then the t-matrix is diagonal in spin space. Furthermore, if the impurity potential is cylindrical, the orbital momentum representation of $t^{\sigma\sigma}(\vec{r}, \vec{r}', \varepsilon)$ with $\sigma \in \{\uparrow, \downarrow\}$ reads

$$t^{\sigma\sigma}(\vec{r}, \vec{r}', \varepsilon) = \frac{1}{2\pi} \sum_m e^{\mathrm{i}m\phi}\, t_m^{\sigma\sigma}(r, r', \varepsilon)\, e^{-\mathrm{i}m\phi'}. \tag{3.68}$$

The derivation of $t_m^{\sigma\sigma}(r, r', \varepsilon)$ is given in Appendix A.

3.8.3 Residual resistivity tensor from linear response theory

In Sec. 2.6.1, we discussed the spin-spin correlation function (magnetic susceptibility) within the Kubo formalism to study the linear response of our system to a time-dependent external magnetic field. A similar approach can be used to study the response of our system to external perturbing electric fields. Indeed using the Kubo linear response formalism [156], we can show that the components of the resistivity tensor, $\rho_{\gamma\gamma'}$, measuring the potential drop in direction γ after applying an electric field in direction γ', in the DC limit $\omega \to 0$ are given in terms of the scattering solution $\varphi_{\varepsilon m\alpha}$ by

$$\rho_{\gamma\gamma'} = \lim_{\omega\to 0} \frac{\pi\omega}{S n_{\mathrm{e}}^2 e^2} \sum_{i,j} \delta(\varepsilon_j - \varepsilon_i - \hbar\omega)(f(\varepsilon_i) - f(\varepsilon_j)) \times \langle\varphi_i|\, m^*\hat{v}_\gamma\, |\varphi_j\rangle \langle\varphi_j|\, m^*\hat{v}_{\gamma'}\, |\varphi_i\rangle \quad , \tag{3.69}$$

where $\gamma, \gamma' \in \{x, y\}$, the indices i, j stand each for (ε, m, α), n_{e} is the surface electronic density, S denotes the area of the surface, e is the electron charge, and $f(\varepsilon_i) = \Theta(\varepsilon_{\mathrm{F}} - \varepsilon_i)$ is the occupation number for the energy level ε_i at $T = 0$ K. Here, n_{e} is related to the Fermi wave numbers of the two bands, $k_{\mathrm{F}+}$ and $k_{\mathrm{F}-}$, by

$$n_{\mathrm{e}} = \frac{1}{4\pi}\left(k_{\mathrm{F}+}^2 + k_{\mathrm{F}-}^2\right) \quad , \tag{3.70}$$

and in low impurity limit, the factor $\frac{1}{S}$ from Eq. (3.69) represents the impurity density n_i. Also, one needs in Eq. (3.69) the relativistic velocity operator: $\hat{\vec{v}} = \dot{\hat{\vec{r}}} = \frac{\mathrm{i}}{\hbar}[\boldsymbol{H}_{\mathrm{R}}, \hat{\vec{r}}]$ with $\hat{\vec{r}}$ being the position operator, *i.e.*,

$$\begin{aligned} \hat{v}_x &= -\mathrm{i}\frac{\hbar}{m^*}\frac{\partial}{\partial x} + \frac{\hbar}{m^*}k_{\mathrm{so}}\boldsymbol{\sigma}_y \quad , \\ \hat{v}_y &= -\mathrm{i}\frac{\hbar}{m^*}\frac{\partial}{\partial y} - \frac{\hbar}{m^*}k_{\mathrm{so}}\boldsymbol{\sigma}_x \quad . \end{aligned} \tag{3.71}$$

In addition to the prefactor ω, the summation over states i and j in Eq. (3.69) gives rise to another factor ω, since ε_i must satisfy the condition, $\varepsilon_{\rm F} - \hbar\omega \leq \varepsilon_i \leq \varepsilon_{\rm F}$. In spite of this, the right-hand side of Eq. (3.69) takes a finite limiting value in the limit of $\omega \to 0$, since the matrix elements $\langle\varphi_i| m^* \hat{v}_\gamma |\varphi_j\rangle$ evaluated for the asymptotic scattering region ($r \to \infty$) diverge as $\frac{1}{\omega}$ in the limit of $\omega \to 0$, as shown in Appendix D. By inserting the matrix elements of the momentum operators in the limit of $\omega \to 0$ given in Appendix D into Eq. (3.69), one can derive the most general expression for the diagonal components of the resistivity tensor,

$$\rho_{\gamma\gamma} = \frac{\hbar k_{\rm FM}^2}{8\pi S n_{\rm e}^2 e^2} \sum_{m\alpha, m'\alpha'} \Big| (\delta_{m',m+1} \pm \delta_{m',m-1})\delta_{\alpha\alpha'} + \sum_{l\alpha''} C(m\alpha, l\alpha'') C^*(m'\alpha', l+1\alpha'') \pm \sum_{l\alpha''} C(m\alpha, l\alpha'') C^*(m'\alpha', l-1\alpha'') \Big|^2 \quad , \tag{3.72}$$

where $k_{\rm FM} = k_{\rm M}(\varepsilon_{\rm F})$ and the plus and minus signs correspond to ρ_{xx} and ρ_{yy}, respectively. In deriving Eq. (3.72) we replaced in (3.69) the sum $\sum_i$ over discrete states by $\frac{1}{2\pi}\sum_{m=-\infty}^{+\infty}\sum_{\alpha=\pm}\int_0^{+\infty} k_\alpha {\rm d}k_\alpha$. The scattering coefficients $C(m\alpha, m'\alpha')$ are implicitly energy dependent. After integrating over k_α these coefficients will be taken at the Fermi level, $\varepsilon_{\rm F}$. In the case of absence of the impurity, the resistivity vanishes since the scattering coefficients are given in this case simply by $C(m\alpha, m'\alpha') = \delta_{mm'}\delta_{\alpha\alpha'} e^{-{\rm i}(m+1/2)\pi}$. If the scattering potential is cylindrically symmetric as seen from Eq. (3.67), the scattering coefficient $C(m\alpha, m'\alpha')$ becomes diagonal with respect to m and m', and the expression for the resistivity, Eq. (3.72), is further simplified as

$$\rho_{\gamma\gamma} = \frac{\hbar k_{\rm FM}^2}{8\pi S n_{\rm e}^2 e^2} \sum_{m\alpha, m'=m\pm1\ \alpha'} \Big| \delta_{\alpha\alpha'} + \sum_{\alpha''} C(m\alpha, m\alpha'') C^*(m'\alpha', m'\alpha'') \Big|^2 \quad . \tag{3.73}$$

Obviously, the two diagonal components, ρ_{xx} and ρ_{yy}, are identical in this case.

3.8.4 Resistivity tensor in absence of the spin-orbit interaction

Here, we consider the limit of $k_{\rm so} \to 0$ to derive the expression of the residual resistivity induced by a localized impurity for the 2D free-electron gas without the Rashba spin-orbit term. This may be useful since the derivation of this quantity has not appeared in the literature to our knowledge. For this purpose, it is better to choose energy ε, orbital angular momentum m, and spin index σ as the quantum numbers for the description of scattering states, where the spin quantization axis is chosen as the z axis as in previous sections. Namely, instead of Eqs. (3.58) and (3.59), we employ

$$\tilde{\psi}^{\rm in}_{\varepsilon m\sigma}(\vec{r}) = \frac{1}{2} e^{-\frac{2m+1}{4}\pi{\rm i}} H_m^{(2)}(kr) e^{{\rm i}m\phi} |\sigma\rangle \quad , \tag{3.74}$$

and

$$\tilde{\psi}^{\rm out}_{\varepsilon m\sigma}(\vec{r}) = \frac{1}{2} e^{\frac{2m+1}{4}\pi{\rm i}} H_m^{(1)}(kr) e^{{\rm i}m\phi} |\sigma\rangle \quad , \tag{3.75}$$

as the incident and scattered electron wave functions, where $k = \sqrt{2m^*\varepsilon}/\hbar$, $|\uparrow\rangle = (1,0)$, and $|\downarrow\rangle = (0,1)$. Then, the wave function of an incident electron with quantum state (ε, m, σ) scattering elastically from a non-cylindrical impurity potential placed at the origin is expressed as

$$\tilde{\varphi}_{\varepsilon m\sigma}(\vec{r}) = \tilde{\psi}^{\rm in}_{\varepsilon m\sigma}(\vec{r}) + \sum_{m',\sigma'} \tilde{C}(m\sigma, m'\sigma')\tilde{\psi}^{\rm out}_{\varepsilon m'\sigma'}(\vec{r}) \quad . \tag{3.76}$$

By following the same procedure, we can easily show that the resistivity tensor for the present case with $\alpha_{\rm so} = 0$ is given exactly in the same form as Eq. (3.72), except that $k_{{\rm F}\alpha}$ is replaced by $k_{\rm F} = \sqrt{2m^*\varepsilon_{\rm F}}/\hbar$, the scattering coefficients of the type $C(m\alpha, m'\alpha')$ are replaced by $\tilde{C}(m\sigma, m'\sigma')$, and further the summation over band indices is replaced by the one over spin indices. Furthermore, if the t-matrix is diagonal with respect to electron spin and the impurity potential has cylindrical symmetry, we can derive a simplified expression corresponding to Eq. (3.73),

$$\rho_{\gamma\gamma} = \frac{\hbar k_{\rm F}^2}{8\pi S n_{\rm e}^2 e^2} \sum_{m,m\prime=m\pm1,\sigma} \left|1 + \tilde{C}(m\sigma, m\sigma)\tilde{C}^*(m'\sigma, m'\sigma)\right|^2 \quad , \tag{3.77}$$

where it should be noted that, in contrast to the Rashba electrons with a finite $\alpha_{\rm so}$, the spin-flip scattering does not occur in the present case. The scattering coefficient in the above equation can be expressed by using the phase shift as:

$$\tilde{C}(m\sigma, m\sigma) = e^{-(m+\frac{1}{2})\pi{\rm i}+2{\rm i}\delta_m^{\sigma\sigma}(\varepsilon)} \quad . \tag{3.78}$$

By inserting this expression into Eq. (3.77), we obtain finally

$$\rho_{\gamma\gamma} = \frac{2\hbar}{S n_{\rm e} e^2} \sum_{\sigma=\uparrow\downarrow} \sum_{m=-\infty}^{+\infty} \sin^2\left[\delta_{m+1}^{\sigma\sigma}(\varepsilon_{\rm F}) - \delta_m^{\sigma\sigma}(\varepsilon_{\rm F})\right] \quad , \tag{3.79}$$

where we used the relation $k_{\rm F}^2 = 2\pi n_{\rm e}$. This is a modification of Friedel's result [124] for the residual resistivity of a single impurity in a 3D electron gas to the case of an impurity in a 2D electron gas without the Rashba SOI term. The only difference is the scattering phase space of momentum transfer in the field direction, which is larger in the 3D case than in 2D. This is taken care of by the multiplicity $\ell + 1$ of each angular momentum component as shown in Eq. (3.55).

3.8.5 Residual resistivity tensor within the s-wave approximation

We aim at deriving the general expression of the impurity resistivity when the t-matrix is given by Eq. (3.13). First, we note that by using Eq. (3.67), the scattering coefficients

$C(m\alpha, m'\alpha')$ for m and m' equal to 0 or -1 are given by:

$$\begin{aligned} C(0\alpha, 0\alpha') &= \frac{1}{\mathrm{i}}\delta_{\alpha\alpha'} - \frac{\sqrt{k_\alpha k_{\alpha'}}}{2k_{\mathrm{M}}} t^{\uparrow\uparrow}(\varepsilon) \quad , \\ C(-1\alpha, -1\alpha') &= \mathrm{i}\,\delta_{\alpha\alpha'} + \frac{\sqrt{k_\alpha k_{\alpha'}}}{2k_{\mathrm{M}}} s(\alpha)s(\alpha')\, t^{\downarrow\downarrow}(\varepsilon) \quad , \\ C(0\alpha, -1\alpha') &= \frac{\sqrt{k_\alpha k_{\alpha'}}}{2\mathrm{i}k_{\mathrm{M}}} s(\alpha')\, t^{\downarrow\uparrow}(\varepsilon) \quad , \\ C(-1\alpha, 0\alpha') &= \frac{\sqrt{k_\alpha k_{\alpha'}}}{2\mathrm{i}k_{\mathrm{M}}} s(\alpha)\, t^{\uparrow\downarrow}(\varepsilon) \quad , \end{aligned} \tag{3.80}$$

where $s(\alpha)$ is defined by $s(\pm 1) = \mp 1$. For m and m' larger than 0 or smaller than -1, we have

$$C(m\alpha, m'\alpha') = \delta_{mm'}\delta_{\alpha\alpha'} e^{-\mathrm{i}\left(m+\frac{1}{2}\right)\pi} \quad . \tag{3.81}$$

The expression of the impurity resistivity can be obtained by inserting Eqs. (3.80) and (3.81) into Eq. (3.72), where twelve pairs of (m, m') make a non-vanishing contribution to the resistivity. After a lengthy calculation, one obtains

$$\rho_{\gamma\gamma} = \frac{\hbar k_{\mathrm{FM}}^2}{2\pi S n_e^2 e^2}\Big[\sum_{\sigma,\sigma'} |t^{\sigma\sigma'}(\varepsilon)|^2 - \left(\frac{k_{\mathrm{so}}}{k_{\mathrm{FM}}}\right)^2 (M(\varepsilon) \mp N(\varepsilon))\Big] \quad , \tag{3.82}$$

with

$$M(\varepsilon) \equiv \mathrm{Re}\Big([t^{\uparrow\uparrow}(\varepsilon)]^*\, t^{\downarrow\downarrow}(\varepsilon)\Big) + \frac{1}{2}(|t^{\uparrow\downarrow}(\varepsilon)|^2 - |t^{\downarrow\uparrow}(\varepsilon)|^2)^2 \quad , \tag{3.83}$$

$$\begin{aligned} N(\varepsilon) \equiv \mathrm{Re}\Big([t^{\uparrow\downarrow}(\varepsilon)]^*\, t^{\downarrow\uparrow}(\varepsilon)\Big) - \frac{1}{2}\mathrm{Re}\Big[&([t^{\uparrow\uparrow}(\varepsilon)]^* - [t^{\downarrow\downarrow}(\varepsilon)]^*)\, t^{\downarrow\uparrow}(\varepsilon) \\ &-(t^{\uparrow\uparrow}(\varepsilon) - t^{\downarrow\downarrow}(\varepsilon))\,[t^{\uparrow\downarrow}(\varepsilon)]^*\Big]^2 \quad , \end{aligned} \tag{3.84}$$

where the t-matrix should be evaluated at the Fermi energy and the negative and positive signs in Eq. (3.82) correspond to ρ_{xx} and ρ_{yy}, respectively. In deriving the above equations, we have used the general relation for the t-matrix (optical theorem), $\boldsymbol{t}(\varepsilon) - \boldsymbol{t}^\dagger(\varepsilon) = -\mathrm{i}\,\boldsymbol{t}(\varepsilon)\,\boldsymbol{t}^\dagger(\varepsilon)$, implying in the case of a 2×2 matrix that:

$$\begin{aligned} \mathrm{Im}\, t^{\uparrow\uparrow}(\varepsilon) &= -\frac{1}{2}\left(|t^{\uparrow\uparrow}(\varepsilon)|^2 + |t^{\downarrow\uparrow}(\varepsilon)|^2\right) \quad , \\ \mathrm{Im}\, t^{\downarrow\downarrow}(\varepsilon) &= -\frac{1}{2}\left(|t^{\downarrow\downarrow}(\varepsilon)|^2 + |t^{\uparrow\downarrow}(\varepsilon)|^2\right) \quad , \\ [t^{\uparrow\downarrow}(\varepsilon)]^* - t^{\downarrow\uparrow}(\varepsilon) &= \mathrm{i}\left(t^{\uparrow\uparrow}(\varepsilon)\,[t^{\uparrow\downarrow}(\varepsilon)]^* + [t^{\downarrow\downarrow}(\varepsilon)]^*\, t^{\downarrow\uparrow}(\varepsilon)\right) \quad . \end{aligned} \tag{3.85}$$

Because of the above relations, $M(\varepsilon)$ and $N(\varepsilon)$ in Eqs. (3.83) and (3.84) may be expressed in many apparently different but equivalent ways. Although the t-matrix has no spin-orbit interaction it can have non diagonal elements due to a non-collinear orientation of the magnetic moment according to the z-axis perpendicular to the surface plane (see Sec. 3.8.6).

3.8.6 Residual resistivity tensor results and discussions

We investigate the example of Fe adatoms on Au(111) surface with an area $S = 1\ \mathrm{m}^2$ (unit area) similarly to magnetic interactions among magnetic adatoms. We will consider that the Fe impurities are described with the t-matrix given in Eq. (3.13). The advantages of this approximation are the fast numerical evaluation of the scattering coefficients given in Eq. (3.67) and an easy tracking of the impact of scattering on the resistivity. Furthermore, since our scheme is based on linear response theory, only the phase shift at the Fermi energy is essential. Considering the density of states for Fe adatom shown in Fig. 3.2a we can approximate $\delta_0^{\downarrow\downarrow}(\varepsilon_\mathrm{F}) = \frac{\pi}{2}$ in the minority-spin channel and the majority-spin channel is considered fully occupied, thus, the corresponding phase shift is set to $\delta_0^{\uparrow\uparrow}(\varepsilon_\mathrm{F}) = \pi$. In contrast, the phase shift for the non-magnetic impurity is shown in Fig. 3.2b where the charge conservation (see Friedel sum rule in Eq. (3.14)) imposes then that $\delta_0^{\uparrow\uparrow}(\varepsilon_\mathrm{F}) = \delta_0^{\downarrow\downarrow}(\varepsilon_\mathrm{F}) = \frac{3\pi}{4}$.

Considering the approximations mentioned above one can investigate the residual resistivity for both cases: magnetic and non-magnetic Fe adatoms. To start our analysis, we consider a magnetic moment pointing perpendicular to the surface. Also to make our study general, we explore different SOI strengths, which then would correspond to the deposition of the impurities on different substrates. To make this type of investigations consistent with each other, the energy of the highest occupied state of the Rashba electron gas measured from the bottom of the energy dispersion curve, $\varepsilon_\mathrm{F}^\mathrm{Rashba} = \varepsilon_\mathrm{F} + \frac{\hbar^2}{2m^*}k_\mathrm{so}^2$, is set to a constant, 480 meV for the case of Au(111) surface state characterized by an effective mass $m^* = 0.255\, m_\mathrm{e}$ [119]. By changing k_so, ε_F is modified such that $\varepsilon_\mathrm{F}^\mathrm{Rashba}$ does not vary. By inserting $t^{\uparrow\uparrow}(\varepsilon_\mathrm{F}) = \mathrm{i}\,(e^{\mathrm{i}\delta_0^{\uparrow\uparrow}(\varepsilon_\mathrm{F})} - 1)$, $t^{\downarrow\downarrow}(\varepsilon_\mathrm{F}) = \mathrm{i}\,(e^{\mathrm{i}\delta_0^{\downarrow\downarrow}(\varepsilon_\mathrm{F})} - 1)$, and $t^{\uparrow\downarrow}(\varepsilon_\mathrm{F}) = t^{\downarrow\uparrow}(\varepsilon_\mathrm{F}) = 0$ into Eq. (3.82), we obtain as the resistivity induced by a magnetic adatom with its magnetic moment pointing to the normal direction,

$$\rho_{\gamma\gamma} = \frac{2\hbar k_\mathrm{FM}^2}{\pi S n_\mathrm{e}^2 e^2}\left[\sin^2(\delta^\uparrow)+\sin^2(\delta^\downarrow)-\left(\frac{k_\mathrm{so}}{k_\mathrm{FM}}\right)^2\sin(\delta^\uparrow)\sin(\delta^\downarrow)\cos(\delta^\uparrow-\delta^\downarrow)\right] \quad , \tag{3.86}$$

where $\delta^\uparrow$ and $\delta^\downarrow$ are abbreviations of $\delta_0^{\uparrow\uparrow}(\varepsilon_\mathrm{F})$ and $\delta_0^{\downarrow\downarrow}(\varepsilon_\mathrm{F})$, respectively. Thus, for the non-magnetic adatom with $\delta^\uparrow = \delta^\downarrow = \frac{3\pi}{4}$,

$$\rho_{\gamma\gamma} = \frac{2\hbar k_\mathrm{FM}^2}{\pi S n_e^2 e^2}\left[1 - \frac{1}{2}\left(\frac{k_\mathrm{so}}{k_\mathrm{FM}}\right)^2\right] \quad , \tag{3.87}$$

$\rho_{\gamma\gamma}$ is always a positive quantity and for the magnetic adatom with $\delta^\uparrow = \pi$ and $\delta^\downarrow = \frac{\pi}{2}$, we simply have

$$\rho_{\gamma\gamma} = \frac{2\hbar k_\mathrm{FM}^2}{\pi S n_e^2 e^2} \quad , \tag{3.88}$$

where k_FM and n_e are related to $\varepsilon_\mathrm{F}^\mathrm{Rashba}$, which is kept constant in the numerical calculation, by $k_\mathrm{FM}^2 = \frac{2m^*\varepsilon_\mathrm{F}^\mathrm{Rashba}}{\hbar^2}$ and $n_e = \frac{m^*\varepsilon_\mathrm{F}^\mathrm{Rashba}}{\pi\hbar^2} + \frac{k_\mathrm{so}^2}{2\pi}$. The latter leads to a quadratic decrease of the prefactor $\frac{2\hbar k_\mathrm{FM}^2}{\pi S n_e^2 e^2}$ and thus of the residual resistivity with respect to k_so^2. This simply indicates that the more available electrons, the more conducting the system

becomes. The intriguing dependence of n_e on the SOI strength can be traced back to the particular behavior of the density of states of the Rashba electron gas, which is characterized by two regimes induced by the SOI and defined by the two regions of the energy dispersion curve that show a crossing at $k = 0$ (see Eq. (3.4)). At energies below the crossing, the corresponding density of states follows a quasi one-dimensional behavior where a van Hove singularity occurs at the bottom of the bands. Above the crossing, the density of states is a constant as expected for a 2D electron gas. By increasing the SOI strength, the quasi one-dimensional region becomes larger in order to keep $\varepsilon_\mathrm{F}^\mathrm{Rashba}$ constant, which leads to the quadratic dependence of n_e on k_so and explains the strong drop of the residual resistivity when increasing the SOI strength.

The latter can be observed in Fig. 3.11, where the longitudinal residual resistivity as function of the SOI strength is depicted. The transversal residual resistivity is not shown since it is zero for the two cases considered: magnetic (out-of-plane moment) and non-magnetic adatoms. Interestingly, magnetism and the SOI strength have opposite impact on the residual resistivity. This holds for spin-dependent phase shifts that conserve the number of electrons n_e of the impurity after spin-polarization. Indeed, as may be seen from Eq. (3.86), in contrast to magnetism, the SOI tends to decrease the resistivity. The largest resistivity is found when the SOI is switched off, This would be the case for a Cu(111) surface for example. For the phase shifts we used to model the magnetic impurity ($\delta^\uparrow = \pi$, $\delta^\uparrow = \frac{\pi}{2}$) and the non-magnetic impurity ($\delta^\uparrow = \delta^\uparrow = \frac{3\pi}{4}$), the residual resistivity is independent from the magnetic nature of the adatom, as can be deduced from Eq.(3.86)

$$\rho_{\gamma\gamma} = \frac{4\hbar}{S n_\mathrm{e} e^2}\Big[\sin^2(\delta^\uparrow) + \sin^2(\delta^\downarrow)\Big] \quad . \tag{3.89}$$

Fermi surface analysis for the Residual resistivity tensor

Now, we address the dependence of the residual resistivity on the magnetism of the impurity by analyzing the different scattering processes allowed at the Fermi surface. The possible elastic scattering processes can be found by evaluating the probability for an electron scattering from a state $|\psi_{\vec{k}\alpha}\rangle$ to a state $|\psi_{\vec{k}'\alpha'}\rangle$:

$$P^{\alpha\alpha'}_{\vec{k}\vec{k}'} = \frac{2\pi}{\hbar}|\,\langle\psi_{\vec{k}'\alpha'}|\,\boldsymbol{t}(\varepsilon)\,|\psi_{\vec{k}\alpha}\rangle\,|^2\,\delta(\varepsilon_\alpha(\vec{k}) - \varepsilon_{\alpha'}(\vec{k}')) \quad , \tag{3.90}$$

where $\psi_{\vec{k}\alpha}$ are given by Eq. (3.2) and α is the band index. If the impurity is non-magnetic, the diagonal elements of the t-matrix in spin space are equal: $t^{\uparrow\uparrow}(\varepsilon) = t^{\downarrow\downarrow}(\varepsilon) = t(\varepsilon)$. In this case, the electron scattering probabilities are given by

$$P^{\alpha\alpha'}_{\vec{k}\vec{k}'} = \frac{\pi}{2\hbar}|t(\varepsilon)|^2(1 + \alpha\,\alpha'\cos(\phi_{\vec{k}} - \phi_{\vec{k}'}))\,\delta(\varepsilon_\alpha(\vec{k}) - \varepsilon_{\alpha'}(\vec{k}')) \quad , \tag{3.91}$$

where $\alpha\,\alpha'$ equals 1 for intra-band scattering transitions ($\alpha = \alpha'$) or -1 for inter-band transitions ($\alpha \neq \alpha'$). This equation shows that inter-band and intra-band transitions flipping the spin are not allowed since in these cases, $\phi_{\vec{k}} - \phi_{\vec{k}'} = \pi$ with $\alpha\,\alpha' = 1$ and $\phi_{\vec{k}} - \phi_{\vec{k}'} = 0$ with $\alpha\,\alpha' = -1$, respectively (see Fig. 3.12a). In the case of a magnetic impurity with a moment perpendicular to the surface, the t-matrix is given by Eq. (3.12) and all transitions

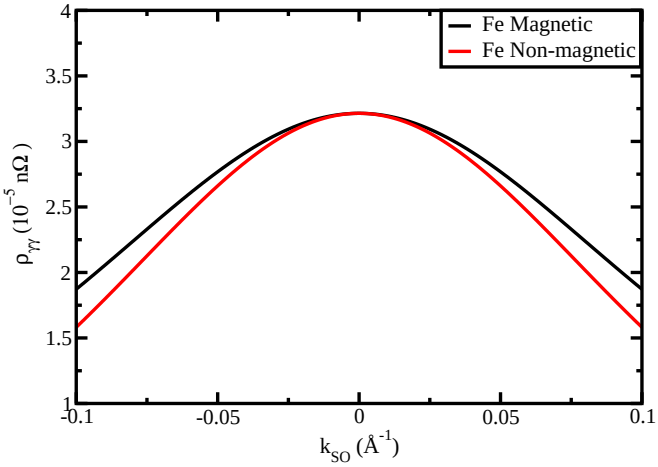

Figure 3.11: Evolution of the diagonal components of the resistivity tensor as a function of the spin-orbit wave vector magnitude (k_{so}) for a magnetic and a non-magnetic Fe impurity.

are allowed, even those leading to a spin-flip, as depicted in Fig. 3.12b. Here the electron scattering probabilities

$$P^{\alpha\alpha'}_{\vec{k}\vec{k}'} = \frac{2\pi}{\hbar}|t^{\uparrow\uparrow}(\varepsilon) + \alpha\,\alpha' t^{\downarrow\downarrow}(\varepsilon)\, e^{i(\phi_{\vec{k}}-\phi_{\vec{k}'})}|^2\, \delta(\varepsilon_\alpha(\vec{k}) - \varepsilon_{\alpha'}(\vec{k}')) \quad , \tag{3.92}$$

which is different from zero independently from the value of $\phi_{\vec{k}} - \phi_{\vec{k}'}$. This is due to the magnetic moment of the impurity which breaks the time-reversal symmetry. Thus, there are more scattering possibilities than in the non-magnetic case, and therefore for magnetic impurities a higher residual resistivity is expected compared to non-magnetic impurities in-line with Fig. 3.11.

Residual resistivity tensor for magnetic moments breaking cylindrical symmetry

Up to now, the magnetic moment was considered perpendicular to the surface plane. To generalize our study, we explore the impact of arbitrary orientations, $\vec{e}_{\vec{\mathrm{M}}}$, of the impurity moment, $\vec{\mathrm{M}}$, on the residual resistivity. The resistivity is a tensor, and contrary to the case of an out-of-plane magnetic orientation, its off-diagonal elements become finite for arbitrary magnetization directions giving rise to the AMR and PHE. To tackle this problem, we rotate the impurity magnetic moment pointing initially normal to the surface plane, $\vec{e}_z$, by means of the conventional 3×3 rotation matrices $\mathcal{R} \in \mathrm{SO}(3)$ by a polar angle $\theta_{\vec{\mathrm{M}}}$ between the direction of the magnetic moment and the z-axis and an azimuthal angle $\phi_{\vec{\mathrm{M}}}$, $\vec{e}_{\vec{\mathrm{M}}} = \mathcal{R}_z(\phi_{\vec{\mathrm{M}}})\mathcal{R}_y(\theta_{\vec{\mathrm{M}}})\,\vec{e}_z$. This translates to a unitary transformation of the t-matrix in spin space $\boldsymbol{t}'(\vec{r},\vec{r}',\varepsilon) = \boldsymbol{U}(\theta_{\vec{\mathrm{M}}},\phi_{\vec{\mathrm{M}}})\,\boldsymbol{t}(\vec{r},\vec{r}',\varepsilon)\,\boldsymbol{U}^\dagger(\theta_{\vec{\mathrm{M}}},\phi_{\vec{\mathrm{M}}})$. $\boldsymbol{U}(\theta_{\vec{\mathrm{M}}},\phi_{\vec{\mathrm{M}}}) =$

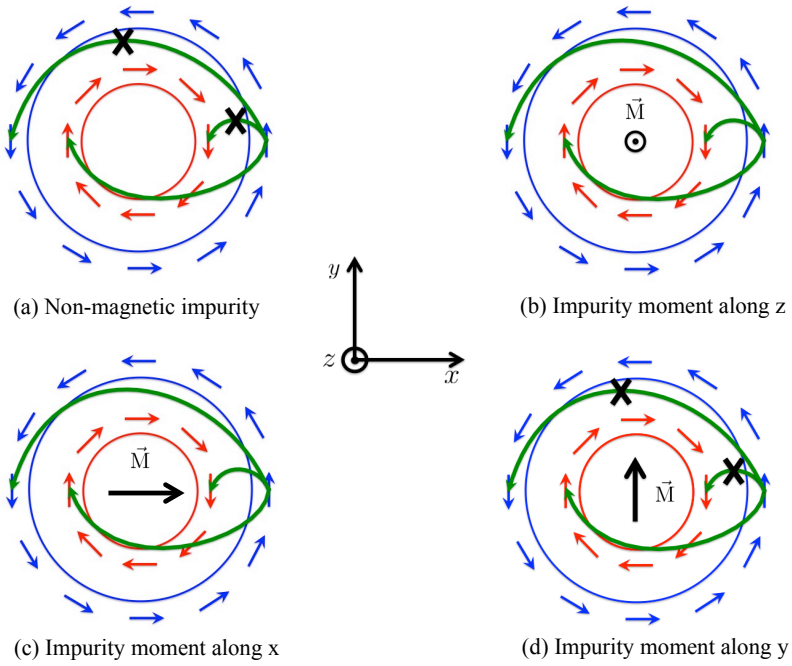

(a) Non-magnetic impurity (b) Impurity moment along z

(c) Impurity moment along x (d) Impurity moment along y

Figure 3.12: Fermi surfaces scattering processes of Rashba electrons at a non-magnetic impurity (a), magnetic impurity with an out-of-plane magnetic moment (b), in-plane magnetic moment pointing along the x-direction (c) and along the y-direction (d). The transitions between circles with different colors are interband transitions, while transitions between circles with the same color are intraband transitions. The green arrows indicate the connection between the initial and final state. The crosses indicate prohibited scattering processes, while the black arrows at the center of the Fermi contours represent the direction of the impurity magnetic moment.

$\boldsymbol{U}(\mathcal{R}_z, \phi_{\vec{\mathrm{M}}})\,\boldsymbol{U}(\mathcal{R}_y, \theta_{\vec{\mathrm{M}}})$ are the conventional rotation operators in SU(2) whose representation in terms of a 2×2 matrix is given by $\boldsymbol{U}(\mathcal{R}_\gamma, \beta) = \cos(\beta/2) \otimes \mathbb{1}_2 - i \sin(\beta/2)\, \boldsymbol{\sigma}_\gamma$. The t-matrix for an arbitrary rotation angle of the moment can then be expressed in terms of the spin diagonal elements, $t^{\uparrow\uparrow}(\varepsilon)$ and $t^{\downarrow\downarrow}(\varepsilon)$, describing the out-of-plane moment (see Eq. (3.12)) as:

$$\boldsymbol{t}'(\varepsilon) = \frac{1}{2}(t^{\uparrow\uparrow}(\varepsilon) + t^{\downarrow\downarrow}(\varepsilon))\,\mathbb{1}_2 + \frac{1}{2}(t^{\uparrow\uparrow}(\varepsilon) - t^{\downarrow\downarrow}(\varepsilon))\,\vec{\boldsymbol{\sigma}} \cdot \vec{e}_{\vec{\mathrm{M}}} \quad , \tag{3.93}$$

where for simplicity we omitted the $\vec{r}$ dependence in the t-matrix. For given values of $\{\theta_{\vec{\mathrm{M}}}, \phi_{\vec{\mathrm{M}}}\}$ the matrix $\mathbf{t}'(\vec{r}, \vec{r}', \varepsilon)$ might have non-zero off-diagonal components. We note that we chose to define the azimuthal angle with respect to the x-axis being the direction of the perturbing current. The longitudinal and transversal components of the residual resistivity in the whole phase space of rotation angles is depicted in Fig. 3.13a and b. The images exhibit a clearly visible angular dependence. The anisotropy of the resistivity is in the order of 10^{-8} nΩ. In case of the longitudinal resistivity this anisotropy modifies the isotropic contribution of the longitudinal resistivity, which is in the order of 3.180×10^{-5} nΩ by about ± 0.14 %. Since for the transversal resistivity the isotropic contribution is exactly zero, the anisotropies are given as absolute values.

Angular dependence of the residual resistivity tensor

Now we turn to the analysis of the angular dependence of the resistivity anisotropy. To the best of our knowledge, no phenomenological functional form for such a general angular dependence is available in the literature contrary to the case, for example, where the magnetization is lying in-plane [157]. Therefore to simplify our analysis, we focus first on the particular orientation of the magnetic moment along the x-direction. There, the t-matrix given by Eq. (3.93) is expressed as

$$\boldsymbol{t}'(\varepsilon) = \frac{1}{2}\begin{pmatrix} t^{\uparrow\uparrow}(\varepsilon) + t^{\downarrow\downarrow}(\varepsilon) & t^{\uparrow\uparrow}(\varepsilon) - t^{\downarrow\downarrow}(\varepsilon) \\ t^{\uparrow\uparrow}(\varepsilon) - t^{\downarrow\downarrow}(\varepsilon) & t^{\uparrow\uparrow}(\varepsilon) + t^{\downarrow\downarrow}(\varepsilon) \end{pmatrix} \quad , \tag{3.94}$$

where $t^{\uparrow\uparrow}(\varepsilon)$ and $t^{\downarrow\downarrow}(\varepsilon)$ are the upper and lower diagonal components of the t-matrix when the magnetic moment points along the z-direction. As we will discuss below, this gives rise to a non-zero off-diagonal contribution in the resistivity tensor and contributes to the PHE even without spin-orbit contribution at the impurity site. When the magnetic moment is in the surface plane ($\theta_{\vec{\mathrm{M}}} = \frac{\pi}{2}$), Fig. 3.13c and d show the behaviour of the diagonal and off-diagonal components of the resistivity tensor, respectively, as function of the azimuthal angle $\phi_{\vec{\mathrm{M}}}$. The trace of the resistivity tensor is conserved under these azimuthal rotations ($\rho_{xx} + \rho_{yy} = \text{ constant}, \forall\, \phi_{\vec{\mathrm{M}}}$) while the off-diagonal components are related by $\rho_{xy} = \rho_{yx}$. The diagonal components of the resistivity tensor (Fig. 3.13c) can be fitted with the AMR functional form given by Thompson et al.[157]: $\rho_{\gamma\gamma} = \rho_\perp + (\rho_\parallel - \rho_\perp)\, \cos^2(\phi_{\vec{\mathrm{M}}})$, where $\rho_\parallel$ and $\rho_\perp$ define the residual resistivities when the moment is respectively parallel and perpendicular to the current. In our particular case, the current is pointing along the x-direction, thus $\rho_\parallel = \rho_{xx}(\phi_{\vec{\mathrm{M}}} = 0)$ and $\rho_\perp = \rho_{xx}(\phi_{\vec{\mathrm{M}}} = \frac{\pi}{2})$. It turns out that $(\rho_\parallel - \rho_\perp)$, *i.e.* the maximal value of the AMR, is a positive quantity as expected for a Rashba electron gas [158]. This can be explained by analyzing the different scattering processes on the

Fermi surface when the impurity magnetic moment is in-plane (see Figs. 3.12 (c) and (d)). As done previously, the idea is to evaluate the scattering probabilities for an arbitrary rotation of the magnetic moment (see Eq. (3.93)). Here we provide the results obtained for scattering processes from $\phi_{\vec{k}} = 0$ to $\phi_{\vec{k}'} = 0$ or π. If $\phi_{\vec{k}'} - \phi_{\vec{k}} = 0$ only inter-band transitions, *i.e.* $\alpha \neq \alpha'$, can contribute:

$$P^{\alpha\alpha'}_{\vec{k}\vec{k}'} = \frac{2\pi}{\hbar}|t^{\uparrow\uparrow}(\varepsilon) - t^{\downarrow\downarrow}(\varepsilon)|^2(\cos^2\theta_{\vec{\mathrm{M}}} + \sin^2\theta_{\vec{\mathrm{M}}}\cos^2\phi_{\vec{\mathrm{M}}})\,\delta(\varepsilon_\alpha(\vec{k}) - \varepsilon_{\alpha'}(\vec{k}')) \quad , \tag{3.95}$$

which is zero if the moment points along the y-direction. This is the same result obtained for intra-band scattering probability, $P^{\alpha\alpha}_{\vec{k}\vec{k}'}$, when $\phi_{\vec{k}'} - \phi_{\vec{k}} = \pi$. For the later angle configuration, the inter-band scattering probability is non-zero independently from the rotation angle of the moment:

$$P^{\alpha\alpha'}_{\vec{k}\vec{k}'} = \frac{2\pi}{\hbar}|t^{\uparrow\uparrow}(\varepsilon) + t^{\downarrow\downarrow}(\varepsilon) + \alpha(t^{\uparrow\uparrow}(\varepsilon) - t^{\downarrow\downarrow}(\varepsilon))\sin\theta_{\vec{\mathrm{M}}}\sin\phi_{\vec{\mathrm{M}}}|^2\,\delta(\varepsilon_\alpha(\vec{k}) - \varepsilon_{\alpha'}(\vec{k}')) \quad . \tag{3.96}$$

To summarize, when the magnetic moment points along the current direction (x-direction) the back-scattering is due to inter-band and intra-band scattering. However when the magnetic moment is perpendicular to the current direction then the back-scattering is only originating from inter-band transitions, which induces a smaller residual resistivity and therefore gives a positive maximal value of the AMR, *i.e.* $\rho_\parallel > \rho_\perp$. Similar scattering processes are possible when the moment points along the x-direction or the z-direction, which explains that the resistivities are the same for both magnetic orientations. On the other hand the off-diagonal components of the resistivity tensor (Fig. 3.13d) could be fitted with the PHE functional form [157] $\rho_{\gamma\gamma'} = (\rho_\parallel - \rho_\perp)\,\cos(\phi_{\vec{\mathrm{M}}})\sin(\phi_{\vec{\mathrm{M}}})$. We notice that for the considered polar angles ($\theta_{\vec{\mathrm{M}}} = \frac{\pi}{2}, \theta_{\vec{\mathrm{M}}} = \frac{\pi}{4}$), $\rho_{\gamma\gamma'}$ changes sign when $\phi_{\vec{\mathrm{M}}}$ crosses $\frac{\pi}{2}$ (Fig. 3.13d). This is accompanied by a direction switch of the Hall like electric field originating from the PHE.

Let us go back to the general case, where the magnetic moment points in arbitrary orientations. As mentioned earlier, a phenomenological functional form for the residual resistivity has not been proposed up to now. In Appendix E, we derive phenomenological functional forms for the residual resistivity tensor and show that the longitudinal and transversal parts follow a simple angular dependence:

$$\rho_{xx} = \rho_\parallel - (\rho_\parallel - \rho_\perp)\sin^2(\phi_{\vec{\mathrm{M}}})\sin^2(\theta_{\vec{\mathrm{M}}}) \quad , \tag{3.97}$$

$$\rho_{xy} = (\rho_\parallel - \rho_\perp)\cos(\phi_{\vec{\mathrm{M}}})\sin(\phi_{\vec{\mathrm{M}}})\sin^2(\theta_{\vec{\mathrm{M}}}) \quad . \tag{3.98}$$

These equations describe perfectly the angular dependence plotted for instance in Fig. 3.13c and d with the polar angle $\theta_{\vec{\mathrm{M}}} = \frac{\pi}{2}$ (black curve) and $\theta_{\vec{\mathrm{M}}} = \frac{\pi}{4}$ (red curve). Alternatively, one may also derive the angular dependence of the diagonal components of the resistivity tensor directly from Eq. (3.82). By applying the aforementioned unitary transformations in spin space, Eq. (3.93), to the t-matrix and substituting its matrix elements into Eq. (3.82) one yields the diagonal components of the resistivity. In the present case, the second terms of $M(\varepsilon)$ and $N(\varepsilon)$, which are proportional to the fourth power of $t^{\sigma\sigma'}(\varepsilon)$, vanish identi-

cally and one obtains

$$\begin{aligned}\rho_{xx} = \frac{2\hbar k_{\mathrm{FM}}^2}{\pi S n_{\mathrm{e}}^2 e^2}\Bigg[& \sin^2(\delta^{\uparrow}) + \sin^2(\delta^{\downarrow}) \\ & - \left(\frac{k_{\mathrm{so}}}{k_{\mathrm{FM}}}\right)^2 \sin(\delta^{\uparrow})\sin(\delta^{\downarrow})\cos(\delta^{\uparrow}-\delta^{\downarrow}) \\ & - \left(\frac{k_{\mathrm{so}}}{k_{\mathrm{FM}}}\right)^2 \frac{1}{2}\sin^2(\delta^{\uparrow}-\delta^{\downarrow})\sin^2\theta_{\vec{\mathrm{M}}}\sin^2\phi_{\vec{\mathrm{M}}}\Bigg] \quad ,\end{aligned} \tag{3.99}$$

where similarly to Eq. (3.86), $\delta^{\uparrow}$ and $\delta^{\downarrow}$ are respectively abbreviations of $\delta_0^{\uparrow\uparrow}(\epsilon_{\mathrm{F}})$ and $\delta_0^{\downarrow\downarrow}(\epsilon_{\mathrm{F}})$. Thus, the magnitude of the AMR, *i.e.*, $\rho_{\parallel} - \rho_{\perp}$ in Eq. (3.97) is given by

$$\rho_{\parallel} - \rho_{\perp} = \frac{\hbar k_{\mathrm{so}}^2}{\pi S n_{\mathrm{e}}^2 e^2}\sin^2(\delta^{\uparrow}-\delta^{\downarrow}) \geq 0 \quad , \tag{3.100}$$

indicating that the maximal value of the AMR occurs when the difference between the phase shifts of both spin components becomes equal to $\frac{\pi}{2}$.

3.9 Orbital magnetization in a Rashba electron gas

So far, we have seen that the deposition of magnetic impurities on a Rashba electron gas generates numerous effects including: RKKY exchange interactions among magnetic impurities and magnetotransport properties. Here, we address the lifting of the orbital degeneracy in the Rashba electron gas due to the presence of magnetic impurities. The orbital magnetization originates from a different source than the spin magnetization. The latter one is due to a spin-splitting between the majority and minority spin channels, while former one arises from bound currents. Classically, the orbital magnetization and these bound currents are related via:

$$\vec{j}(\vec{r}) = \vec{\nabla}_{\vec{r}} \times \vec{m}_l(\vec{r}) \quad , \tag{3.101}$$

where $\vec{m}_l(\vec{r})$ is the orbital magnetization density, $\vec{j}(\vec{r})$ is the bound current density. In equilibrium, $\vec{j}(\vec{r})$ fulfills the continuity equation for the charge density:

$$\frac{\partial n(\vec{r})}{\partial t} + \vec{\nabla}_{\vec{r}} \cdot \vec{j}(\vec{r}) = 0 \quad . \tag{3.102}$$

In quantum mechanics the existence of bound currents requires the breaking of time reversal symmetry combined with the SOI, which is described by the term linear in momentum in the Rashba Hamiltonian $\boldsymbol{H}_{\mathrm{R}}$ (see Eq. (3.1)). The breaking of time reversal symmetry is provided by the spin moment carried by magnetic impurities. More recently, a new way of coupling the spin and orbital moments has been found [159, 77]. Indeed, non-collinear spin textures create a vector potential that couples the spin degree of freedom to orbital one. In order to illustrate this, we consider a 2D electron gas coupled to a magnetic spin texture:

$$\boldsymbol{H}_{\mathrm{nc}} = \frac{\vec{p}^{\,2}}{2m_{\mathrm{e}}}\mathbb{1}_2 + J_{\mathrm{c}}\,\vec{n}(\vec{r})\cdot\vec{\boldsymbol{\sigma}} \quad . \tag{3.103}$$

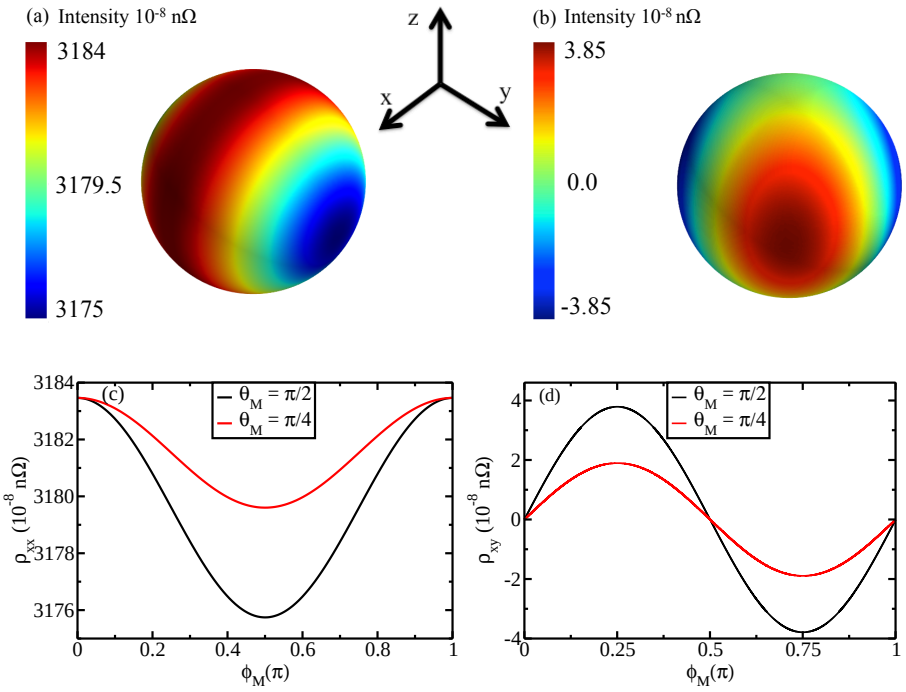

Figure 3.13: Evolution of the components of the residual resistivity tensor as function of the orientation of the magnetic moment in all 4π spatial directions: (a) longitudinal component (ρ_{xx}), (b) transversal component (ρ_{xy}). Every point on the sphere corresponds to a given orientation of the magnetic moment. Evolution of the residual resistivity tensor components while changing only $\phi_{\vec{M}}$ when the magnetic moment is pointing in-plane along the x-direction: (c) longitudinal and (d) transversal component. Here we plotted the following cases $\theta_{\vec{M}} = \frac{\pi}{2}$ (black curve) and $\theta_{\vec{M}} = \frac{\pi}{4}$ (red curve).

$\boldsymbol{H}_{\text{nc}}$ is the Hamiltonian describing the 2D electron gas in presence of the spin texture, J_{c} represents the coupling parameter of the electrons to the magnetic texture, $\vec{n}(\vec{r})$ is the direction of the magnetization field. When applying an SU(2) gauge transformation $U(\vec{r}) = e^{i\vec{w}(\vec{r})\cdot\vec{\boldsymbol{\sigma}}}$ ($\vec{w}(\vec{r})$ describes the spin rotation) that diagonalizes the Hamiltonian at each point $\vec{r}$, we obtain the Hamiltonian $\boldsymbol{H}'_{\text{nc}}$ in the local frame of the magnetization:

$$\boldsymbol{H}'_{\text{nc}} = \frac{\vec{\boldsymbol{\Pi}}^2}{2m_{\text{e}}} + J_{\text{c}}\,\boldsymbol{\sigma}_z \quad . \tag{3.104}$$

$\vec{\boldsymbol{\Pi}}$ is the kinetic momentum and contains two contributions:

$$\begin{aligned} \boldsymbol{\Pi}_\mu &= p_\mu\,\mathbb{1}_2 - \hbar \sum_{\nu=x,y,z} \partial_\mu w_\nu(\vec{r})\,\boldsymbol{\sigma}_\nu \quad . \\ &= p_\mu\,\mathbb{1}_2 - \boldsymbol{A}^\mu_{nc}(\vec{r}) \quad . \end{aligned} \tag{3.105}$$

where $\mu = \{x, y\}$, $\vec{\boldsymbol{A}}_{\text{nc}}(\vec{r})$ can be viewed as a gauge-field. Since $[\boldsymbol{A}^x_{\text{nc}}, \boldsymbol{A}^y_{\text{nc}}] \neq 0$, it makes $\vec{\boldsymbol{A}}_{\text{nc}}(\vec{r})$ a non-abelian gauge field often called the Yang-Mills field [160]. The kinetic energy is then constituted of four terms:

$$\frac{\vec{\boldsymbol{\Pi}}^2}{2m_{\text{e}}} = \frac{1}{2m_{\text{e}}}\left[\vec{p}^{\,2} + \vec{\boldsymbol{A}}_{\text{nc}}(\vec{r})\cdot\vec{p} + \vec{p}\cdot\vec{\boldsymbol{A}}_{\text{nc}}(\vec{r}) + \left(\vec{\boldsymbol{A}}_{\text{nc}}(\vec{r})\right)^2\right] \quad . \tag{3.106}$$

The first term in the previous equation is a spin independent part, the second term couples the orbital degree of freedom to the spin, while the third term gives a Zeeman-like contribution and the last term is a non-spin-dependent potential-like contribution. Therefore, one can see that non-collinear spin moments contribute to the Hamiltonian in a similar way as the SOI does and give rise to a finite orbital magnetization.

3.9.1 Rashba spin-orbit interaction as a vector field

The linear term in momentum accounting for the SOI in the Rashba Hamiltonian (see Eq. (3.1)) can be viewed as a gauge field, similarly to the gauge field of a 2D electron gas coupled to a non-collinear spin texture, the spin-orbit gauge field $\vec{\boldsymbol{A}}_{\text{so}}$ is a non-abelian. The formulation of the SOI in terms of gauge field allows to interpret Rashba electron as a free 2D electrons with spin-dependent phases. The spin-orbit (SO) gauge field is defined as [161, 162]:

$$\vec{\boldsymbol{A}}_{\text{so}} = \frac{m^* c\,\alpha_{\text{so}}}{e\hbar}\,(-\boldsymbol{\sigma}_y, \boldsymbol{\sigma}_x) \quad , \tag{3.107}$$

The Rashba Hamiltonian from Eq. (3.1) is re-expressed using the SO gauge field as:

$$\begin{cases} \boldsymbol{H}_{\text{R}} = \frac{1}{2m^*}\left(\vec{p} - \frac{e}{c}\vec{\boldsymbol{A}}_{\text{so}}\right)^2 - V_{\text{so}}\,\mathbb{1}_2 \quad , \\ V_{\text{so}} = \frac{m^*\alpha_{\text{so}}^2}{\hbar^2} \quad \text{is a constant} \quad . \end{cases} \tag{3.108}$$

The previous equation shows that due to the presence of the SO gauge field, the kinetic momentum $\vec{p}$ is corrected, thus, we expect a correction of the current operator which is

the main ingredient required to access the orbital magnetization. In order to derive the expression of the current operator in presence of the SO gauge field, we start from the time-dependent Schrödinger equation for Rashba electrons:

$$\mathrm{i}\hbar\frac{\partial\psi(\vec{r},t)}{\partial t} = \boldsymbol{H}_{\mathrm{R}}\,\psi(\vec{r},t) \quad , \tag{3.109}$$

which is used to write a continuity equation for the electron density $n(\vec{r},t) = |\psi(\vec{r},t)|^2$. From the continuity equation given in Eq. (3.102), one can easily identify the divergence of the current density $\vec{j}(\vec{r},t)$, thus, defining the current operator $\hat{\vec{\boldsymbol{j}}}$ as:

$$\hat{\vec{\boldsymbol{j}}} = \frac{\hbar}{2m^*\mathrm{i}}\lim_{\vec{r}'\to\vec{r}}(\vec{\nabla}_{\vec{r}} - \vec{\nabla}_{\vec{r}'}) - \frac{e}{m^*c}\lim_{\vec{r}'\to\vec{r}}\vec{\boldsymbol{A}}_{\mathrm{so}} \quad . \tag{3.110}$$

The details of derivation for the current operator are given Appendix F. The first term in Eq. (3.110) is the paramagnetic contribution to the current operator, while the second term is a diamagnetic-like contribution due to the SO gauge field. In presence of a finite spin magnetization, an extra Zeeman-like contribution to the current is present and reads [163]:

$$\hat{\vec{\boldsymbol{j}}}_{\mathrm{z}} = \frac{\hbar}{2m^*}\lim_{\vec{r}'\to\vec{r}}\vec{\nabla}_{\vec{r}}\times\vec{\boldsymbol{\sigma}} \quad . \tag{3.111}$$

The latter one can be derived from an expansion of the Dirac equation and retaining terms up $\frac{v^2}{c^2}$, similarly to the procedure discussed in Sec. 2.4.5 to obtain the SOI. Combining Eq. (2.26) and Eq. (3.111) the Zeeman current density $\vec{j}_{\mathrm{z}}(\vec{r})$ can be related to induced spin magnetization density given in Eq. (3.22) via:

$$\vec{j}_{\mathrm{z}}(\vec{r}) = \int_{-\infty}^{\varepsilon_{\mathrm{F}}}\mathrm{d}\varepsilon\,\vec{\nabla}_{\vec{r}}\times\vec{m}(\vec{r},\varepsilon) \quad . \tag{3.112}$$

The previous equation shows that the connection between the Zeeman current density and the spin magnetization is similar to the relation of the current density (excluding the Zeeman contribution) and the orbital magnetization given in Eq. (3.101).

3.9.2 Ground state charge current induced by a single magnetic impurity on a Rashba electron gas

As discussed previously, the introduction of a magnetic moment breaking the time reversal symmetry in the system is expected to create a finite orbital moment due to the presence of the SOI. This can be achieved by the deposition of magnetic impurities on the Rashba electron gas. The Green function connecting a point $\vec{r}$ to $\vec{r}'$ within the Rashba electron gas in presence of magnetic impurities is given similarly to Eq. (3.36) by:

$$\boldsymbol{G}(\vec{r},\vec{r}',\varepsilon) = \boldsymbol{G}^{\mathrm{R}}(\vec{r},\vec{r}',\varepsilon) + \sum_{ij}\boldsymbol{G}^{\mathrm{R}}(\vec{r},\vec{R}_i,\varepsilon)\,\boldsymbol{T}_{ij}(\varepsilon)\,\boldsymbol{G}^{\mathrm{R}}(\vec{R}_j,\vec{r}',\varepsilon) \quad . \tag{3.113}$$

The sum runs over the number of magnetic impurities and $\boldsymbol{T}_{ij}(\varepsilon)$ is the full scattering matrix connecting two impurities located at the positions $\vec{R}_i$ and $\vec{R}_j$ respectively. $\boldsymbol{G}^{\mathrm{R}}(\vec{r},\vec{r}',\varepsilon)$

is the Rashba Green function defined in Eq. (3.6). When dealing with a single impurity Eq. (3.35) reduces simply to $\boldsymbol{T}_{ij}(\varepsilon) = \boldsymbol{t}_i(\varepsilon)\,\delta_{ij}$, the ground state charge current can be computed analytically. First, we start from the definition of the current density:

$$\vec{j}(\vec{r}) = -\frac{1}{\pi}\,\mathrm{Im}\int_{-\infty}^{\varepsilon_\mathrm{F}} \mathrm{d}\varepsilon\,\mathrm{Tr}_\sigma\,\hat{\vec{\boldsymbol{j}}}\,\boldsymbol{G}(\vec{r},\vec{r}\,',\varepsilon) \quad . \tag{3.114}$$

The current operator given in Eq (3.110) contains a gradient acting on the Green function. Then, if the moment is pointing along the z-direction *i.e.* perpendicular to the plane containing the Rashba electron gas, the cylindrical symmetry of the latter one is still conserved, therefore, it is convenient to use cylindrical coordinates to compute the ground state charge current. The gradient in cylindrical coordinates is expressed as:

$$\vec{\nabla}_{\vec{r}} = \frac{\partial}{\partial r}\,\vec{e}_r + \frac{1}{r}\,\frac{\partial}{\partial\theta}\,\vec{e}_\theta \quad . \tag{3.115}$$

$\vec{e}_r$ is the radial unit vector and $\vec{e}_\theta$ is the azimuthal unit vector. The gradient can be defined with respect to the position of the impurities $\vec{R}_i$ as:

$$\vec{\nabla}_{\vec{r}_i} = \frac{\partial}{\partial r_i}\,\vec{e}_{r_i} + \frac{1}{r_i}\,\frac{\partial}{\partial\theta_i}\,\vec{e}_{\theta_i} \quad , \tag{3.116}$$

where $\vec{r}_i = \vec{r} - \vec{R}_i$. The radial dependence is only in the Rashba Green function $\boldsymbol{G}^\mathrm{R}(\vec{r},\vec{R}_i,\varepsilon) = \boldsymbol{G}^\mathrm{R}(\vec{r}_i,\varepsilon)$, therefore, the gradient present in the current operator is acting on the latter one and reads:

$$\vec{\nabla}_{\vec{r}_i}\,\boldsymbol{G}(\vec{r}_i,\varepsilon) = \begin{pmatrix} \frac{\partial G_\mathrm{D}}{\partial r_i}\,\vec{e}_{r_i} & e^{-\mathrm{i}\theta_i}\left[-\frac{\partial G_\mathrm{ND}}{\partial r_i}\,\vec{e}_{r_i} + \mathrm{i}\,\frac{G_\mathrm{ND}}{r_i}\,\vec{e}_{\theta_i}\right] \\ e^{\mathrm{i}\theta_i}\left[\frac{\partial G_\mathrm{ND}}{\partial r_i}\,\vec{e}_{r_i} + \mathrm{i}\,\frac{G_\mathrm{ND}}{r_i}\,\vec{e}_{\theta_i}\right] & \frac{\partial G_\mathrm{D}}{\partial r_i}\,\vec{e}_{r_i} \end{pmatrix} \quad . \tag{3.117}$$

The previous equation shows that the computation of $\vec{\nabla}_{\vec{r}_i}\,\boldsymbol{G}(\vec{r}_i,\varepsilon)$ requires the evaluation of $\frac{\partial G_\mathrm{D}}{\partial r_i}$ and $\frac{\partial G_\mathrm{ND}}{\partial r_i}$, G_D and G_ND are given by a linear combinations of cylindrical Hankel functions of zero and first order, respectively (see Eqs. (3.7) and (3.8)). The first order derivatives of cylindrical Hankel functions of n-th order are given by the following recursive relations:

$$\frac{dH_n(x)}{dx} = \left[\frac{n\,H_n(x)}{x} - H_{n+1}(x)\right] \quad . \tag{3.118}$$

To access the first order derivative of G_D and G_ND, we only need the first order derivatives of $H_0(x)$ and $H_1(x)$:

$$\begin{cases} \frac{dH_0(x)}{dx} = -H_1(x) & , \\ \frac{dH_1(x)}{dx} = \left[\frac{H_1(x)}{x} - H_2(x)\right] & . \end{cases} \tag{3.119}$$

After computing $\vec{\nabla}_{\vec{r}_i}\,\boldsymbol{G}(\vec{r}_i,\varepsilon)$, we have access to the current density. If we assume that the spin moment points out along the z-axis, then the cylindrical symmetry of the Rashba electron gas is preserved, therefore, the current density has only an azimuthal component:

$$\vec{j}(\vec{r}) = -\frac{\hbar}{\pi m^*}\,\mathrm{Im}\int_{-\infty}^{\varepsilon_\mathrm{F}} \mathrm{d}\varepsilon\,\left[\frac{G_\mathrm{ND}^2}{r} - \frac{2m^*\alpha_\mathrm{so}}{\hbar}G_\mathrm{D}G_\mathrm{ND}\right]\,\Delta t_i(\varepsilon)\,\vec{e}_\theta \quad , \tag{3.120}$$

where G_{D} and G_{ND} are functions of r and ε. $\vec{j}(\vec{r})$ on depends the intrinsic properties of the impurity, this is encoded in $\Delta t_i(\varepsilon) = \left(t_i^{\uparrow\uparrow}(\varepsilon) - t_i^{\downarrow\downarrow}(\varepsilon)\right)$. The first term in Eq. (3.120) represents the paramagnetic part of the current density, while the second is the diamagnetic part. $\vec{j}(\vec{r})$ has no dependence on $\vec{e}_r$, thus, it is expected to be swirling around the magnetic impurity i. An example is shown in Fig. 3.14 for an Fe impurity on the Rashba surface states of Au(111). The parameters are extracted from first-principles electronic structure calculations (see Sec. 3.4.1). Fig. 3.14 shows a dissipationless ground state charge current in agreement with the continuity equation. Eq. (3.120) also shows in a trivial way that in order to obtain a finite ground state charge current (*i.e.* an orbital magnetization), on the one hand, we need a spin moment that breaks the time reversal symmetry with $t_i^{\uparrow\uparrow}(\varepsilon) \neq t_i^{\downarrow\downarrow}(\varepsilon)$. On the other hand, broken spatial inversion symmetry and spin-orbit interaction giving rise to a nonzero G_{ND}. Similar observations where made for magnetic impurities on superconductors with a Rashba spin-orbit interaction in Ref. [164].

When the spin moment points along the x-direction (in the plane containing the Rashba electron gas), the cylindrical symmetry is broken, we obtain a more complicated expression for the current density:

$$\begin{aligned}\vec{j}(\vec{r}) = -\frac{\hbar}{\pi m^*}\mathrm{Im}\int_{-\infty}^{\varepsilon_{\mathrm{F}}} \mathrm{d}\varepsilon \Bigg(& \left[G_{\mathrm{ND}}\frac{\partial G_{\mathrm{D}}}{\partial r} - G_{\mathrm{D}}\frac{\partial G_{\mathrm{ND}}}{\partial r}\right] \Delta t_i(\varepsilon)\, \sin\theta\, \vec{e}_r \\ & + 4\,\frac{G_{\mathrm{D}}\, G_{\mathrm{ND}}}{r}\,\Delta t_i(\varepsilon)\,\cos\theta\,\vec{e}_\theta - \frac{m^*\alpha_{\mathrm{so}}}{\hbar}\left[G_{\mathrm{ND}}^2 + G_{\mathrm{D}}^2\right]\,\Delta t_i(\varepsilon)\,\sin\theta\,\vec{e}_r \\ & + \frac{m^*\alpha_{\mathrm{so}}}{\hbar}\left[G_{\mathrm{ND}}^2 - G_{\mathrm{D}}^2\right]\,\Delta t_i(\varepsilon)\,\cos\theta\,\vec{e}_\theta\Bigg) \quad .\end{aligned} \tag{3.121}$$

The current has components along the radial direction $\vec{e}_r$, however, it remains dissipationless. The first two terms are coming from the paramagnetic part, while the two last ones are originating from the diamagnetic part of the current operator.

3.9.3 Orbital magnetization of magnetic impurities on a Rashba electron gas from ground state charge currents

So far, we have seen that the breaking of time and space inversion symmetry, in presence of the SOI as shown in Eq. (3.120) allows the existence of ground state charge currents. These currents give rise to a finite orbital magnetization within the Rashba electron gas. In the absence of free charge currents and time-dependent external fields, the orbital magnetization $\vec{m}_l(\vec{r})$ can be related to the ground state charge current via Eq. (3.101) as discussed in Ref. [165]. The confinement of Rashba electrons in two dimensions constrains the direction of the orbital magnetization along the z-axis (*i.e.* $\vec{m}_l(\vec{r}) = m_{l,z}(\vec{r})\,\vec{e}_z$). This uniquely defines the orbital magnetization from the ground state charge current. Indeed, any arbitrary function $\vec{\nabla}_{\vec{r}}\,\xi(\vec{r})$ (with $\vec{\nabla}_{\vec{r}} \times \vec{\nabla}_{\vec{r}}\,\xi(\vec{r}) = 0$) which can be added to the orbital magnetization to generate the same ground state charge current density has to be zero since $\vec{\nabla}_{\vec{r}}\,\xi(\vec{r}) = \frac{\partial}{\partial z}\,\xi(x,y)\,\vec{e}_z = 0$. Therefore, the orbital magnetization can be evaluated using the classical formula:

$$\vec{M}_l = \frac{1}{2c}\int_S \mathrm{d}\vec{r}\,\vec{r}\times\vec{j}(\vec{r}) \quad . \tag{3.122}$$

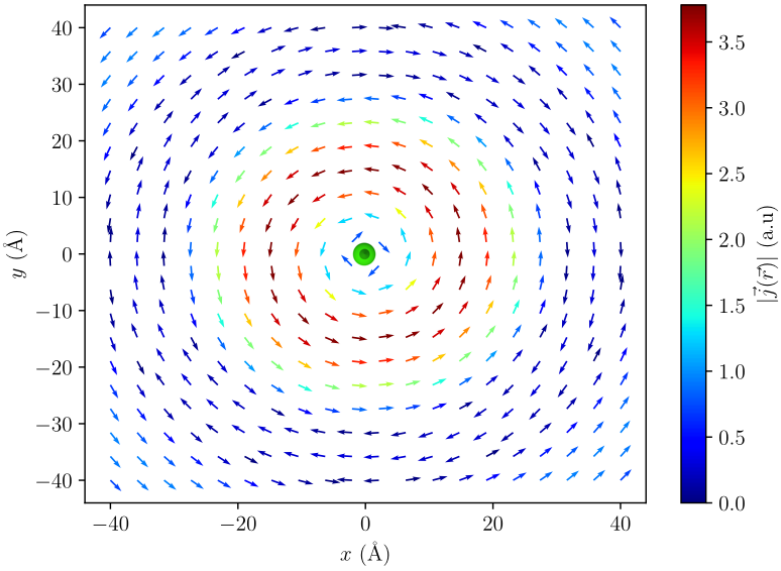

Figure 3.14: Current density induced by a single Fe impurity on a Au(111) with a magnetic moment perpendicular to surface plane (along the z-axis). $\alpha_{\mathrm{so}} = -0.4$ eV Å and $m^* = 0.26\, m_{\mathrm{e}}$ are the Rashba model parameters for the Au(111) surface state. The Fe impurity is considered in the s-wave approximation (see Sec. 3.3). The current density is swirling around the magnetic impurity.

S represents the area of the Rashba electron gas. Eq. (3.122) gives access to the total induced orbital magnetization in the surrounding electron gas but not the orbital magnetization density $\vec{m}_l(\vec{r})$. Furthermore, the current density is oscillating and decaying with the distance as can be seen from Fig. 3.14. However, one needs to integrate numerically $\vec{r} \times \vec{j}$ for which the decay with the distance is slower. An alternative route to obtain the orbital magnetization density is by using Eq. (3.101), and rewriting it as a Poisson equation:

$$\begin{aligned} \vec{\nabla}_{\vec{r}} \times \vec{j}(\vec{r}) &= \vec{\nabla}_{\vec{r}} \times \vec{\nabla}_{\vec{r}} \times \vec{m}_l(\vec{r}) \quad , \\ &= \vec{\nabla}_{\vec{r}} \left(\vec{\nabla}_{\vec{r}} \cdot \vec{m}_l(\vec{r}) \right) - \vec{\nabla}^2_{\vec{r}} \cdot \vec{m}_l(\vec{r}) \quad . \end{aligned} \tag{3.123}$$

For two dimensional systems, the previous equation reduces to:

$$\partial_x \, j_y(\vec{r}) - \partial_y \, j_x(\vec{r}) = -\vec{\nabla}^2_{\vec{r}} \, m_{l,z}(\vec{r}) \quad . \tag{3.124}$$

The previous equation is solved numerically using a Fourier transform, the orbital magnetization $m_{l,z}(\vec{k})$ in Fourier space reads:

$$m_{l,z}(\vec{k}) = \mathrm{i} \, \frac{k_y \, j_x(\vec{k}) - k_x \, j_y(\vec{k})}{k_x^2 + k_y^2} \quad , \tag{3.125}$$

where $j_\alpha(\vec{k})$ is the Fourier transform of $j_\alpha(\vec{r})$ defined as:

$$j_\alpha(\vec{k}) = \sum_{i=1}^{N_\mathrm{r}} j_\alpha(\vec{r}_i) \, e^{\mathrm{i}\vec{k}\cdot\vec{r}_i} \quad . \tag{3.126}$$

In practice, we considered $N_\mathrm{r} = 1000 \times 1000$, which is the number of grid points in real space contained in a squared simulation box. For an Fe impurity deposited on Au(111), we choose a box of 400 Å×400 Å. This ensures that $\vec{j}(\vec{r}) = 0$ at the edges of the box to avoid interactions between the Fe impurity and its periodic copies. $m_{l,z}(\vec{k})$ is then Fourier transformed back to real space giving access to $m_{l,z}(\vec{r})$. The results obtained for a single Fe impurity deposited on Au(111) are discussed in the next section.

3.9.4 Orbital magnetization of a single adatom on a Rashba electron

We computed the orbital magnetization $m_{l,z}(\vec{r})$ induced by a single Fe impurity deposited on a Rashba electron gas parametrized for Au(111) surface state. The map is shown in Fig. 3.15. The spin moment points along the z-axis, we observe isotropic Friedel oscillations in the induced orbital magnetization around the Fe defect. The oscillations have two characterizing wave lengths, a short one which is the Fermi wave length $\lambda_\mathrm{F} \sim 18.5$ Å and a long one induced by the SO interaction $\lambda_\mathrm{so} \sim 240$ Å. The oscillations decay as $\frac{1}{r}$ which is slower than the induced spin magnetization (see Sec. 3.4.2). However, $m_{l,z}(\vec{r})$ is one order of magnitude smaller than the induced spin magnetization [126]. The net orbital and spin magnetizations induced in the simulation box are $M_{l,z} = 0.58 \, \mu_\mathrm{B}$ and $M_{s,z} = 2.11 \, \mu_\mathrm{B}$, respectively.

Fig. 3.16 shows the orbital magnetization when the spin moment points along the x-direction (in the surface plane). The cylindrical symmetry is broken as shown in Eq. (3.121)

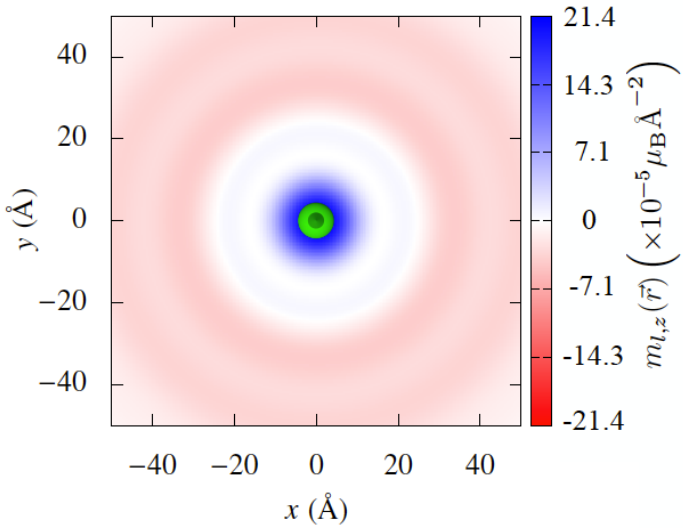

Figure 3.15: Induced orbital magnetization map for an Fe adatom deposited on Rashba electron gas, $\alpha_{so} = -0.4$ eV Å and $m^* = 0.26\,m_e$ are the Rashba model parameters for the Au(111) surface state. The Fe impurities are given in the s-wave approximation (see Sec. 3.3). The spin moment points along the z-axis. The orbital magnetization consists of concentric rings centered around the Fe impurity oscillating with two characteristic wave lengths λ_F and λ_{so}.

for the current density. We also find two oscillation wave lengths (λ_F and λ_{so}), while $m_{l,z}(\vec{r})$ oscillates around a positive value for $x < 0$ and around a negative value for $x > 0$. However, the oscillations are less pronounced compared to the case where the impurity has a moment along the z-axis. The order of magnitude and the asymptotic behavior of $m_{l,z}(\vec{r})$ at large distances are similar to the out of plane configuration. As shown in Fig. 3.16 $m_{l,z}(x,y) = -m_{l,z}(-x,y)$, therefore, the net induced orbital magnetization in the simulation box vanishes *i.e.* $M_{l,z} = 0\,\mu_B$, the net induced spin magnetization vanishes as well.

3.9.5 Orbital magnetization of a dimer on a Rashba electron gas from ground state charge currents

After discussing the induced orbital magnetization by a single Fe impurity, we now explore possible interesting effects that can be observed in the orbital magnetization induced by clusters containing more impurities, starting with a dimer of Fe atoms at $d = 10.42$ Å from each other along the x-direction. The interaction of the two Fe impurities via the Rashba electron gas leads to an antiferromagnetic isotropic exchange interaction $J = 3.45$ meV. And the DM vector points in y-direction according to the Moriya rules with an amplitude $D = 0.96$ meV. The magnetic anisotropy is $K = -6.0$ meV favoring an out of plane orientation (see Sec. 3.7). The resulting magnetic ground state is non-collinear, one impurity moment points along the z-axis, while the second is oriented in the opposite

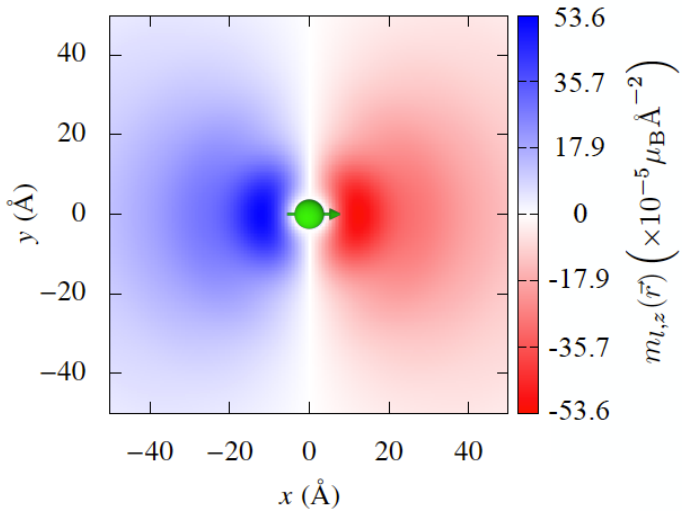

Figure 3.16: Induced orbital magnetization map for an Fe adatom deposited on Rashba electron gas, $\alpha_{so} = -0.4$ eV Å and $m^* = 0.26\,m_e$ are the Rashba model parameters for the Au(111) surface state. The Fe impurities are given in the s-wave approximation (see Sec. 3.3). The spin moment points along the x-axis. The orbital magnetization is strongly anisotropic since $m_l^z(<) > 0$ for $x(>) < 0$, it also has two characteristic wave lengths λ_F and λ_{so}.

direction. The opening angle between the moments is $\theta_0 = 171°$.

In Fig. 3.17, we display the map of the orbital magnetization. The cylindrical symmetry in the Rashba electron gas is broken due to the presence of the two impurities. We also notice that for $x < 0$ and close to the impurity $m_{l,z}(\vec{r}) > 0$, this is similar to the single impurity with a spin moment along the z-direction. The opposite is observed for $x > 0$. Between the two impurities $m_{l,z}(\vec{r})$ tends to zero for $x \sim 0$ due to destructive interferences. The oscillation period is similar the single impurity case with $\lambda_F \sim 18.5$ Å. Furthermore, the orbital magnetization is of the same order of magnitude compared to the single impurity configuration, which means that the multiple scattering effects do not enhance the orbital magnetization within the Rashba electron gas. The net induced orbital and spin magnetizations in the simulation box are $M_{l,z} = 0.08\,\mu_B$ and $M_{s,z} = 0.04\,\mu_B$, respectively. Finally, when we ignore the DM-interactions, the angle between magnetic moments of the impurities is $\theta_0 = 180°$ and $m_{l,z}(x, y) = -m_{l,z}(-x, y)$. Thus, the net induced orbital magnetization in the simulation box vanishes.

3.9.6 Orbital magnetization of trimer on a Rashba electron gas from ground state charge currents

After studying the orbital magnetization induced by one and two Fe adatoms, we computed $m_{l,z}(\vec{r})$ for a trimer of Fe atoms deposited on an equilateral triangle keeping the distance considered for the dimer ($d = 10.42$ Å). In this case, the isotropic exchange coupling is

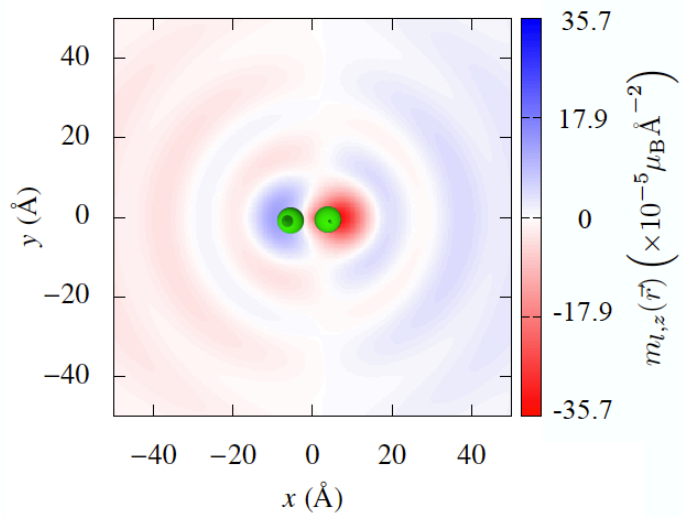

Figure 3.17: Induced orbital magnetization map for a dimer of Fe adatoms deposited along the x-axis on Rashba electron gas, $\alpha_{so} = -0.4$ eV Å and $m^* = 0.26\,m_e$ are the Rashba model parameters for the Au(111) surface state. The Fe impurities are given in the s-wave approximation (see Sec. 3.3). The magnetic ground state is non-collinear.

antiferromagnetic with $J = 3.51$ meV. The Dzyaloshinskii-Moriya vector amplitude is $D = 1$ meV, it points in the perpendicular direction to the connecting vectors between Fe adatoms. The magnetic anisotropy is $K = -6$ meV. The magnetic ground state consists of three moments almost parallel to the z-axis, where two magnetic moments are tilted with an angle of 10° from the z-axis and the third one points in the opposite direction with an angle of 173° as discussed in Sec. 3.7.

We show in Fig. 3.18 the induced orbital magnetization density map. There is an interference pattern due to the presence of the three Fe impurities, we see a distinct constructive interference at the center of mass of the trimer. The orientation of the magnetic moments breaks the C_{3v} symmetry causing highly anisotropic oscillations in $m_{l,z}(\vec{r})$, which has two different wavelengths (λ_F and λ_{so}) as discussed earlier for a single Fe adatom and displays a similar $\frac{1}{r}$ decay of the oscillations at large distances. The net induced orbital magnetization in the simulation box is $M_{l,z} = 0.02\,\mu_B$, while the induced spin magnetization is $M_{s,z} = 0.05\,\mu_B$.

The trimer is more interesting than the single atom or the dimer since when the chirality is non-vanishing, we expect a finite orbital magnetization in absence of the SOI (see the discussion in Sec. 3.9). The orbital magnetization originates from the chirality of the magnetic structure [67]. For this reason, we computed the orbital magnetization for the trimer considered previously, without SOI. The result is shown in Fig. 3.19. The obtained $m_{l,z}(\vec{r})$ is two orders of magnitude smaller compared the case where the SOI was present. It has a three fold rotation symmetry (symmetry of the lattice) independently from the symmetry of the spin moments. We can explain the presence of an induced orbital magne-

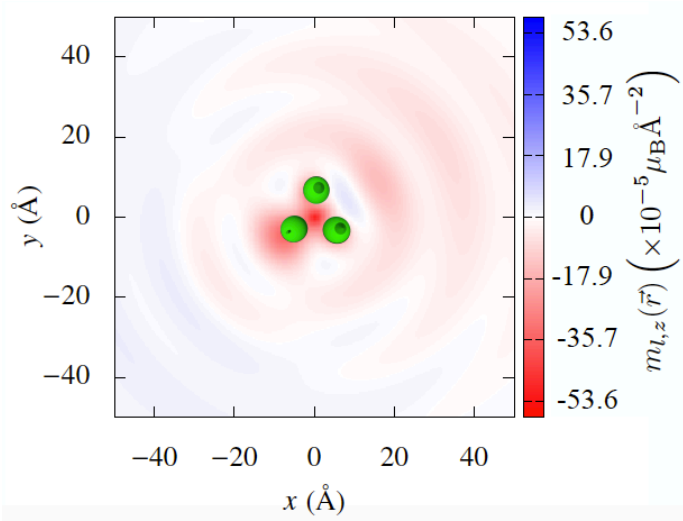

Figure 3.18: Induced orbital magnetization map for a timer of Fe adatoms in an equilateral triangle geometry, deposited on Rashba electron gas, $\alpha_{so} = -0.4$ eV Å and $m^* = 0.26\,m_e$ are the Rashba model parameters for the Au(111) surface state. The Fe impurities are given in the s-wave approximation (see Sec. 3.3). The non-collinear magnetic ground state is resulting from competing interactions as discussed in Sec. 3.5.

tization without spin-orbit interaction by computing analytically the ground state charge currents [166]. First, we expand the Green function in Eq. (3.113) into Born series:

$$\begin{aligned} \boldsymbol{G}(\vec{r},\vec{r}',\varepsilon) = \boldsymbol{G}^{\mathrm{R}}(\vec{r},\vec{r}',\varepsilon) &+ \boldsymbol{G}^{(1)}(\vec{r},\vec{r}',\varepsilon) \\ &+ \boldsymbol{G}^{(2)}(\vec{r},\vec{r}',\varepsilon) + \boldsymbol{G}^{(3)}(\vec{r},\vec{r}',\varepsilon) \\ &+ \boldsymbol{G}^{(4)}(\vec{r},\vec{r}',\varepsilon) + \boldsymbol{G}^{(5)}(\vec{r},\vec{r}',\varepsilon) + \ldots \quad . \end{aligned} \tag{3.127}$$

The previous equation represents an expansion up to the fifth order of the multiple scattering problem. In principle, an expansion up to the third order is enough to show the contribution of the three atoms simultaneously to the current and the orbital magnetization. The higher powers of the expansion can be viewed as higher order contributions and are to be estimated as well. The different elements of the expansion $G^{(i)}(\vec{r},\vec{r}',\varepsilon)$ are given by:

$$\boldsymbol{G}^{(1)}(\vec{r},\vec{r}',\varepsilon) = \sum_i \boldsymbol{G}^{\mathrm{R}}(\vec{r},\vec{r_i},\varepsilon)\,\boldsymbol{t}_i(\varepsilon)\,\boldsymbol{G}^{\mathrm{R}}(\vec{r_i},\vec{r}',\varepsilon) \quad , \tag{3.128}$$

$$\begin{aligned} \boldsymbol{G}^{(2)}(\vec{r},\vec{r}',\varepsilon) = \sum_{ij} &\boldsymbol{G}^{\mathrm{R}}(\vec{r},\vec{r_i},\varepsilon)\,\boldsymbol{t}_i(\varepsilon)\,\boldsymbol{G}^{\mathrm{R}}(\vec{r_i},\vec{r_j},\varepsilon) \\ &\times \boldsymbol{t}_j(\varepsilon)\,\boldsymbol{G}^{\mathrm{R}}(\vec{r_j},\vec{r}',\varepsilon) \quad , \end{aligned} \tag{3.129}$$

$$\begin{aligned}\boldsymbol{G}^{(3)}(\vec{r},\vec{r}',\varepsilon) = \sum_{ijk} &\boldsymbol{G}^{\mathrm{R}}(\vec{r},\vec{r_i},\varepsilon)\,\boldsymbol{t}_i(\varepsilon)\,\boldsymbol{G}^{\mathrm{R}}(\vec{r_i},\vec{r_j},\varepsilon)\,\boldsymbol{t}_j(\varepsilon) \\ &\times \boldsymbol{G}^{\mathrm{R}}(\vec{r_j},\vec{r_k},\varepsilon)\boldsymbol{t}_k(\varepsilon)\,\boldsymbol{G}^{\mathrm{R}}(\vec{r_k},\vec{r}',\varepsilon) \quad ,\end{aligned} \tag{3.130}$$

$$\begin{aligned}\boldsymbol{G}^{(4)}(\vec{r},\vec{r}',\varepsilon) = \sum_{ijkm} &\boldsymbol{G}^{\mathrm{R}}(\vec{r},\vec{r_i},\varepsilon)\,\boldsymbol{t}_i(\varepsilon)\,\boldsymbol{G}^{\mathrm{R}}(\vec{r_i},\vec{r_j},\varepsilon)\,\boldsymbol{t}_j(\varepsilon) \\ &\times \boldsymbol{G}^{\mathrm{R}}(\vec{r_j},\vec{r_k},\varepsilon)\boldsymbol{t}_k(\varepsilon)\,\boldsymbol{G}^{\mathrm{R}}(\vec{r_k},\vec{r_m},\varepsilon) \\ &\times \boldsymbol{t}_m(\varepsilon)\,\boldsymbol{G}^{\mathrm{R}}(\vec{r_m},\vec{r}',\varepsilon) \quad ,\end{aligned} \tag{3.131}$$

$$\begin{aligned}\boldsymbol{G}^{(5)}(\vec{r},\vec{r}',\varepsilon) = \sum_{ijkml} &\boldsymbol{G}^{\mathrm{R}}(\vec{r},\vec{r_i},\varepsilon)\,\boldsymbol{t}_i(\varepsilon)\,\boldsymbol{G}^{(}\vec{r_i},\vec{r_j},\varepsilon)\,\boldsymbol{t}_j(\varepsilon) \\ &\times \boldsymbol{G}^{\mathrm{R}}(\vec{r_j},\vec{r_k},\varepsilon)\,\boldsymbol{t}_k(\varepsilon)\,\boldsymbol{G}^{\mathrm{R}}(\vec{r_k},\vec{r}',\varepsilon)\,\boldsymbol{t}_m(\varepsilon) \\ &\times \boldsymbol{G}^{\mathrm{R}}(\vec{r_m},\vec{r}',\varepsilon)\,\boldsymbol{t}_l(\varepsilon)`\,\boldsymbol{G}^{\mathrm{R}}(\vec{r_l},\vec{r}',\varepsilon) \quad .\end{aligned} \tag{3.132}$$

In absence of the SOI, the SO gauge field vanishes and the current operator given in Eq. (3.110) reduces to the paramagnetic contribution and reads:

$$\hat{\vec{j}} = \frac{\hbar}{2m^*\mathrm{i}} \lim_{\vec{r}'\to\vec{r}} (\vec{\nabla}_{\vec{r}} - \vec{\nabla}_{\vec{r}'}) \quad . \tag{3.133}$$

The paramagnetic current density is computed using Eq. (3.114), where the Green function is given by Eq. (3.127) and only the third ($\vec{j}^{\,(3)}(\vec{r})$) and the fifth ($\vec{j}^{\,(5)}(\vec{r})$) order contribution are non-zero due to the cyclic properties of the trace, thus, the current density is given a sum of these two remaining terms:

$$\vec{j}(\vec{r}) = \vec{j}^{\,(3)}(\vec{r}) + \vec{j}^{\,(5)}(\vec{r}) \quad . \tag{3.134}$$

The third and the fifth order contributions are given by a convolution of Rashba Green functions. At a point $\vec{r}$ away from the trimer, the Rashba Green function decays as $\frac{1}{\sqrt{r}}$, thus, we expect the fifth contribution to be smaller compared to the third one. $\vec{j}^{\,(3)}(\vec{r})$ is given by:

$$\begin{aligned}\vec{j}^{\,(3)}(\vec{r}) = \sum_{ijk} &\vec{\nabla}_{\vec{r}}\,\boldsymbol{G}^{\mathrm{R}}(\vec{r},\vec{r_i},\varepsilon)\,\boldsymbol{G}^{\mathrm{R}}(\vec{r_i},\vec{r_j},\varepsilon)\,\boldsymbol{G}^{\mathrm{R}}(\vec{r_j},\vec{r_k},\varepsilon) \\ &\times \boldsymbol{G}^{\mathrm{R}}(\vec{r_k},\vec{r},\varepsilon)\,\big[\mathrm{Tr}_\sigma\,\boldsymbol{t}_i(\varepsilon)\,\boldsymbol{t}_j(\varepsilon)\,\boldsymbol{t}_k(\varepsilon) \\ &- \mathrm{Tr}_\sigma\,\boldsymbol{t}_k(\varepsilon)\,\boldsymbol{t}_j(\varepsilon)\,\boldsymbol{t}_i(\varepsilon)\big] \quad ,\end{aligned} \tag{3.135}$$

and $\vec{j}^{\,(5)}(\vec{r})$ reads:

$$\begin{aligned}\vec{j}^{\,(5)}(\vec{r}) = \sum_{ijkml} &\vec{\nabla}_{\vec{r}}\,\boldsymbol{G}^{\mathrm{R}}(\vec{r},\vec{r_i},\varepsilon)\,\boldsymbol{G}^{\mathrm{R}}(\vec{r_i},\vec{r_j},\varepsilon)\,\boldsymbol{G}^{\mathrm{R}}(\vec{r_j},\vec{r_k},\varepsilon) \\ &\times \boldsymbol{G}^{\mathrm{R}}(\vec{r_k},\vec{r_m},\varepsilon)\,\boldsymbol{G}^{\mathrm{R}}(\vec{r_m},\vec{r_l},\varepsilon)\,\boldsymbol{G}^{\mathrm{R}}(\vec{r_l},\vec{r},\varepsilon) \\ &\times \big[\mathrm{Tr}_\sigma\,\boldsymbol{t}_i(\varepsilon)\,\boldsymbol{t}_j(\varepsilon)\,\boldsymbol{t}_k(\varepsilon)\,\boldsymbol{t}_m(\varepsilon)\,\boldsymbol{t}_l(\varepsilon) \\ &- \mathrm{Tr}_\sigma\,\boldsymbol{t}_l(\varepsilon)\,\boldsymbol{t}_m(\varepsilon)\,\boldsymbol{t}_k(\varepsilon)\,\boldsymbol{t}_j(\varepsilon)\,\boldsymbol{t}_i(\varepsilon)\big] \quad .\end{aligned} \tag{3.136}$$

The previous equations can be simplified further using the properties of the Pauli matrices.

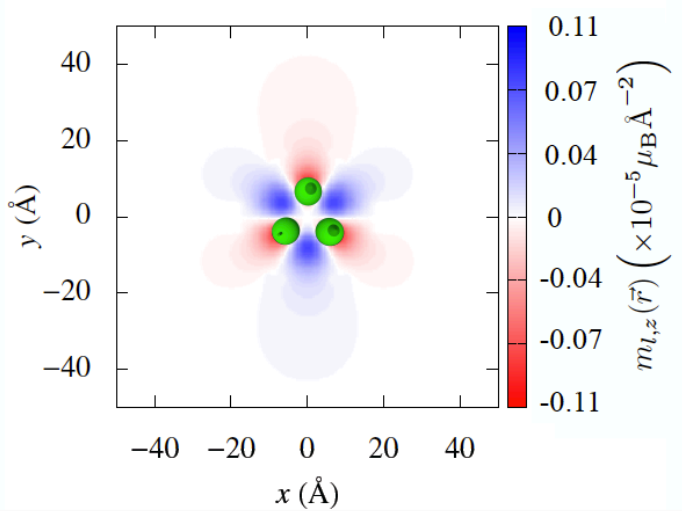

Figure 3.19: Induced orbital magnetization map for a timer of Fe adatoms in an equilateral triangle geometry, deposited on Rashba electron gas, $\alpha_{so} = -0.4$ eV Å and $m^* = 0.26\,m_e$ are the Rashba model parameters for the Au(111) surface state. The SOI is turned off, however, the orbital magnetization is non-zero due to the non-collinearity.

The third order contribution to the current density simply reads:

$$\vec{j}^{(3)}(\vec{r}) = \sum_{ijk} \vec{f}_3(\vec{r})\, \vec{M}_i \cdot (\vec{M}_j \times \vec{M}_k) \quad , \tag{3.137}$$

where $\vec{M}_i$ is the spin moment of the impurity i and $\vec{f}_3(\vec{r})$ is given by:

$$\begin{aligned} \vec{f}_3(\vec{r}) = -\frac{2\hbar}{\pi m^*} \mathrm{Im}\, \vec{\nabla}_{\vec{r}}\, \boldsymbol{G}^{\mathrm{R}}(\vec{r},\vec{r}_i,\varepsilon)\, \boldsymbol{G}^{\mathrm{R}}(\vec{r}_i,\vec{r}_j,\varepsilon) \\ \boldsymbol{G}^{\mathrm{R}}(\vec{r}_j,\vec{r}_k,\varepsilon)\, \boldsymbol{G}^{\mathrm{R}}(\vec{r}_k,\vec{r},\varepsilon) \quad . \end{aligned} \tag{3.138}$$

Similarly the fifth order can be simplified as well:

$$\vec{j}^{(5)}(\vec{r}) = \sum_{ijknl} \vec{f}_5(\vec{r})\, (\vec{M}_i \cdot \vec{M}_j) \left[\vec{M}_k \cdot (\vec{M}_n \times \vec{M}_l)\right] \quad , \tag{3.139}$$

where $\vec{f}_5(\vec{r})$ is given by:

$$\begin{aligned} \vec{f}_5(\vec{r}) = -\frac{4\hbar}{\pi m^*} \mathrm{Im}\, \vec{\nabla}_{\vec{r}}\, \boldsymbol{G}^{\mathrm{R}}(\vec{r},\vec{r}_i,\varepsilon)\, \boldsymbol{G}^{\mathrm{R}}(\vec{r}_i,\vec{r}_j,\varepsilon)\, \boldsymbol{G}^{\mathrm{R}}(\vec{r}_j,\vec{r}_k,\varepsilon) \\ \times\, \boldsymbol{G}^{\mathrm{R}}(\vec{r}_k,\vec{r}_m,\varepsilon)\, \boldsymbol{G}^{\mathrm{R}}(\vec{r}_m,\vec{r}_l,\varepsilon)\, \boldsymbol{G}^{\mathrm{R}}(\vec{r}_l,\vec{r},\varepsilon) \quad . \end{aligned} \tag{3.140}$$

When restricting ourselves to the third order expansion, we find a non-zero ground state charge current which is proportional to the scalar chirality $\vec{j}(\vec{r}) \propto \vec{M}_1 \cdot (\vec{M}_2 \times \vec{M}_3)$. When

System	$M_{l,z}(\mu_B)$	$M_{s,z}(\mu_B)$
Single adatom ($\vec{M}_i \parallel z$)	0.58	2.11
Single adatom ($\vec{M}_i \parallel x$)	0.00	0.00
Dimer	0.08	0.04
Trimer (with SOI)	0.02	0.05
Trimer (without SOI)	0.00	0.64

Table 3.2: Summary of the net orbital and spin magnetizations obtained for the single adatom (with the magnetic moment of the impurity $\vec{M}_i \parallel z$-axis and x-axis, respectively), dimer and trimer (with and without SOI).

this expression for the current density in inserted into Eq. (3.101), we show that $m_{l,z}(\vec{r}) \propto \vec{M}_1 \cdot (\vec{M}_2 \times \vec{M}_3)$. This establishes the connection between the orbital magnetization and the scalar chirality in absence of the SOI. Considering that $m_{l,z}(\vec{r})$ in this scenario is solely related to the chirality of the magnetic texture, it can be referred to as a chiral orbital magnetization. The net induced chiral orbital magnetization in the simulation box vanishes by symmetry, and the induced spin magnetization is $M_{s,z} = 0.64\,\mu_B$. A summary of net induced spin and orbital magnetizations obtained for all the systems considered previously is given in Table 3.2.

In presence of the SOI, the Rashba term contribution and the one from the non-collinearity will compete. For the present case, the former one is much larger. Typically, the induced orbital magnetization $m_{l,z}(\vec{r})$ originating from the SOI is the largest for ferromagnetic structures, and for the one coming from the non-collinearity, it is the largest for non-coplanar structures that maximize the scalar chirality.

3.10 From Rashba surface states to topological insulators

The Rashba Hamiltonian given in Eq. (3.1) is not sufficient to describe the diverse phenomena that emerge on surfaces in presence of the SOI. We now introduce a more general form for the surface Hamiltonian, which can reproduce the Rashba spin splitting as well as other band structures of interest. For example, the generalized surface Hamiltonian can reproduce linear dispersions such as the ones observed on the surface of 3D topological insulators. These materials are insulating in the bulk but host conducting surface states. Recently, they raised a lot of interest due to possible applications in spintronics. They will be discussed in detail in the next chapter.

In order to describe these various systems, one can use a phenomenological $\vec{k}\cdot\vec{p}$ Hamiltonian. For the systems of interest such as Au(111) and Bi_2Se_3(111), the surfaces are non-magnetic and their crystal structure has C_{3v} symmetry. Therefore, the Hamiltonian must conserve time reversal symmetry and be invariant under C_{3v} symmetry operations. Thus, the $\vec{k}\cdot\vec{p}$ Hamiltonian expanded up to third order in k reads [167, 168]:

$$\boldsymbol{H}_{\vec{k}\vec{p}} = \frac{\hbar^2 k^2}{2m^*}\,\mathbb{1}_2 - \alpha_{\mathrm{so}}\left(1+\beta k^2\right)\left(k_x\boldsymbol{\sigma}_y - k_y\boldsymbol{\sigma}_x\right) + \frac{\lambda}{2}\left(k_+^3 + k_-^3\right)\boldsymbol{\sigma}_z \quad . \tag{3.141}$$

The first term represents the parabolic dispersion of the free electron gas, which is degen-

erate in spin as shown Fig. 3.20a. The second term represents the Rashba spin splitting. Its linear contribution in k (*i.e.* when $\beta = 0$, β is the term that corrects the velocity) results in a spin splitting of the two spin-degenerate parabolas as shown in Fig. 3.20b. When the second term includes higher order contributions in k^3 (*i.e.* when $\beta \neq 0$), it leads to a downward bending of the outer Rashba band creating a Dirac-like dispersion (Dirac cone). This downward bending has important consequences since it makes the surface state connect the valence band to the conduction band while closing the band gap as shown in Fig. 3.20c. The closing of the gap at the surface is a characteristic observed in topological materials, such as Chern insulators or topological insulators [16]. The last term in Eq. (3.141) accounts for warping effects that can be observed on constant energy contours in k-space. It leads to a breaking of the rotational symmetry. λ is a parameter that controls the warping strength. The warped band structure is shown Fig. 3.20d.

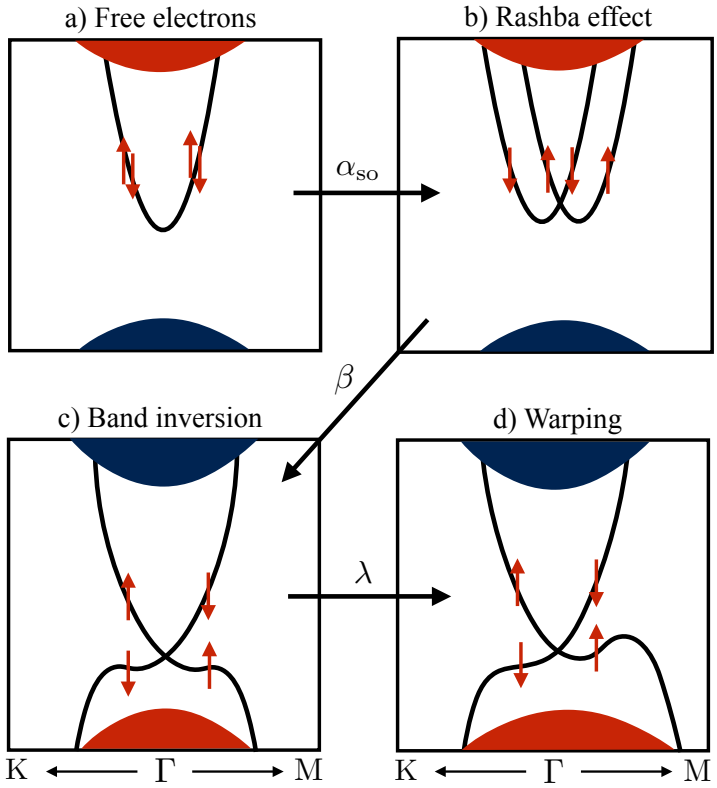

Figure 3.20: Energy dispersion of the surface states obtained using the $\vec{k} \cdot \vec{p}$ Hamiltonian given in Eq. (3.141). Different contributions are added to the Hamiltonian: (a) The spin-degenerate parabolic dispersion. (b) The Rashba spin splitted surface states. (c) The Rashba outer band down-folded due to a correction of the velocity. (d) Hexagonal warping of the constant energy contours breaking rotational symmetry.

The transition from Rashba to topological surface states can be understood by looking at the band structure of semimetals such as Sb. The valence and conduction bands are overlapping in energy as shown schematically in Fig. 3.21b, leading to a negative band gap, which arises due to the SOI. A negative band gap is a signature of the topological character of the Sb band structure. Similarly, to 3D topological insulators, Sb(111) hosts metallic surface states. These states connect the valence band to the conduction band, however, they are distorted compared to the linear dispersion (Dirac cone) observed in 3D topological insulators as shown in Fig. 3.21b and Fig. 3.21c. Near the Γ point the surface states of Sb(111) are reminiscent of Rashba splitted surface states observed on Au(111) as shown in Fig. 3.21a. Nonetheless, for higher energies there is transition to a single Dirac cone similar to the one observed in topological insulators. Therefore, Sb(111) represents a conceptual connection between Rashba spin splitted and topological surface states, since it displays both behaviors depending of the energy range considered.

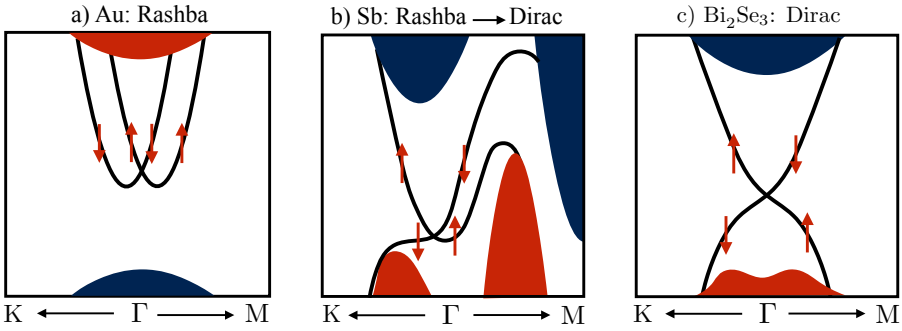

Figure 3.21: Schematic band structures connecting the Rashba spin splitted surfaces states to topological surfaces states: (a) Au(111) (usual Rashba spin splitting). (b) Sb(111) and (c) Bi_2Se_3(111) (Dirac-like dispersions). Sb(111) presents a Rashba-like spin splitted surface state near the band crossing (Dirac point), while it has a single Dirac cone for higher energies similarly to Bi_2Se_3(111).

3.11 Summary and outlook

In this chapter, we used a Rashba Hamiltonian to describe the spin splitting of the surface states due to the SOI in an inversion asymmetric environment. Then, we employed an embedding technique to include non-magnetic and magnetic impurities, which were described by a transition matrix in the s-wave approximation. First, we used a mapping procedure to an extended Heisenberg model, and computed the magnetic interactions analytically in the RKKY approximation. We demonstrated the deep link between the magnetic interactions and the components of the magnetic Friedel oscillations generated by single adatoms. We went beyond the RKKY approximation by considering energy dependent scattering matrices and multiple scattering effects to demonstrate that the size and shape of the nanostructures have a strong impact on the magnitude and sign of the magnetic interactions. We proposed an interesting connection between the DM interaction and the isotropic magnetic exchange interaction, $J(r)$. The DM interaction can be related to

the first-order change in $J(r)$ with respect to the SOI and, even more importantly, the origin of the sign of the DM interaction, *i.e.* defining the chirality, can be interpreted by the increase or decrease in $J(r)$ upon application of the SOI. We considered nano-objects that can be built experimentally, and show that each of the objects behave differently and the stability of their non-collinear chiral spin texture is closely connected with the type of structure built on the substrate.

Second, using linear response theory, we have derived a formulation of the tensor describing the residual electrical resistivity for the particular case of a Rashba electron gas scattering at an impurity that can be magnetic and whose magnetic moment can point in any arbitrary direction. We performed different types of studies and investigated the non-trivial impact of the strength of SOI of the substrate, as well as the role of the magnetism of the impurity and of the orientation of the magnetic moment on the diagonal and off-diagonal elements of the resistivity tensor. For instance, we found that, after scattering, a planar Hall effect and an anisotropic magnetoresistance can occur even without incorporating the SOI at the impurity site, if the orientation of the magnetic moment is not perpendicular to the surface. We derived analytically and generalized the usual phenomenological functional forms of the angular dependence of the resistivity tensor elements to the cases where the magnetization points in arbitrary directions.

Third, we investigated ground state charge currents, which are induced when magnetic impurities are deposited on a Rashba electron gas. We derived an analytical expression for the current operator and found that, adding to the paramagnetic term, a diamagnetic contribution from the spin-orbit gauge field appears. Furthermore, we computed analytically the current density in presence of a single magnetic impurity, which was employed to calculate the induced orbital magnetization. It was computed numerically by solving a Poisson equation in a simulation box. The induced orbital magnetization was found to be one order of magnitude smaller compared to the induced spin magnetization. More complicated nanostructures were also considered such as dimers and trimers. For the trimer structure, when the spin moments are non-coplanar, there is a non-vanishing induced orbital magnetization in absence of the SOI, which is related to the scalar chirality.

We have seen that the interplay between the SOI and magnetism is a source of numerous phenomena. The resistivity tensor was calculated for a single magnetic impurity, the behavior of the resistivity tensor in presence of nanoclusters with topological spin textures such as magnetic Skyrmions remains unexplored. Moreover, adding to induced ground state charge currents in the Rashba electron gas, ground state spin currents occur, which can be used to interpret the previously discussed magnetic interactions.

Chapter 4

Magnetic impurities in topological insulators

Topological insulators represent a new phase of matter which can exist in two (2D) or three dimensions (3D). They are found in semiconductors and thermoelectric materials [16]. This phase originates due to the spin-orbit interaction present in these materials. The main characteristic of topological insulators is that they are insulating in the bulk and conducting at the edges. These edge states are protected by time reversal symmetry and their spin-momentum locking (topological protection) [16]. For 2D topological insulators, the topological protection results in a dissipationless transport even in presence of non-magnetic disorder. Indeed, edge states with quantized conductance were observed experimentally in HgTe quantum wells [12]. For 3D topological insulators backscattering can be allowed depending on the shape of the Fermi surface (this is possible if the Fermi surface has a warping [167]).

The breaking of time reversal symmetry in topological insulators can lead to an opening of a band gap at the Dirac point (crossing of the edges state in the band gap see Fig. 4.1c). This can be a source of numerous exotic effects such as the quantum anomalous Hall effect (QAHE) and dissipationless transport. These effects could be used to build low power consumption devices relying only on the electron spin [169, 170, 171]. Here we investigate the possibility of opening a gap using magnetic impurities and analyze their ground state properties as well as their magnetic excitation spectra.

The chapter is structured as follows: First, we provide a short introduction to topological insulators. Second, we consider Bi_2Te_3 and Bi_2Se_3 as prototypes of 3D topological insulators and discuss their band structure in bulk and thin films. Then, we investigate the ground state properties of $3d$ and $4d$ transition metal impurities embedded in those materials. Magnetic impurities are expected to open a band gap when their magnetic moment points out-of-plane [81, 16]. This gap opening is the key ingredient for the observation of the QAHE. For that reason, a precise description of the MAE is required. Therefore, we systematically investigate the MAE for all the considered impurities using three different computational methods. We also explore the possibility of measuring the MAE and its sign

via inelastic scanning tunneling spectroscopy (ISTS). Theoretically, we access the magnetic excitation spectra within the framework of TD-DFT. Furthermore, the manipulation of the spin states will be addressed by extracting the characteristic lifetimes. Finally, we use the magnetic response function to determine the amount of zero-point spin-fluctuations and their impact on the orientation of the magnetic moment (*i.e.* magnetic anisotropy).

The part of this chapter discussing the impurity-induced in-gap states in Bi_2Te_3 and Bi_2Se_3 was published in Ref. [172]. The section dedicated to the investigation of spin dynamics in topological insulators was also published after the thesis has been submitted in Ref. [173].

4.1 Introduction to topological insulators

Before discussing topological insulators, we first introduce the so-called quantum Hall effect (QHE) which displays chiral edges states. QHE represents the first example where the topology of the band structure was related to physical quantities such as the Hall conductivity. It is a quantized version of the classical Hall effect. It was observed in 2D electronic systems at low temperatures, and under strong magnetic fields applied perpendicularly to the plane containing the electrons [174]. Classically, the electrons can be viewed as charges moving in circles around the magnetic field. At the edges of the sample, the circles can not be completed giving rise to chiral edge states as shown in Fig. 4.1a. An analogous situation takes place in the quantum Hall effect leading to topologically protected edges states.

A similar scenario is observed in 2D topological insulators in absence of magnetic fields (*i.e.* without breaking time reversal symmetry). This mechanism is induced by the spin-orbit interaction (SOI). Indeed, the SOI discussed in Sec. 2.4.5 can be viewed as an effective magnetic field coupling to the electron spin:

$$\boldsymbol{H}_{\text{SOI}} = \vec{B}_{\text{eff}}(\vec{k}) \cdot \vec{\boldsymbol{\sigma}} \quad . \tag{4.1}$$

$\vec{B}_{\text{eff}}(\vec{k})$ is the effective field, it is an odd function of the momentum of the electron $\vec{k}$, thus, electrons moving in opposite directions along the edges have opposite spin polarizations. This is known as the quantum spin Hall effect (QSHE) [14, 175] an illustration is shown in Fig. 4.1b. This figure displays the spin and momentum locking which is a characteristic of topological insulators (also known as helicity). These helical edge states form a Kramers pair. In presence of nonmagnetic disorder, they are protected from backscattering by time reversal symmetry. The helical edge states connect the conduction band to the valence band, they have a linear dispersion and cross in the surface band gap as shown in Fig. 4.1c.

Similarly to the 2D case, 3D topological insulators are insulating bulk material with metallic edges states located at the surface. The first 3D topological insulator discovered experimentally was an alloyed semiconductor $Bi_{1-x}Sb_x$ in Ref. [13]. They used angle resolved photoemission spectroscopy (ARPES) and observed surface states lying in the bulk band gap. Afterwards a multitude of 3D topological insulators was found, such as the ones studied in this thesis namely: Bi_2Se_3 and Bi_2Te_3. Indeed, it was shown in Ref. [176] that Bi_2Se_3 and Bi_2Te_3 are topological insulators, at the surface they host a single Dirac

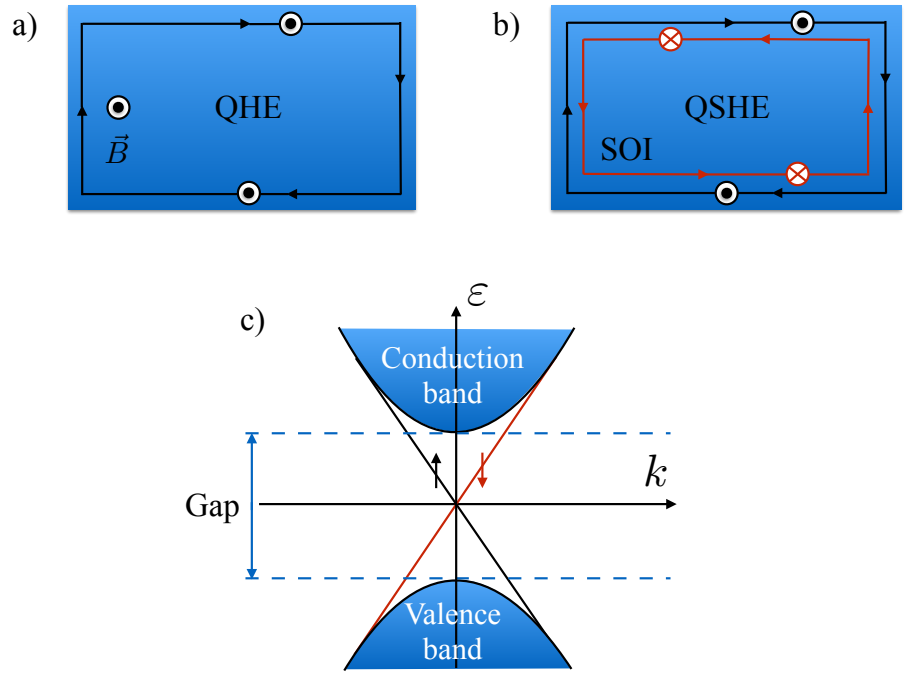

Figure 4.1: Illustration of the edges states hosted in a) Quantum Hall effect: a single edge state is observed with the spin polarization parallel to the external applied magnetic field. The circles with a dot in the center indicate a spin polarization parallel to the z-axis. b) Quantum spin Hall effect (2D topological insulator): two edges propagating in opposite directions with opposite spin polarization, which is due to the spin momentum locking generated by the SOI. The red circles with a cross on top designate a spin polarization antiparallel to the z-axis. c) Linear dispersion of the chiral edge states present in a 2D topological insulator. The edge states have a crossing in the band gap.

cone along the ΓM and KΓ directions of the two dimensional Brillouin zone (M and K are the time-reversal invariant momenta points). Bi_2Se_3 and Bi_2Te_3 surfaces were also investigated experimentally [13, 177, 178]. The linear dispersion of the surface state of a topological insulator (Dirac cone) and the spin momentum locking can be described by a massless Dirac Hamiltonian [16]:

$$\boldsymbol{H}_{\mathrm{D}} = \hbar\, v_{\mathrm{F}} \left(\vec{\boldsymbol{\sigma}} \times \vec{k}\right)_z \quad , \tag{4.2}$$

where v_{F} is the Fermi velocity. The previous Hamiltonian includes two main characteristics of topological insulators: The first one is the spin momentum locking. The second characteristic concerns the so-called Berry phase [15], which is a phase factor that emerges when a quantum state evolves adiabatically in addition to the usual dynamical phase. One cannot get rid of it by choosing a different phase factor for the Hamiltonian eigenstates. The Berry phase γ is defined as:

$$\begin{aligned} \gamma &= -\mathrm{i} \oint \mathrm{d}\vec{k}\, \langle \psi_{\vec{k}} |\, \vec{\nabla}_{\vec{k}}\, | \psi_{\vec{k}} \rangle \quad , \\ &= \oint \mathrm{d}\vec{k}\, \vec{A}_{\vec{k}} \quad . \end{aligned} \tag{4.3}$$

The integral is performed along a contour around $\vec{k} = 0$ in momentum space. $|\psi_{\vec{k}}\rangle$ represent the eigenstates of a Bloch Hamiltonian $H(\vec{k})$. $\vec{A}_{\vec{k}} = -\mathrm{i}\, \langle \psi_{\vec{k}} |\, \vec{\nabla}_{\vec{k}}\, | \psi_{\vec{k}} \rangle$ is the Berry connection. For topological insulators the Berry phase $\gamma = \pi$. This was shown experimentally by mapping the spin texture of the Fermi surface, which was obtained using ARPES [16].

Topological insulators and trivial insulators are two topologically distinct entities. Topology in mathematics is used to distinguish between shapes, for example, a donut and a coffee mug are topologically equivalent, since they can be deformed into each other by a continuous transformation. However, there is no continuous transformation that allows to transform an orange into a donut. The number of holes in the previous example represents a topological invariant. In condensed matter physics, two Bloch Hamiltonians $H(\vec{k})$ and $H'(\vec{k})$ with a gapped energy spectrum are considered topologically equivalent if they can be transformed into each other without closing the gap. In Fig. 4.2, we show a schematic bulk band structure for a trivial and a topological insulator. For the trivial one, we observe a valence band and conduction separated with a band gap. For the topological insulator, a similar setup is observed but a band inversion occurs and the bands display a camel back shape. It can be understood as follows: first the SOI closes the gap, then the hybridization between the conduction and valence bands leads to an opening of the gap once again. The closing of the gap due to the SOI is a signature of the topological non-equivalence between a trivial and a topological insulator. The red and black colors indicate the parity of the wave function associated with each energy band.

The topological invariant is used to distinguish between trivial and topological insulators. The concept of topological invariant was first introduced in the prominent work of Haldane [179] in the context of Chern insulators which are nontrivial insulator with broken time reversal symmetry. They display a QHE without applying an external magnetic field. The connection between the quantum Hall conductivity and the topological invariant

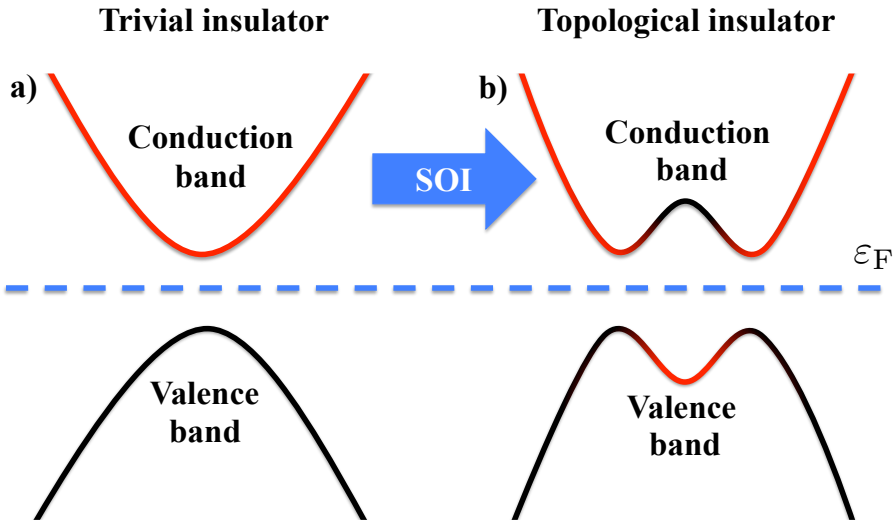

Figure 4.2: Illustration of the transition from a trivial insulator (a) to a topological insulator (b) induced by the spin-orbit interaction (SOI). For topological insulators the valence band displays a Camel back resulting from the band inversion. The colors indicate the parity of the wave functions associated with each band. An inversion of the parity is observed at the center of the bands for the topological insulator (b).

was provided by Thouless-Kohmoto-Nightingale-den Nijs (TKNN) [180] for the anomalous QHE (*i.e.* Chern insulator). The quantum Hall conductivity can be computed starting from the Kubo formula similarly to the resistivity discussed in the previous chapter, it can be expressed in terms of the TKNN topological invariant n as:

$$\sigma_{xy} = \frac{e^2}{\hbar} n \quad . \tag{4.4}$$

σ_{xy} is quantized, n is an integer quantity which provides a connection between the quantum Hall conductivity and the topology of the electronic band structure and reads:

$$\begin{aligned} n &= \frac{1}{2\pi} \int_{S_{\vec{k}}} \mathrm{d}k_x \mathrm{d}k_y \left(\vec{\nabla}_{\vec{k}} \times \vec{A}_{\vec{k}} \right)_z \quad , \\ &= \frac{1}{2\pi} \int_{S_{\vec{k}}} \mathrm{d}k_x \mathrm{d}k_y \left(\vec{\Omega}_{\vec{k}} \right)_z \quad . \end{aligned} \tag{4.5}$$

$S_{\vec{k}}$ is the area of the 2D Brillouin zone and $\vec{\Omega}_{\vec{k}}$ is the Berry curvature. n is often called the Chern number. When the 2D Brillouin is mapped to the surface of a torus, the Chern number can be viewed as the winding number of the phase of the wave function $\psi_{\vec{k}}$. The Chern number is a topological invariant since its is not affected by smooth changes of the Hamiltonian. For 2D topological insulators the Hall conductivity vanishes due to time reversal symmetry and $n = 0$. However, on can define the so-called $\mathbb{Z}_2$ topological invariant. For 2D systems conserving S_z (spin projection along the z-axis), the Chern numbers can be defined for each spin channel $n_\uparrow$ and $n_\downarrow$. The spin Hall conductivity is then given by the difference between the Chern numbers for each spin channel [181]:

$$n_\sigma = \frac{n_\uparrow - n_\downarrow}{2} \quad . \tag{4.6}$$

The $\mathbb{Z}_2$ topological invariant is defined as :

$$n = n_\sigma \bmod 2 \quad . \tag{4.7}$$

The Chern number can be used to predict the appearance of edge states by looking at the bulk band structure. Consider a Chern insulator $(n = 1)$ interfaced with a trivial insulator, for example vacuum $(n = 0)$. At the interface the gap must close to allow the Chern number to change, since these two insulators are topologically distinct. The gap is closed by edge states (interface states). The difference between the number of edge states moving in opposite directions (right and left) is given by the bulk-boundary correspondence [182]:

$$\Delta n = N_r - N_l \quad . \tag{4.8}$$

Δn is the difference between the Chern numbers of each side of the interface. N_r (N_l) is the number of edge states propagating in the right (left) direction. A similar argument can be used to predict the presence of edge states when interfacing a topological insulator with a trivial insulator.

System	a (Å)	c (Å)	μ	ν
Bi_2Te_3	4.383	30.487	0.400	0.212
Bi_2Se_3	4.138	28.64	0.399	0.206

Table 4.1: Crystal structure parameters for Bi_2Te_3 and Bi_2Se_3 [183]. a and c represent the lattice constants, μ and ν are the position of the Bi atoms and the two equivalent Te atom defined in units of primitive translation vectors given in Eq. (4.9).

4.2 Bi_2Te_3 and Bi_2Se_3 as prototypical topological insulators

Bi_2Te_3 and Bi_2Se_3 belong to the same family of compounds. They have a rhombohedral crystal structure with the space group D^5_{3d} ($R\bar{3}m$). As an example, we show the crystal structure of Bi_2Te_3 in Fig. 4.3. The unit cell contains five atoms. The structure consists of a collection of quintuple layers stacked along the z-direction. Each quintuple layer contains two equivalent Bi and Te atoms, while it has one inequivalent Te in the center (see Fig. 4.3). There is a strong interlayer bonding among two atomic layers in the same quintuple layer. However, the coupling is weaker between different quintuple layers since it is mainly due to van der Waals interactions. The rhombohedral primitive vectors are given by:

$$\begin{cases} \vec{v}_1 = (-\frac{a}{2}, -\frac{\sqrt{3}a}{6}, \frac{c}{3}) \\ \vec{v}_2 = (\frac{a}{2}, -\frac{\sqrt{3}a}{6}, \frac{c}{3}) \\ \vec{v}_3 = (0, \frac{\sqrt{3}a}{3}, \frac{c}{3}) \end{cases} \tag{4.9}$$

a and c are the lattice constants, the position of the atoms within the unit cell are given in units of the primitive vectors by: $(\pm\mu, \pm\mu, \pm\mu)$ for the Bi atoms and $(\pm\nu, \pm\nu, \pm\nu)$ for the two equivalent Te atoms, while the central Te is at $(0, 0, 0)$. Table 4.1 summarizes the parameters for the considered structures [183].

The reciprocal lattice vectors are calculated using the real space primitive vectors given in Eq. (4.9). The first Brillouin zone for the three dimensional crystal structure and its corresponding two dimensional surface Brillouin zone are depicted in Fig. 4.3d and Fig. 4.3e, respectively. The different time reversal invariant momentum points (TRIM) are highlighted on the two Brillouin zones. These are points where the Kramers degeneracy occurs (*i.e* $\varepsilon_{\vec{k}\uparrow} = \varepsilon_{\vec{k}\downarrow}$) due to the periodicity of the Brillouin zone [184].

Using the KKR Green function method introduced in Sec. 2.4, we computed the band structure of Bi_2Se_3 for the bulk crystal structure. We self-consistently converged the system which contains 5 atoms per unit cell using a $30 \times 30 \times 30$ k-mesh, then we computed the spectral function [185], using 400 energy points and 200 k-points along each high symmetry direction. The resulting band structure showing the bands connecting the Γ point to the TRIM points at the edges of the Brillouin zone is given in Fig. 4.4c. The Fermi energy (ε_F) is located in the bulk band gap which is around 0.4 eV. At the Γ point, a camel back shape is observed, it is highlighted with a red circle in Fig. 4.4c. This is caused by the SOI. In order to verify that a band inversion occurs for Bi_2Se_3 (*i.e.* Bi_2Se_3 is a topological insulator), Zhang et *al.* [176] followed the approach suggested by Fu and Kane [186]. They analyzed the parity of the Bloch wave functions for the valence band at the Γ point.

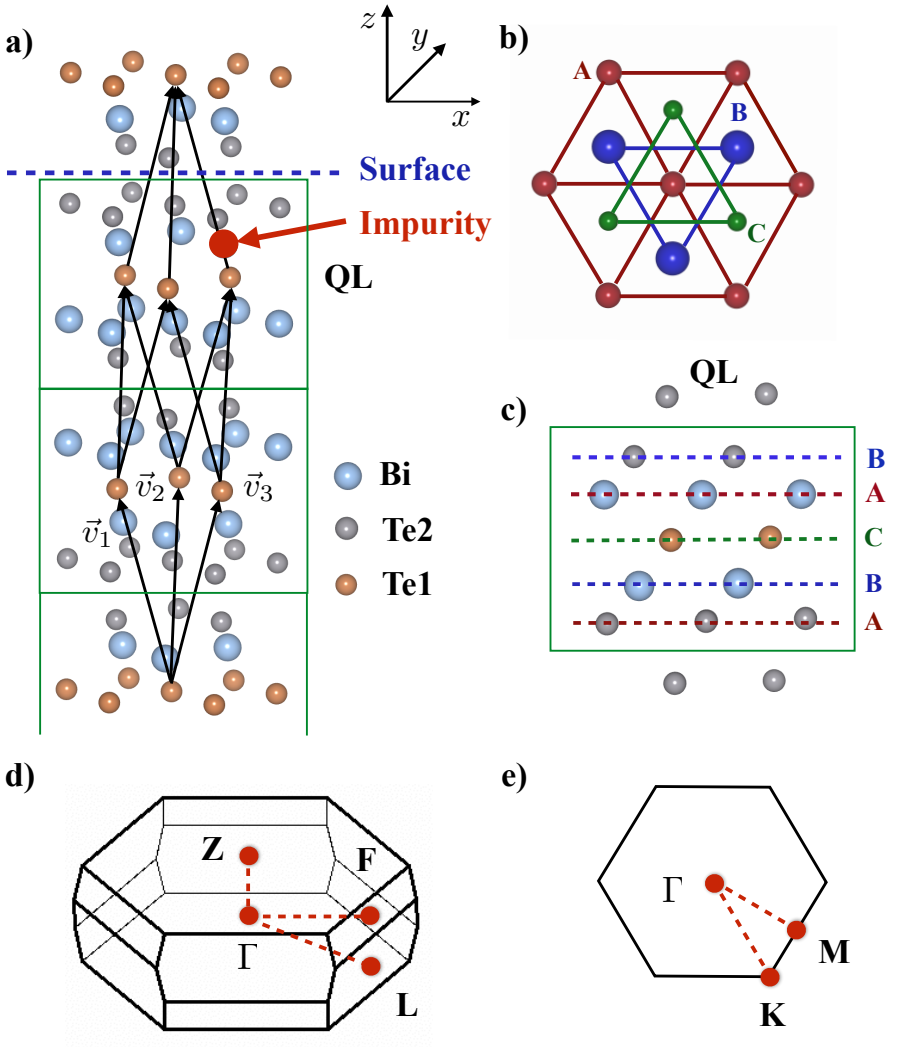

Figure 4.3: a) Crystal structure of Bi_2Te_3 characterized by a primitive unit cell containing five inequivalent atoms (two Bi, two Te2 and one Te1). The rhombohedral primitive vectors$\{\vec{v}_1, \vec{v}_2, \vec{v}_3\}$ are also shown. For the thin film six quintuple layers are used. The cut to create the surface is indicated on the figure. The position of the impurity in the real space calculations is indicated by a red arrow. b) Top view of the crystal structure showing the ABC stacking of the different layers. c) Side view of quintuple layer showing the stacking of the layers along the z-direction. d) 3D Brillouin zone for the bulk crystal structure (rhombohedral). e) 2D projection of the 3D Brillouin zone on the (111) surface, the TRIM points are highlighted in red.

They noticed a change in the parity in presence of the SOI. A detailed analysis explaining the band inversion in terms of the atomic orbitals of Bi $(6s^26p^3)$ and Se $(4s^24p^4)$ atomic levels was also discussed. Very similar features are observed in Fig. 4.4a for the bulk band structure of Bi_2Te_3. The most interesting characteristic of topological insulators is the existence of a topological surface state. The presence of this surface state is justified by the bulk boundary correspondence principle discussed in Sec. 4.1. In order to observe it, we consider a thin film of Bi_2Se_3 (Bi_2Te_3) grown along the (111) direction. The thin film contains six quintuple layers. This is enough to ensure the absence of a direct coupling between the two surfaces of the thin film, since the surface state penetrates only within two quintuple layers [183]. The band structure is shown in Fig. 4.4d. We observe a topological surface state lying within the bulk band gap. It consists of a single Dirac cone with a crossing (Dirac point) located at the Γ point (The red discontinuous lines indicate the upper part of the Dirac cone). A detailed analysis shows that the surface state wave functions near the Γ point have mainly a p-orbital character and a small s-orbital contribution as discussed in Ref. [187]. These surface states are absent for trivial insulators. We also computed the surface band structure for Bi_2Te_3 shown in Fig. 4.4b, similarly to the Bi_2Se_3 surface state, the dispersion is linear along $\Gamma \rightarrow$ K, while it has a more complicated structure along M $\rightarrow \Gamma$. The asymmetric dispersion in Bi_2Te_3 is attributed to the hexagonal warping of the Fermi surface [167].

4.3 Ground state properties of $3d$ and $4d$ magnetic impurities embedded in Bi_2Te_3 and Bi_2Se_3

Here we consider the breaking of time reversal symmetry in topological insulators via magnetic impurity doping. The magnetic interactions among the impurities may lead to ferromagnetic order. If the magnetocrystalline anisotropy favors an out-of-plane orientation (perpendicular to the surface) this is expected to induce the gap opening [81, 16]. Several experimental investigations using angle-resolved photoemission spectroscopy (ARPES) and scanning tunneling spectroscopy (STS) measurements confirmed the existence of a band gap [22, 23, 24]. However, the gap opening in topological insulators is subject to controversy, since other experimental works [25, 26, 27, 28, 29] report the absence of a gap. In Ref. [188], A. M. Black-Schaffer et *al.* used a continuous model and a tight-binding model of a three dimensional topological insulator introducing the topological surface and explained that a gap opens due to magnetic scattering. Also, the presence of charge scattering produces impurity resonances which lead to a filling of the band gap.

In order to settle this controversy, we performed first principles calculations for magnetic impurities embedded in Bi_2Te_3 and Bi_2Se_3 hosts. From our calculations, we confirm the absence of a gap opening due to the presence of the impurity resonances. Also we address the impact of the spin-fluctuations on the magnetic anisotropy energy, which is an essential ingredient for the gap opening as mentioned earlier. A detailed discussion for $3d$ and $4d$ impurities embedded in both hosts is given in the next sections.

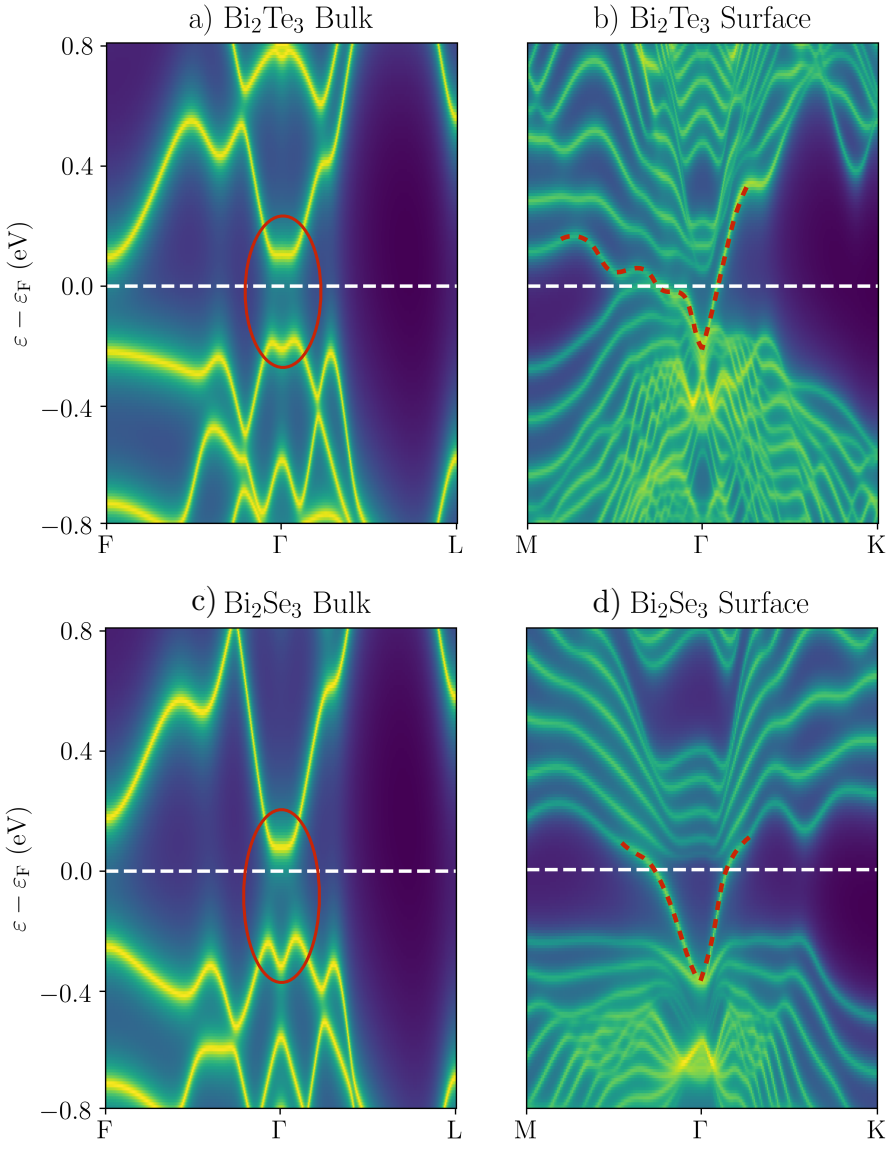

Figure 4.4: a) Band structure for Bi_2Te_3 bulk connecting the Γ point to the F and L points at the edges of the three dimensional Brillouin zone (TRIM points), the red circle highlights the band inversion that occurs in bulk due to the SOI. b) Band structure for a Bi_2Te_3 thin film constituted of 6 quintuple layers oriented in the (111) direction, it connects the Γ point to the M and K points at the edges of the two dimensional Brillouin zone (TRIM points). The discontinuous red lines indicate the upper part of the Dirac cone. c) Same as in (a) but for Bi_2Se_3. d) Same as in (b) but for Bi_2Se_3.

Element	Q	$M^s(\mu_B)$	$M^l(\mu_B)$
Cr (Bi_2Te_3)	5.154	3.843	0.065
Cr (Bi_2Se_3)	4.841	3.671	0.008
Mn (Bi_2Te_3)	6.160	4.412	0.050
Mn (Bi_2Se_3)	5.863	4.421	0.024
Fe (Bi_2Te_3)	7.282	3.395	0.260
Fe (Bi_2Se_3)	6.963	3.482	0.144
Co (Bi_2Te_3)	8.448	2.108	0.883
Co (Bi_2Se_3)	8.136	2.231	0.942

Table 4.2: Ground state properties of $3d$ impurities embedded in Bi_2Te_3 and in Bi_2Se_3 including the valence charge on the impurity Q, the spin moment M_s and the orbital moment M_l.

4.3.1 $3d$ magnetic impurities embedded in Bi_2Te_3 surface

In the following, we use the KKR Green function method in real space (see Sec. 2.4). We investigate the ground state properties of single $3d$ transition metals atoms (Cr, Mn, Fe and Co) embedded in the bulk or at the surface, the latter is simulated with six quintuple layers of Bi_2Te_3 oriented in the (111) direction. The band structure of the system is shown in Fig. 4.4. We started from a pristine Bi_2Te_3 host, then assuming that the perturbation due to the impurity is local, we compute the Green function in a finite region around the defect. Afterwards, the impurity is embedded by solving the Dyson equation for the host Green function and the impurity potential as done in Eq. (2.23). Several cluster sizes were considered. We report on the results obtained using a cluster containing 24 Bi atoms and 31 Te atoms, it also contains 47 empty spheres. Thus, the cluster contains 102 sites in total.

The $3d$ impurities are substituting an atom from the Bi subsurface layer as indicated in Fig. 4.3a (indicated by a red arrow). This position is stable thermodynamically as observed experimentally and predicted from first principles for the case of Fe in Bi_2Te_3 [189, 190]. The ground state of the impurities is self-consistently determined, with the impurity magnetic moment perpendicular to the surface plane (*i.e.* along the z-axis). The obtained valence charge, spin and orbital moments shown in Table 4.2.

The first column in Table 4.2 represents the charge on the impurity site, one can notice that all considered $3d$ impurities are donors of electrons (n-type doping). Similar results were obtained for Fe in Bi_2Te_3 in Ref. [189]. The spin moment M_s is shown in the second column of Table 4.2, it is high for Cr and Mn since they have half filled d-shells, while it decreases for Fe and Co in agreement with Hund's rules. In contrast, the orbital moments are higher for Fe and Co compared to Cr and Mn due to the partial filling of the minority d-orbitals. Cr and Mn have particularly small values for the orbital moments, which may lead to small magnetic anisotropies, which will be discussed in detail in Sec. 4.6.

The local density of states (LDOS) for Cr, Mn, Fe and Co is depicted in Fig. 4.5a. The majority spin channel ($\uparrow$) is represented in full lines, while the minority spin channel ($\downarrow$) is given in dashed lines. On the one hand, the majority-spin channel is fully occupied for all considered elements with the exception of Cr. On the other hand, the minority-spin

channel is partially occupied for Fe and Co and unoccupied for Cr and Mn. This explains why the spin moment diminishes for Fe and Co.

The resonances observed below ε_{F} in the majority-spin channel, and in the minority-spin channel of Fe and Co are the so-called virtual bound states. They originate from the hybridization of the atomic d-orbitals of the impurity with the sp-states of the Bi_2Te_3 host, resulting in a fractional valence charge on the impurity (see Table 4.2). Around ε_{F}, states living in the bulk band gap of the host system are observed, we call them "in-gap states". A detailed discussion of these in-gap states is done in Sec. 4.4.

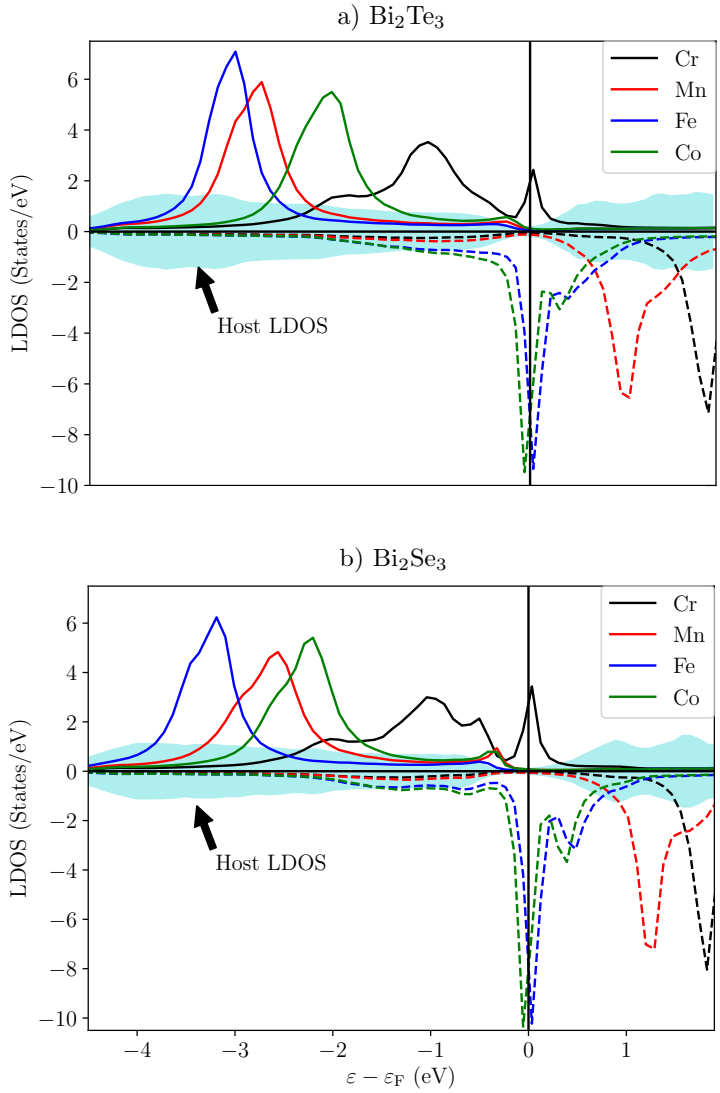

Figure 4.5: a) Spin resolved LDOS for 3d impurities (Cr, Mn, Fe and Co) embedded in Bi_2Te_3 (111) surface at a Bi site from the subsurface layer. The majority-spin channel is represented in full lines, while the minority-spin channel is given in dashed lines. The energies are given with respect to ε_F. The LDOS displays a fully occupied majority-spin channel (except Cr) and a partially occupied minority-spin channel as a function of the filling. The LDOS of the host scaled by a factor five is shown in the background with a light blue. b) Same as in a) but for a Bi_2Se_3 surface.

Element	Q	$M_s(\mu_B)$	$M_l(\mu_B)$
Nb (Bi_2Te_3)	3.488	1.097	-0.143
Nb (Bi_2Se_3)	3.077	0.906	-0.048
Mo (Bi_2Te_3)	4.717	2.678	-0.004
Mo (Bi_2Se_3)	4.316	2.574	-0.093
Tc (Bi_2Te_3)	5.892	2.493	0.202
Tc (Bi_2Se_3)	5.474	2.534	0.079
Ru (Bi_2Se_3)	6.734	0.564	0.378
Pd (Bi_2Se_3)	9.041	0.578	0.135

Table 4.3: Ground state properties of $4d$ impurities embedded in Bi_2Te_3 and in Bi_2Se_3 including the valence charge on the impurity Q, the spin moment M_s and the orbital moment M_l (the negative sign on the orbital moment means that it is antiparallel to M_s).

4.3.2 $4d$ magnetic impurities embedded in Bi_2Te_3 surface

After studying the ground states properties of $3d$ impurities embedded in the Bi_2Te_3 in the previous section, we consider the same setup and dope the system with single $4d$ transition metal impurities instead. The $4d$-orbitals are spatially more extended than the $3d$ ones, therefore, $4d$ impurities have a higher hybridization with the host atoms. Thus, the $4d$ impurities may display very different behaviors depending on the host they are embedded into. We show in Table 4.3 the ground state properties for Nb, Mo and Tc. The $4d$ impurities are all donors. We notice that the number of electrons in Nb changes from 5 to 3.5 due to the strong hybridization with Bi_2Te_3 host, as aforementioned. Also, for Nb the d-shell is less than half filled leading to a spin moment (M_s) antiparallel to the orbital moment (M_l). For Mo and Tc which have a half filled d-shell, they display the highest values for M_s in qualitative agreement with Hund's rules [42].

We show the LDOS for Nb, Mo and Tc in Fig. 4.6a, which displays a sharp $4d$ resonance at ε_F in the majority-spin channel for Nb (full lines), while its minority-spin channel (dashed lines) is flat up to ε_F. The $4d$ resonance in the majority-spin channel shifts downwards for Mo and Tc since the number of electrons increases. We also notice for Mo and Tc that the majority-spin and minority-spin channels are both partially occupied, in contrast to what is observed in $3d$ impurities where the majority-spin channel is always fully occupied. This can be explained by the presence of a stronger exchange splitting in the $3d$ impurities, *i.e.* the $3d$ elements have larger Stoner parameter compared to the $4d$ ones [191].

In addition, we also investigated Rh, Ru and Pd impurities. However, they were found to be nonmagnetic. The analysis of the paramagnetic LDOS shown in Fig. 4.7 reveals that, while moving in the periodic table from Tc towards Pd (adding electrons), the $4d$ resonance is shifted to lower energies leading to a drastic decrease of the LDOS at ε_F. Thus, the Stoner criterion is not fulfilled making Rh, Ru and Pd impurities in Bi_2Te_3 nonmagnetic. Interestingly, the in-gap states are present for both magnetic and nonmagnetic impurities. They are very pronounced for some elements namely Tc, Rh and Pd (The in gap states are located above ε_F for Tc, while in the case of Rh and Pd they are close to ε_F).

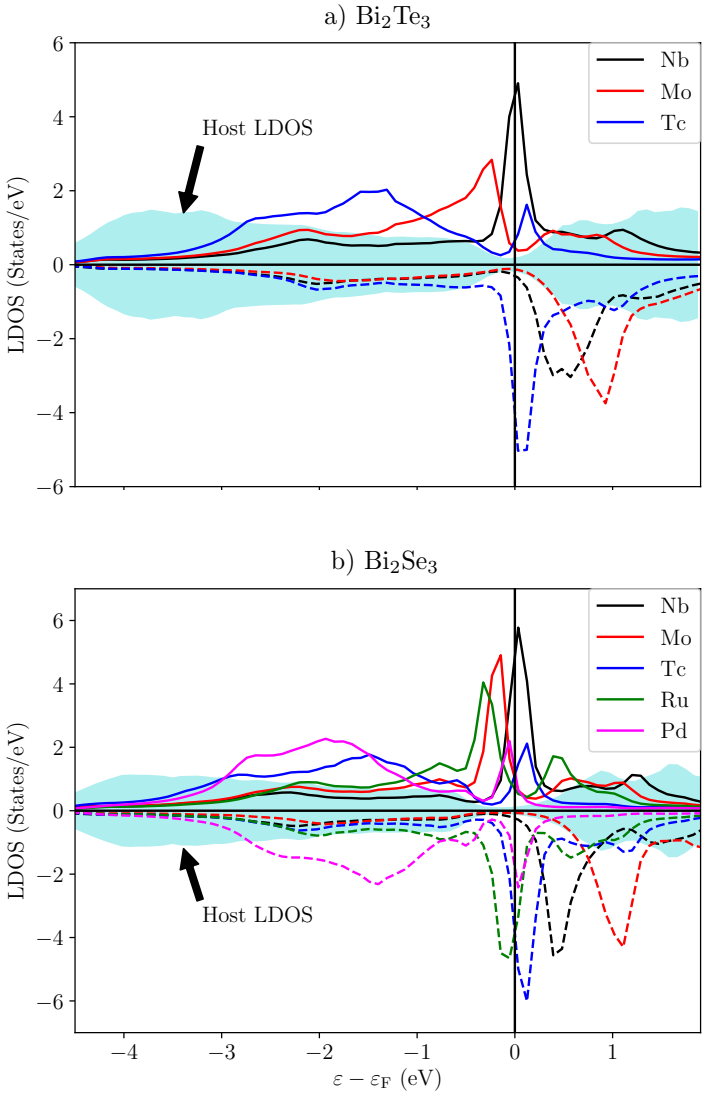

Figure 4.6: a) Spin resolved LDOS for 4d impurities (Nb, Mo, Tc) embedded in Bi_2Te_3 (111) surface at a Bi site from the subsurface layer. The majority channel is represented in full lines, while the minority is given in dashed lines. The energies are given with respect to ε_F. The LDOS displays a partially occupied majority and minority channels due to a weaker exchange splitting compared to the $3d$ impurities. The LDOS of the host scaled by a factor five is shown in the background with a light blue. b) Same as in a) but for a Bi_2Se_3 surface where Ru and Pd are magnetic. Their spin splitting is relatively small explaining the small values for their magnetic moments.

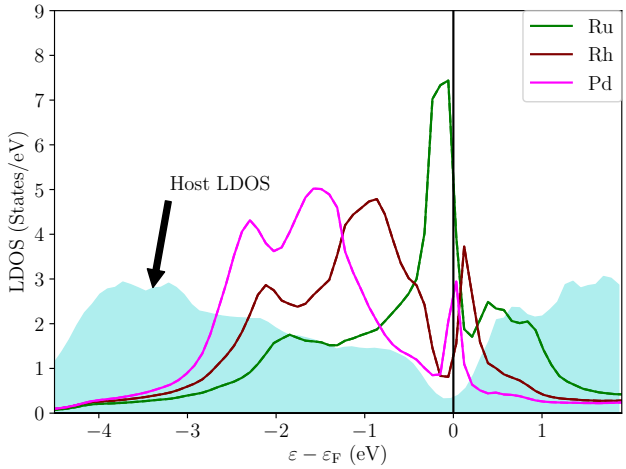

Figure 4.7: Paramagnetic LDOS for nonmagnetic 4d impurities (Ru, Rh, Pd) embedded in Bi_2Te_3 (111) surface at a Bi site from the subsurface layer. The LDOS at ε_F is not high enough to satisfy the Stoner criterion making these elements nonmagnetic. The LDOS of the host scaled by a factor five is shown in the background with a light blue.

4.3.3 $3d$ and $4d$ magnetic impurities embedded in Bi_2Se_3 surface

In order to study the impact of the substrate on the ground state properties of $3d$ and $4d$ single magnetic impurities in topological insulators, we consider a similar setup as in Sec. 4.3.1 but trade Bi_2Te_3 for a Bi_2Se_3 host. Thus, the Te atoms $(5s^2 5p^4)$ are replaced by Se atoms $(4s^2 4p^4)$, note that the lattice parameters are also different. The ground properties for Cr, Mn, Fe and Co in Bi_2Se_3 are shown in Table 4.2. Similarly to the Bi_2Te_3 host, we find that all $3d$ impurities are electron donors. Overall $3d$ impurities donate more electrons and the M_s are slightly changed compared to the Bi_2Te_3 host. However, the orbital moments are more affected, for example M_l for Fe decreased by half compared to the Bi_2Te_3 case. This is because M_l is more sensitive to the details of the hybridization. We also computed the LDOS for these impurities, it is shown in Fig. 4.5b. It displays very similar features compared to the LDOS for $3d$ impurities in Bi_2Te_3. We notice that the occupied $3d$ virtual bound state for the majority-spin channel of Cr is less intense than in Bi_2Te_3, which explains the reduction of its charge compared to the Bi_2Te_3 case.

We now move on to the $4d$ impurities in Bi_2Se_3. The ground state properties are summarized in Table 4.3. Interestingly, Ru and Pd acquire a magnetic moment. This can be explained as follows: Ru and Pd hybridize differently in the Bi_2Se_3 and Bi_2Te_3 hosts. In the former case, the paramagnetic LDOS at ε_F is higher compared to the Bi_2Te_3 case. Thus, the Stoner criterion is satisfied, making Ru and Pd magnetic. Pd is a peculiar case, since it becomes magnetic due to the in-gap state, which provides a high density of states at ε_F. In the Bi_2Te_3 case, the in-gap state was located slightly higher than ε_F as shown in Fig. 4.7, which was not enough to drive Pd to a magnetic state. The magnetic moments

of Ru and Pd are rather small, since the exchange splitting is weak as seen from Fig. 4.6b. As stated earlier, changing the host affects a lot more the ground states properties of $4d$ impurities in contrast to the $3d$ ones, since the $4d$ orbitals hybridize more with the host electrons.

4.4 Investigating the in-gap states

Previously, we have shown the LDOS for $3d$ and $4d$ impurities embedded in Bi_2Te_3 and Bi_2Se_3. Some of the impurities displayed sharp resonances lying within the bulk band gap. They represent in-gap states, these resonances have a spin character and arise due to the hybridization between the impurity and the host states. For the $3d$ elements the in-gap states can be clearly observed in the majority-spin channel since they are located away from the d virtual bound states, while in the minority-spin channel they mix up with the d states as shown in Fig. 4.5a and Fig. 4.5b. For the $4d$ elements, they can be observed for magnetic and nonmagnetic impurities and their presence depends on the chemical nature of the impurity as shown in Fig. 4.6a and Fig. 4.6b.

Interestingly, similar resonances were observed experimentally in Ref. [192] using scanning tunneling spectroscopy (STS) for Co, Ag and Cu impurities deposited on regular metals: for example Ag(111) and Cu(111) surfaces. The in-gap states were located at the bottom of the surface state with a broadening caused by the hybridization with the bulk bands. In-gap states were observed from first principles calculations as well. Indeed in Ref. [193], Lounis et *al.* considered $3d$ and Cu adatoms deposited on a Cu (111) and observed resonances at the bottom of the surface state band in the LDOS. The presence of these peaks is explained by the nature of the impurity potential, and its strength, which can attract or repel electronic states. For metallic systems such as Cu(111) and Ag(111) the resonances were found at the bottom of the surface state band.

In the case of topological insulators, phenomenological models [30, 188] relate the creation of these in-gap states to the presence of topological surface states, our ab-initio simulations demonstrate their existence even in the bulk geometry, ruling out the necessity of the surface states for their creation. We find that these in-gap states can be induced by hybridization with the bulk bands at the bulk band edges or by hybridization with the topological surface state. In order to understand and disentangle the different contributions to the hybridization, we performed calculations for the $3d$ and $4d$ impurities for Bi_2Te_3 and Bi_2Se_3 bulk in addition to the previously discussed surface calculations. Naturally, the impurities are substituting a Bi atom similarly to the surface case. The change in ground state properties namely the charge, spin moments of the impurities is rather small, this can be understood from the fact that the immediate environment of the impurity (nearest neighbors) remains unchanged from surface to bulk. In other words, the topological surface state has a small impact on such properties. A comparison between the ground state properties of $3d$ impurities embedded in Bi_2Te_3 thin film and bulk is shown in Table 4.4.

In Fig. 4.8, we show the LDOS of a magnetic Cr impurity in Bi_2Te_3. This element has been chosen because it presents a very pronounced in-gap state. First, we notice a decrease of ~ 0.1 eV of the bandwidth for the bulk LDOS. This is due to the absence of the hybridization with the surface state. The center of mass of the occupied states seems to move to a lower energy in the bulk case. The in-gap state is still present in the bulk

Element	Q	$M_\mathrm{s}(\mu_\mathrm{B})$	$M_\mathrm{l}(\mu_\mathrm{B})$
$\mathrm{Cr_s}$	5.154	3.843	0.065
$\mathrm{Cr_b}$	5.266	3.823	0.057
$\mathrm{Mn_s}$	6.160	4.412	0.050
$\mathrm{Mn_b}$	6.277	4.335	0.061
$\mathrm{Fe_s}$	7.282	3.395	0.260
$\mathrm{Fe_b}$	7.405	3.294	0.248
$\mathrm{Co_s}$	8.448	2.108	0.883
$\mathrm{Co_b}$	8.571	1.977	0.675

Table 4.4: Ground state properties of $3d$ impurities embedded in Bi_2Te_3 thin film (subscript s) and in Bi_2Te_3 bulk (subscript b), Q is the valence charge on the impurity, M_s is the spin moment and M_l is the orbital moment.

geometry, which means that it is originating from the hybridization with the bulk bands. A detailed analysis of the lm-resolved LDOS shows that the in-gap state is observed in the $\{d_{xy}, d_{x^2-y^2}, d_{xz}, d_{yz}\}$ components of the d orbitals, but not in the d_{z^2} one. Furthermore, the magnetic moment of the impurity is along the z-direction and the C_{3v} symmetry is conserved, which leads to a degeneracy between the $\{d_{xy}, d_{x^2-y^2}\}$ components. The $\{d_{xz}, d_{yz}\}$ components are also degenerate. In the next section, we will discuss the emergence of the in-gap states by means of a simple impurity Anderson model including a bulk gapped band and a topological surface state.

4.5 Anderson model for the in-gap states

In order to explain the origin of the in-gap states observed in the LDOS of a Cr impurity embedded in Bi_2Te_3 (see Fig. 4.8), we use a simple Anderson impurity model. As stated earlier, the in-gap states arise from the hybridization between the d-states of the impurity and the sp-states of the host. Our goal is to understand if and how the hybridization with both bulk and surface states leads to the in-gap states. We consider a minimal model to interpret our first principles calculations, which takes into account an impurity with a single d-orbital (as an example we chose the d_{xy} component). It has two energy levels $\varepsilon_i^{\uparrow}$ and $\varepsilon_i^{\downarrow}$ for the majority and minority spin channels, respectively. This impurity hybridizes with a two dimensional topological insulator surface state, which is characterized by a linear Dirac Hamiltonian, as discussed in Sec. 4.1:

$$\boldsymbol{H}_\mathrm{D} = \hbar\, v_\mathrm{F} \left(\vec{\boldsymbol{\sigma}} \times \vec{k}\right)_z \quad . \tag{4.10}$$

$\boldsymbol{H}_\mathrm{D}$ has the following eigenvalues $\varepsilon_{\vec{k}}^{\pm} = \pm\hbar v_\mathrm{F}\, k$. To account for the bulk bands, we included bulk Bloch states also characterized by the wave vector $\vec{k}$ with the eigenenergies $\varepsilon_{\vec{k}}^{\sigma}$ for each spin channel. The bulk and surface states interact only via the impurity. Thus,

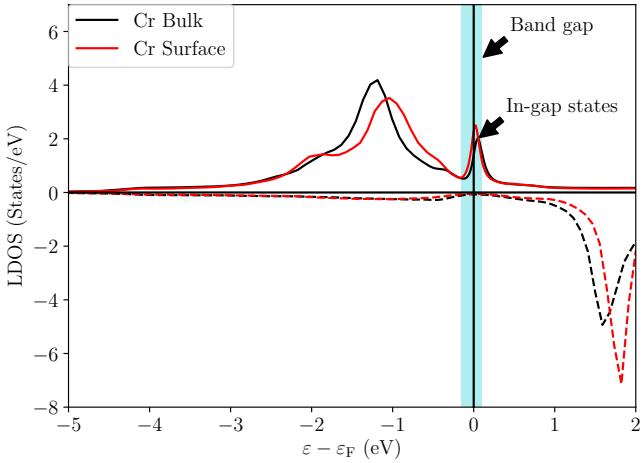

Figure 4.8: Comparison between the spin resolved LDOS of a Cr impurity embedded in Bi_2Te_3 (111) surface (Bi site subsurface layer) and Bi_2Te_3 bulk (Bi site). The majority band is represented in full lines, while the minority is given in dashed lines. The energies are given with respect to ε_F. The in-gap states are present in surface and bulk calculations. The band gap is highlighted with a light blue background.

our system is characterized by a (6×6) Hamiltonian:

$$H_i = \begin{pmatrix} \varepsilon_i^{\uparrow} & 0 & V^{s}_{\vec{k}i} & V^{s}_{\vec{k}i} & V^{b}_{\vec{k}i} & V^{b}_{\vec{k}i} \\ 0 & \varepsilon_i^{\downarrow} & V^{s}_{\vec{k}i} & V^{s}_{\vec{k}i} & V^{b}_{\vec{k}i} & V^{b}_{\vec{k}i} \\ \left(V^{s}_{\vec{k}'i}\right)^* & \left(V^{s}_{\vec{k}'i}\right)^* & 0 & \hbar v_F(k_y + ik_x) & 0 & 0 \\ \left(V^{s}_{\vec{k}'i}\right)^* & \left(V^{s}_{\vec{k}'i}\right)^* & \hbar v_F(k_y - ik_x) & 0 & 0 & 0 \\ \left(V^{b}_{\vec{k}'i}\right)^* & \left(V^{b}_{\vec{k}'i}\right)^* & 0 & 0 & \varepsilon^{\uparrow}_{\vec{k}} & 0 \\ \left(V^{b}_{\vec{k}'i}\right)^* & \left(V^{b}_{\vec{k}'i}\right)^* & 0 & 0 & 0 & \varepsilon^{\downarrow}_{\vec{k}} \end{pmatrix} . \tag{4.11}$$

$V^{b}_{\vec{k}i}$ ($V^{s}_{\vec{k}i}$) represents the coupling of the impurity to the bulk (surface) state. In order to access the impurity LDOS, we compute the local Green function given by:

$$\boldsymbol{G}_i^{\sigma}(\varepsilon) = \frac{1}{\varepsilon - \varepsilon_i^{\sigma} - \Sigma_i^{b}(\varepsilon) - \Sigma_i^{s}(\varepsilon)} \quad , \tag{4.12}$$

where $\Sigma_i^{b}(\varepsilon)$ and $\Sigma_i^{s}(\varepsilon)$ represent the hybridization function for the bulk and surface states, respectively. Using the local Green function, the LDOS $n(\varepsilon)$ is computed as:

$$n(\varepsilon) = -\frac{1}{\pi} \frac{\Delta_b(\varepsilon) + \Delta_s(\varepsilon)}{(\varepsilon - \varepsilon_i^{\sigma} - \Lambda_b(\varepsilon) - \Lambda_s(\varepsilon))^2 + (\Delta_b(\varepsilon) + \Delta_s(\varepsilon))^2} \quad . \tag{4.13}$$

$\Delta_{\rm b}(\varepsilon)$ ($\Delta_{\rm s}(\varepsilon)$) is the imaginary part of the bulk (surface) hybridization function, while $\Lambda_{\rm b}(\varepsilon)$ ($\Lambda_{\rm s}(\varepsilon)$) is the real part of the bulk (surface) hybridization function. The in-gap states are expected to occur when $\varepsilon - \varepsilon_i^\sigma - \Lambda_{\rm b}(\varepsilon) - \Lambda_{\rm s}(\varepsilon) = 0$ and for $(\Delta_{\rm b}(\varepsilon) + \Delta_{\rm s}(\varepsilon))$ small. For the present element, the in gap states shown in Fig. 4.8 are weakly affected when the Cr impurity is moved from the bulk to the surface. In other words, the coupling to the surface is rather small, thus, both $\Lambda_{\rm s}(\varepsilon)$ and $\Delta_{\rm s}(\varepsilon)$ are small.

First, we model the bulk band with a gapped density of states $n_{\rm b}(\varepsilon)$ given by:

$$n_{\rm b}(\varepsilon) = \begin{cases} n_{\rm b} & \text{for} \quad \varepsilon_{\rm bv} < \varepsilon < \varepsilon_{\rm tv} \quad , \\ n_{\rm b} & \text{for} \quad \varepsilon_{\rm bc} < \varepsilon < \varepsilon_{\rm tc} \quad , \\ 0 & \text{elsewhere} \quad . \end{cases} \tag{4.14}$$

$n_{\rm b}$ is the occupation number in the valence and conduction band. $\varepsilon_{\rm bv}$ ($\varepsilon_{\rm bc}$) and $\varepsilon_{\rm tv}$ ($\varepsilon_{\rm tc}$) represent the bottom and the top of the valence (conduction) band, respectively. The energies corresponding to the bottom of the valence and the top of the conduction are cutoffs for numerical convenience (not realistic values). $\Sigma_i^{\rm b}(\varepsilon)$ can be computed analytically assuming that $V_{\vec{k}i}^{\rm b}$ depends only weakly on $\vec{k}$:

$$\begin{aligned} \Sigma_i^{\rm b}(\varepsilon + {\rm i}\eta) &= \sum_{\vec{k}} \frac{|V_{\vec{k}i}^{\rm b}|^2}{\varepsilon - \varepsilon_{\vec{k}} + {\rm i}\eta} \quad , \\ &= |\langle V_{\vec{k}i}^{\rm b}\rangle|^2 \sum_{\vec{k}} \frac{1}{\varepsilon - \varepsilon_{\vec{k}} + {\rm i}\eta} \quad , \\ &= \Lambda_{\rm b}(\varepsilon) + {\rm i}\,\Delta_{\rm b}(\varepsilon) \quad . \end{aligned} \tag{4.15}$$

Then, the real and imaginary parts of $\Sigma_i^{\rm b}(\varepsilon + {\rm i}\eta)$ read:

$$\Lambda_{\rm b}(\varepsilon + {\rm i}\eta) = -\frac{n_{\rm b}|\langle V_{\vec{k}i}^{\rm b}\rangle|^2}{2} \left[\ln\left(\frac{(\varepsilon - \varepsilon_{\rm tv})^2 + \eta^2}{(\varepsilon - \varepsilon_{\rm bv})^2 + \eta^2}\right) + \ln\left(\frac{(\varepsilon - \varepsilon_{\rm tc})^2 + \eta^2}{(\varepsilon - \varepsilon_{\rm bc})^2 + \eta^2}\right)\right] \quad . \tag{4.16}$$

$$\begin{aligned} \Delta_{\rm b}(\varepsilon + {\rm i}\eta) = {} & n_{\rm b}|\langle V_{\vec{k}i}^{\rm b}\rangle|^2 \left[\arctan\left(\frac{\varepsilon - \varepsilon_{\rm tv}}{\eta}\right) - \arctan\left(\frac{\varepsilon - \varepsilon_{\rm bv}}{\eta}\right)\right] \\ & + n_{\rm b}|\langle V_{\vec{k}i}^{\rm b}\rangle|^2 \left[\arctan\left(\frac{\varepsilon - \varepsilon_{\rm tc}}{\eta}\right) - \arctan\left(\frac{\varepsilon - \varepsilon_{\rm bc}}{\eta}\right)\right] \quad . \end{aligned} \tag{4.17}$$

The bulk hybridization function is shown in Fig. 4.9. The parameters used in the model to qualitatively reproduce the position and the width of the d_{xy} peak are given in Table 4.5. We also show in Fig. 4.9 the majority LDOS for the Cr impurity since it is where the in-gap states are visible in the first principles calculations. Indeed, we observe in-gap states at the bulk band edges. This is to be expected and can be seen from the real part of the hybridization function. However, they seem to emerge from the lower band edge in contrast to what is observed from first principles as shown in Fig. 4.8.

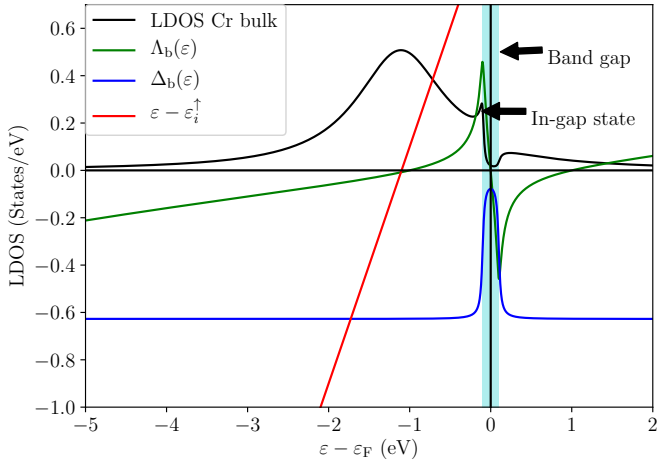

Figure 4.9: The black curve represents the majority LDOS of Cr in Bi_2Te_3 within the Anderson model. The green and blue curves represent the real and imaginary parts of the bulk hybridization function, respectively. The red line represents $\varepsilon - \varepsilon_i^\uparrow$, where $\varepsilon_i^\uparrow$ is the energy level of the majority spin channel. The light blue background indicates the gap region. The model parameters are given in Table 4.5.

Element	$\varepsilon_i^\uparrow$	ε_{bv}	ε_{tv}	ε_{bc}	ε_{tc}	n_b	$V_{\vec{k}i}^b$	η
Cr	-1.10	-10	-0.1	0.1	10	0.15	1.15	0.02

Table 4.5: Anderson model parameters used to compute the bulk hybridization function and for majority LDOS of Cr. η is an artificial broadening added to mimic the small imaginary part of the energy included in the first principles simulations. All the parameters are given in eV except n_b which is given in states/eV.

We now investigate the contribution of the topological surface state described by the Dirac Hamiltonian $\boldsymbol{H}_D$. Its hybridization with the impurity is characterized by the function $\Sigma_i^s(\varepsilon)$, which can be estimated assuming that the LDOS of the surface states is linear within a certain energy window and is then connected to the flat bulk bands, which is needed to avoid spurious peaks in $\Lambda_s(\varepsilon)$ at $\varepsilon = \pm\varepsilon_0$:

$$n_s(\varepsilon) = \begin{cases} \frac{|\varepsilon|}{\varepsilon_0^2} & \text{for} \quad -\varepsilon_0 < \varepsilon < \varepsilon_0 \quad , \\ \frac{1}{\varepsilon_0} & \text{for} \quad \varepsilon_{tv} < \varepsilon < -\varepsilon_0 \quad , \\ \frac{1}{\varepsilon_0} & \text{for} \quad \varepsilon_0 < \varepsilon < \varepsilon_{tc} \quad , \\ 0 & \text{elsewhere} \quad . \end{cases} \tag{4.18}$$

ε_0 is the cutoff energy determining where the linear dispersion ends. When assuming that

$V^{\mathrm{s}}_{\vec{k}i}$ depends weakly on $\vec{k}$ then the real part of $\Sigma^{\mathrm{s}}_i(\varepsilon)$ is given by:

$$\begin{aligned}\Lambda_{\mathrm{s}}(\varepsilon+\mathrm{i}\eta) = &\frac{|\langle V^{\mathrm{s}}_{\vec{k}i}\rangle|^2\varepsilon}{2\varepsilon_0^2}\left[\ln\left(\frac{\varepsilon^2+\eta^2}{(\varepsilon+\varepsilon_0)^2+\eta^2}\right)-\ln\left(\frac{(\varepsilon-\varepsilon_0)^2+\eta^2}{\varepsilon^2+\eta^2}\right)\right]\\ &+\frac{|\langle V^{\mathrm{s}}_{\vec{k}i}\rangle|^2\eta}{\varepsilon_0^2}\left[2\arctan\left(\frac{\varepsilon}{\eta}\right)-\arctan\left(\frac{\varepsilon+\varepsilon_0}{\eta}\right)-\arctan\left(\frac{\varepsilon-\varepsilon_0}{\eta}\right)\right]\\ &-\frac{|\langle V^{\mathrm{s}}_{\vec{k}i}\rangle|^2}{2\varepsilon_0}\left[\ln\left(\frac{(\varepsilon+\varepsilon_0)^2+\eta^2}{(\varepsilon-\varepsilon_{\mathrm{bv}})^2+\eta^2}\right)+\ln\left(\frac{(\varepsilon-\varepsilon_{\mathrm{tc}})^2+\eta^2}{(\varepsilon-\varepsilon_0)^2+\eta^2}\right)\right] \quad .\end{aligned} \tag{4.19}$$

And the imaginary part reads:

$$\begin{aligned}\Delta_{\mathrm{s}}(\varepsilon+\mathrm{i}\eta) = &\frac{|\langle V^{\mathrm{s}}_{\vec{k}i}\rangle|^2\eta}{2\varepsilon_0^2}\left[\ln\left(\frac{\varepsilon^2+\eta^2}{(\varepsilon+\varepsilon_0)^2+\eta^2}\right)-\ln\left(\frac{(\varepsilon-\varepsilon_0)^2+\eta^2}{\varepsilon^2+\eta^2}\right)\right]\\ &+\frac{|\langle V^{\mathrm{s}}_{\vec{k}i}\rangle|^2\varepsilon}{\varepsilon_0^2}\left[2\arctan\left(\frac{\varepsilon}{\eta}\right)-\arctan\left(\frac{\varepsilon+\varepsilon_0}{\eta}\right)-\arctan\left(\frac{\varepsilon-\varepsilon_0}{\eta}\right)\right]\\ &+\frac{|\langle V^{\mathrm{s}}_{\vec{k}i}\rangle|^2}{\varepsilon_0}\left[\arctan\left(\frac{\varepsilon+\varepsilon_0}{\eta}\right)-\arctan\left(\frac{\varepsilon-\varepsilon_{\mathrm{bv}}}{\eta}\right)\right]\\ &+\frac{|\langle V^{\mathrm{s}}_{\vec{k}i}\rangle|^2}{\varepsilon_0}\left[\arctan\left(\frac{\varepsilon-\varepsilon_{\mathrm{tc}}}{\eta}\right)-\arctan\left(\frac{\varepsilon-\varepsilon_0}{\eta}\right)\right] \quad .\end{aligned} \tag{4.20}$$

For simplicity these equations have been derived assuming that the Dirac point is located at $\varepsilon_{\mathrm{D}} = 0$. The expression for a finite ε_{D} can be obtained by replacing ε with $\varepsilon - \varepsilon_{\mathrm{D}}$ in Eqs. (4.19) and (4.20). If we consider Eq. (4.13) only in the presence of the topological surface state, then to obtain an in-gap state: $\varepsilon - \varepsilon_i^{\uparrow} = \Lambda_{\mathrm{s}}(\varepsilon)$ and $\Delta_{\mathrm{s}}(\varepsilon)$ must be small. *i.e* $\Lambda_{\mathrm{s}}(\varepsilon)$ and $\varepsilon - \varepsilon_i^{\uparrow}$ must intersect near ε_{D}. We take the example of a coupling to the surface state $V^{\mathrm{s}}_{\vec{k}i} = 0.25$ eV (smaller compared to the bulk one since the coupling to the surface is rather small) and plot in Fig. 4.10 the real and imaginary parts of $\Sigma^{\mathrm{s}}_i(\varepsilon)$ and $\varepsilon - \varepsilon_i^{\uparrow}$. The crossing near ε_{D} leading to an in-gap state is not observed for this particular case. It can occur for strong coupling constants, but this goes against what is observed from first principles, where obviously the coupling to the surface state is not strong enough to create in-gap states.

Element	$\varepsilon_i^{\uparrow}$	$\varepsilon_{\mathrm{bv}}$	$\varepsilon_{\mathrm{tc}}$	ε_0	$V^{\mathrm{s}}_{\vec{k}i}$	ε_{D}	η
Cr	-1.10	-10	10	0.3	0.25	0.2	0.02

Table 4.6: Anderson model parameters used to compute the surface hybridization function, and center of the majority spin channel of Cr. We used the same η as in to the bulk case. All the parameters are given in eV.

The model qualitatively reproduces the in-gap state observed from first-principles, which originates from the coupling to the bulk band edges. A very important outcome of the model is that the presence of the in-gap states requires that the impurity d-peak should be close to the band gap edges, this ensures the presence of electrons that will be localized at the band edges (example: majority spin channel of Co, Mn and Fe in Bi_2Te_3).

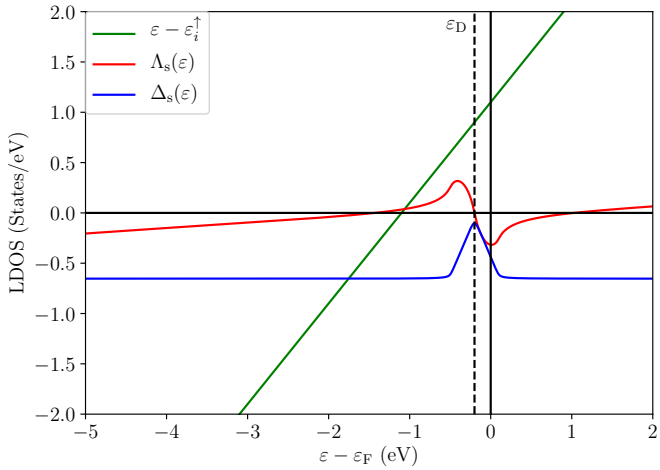

Figure 4.10: The red and blue curves represent the real and imaginary parts of the surface hybridization function, respectively. While the green curve shows $\varepsilon - \varepsilon_i^{\uparrow}$. The Dirac point is located at $\varepsilon_D = -0.2$ eV. The used model parameters are given in Table 4.6.

However, a d-peak located too close to the band edges will induce in-gap states but those will be merged with the d-peaks (example: minority spin channel of Fe and Co in Bi_2Te_3). That explains why Cr is the best choice to observe these in-gap states decoupled from the usual virtual bound states.

4.6 Magnetocrystalline anisotropy

We now discuss the magnetocrystalline anisotropy energy (MAE) for $3d$ and $4d$ impurities embedded Bi_2Te_3 using a setup similar to Sec. 4.3.1. As mentioned earlier, the sign of the MAE was invoked as an ingredient to functionalize the topological surface state by opening a gap if the magnetic moments are perpendicular to the surface. Also the exploration of the magnetic stability and manipulation of their spin hinge on the MAE. We apply three different methods to extract the MAE. The magnetic moments are self-consistently converged along z-axis in all the methods. First, we use band energy differences relying on the magnetic force theorem discussed in Sec. 2.5.1: a one shot calculation where the magnetic moments are rotated to the x-axis is performed, the anisotropy is obtained from the band energy difference for the two magnetic configurations. Second, the torque method, the details are discussed in Sec. 2.5.2 we compute the magnetic torque for two deviation angles 45° (away from self-consistency) and 5° (near self-consistency) from the z-axis. Finally, we extract the MAE from the static magnetic susceptibility obtained from TD-DFT mapped into the phenomenological LLG equation (see Sec. 2.6.4).

We compare the three different methods and discuss the validity of the magnetic force theorem for the considered impurities, then we study the behavior of MAE with respect

to the real space cluster size. We also computed the MAE of the impurities embedded in a Bi_2Se_3 surface. Finally, we explore the impact of the topological surface state by comparing the MAE obtained for the same impurities embedded in the bulk and in the surface.

4.6.1 Magnetocrystalline anisotropy for $3d$ and $4d$ impurities in Bi_2Te_3

The MAE shown in Fig. 4.11a for Cr, Mn, Fe and Co is obtained using the different methods mentioned previously. Cr and Fe present an in-plane magnetic anisotropy, *i.e.* $\mathcal{K} = \varepsilon_{\text{band}}(\vec{M}_{\text{s}} \parallel z) - \varepsilon_{\text{band}}(\vec{M}_{\text{s}} \parallel x) > 0$, while for Mn and Co the easy axis is out-of-plane ($\mathcal{K} < 0$). Mn displays a small MAE, this can be understood when using the so-called Bruno formula [107], where the magnetic anisotropy is related to the orbital moment. In our sign convention: $\mathcal{K} \propto -\zeta^2 \left(M_{\text{l}}^z - M_{\text{l}}^x\right)$. ζ represents the spin-orbit interaction constant for the magnetic atom and M_{l}^z (M_{l}^x) is the value of the orbital moment when the spin moment points along the z-axis (x-axis). From this formula, one expects a low MAE when the orbital moment is small. Also, the spin moment should preferably point along the direction maximizing the orbital moment. Thus, Cr and Mn are expected to have a weak MAE since they exhibit small orbital moments (as shown in Table 4.2). However, in the case of Cr, the MAE is around ~ 1 meV in disagreement with Bruno's formula. Fe and Co display large orbital moments resulting in a relatively large MAE. The direction of the easy axis for Fe and Co can also be explained using Bruno's formula, since Fe (Co) displays a larger orbital moment when the spin moment is in-plane (out-of-plane) as shown in Fig. 4.12a. Moreover, Fig. 4.11a also shows that the four different calculations are in good agreement for Cr and Mn, however, for Fe and Co, $\mathcal{K}_{\text{Torque}(45^\circ)}$ and $\mathcal{K}_{\text{Eband}}$ differs from $\mathcal{K}_{\text{Torque}(5^\circ)}$ and $\mathcal{K}_{\text{Susc}}$ by a few meV's.

In order to explain these differences, we show in Fig. 4.12a the change in the ground state properties of the impurity upon 90° rotation of the magnetic moment ($z \rightarrow x-$axis) for the considered $3d$ impurities (one shot calculation). There is a large change in the charge and spin moment for Fe and Co compared to Cr and Mn. This can be traced back to the LDOS. Indeed, Fe and Co display a high LDOS at ε_{F}, thus, a rotation of the magnetic moments leads to change in the position of the $3d$ peak around ε_{F} causing a large change in the charge (*i.e.* in the density). The latter one violates the assumptions justifying the magnetic force theorem (in the frozen potential approximation). Similar effects where observed for Co adatoms deposited on a Cu(111) surface in Ref. [194]. This indicates that one has to be careful with the magnitude of the rotation angle used to extract the MAE. Thus, a small deviation angle should be considered. Furthermore, the use of the torque method implicitly including the Lloyd's formula (see Sec. 2.4.4) with a small deviation angle corrects for such errors. One can show that the magnetic susceptibility includes such corrections as well. Indeed, $\mathcal{K}_{\text{Susc}}$ and $\mathcal{K}_{\text{Torque}(5^\circ)}$ can be connected. One can derive a formula for the torque following the same steps as in Sec. 2.5.2 but considering that the easy axis is along the z-direction and assuming a small rotation angle θ in the (xz)-plane,

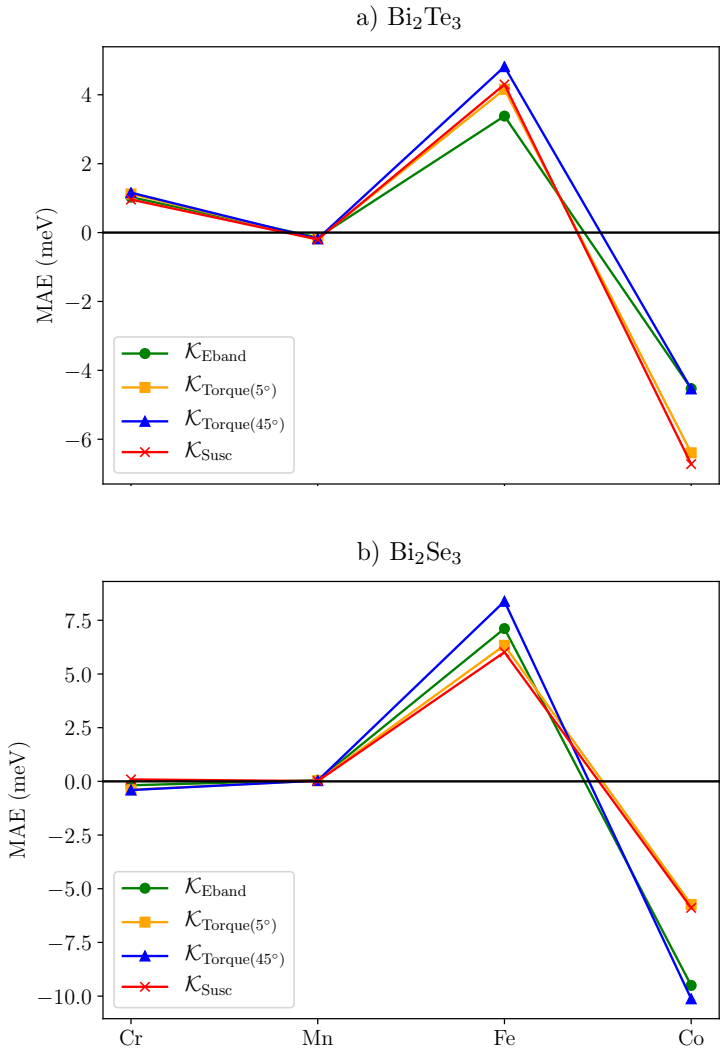

Figure 4.11: a) Comparison of the MAE for $3d$ impurities embedded in Bi_2Te_3 (111) surface at a Bi site from the subsurface layer. The green curve is obtained using the band energy differences (90° rotation of the spin moment). The orange curve is obtained using the torque method with the spin moment tilted 5° away from the z-axis. The blue curve is obtained using the torque method with the spin moment tilted 45° away from the z-axis. The red curve is obtained from the static part of the magnetic susceptibility (linear response). b) Same as in a) but for a Bi_2Se_3 surface. For Cr the easy axis of changed from in-plane to out-of-plane.

then the torque reads:

$$\begin{aligned} T_\theta &= \frac{\partial \varepsilon_{\text{band}}}{\partial \theta} \quad , \\ &= -\frac{1}{\pi} \,\text{Im}\,\text{Tr}_\sigma \int_{-\infty}^{\varepsilon_\text{F}} \mathrm{d}\varepsilon \,(\varepsilon - \varepsilon_\text{F}) \,\frac{\partial \boldsymbol{G}(\varepsilon)}{\partial \theta} \quad . \end{aligned} \tag{4.21}$$

The first order derivative of the Green function can be expressed using the Kohn-Sham Hamiltonian (see Sec.2.5.2):

$$\frac{\partial \boldsymbol{G}(\varepsilon)}{\partial \theta} = \boldsymbol{G}(\varepsilon) \,\frac{\partial \boldsymbol{H}_\text{KS}}{\partial \theta} \,\boldsymbol{G}(\varepsilon) \quad . \tag{4.22}$$

Assuming that the length of $\vec{B}_\text{xc}$ remains unchanged upon a rotation with a small angle θ, $\boldsymbol{H}_\text{KS}$ and θ are simply related via:

$$\begin{aligned} \boldsymbol{H}_\text{KS} &= H_0 \,\mathbb{1}_2 + B_\text{xc} \,\vec{\boldsymbol{\sigma}} \cdot \vec{e}_M \quad . \\ &= H_0 \,\mathbb{1}_2 + B_\text{xc} \,\boldsymbol{\sigma}_x \sin\theta + B_\text{xc} \,\boldsymbol{\sigma}_z \cos\theta \quad . \end{aligned} \tag{4.23}$$

H_0 is the part of the Hamiltonian which is independent of θ. Using Eq. (4.23), we can compute the first order derivative of $\boldsymbol{H}_\text{KS}$ according to θ:

$$\frac{\partial \boldsymbol{H}_\text{KS}}{\partial \theta} = B_\text{xc} \,\left[\boldsymbol{\sigma}_x \cos\theta - \boldsymbol{\sigma}_z \sin\theta\right] \quad . \tag{4.24}$$

When combining the previous equation with Eq. (4.21) and Eq. (4.22), we obtain the following expression for the torque:

$$\begin{aligned} T_\theta &= -\frac{1}{\pi} \,\text{Im}\,\text{Tr}_\sigma \int_{-\infty}^{\varepsilon_\text{F}} \mathrm{d}\varepsilon \,(\varepsilon - \varepsilon_\text{F}) \,B_\text{xc} \,\boldsymbol{G}(\varepsilon) \,\left[\boldsymbol{\sigma}_x \cos\theta - \boldsymbol{\sigma}_z \sin\theta\right] \boldsymbol{G}(\varepsilon) \quad . \\ &= -\frac{1}{\pi} \,\text{Im}\,\text{Tr}_\sigma \int_{-\infty}^{\varepsilon_\text{F}} \mathrm{d}\varepsilon \,B_\text{xc} \,\left[\boldsymbol{G}(\varepsilon) \,\boldsymbol{\sigma}_x \cos\theta - \boldsymbol{G}(\varepsilon) \,\boldsymbol{\sigma}_z \sin\theta\right] \quad . \end{aligned} \tag{4.25}$$

The previous expression was obtained after performing a partial integration as done in Sec. 2.5.2. When considering a small rotation angle, then $\boldsymbol{G}(\varepsilon)$, *i.e.* the Green function for the rotated $\vec{B}_\text{xc}$ can be related to the unperturbed Green function $\boldsymbol{G}_0(\varepsilon)$ of the system where $\vec{B}_\text{xc}$ points along the z-axis via:

$$\boldsymbol{G}(\varepsilon) \approx \boldsymbol{G}_0(\varepsilon) + \boldsymbol{G}_0(\varepsilon) \,\Delta\vec{B}_\text{xc} \cdot \vec{\boldsymbol{\sigma}} \,\boldsymbol{G}_0(\varepsilon) \quad . \tag{4.26}$$

$\Delta\vec{B}_\text{xc}$ is given by:

$$\begin{aligned} \Delta\vec{B}_\text{xc} &= B_\text{xc} \,\left(\sin\theta, 0, \cos\theta - 1\right) \quad , \\ &\approx B_\text{xc} \,\left(\theta, 0, -\frac{\theta^2}{2}\right) \quad . \end{aligned} \tag{4.27}$$

The last expression from the previous equation was obtained assuming that the rotation angle θ is small. We now replace $\boldsymbol{G}(\varepsilon)$ in Eq. (4.25) by its expression in Eq. (4.26), we

also expand $\cos\theta$ and $\sin\theta$ for θ small and retain only the linear terms:

$$\begin{aligned} T_\theta &= -\frac{1}{\pi}\,\mathrm{Im}\,\mathrm{Tr}_\sigma \int_{-\infty}^{\varepsilon_\mathrm{F}} \mathrm{d}\varepsilon\, B_\mathrm{xc}\left[\boldsymbol{\sigma}_x\,\boldsymbol{G}_0(\varepsilon)\,\boldsymbol{\sigma}_x\,\boldsymbol{G}_0(\varepsilon)\,B_\mathrm{xc} - \boldsymbol{\sigma}_z\,\boldsymbol{G}_0(\varepsilon)\right]\theta \quad . \\ &= B_\mathrm{xc}\,\left[\chi^0_{xx}(0)\,B_\mathrm{xc} - M_z\right]\,\theta \quad . \end{aligned} \tag{4.28}$$

$\chi^0_{xx}(0)$ is the static Kohn-Sham magnetic susceptibility defined in Eq. (2.108) and M_z is the length of the magnetic moment in the z-direction when $B_\mathrm{xc} \parallel z$-axis. Using the definition of the spin-flip magnetic susceptibility given in Eq. (2.116) in the static limit (*i.e.* $\chi^0_{xy}(0) = \chi^0_{yx}(0) = 0$) and that x and y-directions are equivalent (uniaxial system), the torque reads:

$$T_\theta = B_\mathrm{xc}\,\left[2\,\chi^0_{+-}(0)\,B_\mathrm{xc} - M_z\right]\,\theta \quad . \tag{4.29}$$

The transversal exchange-correlation kernel $K^\mathrm{xc}_\perp$ and B_xc are related via:

$$B_\mathrm{xc} = \frac{K^\mathrm{xc}_\perp M_\mathrm{z}}{2} \quad \text{with} \quad K^\mathrm{xc}_\perp = \left(\chi^0_{+-}(0)\right)^{-1} - \chi^{-1}_{+-}(0) \quad . \tag{4.30}$$

Relying on the previous equations, we can then express T_θ in terms of the static magnetic susceptibilities (Kohn-Sham and enhanced) as:

$$T_\theta = -\frac{M_z^2}{2}\,\left[\chi^{-1}_{+-}(0) - \chi^0_{+-}(0)\,\chi^{-2}_{+-}(0)\right]\,\theta \quad . \tag{4.31}$$

$\chi_{+-}(0)$ is the static magnetic susceptibility obtained from TD-DFT, which can be related to $\mathcal{K}_\mathrm{Susc}$ via $\chi_{+-}(0) = \frac{M_z^2}{4\mathcal{K}_\mathrm{Susc}}$ (see Sec. 2.6.4). Thus, we can now write T_θ in terms of $\mathcal{K}_\mathrm{Susc}$ as:

$$T_\theta = -\left(2\mathcal{K}_\mathrm{Susc} - \frac{8\chi^0_{+-}(0)\mathcal{K}^2_\mathrm{Susc}}{M_z^2}\right)\theta \quad . \tag{4.32}$$

The torque T_θ can also be written as:

$$\begin{aligned} T_\theta &= \frac{\partial \varepsilon_\mathrm{int}}{\partial\theta} \quad \text{and} \quad \varepsilon_\mathrm{int} = \mathcal{K}_{\mathrm{Torque}(5^\circ)}\,\cos^2\theta \quad . \\ &= -2\,\mathcal{K}_{\mathrm{Torque}(5^\circ)}\,\sin\theta\cos\theta \quad . \end{aligned} \tag{4.33}$$

After expanding for a small angle T_θ reads:

$$T_\theta = -2\,\mathcal{K}_{\mathrm{Torque}(5^\circ)}\,\theta \quad . \tag{4.34}$$

When comparing Eq. (4.32) and Eq. (4.34), we establish a relation between $\mathcal{K}_{\mathrm{Torque}(5^\circ)}$ and $\mathcal{K}_\mathrm{Susc}$:

$$\begin{aligned} \mathcal{K}_\mathrm{Susc} &= \frac{\mathcal{K}_{\mathrm{Torque}(5^\circ)}}{\left(1 - \frac{4\chi^0_{+-}(0)\mathcal{K}_\mathrm{Susc}}{M_z^2}\right)} \quad , \\ &\sim \frac{\mathcal{K}_{\mathrm{Torque}(5^\circ)}}{\left(1 + \frac{B^\mathrm{a}}{B_\mathrm{xc}}\right)} \quad . \end{aligned} \tag{4.35}$$

$B^{\mathrm{a}} = -\frac{2\mathcal{K}_{\mathrm{Susc}}}{M_z}$ is the anisotropy field given in Eq. (2.131) and $B_{\mathrm{xc}} \sim \frac{M_z}{2\chi^0_{+-}(0)}$ (see Eq. (2.122)). $\mathcal{K}_{\mathrm{Susc}}$ and $\mathcal{K}_{\mathrm{Torque}(5^\circ)}$ are close to each other since when evaluating $\mathcal{K}_{\mathrm{Susc}}$, one considers a small perturbation with respect to the initial state. However, $\mathcal{K}_{\mathrm{Susc}}$ is a renormalized quantity as shown in Eq. (4.35), if the renormalization is important $\mathcal{K}_{\mathrm{Susc}}$ and $\mathcal{K}_{\mathrm{Torque}(5^\circ)}$ may differ. Using the torque method at 5° is more reliable than the band energy based method. But one has to be careful when comparing with experimental measurements. In our view, $\mathcal{K}_{\mathrm{Susc}}$ and $\mathcal{K}_{\mathrm{Torque}(5^\circ)}$ should be used when comparing to possible future ISTS experiments. Since in such experiments the deviation of the magnetic moment from its easy axis are rather small. The renormalization of the MAE shown in Eq. (4.35) is similar to the one observed for magnetic interactions when they are computed from the magnetic susceptibility [195, 196].

We now move on to discuss the MAE for $4d$ impurities, the MAE for Nb, Mo and Tc is shown in Fig. 4.13a. All the $4d$ elements display an in-plane magnetic anisotropy. Nb has a rather large MAE. Once more, the small value of the orbital moment for Mo induces a small MAE. Nb and Tc have large orbital moments (see Table 4.3). As shown in Fig. 4.12b, there are large changes in ΔQ (change in the valence charge) and ΔM_{s} upon a rotation of the spin moment from the z-axis to the x-axis for Tc. This is due to a high LDOS at ε_{F} (see Fig. 4.6a). Therefore, $\{\mathcal{K}_{\mathrm{Torque}(45^\circ)}, \mathcal{K}_{\mathrm{Eband}}\}$ and $\{\mathcal{K}_{\mathrm{Torque}(5^\circ)}, \mathcal{K}_{\mathrm{Susc}}\}$ give different results for the MAE. An exception is made for Nb even though the LDOS presents a sharp peak at ε_{F}, the change in the charge and spin moment is small as shown in Fig. 4.12b. This indicates that the majority-spin band of Nb is weakly affected by the rotation of the spin moment. Thus, the different methods are in a good agreement.

4.6.2 Magnetocrystalline anisotropy and real space cluster size

In the last section, we have shown the MAE for $3d$ and $4d$ impurities in Bi_2Te_3 using a real space cluster containing 102 sites. A natural question rises: Since the MAE is a non-local quantity (as discussed in Sec. 2.5.1), how does it depend on the real space cluster size? In Ref. [112], it was predicted that substrates with heavy elements, which can be easily spin polarized by a proximity effect can lead to non-trivial contributions to the non-local part of the MAE. Therefore, we show in Fig. 4.14, the dependence of the MAE for the considered $3d$ impurities as a function of the number of sites in the real space cluster ($\mathrm{N_{sites}}$). We notice a change in the amplitude of the MAE for all the considered elements. Nonetheless, the easy axis remains in-plane for Cr and Fe and out-of-plane for Mn and Co. We also notice that independently from the size of the cluster $\{\mathcal{K}_{\mathrm{Torque}(5^\circ)}, \mathcal{K}_{\mathrm{Susc}}\}$ give very similar results. Overall for all the $3d$ elements the MAE is stable regarding the number of sites in the real space cluster. This can be attributed to a lower induced spin polarization in the topological insulator in comparison with a Pt surface for example [112].

We also did a similar analysis for the $4d$ elements, since the latter ones tend to hybridize more with the substrate as discussed in Sec. 4.3.3. The results are shown in Fig. 4.15. Nb and Mo display a change in the MAE when $\mathrm{N_{sites}}$ increases. These changes are relatively small and do not affect the direction of the easy axis. In contrast, for Tc there is a "jump" in the MAE from 1.2 meV (in-plane) to -0.6 meV (out-of-plane) when $\mathrm{N_{sites}}$ changes from 60 sites to 80. This can be understood from the LDOS of Tc shown in Fig. 4.6a. We see that Tc has a very flat LDOS compared to Nb and Mo due to a higher hybridization

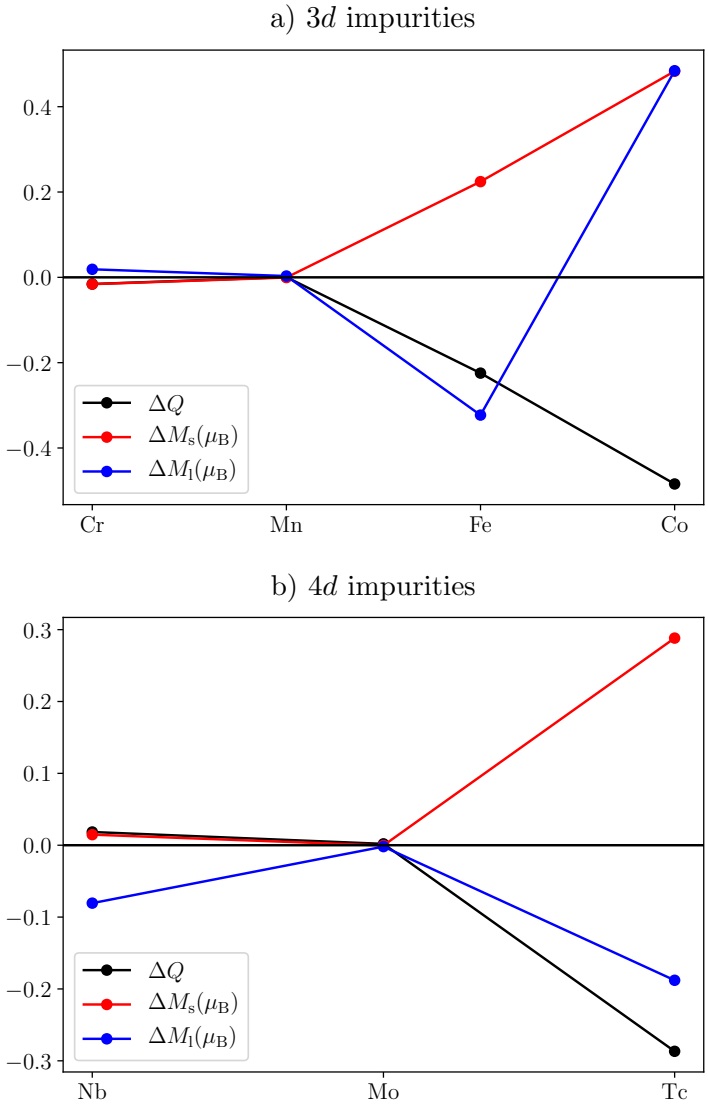

Figure 4.12: a) Change in the valence charge of the impurity $\Delta Q = Q^z - Q^x$ (black curve), spin moment $\Delta M_\mathrm{s} = M_\mathrm{s}^z - M_\mathrm{s}^x$ (red curve) and orbital moment $\Delta M_\mathrm{l} = M_\mathrm{l}^z - M_\mathrm{l}^x$ (blue curve) upon a rotation of the spin moment from z-axis to the x-axis. The $3d$ impurities are embedded in a Bi_2Te_3 (111) surface at a Bi site from the subsurface layer. For Fe and Co, ΔQ and ΔM_s are relatively large invalidating the use of the magnetic force theorem in this way. b) Same as in a) but for $4d$ impurities. ΔQ and ΔM_s are also large for Tc.

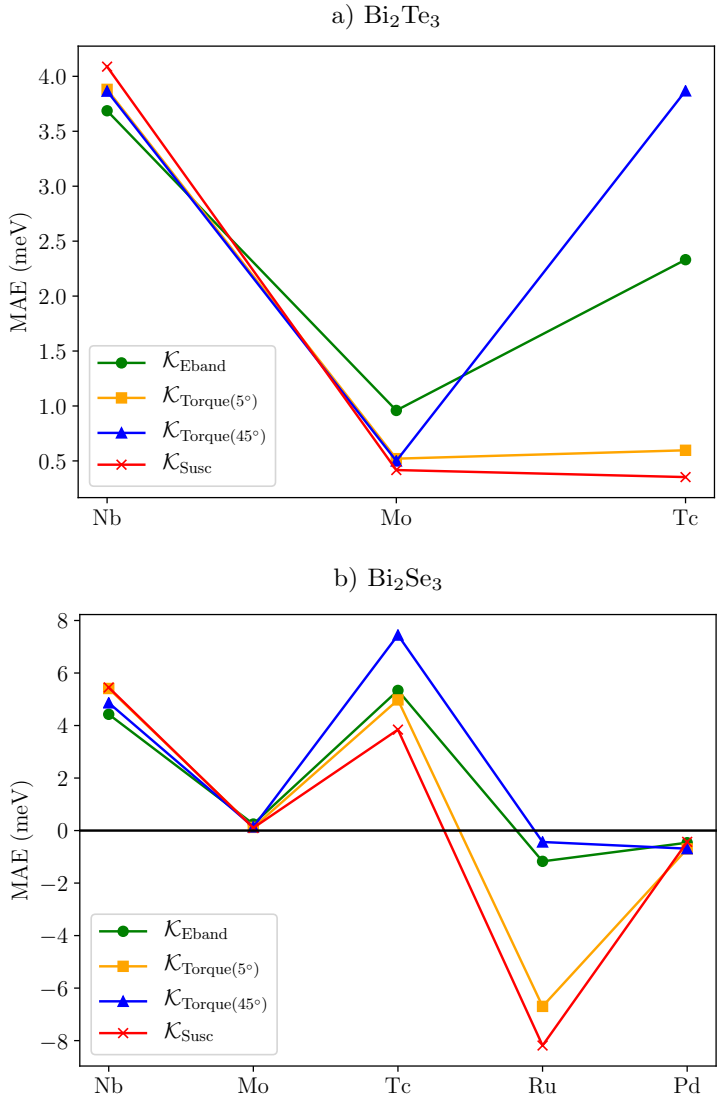

Figure 4.13: a) Comparison of the MAE for $4d$ impurities embedded in Bi_2Te_3 (111) surface at a Bi site from the subsurface layer. The green curve is obtained using the band energy differences (90° rotation of the spin moment). The orange curve is obtained using the torque method with the spin moment tilted 5° away from the z-axis. The blue curve is obtained using the torque method with the spin moment tilted 45° away from the z-axis. The red curve is obtained from the static part of the magnetic susceptibility (linear response). b) Same as in a) but for a Bi_2Se_3 surface. Ru is magnetic and displays a large MAE ($\mathcal{K}_{\text{Susc}} \sim 8$ meV), while Pd shows a relatively small MAE.

Elements	Cr	Mn	Fe	Co
$\mathcal{K}_{\text{Torque}(5^\circ)}(Bi_2Te_3)$	1.123	-0.183	4.158	-6.393
$\mathcal{K}_{\text{Torque}(5^\circ)}(Bi_2Se_3)$	-0.392	0.035	6.336	-5.733
$\mathcal{K}_{\text{Susc}}(Bi_2Te_3)$	0.959	-0.201	4.302	-6.725
$\mathcal{K}_{\text{Susc}}(Bi_2Se_3)$	0.088	0.005	6.018	-5.894

Table 4.7: Comparison between the MAE of $3d$ impurities obtained with $\mathcal{K}_{\text{Torque}(5^\circ)}$ and $\mathcal{K}_{\text{Susc}}$ embedded in two different hosts Bi_2Te_3 and Bi_2Se_3. The real space cluster contains 102 sites.

making the surrounding substrate atoms more sensitive to Tc, which impacts the non-local part of the MAE.

4.6.3 Magnetocrystalline anisotropy for $3d$ and $4d$ impurities in Bi_2Se_3

From the comparison between the ground state properties of $3d$ and $4d$ in Bi_2Te_3 and Bi_2Se_3 done in Sec. 4.3.3, we noticed that changing the substrate affects the ground state properties, particularly the orbital moments. This suggests that the MAE might also be affected considerably when trading Bi_2Te_3 for Bi_2Se_3 (according to Bruno's formula). Therefore, we once more consider a similar setup as in Sec. 4.3.1 and compute the MAE for $3d$ and $4d$ impurities in Bi_2Se_3. Similarly to the Bi_2Te_3 case and for the same reasons, the MAE obtained using different methods may differ.

$\mathcal{K}_{\text{Torque}(5^\circ)}$ and $\mathcal{K}_{\text{Susc}}$ obtained for $3d$ impurities in Bi_2Se_3 is compared to the MAE's obtained in the Bi_2Te_3 host (Fig. 4.11b). Cr and Mn have a very small anisotropy, with a noticeable decrease for Cr. The easy axis changed from in-plane to out-of-plane compared to the Bi_2Te_3 case. For Fe and Co the easy axis remains the same, while the MAE increases by almost 2 meV for Fe and decreased by 1 meV for Co. Overall, we observe the same trend for the MAE with band filling of the $3d$ elements compared to the Bi_2Te_3 host. A comparison of the values of the MAE is shown in the Table 4.7.

We now turn to the $4d$ elements. The MAE is shown in Fig. 4.13b, from which one notices that Nb, Mo, and Tc have an in-plane easy axis as in the Bi_2Te_3 case. For instance, the strong hybridization of Tc with the substrate leads to a drastic change in the MAE. $\mathcal{K}_{\text{Susc}}$ increases from 0.4 meV to 3.9 meV. A similar trend is followed by Nb, where $\mathcal{K}_{\text{Susc}}$ went from 4.0 meV to 5.5 meV, while it remains weak for Mo. Ru, which is non magnetic in the Bi_2Te_3 host displays a relatively large out-of-plane MAE of -8.2 meV. Finally Pd shows a weak out-of-plane anisotropy of -0.4 meV as well. In summary, the $4d$ elements are once more the ones most affected by the change of the substrate due to their strong hybridization. A comparison of the values of the MAE for the $4d$ impurities in the two hosts is given in Table 4.8.

4.6.4 Magnetocrystalline anisotropy for $3d$ and $4d$ impurities in bulk Bi_2Te_3

We finish our discussion about the MAE of $3d$ and $4d$ impurities in topological insulators by studying its dependence on the surface state. Therefore, we consider $3d$ and $4d$

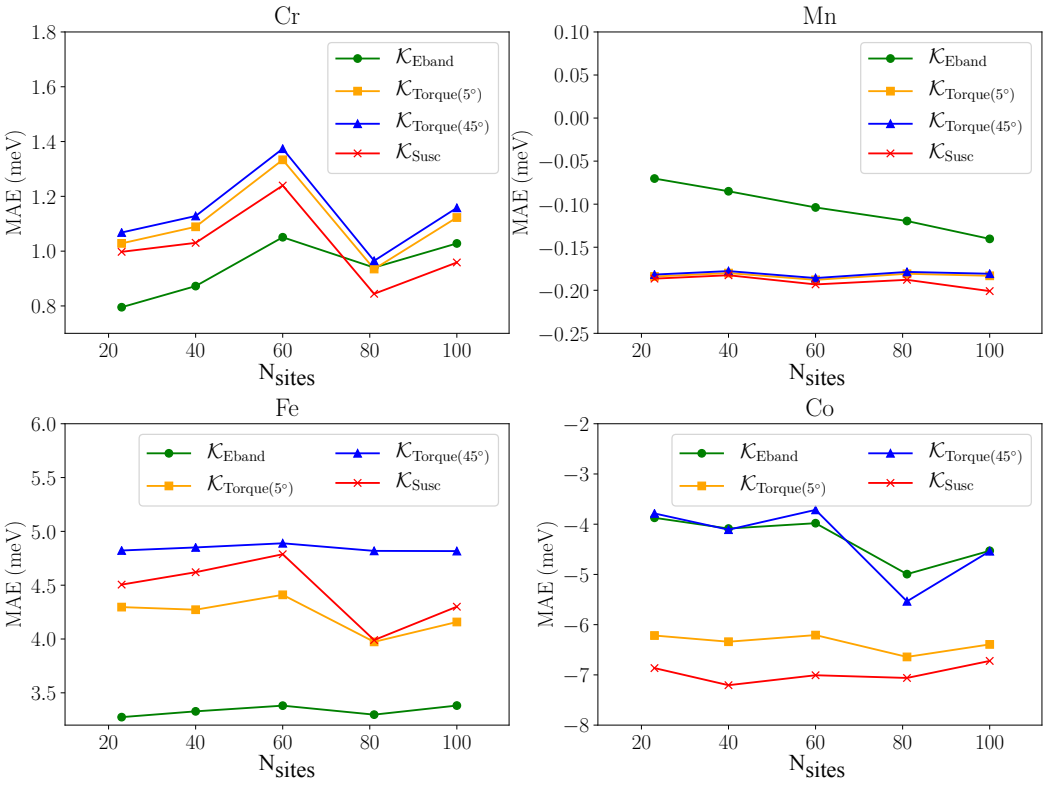

Figure 4.14: Study of MAE of $3d$ impurities embedded in Bi_2Te_3 (111) surface at a Bi site from the subsurface layer as a function of the real space cluster size (N_{sites}). For each impurity a comparison of four different methods determining the MAE is made. The green curve is obtained using the band energy differences (90° rotation of the spin moment). The orange curve is obtained using the torque method with the spin moment tilted 5° away from the z-axis. The blue curve is obtained using the torque method with the spin moment tilted 45° away from the z-axis. The red curve is obtained from the static part of the magnetic susceptibility (linear response).

Elements	Nb	Mo	Tc	Ru	Pd
$\mathcal{K}_{\text{Torque}(5^\circ)}(Bi_2Te_3)$	3.881	0.520	0.597	- - -	- - -
$\mathcal{K}_{\text{Torque}(5^\circ)}(Bi_2Se_3)$	5.410	0.120	4.976	-6.695	-0.697
$\mathcal{K}_{\text{Susc}}(Bi_2Te_3)$	4.090	0.417	0.353	- - -	- - -
$\mathcal{K}_{\text{Susc}}(Bi_2Se_3)$	5.452	0.101	3.847	-8.189	-0.431

Table 4.8: Comparison between the MAE of $4d$ impurities obtained with $\mathcal{K}_{\text{Torque}(5^\circ)}$ and $\mathcal{K}_{\text{Susc}}$ embedded in two different hosts Bi_2Te_3 and Bi_2Se_3. The real space cluster contains 102 sites.

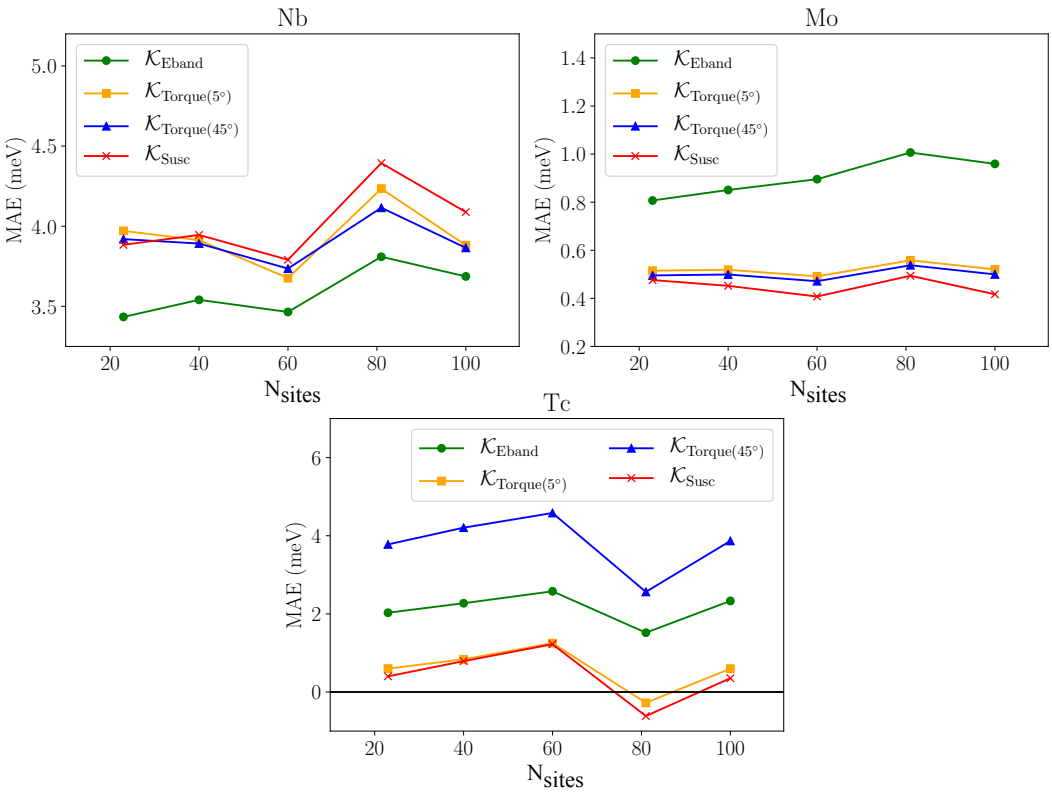

Figure 4.15: Study of MAE of $4d$ impurities embedded in Bi_2Te_3 (111) surface at a Bi site from the subsurface layer as a function of the real space cluster size (N_{sites}). For each impurity a comparison of four different methods determining the MAE is made. The green curve is obtained using the band energy differences (90° rotation of the spin moment). The orange curve is obtained using the torque method with the spin moment tilted 5° away from the z-axis. The blue curve is obtained using the torque method with the spin moment tilted 45° away from the z-axis. The red curve is obtained from the static part of the magnetic susceptibility (linear response).

impurities in bulk Bi_2Te_3 embedded at a Bi site. In presence of inversion symmetry no surface states are observed, thus, we can compare the MAE obtained for bulk with the one previously computed for the Bi_2Te_3 (111) surface, and explicitly identify the surface state contribution to the MAE. The bulk structure is uniaxial, therefore, we expect a non negligible MAE. A comparison between the MAE obtained for the bulk Bi_2Te_3 and surface is shown in Fig. 4.16a. Interestingly, despite a rather small hybridization with the surface state as discussed in Sec. 4.5, when switching from surface to bulk the easy axis of Cr changes from in-plane to out-of-plane with an absolute value of the MAE of $\sim$ 1 meV. This can be understood by considering that MAE is related to anisotropy in the orbital moments (Bruno fomula), which are more sensitive to hybridization details. For Mn in bulk, the MAE is small similarly to the surface case. Fe and Co have the same easy axis. However, there is a decrease of the MAE, which can be attributed to the missing contribution from the surface state. Indeed, there is a change in the intensity and occupation of the in-gap states generated in the bulk or at the surface of the topological insulator, which makes the MAE more sensitive to the surface state. Furthermore, we also compared the MAE energies for the $4d$ elements in Fig. 4.16b. We notice that the MAE for Nb decreased substantially (3 meV), it is still small for Mo and unaltered for Tc. In conclusion, the surface state has important an impact for some elements such as Cr, Co and Nb, while, it has a weak impact or none for other elements like Mn and Mo. The latter ones are those for which either the in-gap state intensity is very small (Mn) or is located away from ε_F (Mo).

As an important remark, it is worth mentioning that for some elements such as Tc and Co, $\mathcal{K}_{\text{Torque}(5^\circ)}$ and $\mathcal{K}_{\text{Susc}}$ do not have a good agreement in the bulk compared to the surface. As stated earlier in Sec. 4.6.1, they may lead to different results.

4.7 Spin dynamics of $3d$ and $4d$ impurities in topological insulators

After a detailed discussion of the ground state properties and the MAE of $3d$ and $4d$ impurities embedded in Bi_2Te_3 and Bi_2Se_3, we now study their spin dynamics. We aim at investigating the ability of exciting and manipulating them with ISTS. Furthermore, our goal is to explore the basic characteristic of the spin excitations such as their lifetimes and their energy range, which have been so far limited to metals, semi-insulating/insulating films [37, 197, 198, 199, 200]. The computation of the dynamical magnetic susceptibility ($\chi_{\alpha\beta}(\omega)$) within linear response theory allows to access the response of the system to an external frequency dependent magnetic field $\delta\vec{B}(\omega)$ (see Sec. 2.6.1).

We focus on transverse spin excitations, which were observed experimentally for impurities on surfaces using ISTS as done in Refs. [198, 201, 202, 203, 37, 204]. The signature of the spin excitations is usually observed as steps in the differential conductance curves, which can be traced back to the transverse spins excitations in the transverse magnetic susceptibility [37]. Several first principles calculations were performed to investigate transversal spin excitations of magnetic atoms deposited on nonmagnetic surfaces in Ref. [40, 205, 206], using the KKR Green function method. Thus, the concept of simulating transverse spin excitations in magnetic atoms is well established. A more recent investigation that includes the SOI was done in Ref. [41]. The SOI generates a magnetic

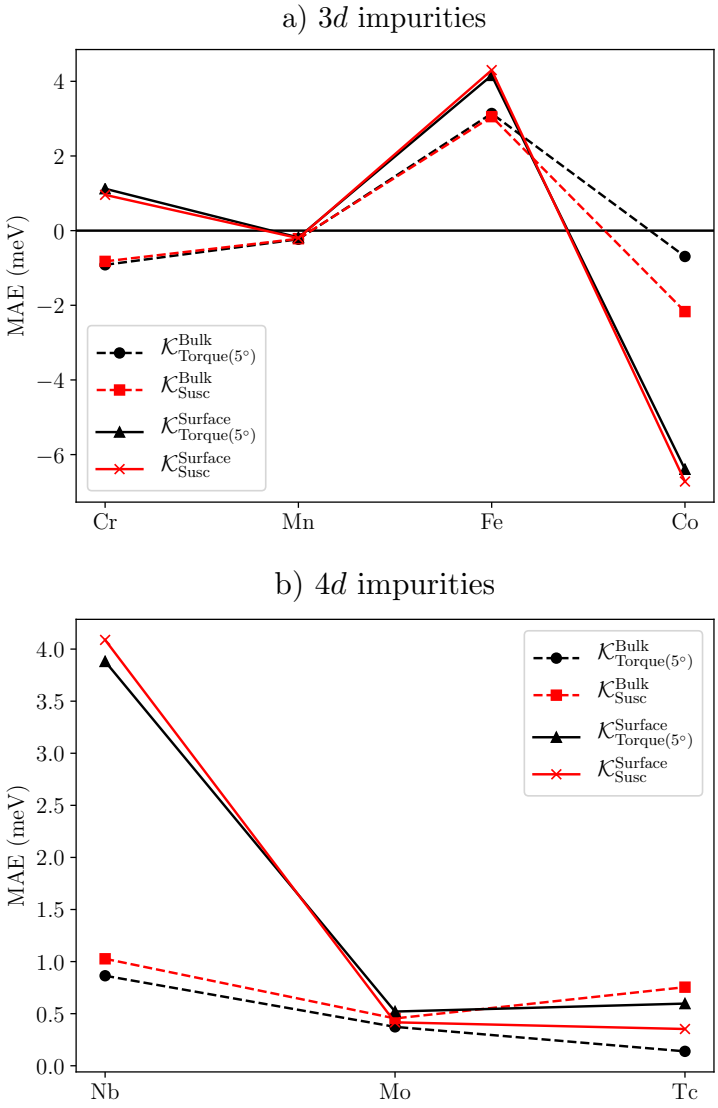

Figure 4.16: a) Comparison between the MAE of $3d$ impurities embedded in Bi_2Te_3 (111) surface at a Bi site from the subsurface layer, and $3d$ impurities embedded in Bi_2Te_3 bulk (Bi site). The black curve is obtained using the torque method with the spin moment tilted 5° away from the z-axis. The red curve is obtained from the static part of the magnetic susceptibility (linear response). Due to the presence of inversion symmetry (bulk), the easy axis for Cr impurities changed from in-plane to out-of-plane. b) Same as in a) but for $4d$ impurities. The MAE of Nb diminished considerably when moving from the surface to the bulk.

anisotropy resulting in an anisotropy field (see Sec. 4.6.1), which leads to an opening of a gap in the magnetic spectrum.

We perform a systematic investigation of the transversal spin excitations of $3d$ and $4d$ impurities in Bi_2Te_3 and Bi_2Se_3. The intricate interplay between the strong spin-orbit interaction of the topological insulator and the presence of the surface state will be explored in the context of spin excitations. The impact of the topological surface state on the spin dynamics was investigated by comparing the spin excitations obtained for $3d$ and $4d$ impurities embedded in bulk Bi_2Te_3 to the ones obtained at the surface. As will be shown in Sec. 4.7.2, dynamical corrections can be important. There is a shift in the position of the resonances observed in the spin excitation spectrum away from the values predicted using the ground state quantities.

4.7.1 Transversal dynamical response

In practice, the impurities display a relatively large magnetic moment while the induced moments in the surrounding substrate atoms are rather small. Therefore, we compute the magnetic susceptibility only at the impurity site, but we include the contribution of the surroundings to the kernel computed at the impurity site (the procedure to compute the kernel is shown in Sec. 2.6.2). In order to access the spin excitation spectrum, we define a spatially averaged quantity at the impurity site. This quantity contains the magnetic response of the impurity to an external frequency dependent magnetic field and is defined as:

$$\chi_{\alpha\beta}(\omega) = \int d\vec{r} \int d\vec{r}' \, \chi_{\alpha\beta}(\vec{r}, \vec{r}', \omega) \quad . \tag{4.36}$$

The integrals are performed over the cell containing the impurity and $\chi_{\alpha\beta}(\vec{r}, \vec{r}', \omega)$ is the enhanced magnetic susceptibility defined in Sec. 2.6.1. $\chi_{\alpha\beta}(\omega)$ is a rank 2 tensor ($\{\alpha, \beta\} = \{x, y, z, n\}$, n is for the charge) and ω is the frequency. Considering that the magnetization is along the z-direction and that we focus on the transverse response, we compute the spin-flip magnetic susceptibility containing all the components of the xy-block given as:

$$\chi_{+-}(\omega) = \frac{1}{4}(\chi_{xx}(\omega) - \mathrm{i}\chi_{xy}(\omega) + \mathrm{i}\chi_{yx}(\omega) + \chi_{yy}(\omega)) \quad , \tag{4.37}$$

which measures the probability of lowering the spin by $\hbar$ when extracting the imaginary part.

4.7.2 Spin excitations of $3d$ impurities in Bi_2Te_3

Here we discuss the spin excitation spectrum for Cr, Mn, Fe and Co. In Fig. 4.17a we show the imaginary part of the transverse magnetic susceptibility, which represents the density of states of the magnetic excitations. In the absence of an external magnetic field, the position of the resonance is located at finite frequency. This is a consequence of spin rotational symmetry breaking (*i.e.* no Goldstone mode) due to the magnetic anisotropy (SOI), which provides an energy barrier that the moment has to overcome in order to be excited. The lifetime of the excitations τ is related to the inverse of the full width at half maximum (FWHM) Γ of the resonance with $\tau = \frac{\hbar}{\Gamma}$.

The dashed lines in Fig. 4.17 represent the position of the resonance obtained using the ground state quantities only [41]:

$$\omega_{\text{max}}^{\text{gs}} = -\frac{2\gamma \mathcal{K}_{\text{Torque}(5^\circ)}}{M_\text{s}} \tag{4.38}$$

assuming $\gamma = 2$ (gyromagnetic ratio), $\mathcal{K}_{\text{Torque}(5^\circ)}$ is the MAE obtained using the torque method at 5° and M_s is the spin moment. $\omega_{\text{max}}^{\text{gs}}$ is in a qualitative agreement with the resonance observed in our dynamical calculations, however, it fails to give a quantitative description highlighting the importance of dynamical corrections to γ.

In order to include these dynamical corrections, we consider the mapping of the dynamical spin-flip magnetic susceptibility $\chi_{+-}(\omega)$ obtained from our TD-DFT calculations to a generalized LLG equation, which includes a tensorial damping and nutation [115]. The details of the mapping are given in Sec. 2.6.4, where we have shown that the spin-flip magnetic susceptibility within the generalized LLG model reads:

$$\chi_{+-}^{\text{LLG}}(\omega) = \frac{1}{2} \frac{M_\text{s}\gamma}{-\frac{2\mathcal{K}_{\text{Susc}}\gamma}{M_\text{s}} - (1 + \mathcal{G}_\perp^a + \text{i}\mathcal{G}_\parallel^s)\,\omega + (-\mathcal{I}_\parallel^s + \text{i}\mathcal{I}_\perp^a)\,\omega^2} \quad . \tag{4.39}$$

$\mathcal{G}_\parallel^s$ ($\mathcal{I}_\parallel^s$) and $\mathcal{G}_\perp^a$ ($\mathcal{I}_\perp^a$) represents the symmetric and antisymmetric transversal components of damping (nutation) tensor, respectively. These parameters are defined in Sec. 2.6.4. They are extracted using Eq. (2.138) to fit $\{\chi_{xx}(\omega), \chi_{xy}(\omega)\}$ obtained from TD-DFT. In Ref. [207], it is shown that $\mathcal{G}_\parallel^s \propto n^\downarrow(\varepsilon_\text{F})\, n^\uparrow(\varepsilon_\text{F})$, where $n^\downarrow(\varepsilon_\text{F})$ ($n^\uparrow(\varepsilon_\text{F})$) is the LDOS at ε_F for the minority (majority) spin channel. This connection between the damping and the electronic structure can be understood in the following way: when there are no states at ε_F, the coupling between the impurity and the host electrons is weak, therefore, the excitation has a longer lifetime with a small damping. In fact the product of density of states at ε_F measures the density of electron-hole excitations of opposite spin, providing the main mechanism for lowering the lifetime of the spin excitations. $\mathcal{G}_\perp^a$ accounts for the change of the gyromagnetic ratio. Indeed, we can define an effective one, $\gamma_{\text{eff}} = \frac{\gamma}{1+\mathcal{G}_\perp^a}$. This shift of γ is attributed to the hybridization with the host as well, since in the limit $n^\downarrow(\varepsilon_\text{F}) = n^\uparrow(\varepsilon_\text{F}) = 0$ one recovers $\gamma = 2$ as shown in Ref. [207].

From Eq. (4.39) and if one does not include the imaginary terms, we expect a resonance when $-\frac{2\mathcal{K}_{\text{Susc}}\gamma}{M_\text{s}} - \omega - \mathcal{G}_\perp^a\omega - \mathcal{I}_\parallel^s\omega^2 = 0$. This provides an approximate threshold for the nutation term to become relevant for the spin-excitational behavior, when the resonance is located at frequencies $\omega > \omega_\text{c} = \frac{\mathcal{G}_\perp^a}{\mathcal{I}_\parallel^s}$, it is affected by the nutation. When neglecting the contribution of the nutation, the resonance frequency is given by:

$$\omega_{\text{max}}^{\text{NI}} = -\frac{\gamma}{\sqrt{1 + \left(\mathcal{G}_\parallel^s\right)^2 + 2\mathcal{G}_\perp^a + \left(\mathcal{G}_\perp^a\right)^2}} \frac{2\mathcal{K}_{\text{Susc}}}{M_\text{s}} \quad , \tag{4.40}$$

where $\omega_{\text{max}}^{\text{NI}}$ is defined as the resonance frequency without including the nutation. We see that the resonance frequency is renormalized by $\mathcal{G}_\parallel^s$ and $\mathcal{G}_\perp^a$, which account for the damping of the precession and the renormalization of γ, respectively.

The LLG parameters obtained for $3d$ impurities embedded in Bi_2Te_3 are shown in Table 4.9. The MAE and ω_{max} are given in meV, the symmetric and antisymmetric transversal

Element	$M_s(\mu_B)$	$\mathcal{G}^s_\parallel$	$\mathcal{G}^a_\perp$	$\mathcal{I}^s_\parallel$	$\mathcal{I}^a_\perp$	$\mathcal{K}_{\text{Susc}}$	$\omega^{\text{NI}}_{\text{max}}$	$\frac{\omega_c}{\omega^{\text{NI}}_{\text{max}}}$
Cr (Bi_2Te_3)	3.844	0.018	-0.245	0.003	0.002	0.959	1.322	58
Cr (Bi_2Se_3)	3.671	0.037	-0.153	0.000	0.001	0.090	0.115	2455
Mn (Bi_2Te_3)	4.412	0.000	0.109	0.000	0.000	-0.201	0.164	20921
Mn (Bi_2Se_3)	4.421	0.000	0.101	0.000	0.000	0.005	0.004	309979
Fe (Bi_2Te_3)	3.395	0.143	0.286	-0.002	-0.002	4.302	3.917	34
Fe (Bi_2Se_3)	3.482	0.112	0.125	0.001	-0.001	6.019	6.113	16
Co (Bi_2Te_3)	2.109	0.164	0.274	0.000	-0.004	-6.725	9.926	27
Co (Bi_2Se_3)	2.231	0.012	0.196	0.003	0.000	-5.894	8.833	8

Table 4.9: LLG parameters for $3d$ impurities embedded in Bi_2Te_3 and in Bi_2Se_3 obtained from fitting the magnetic susceptibility computed using TD-DFT. M_s is the spin moment, $\mathcal{G}^s_\parallel$ and $\mathcal{G}^a_\perp$ are the transversal components of the damping tensor, $\mathcal{I}^s_\parallel$ and $\mathcal{I}^a_\perp$ transversal components of the nutation tensor, they are given in meV^{-1}. $\mathcal{K}_{\text{Susc}}$ is the MAE obtained from the magnetic susceptibility. $\omega^{\text{NI}}_{\text{max}}$ is the resonance frequency without including nutation (in meV) and the ratio $\frac{\omega_c}{\omega^{\text{NI}}_{\text{max}}}$ informs us about the relevance of the nutation.

part of the nutation tensor $\mathcal{I}^s_\parallel$ and $\mathcal{I}^a_\perp$ are given in meV^{-1}. High values for $\mathcal{G}^s_\parallel$ correlates with a high values of the LDOS at ε_F. This explains the higher values obtained for Fe and Co compared to those of Cr and Mn since the former ones present a resonance in the lower spin channel at ε_F. The negative sign of $\mathcal{G}^a_\perp$ for Cr predicts an enhancement of the gyromagnetic ratio (*i.e.* $\gamma_{\text{eff}} > 2$) while it is reduced for the rest of the $3d$ elements. The position of the resonance frequency is proportional to the MAE in agreement with Eq. (4.40). We show in the last column of Table 4.9 the ratio $\frac{\omega_c}{\omega^{\text{NI}}_{\text{max}}} \gg 1$ for all $3d$ elements, concluding that the nutation has no significant impact on the resonances observed for $3d$ elements in Bi_2Te_3. A summary of the lifetimes of the spin excitations is shown in Fig. 4.18.

4.7.3 Spin excitations of $4d$ impurities in Bi_2Te_3

We now replace $3d$ impurities with $4d$ and compute the spin excitation spectrum, it is shown in Fig. 4.19a. Mo and Tc present sharp resonances resulting in high lifetimes as displayed in Fig. 4.18, these resonances are located at very low frequency due to their small MAE. Nb has a broad peak (small τ) situated at rather high frequency due to its large MAE and small value of the spin moment.

The fitted LLG parameters obtained from the spin excitation spectra are displayed in Table 4.10. Similarly to the $3d$ case, a large LDOS at ε_F induces large values for $\mathcal{G}^s_\parallel$. $\gamma_{\text{eff}} > 2$ is slightly enhanced for Nb since $\mathcal{G}^a_\perp < 0$ while $\gamma_{\text{eff}} < 2$ for Mo and Tc. The ratio $\frac{\omega_c}{\omega^{\text{NI}}_{\text{max}}} \gg 1$ for Mo and Tc, thus, the nutation is not affecting their spectrum. However, for Nb $\frac{\omega_c}{\omega^{\text{NI}}_{\text{max}}} \simeq 1$, therefore, one expects the nutation coefficient $\mathcal{I}^s_\parallel$ to have a non-negligible impact on the resonance frequency. Indeed, $\omega^{\text{NI}}_{\text{max}}$ shown in Table 4.10 does not include the nutation correction. When we extract it directly from the spectrum in Fig. 4.19a, we see that $\omega_{\text{max}} = 17.610$ meV instead of $\omega^{\text{NI}}_{\text{max}} = 16.313$ meV, which is the

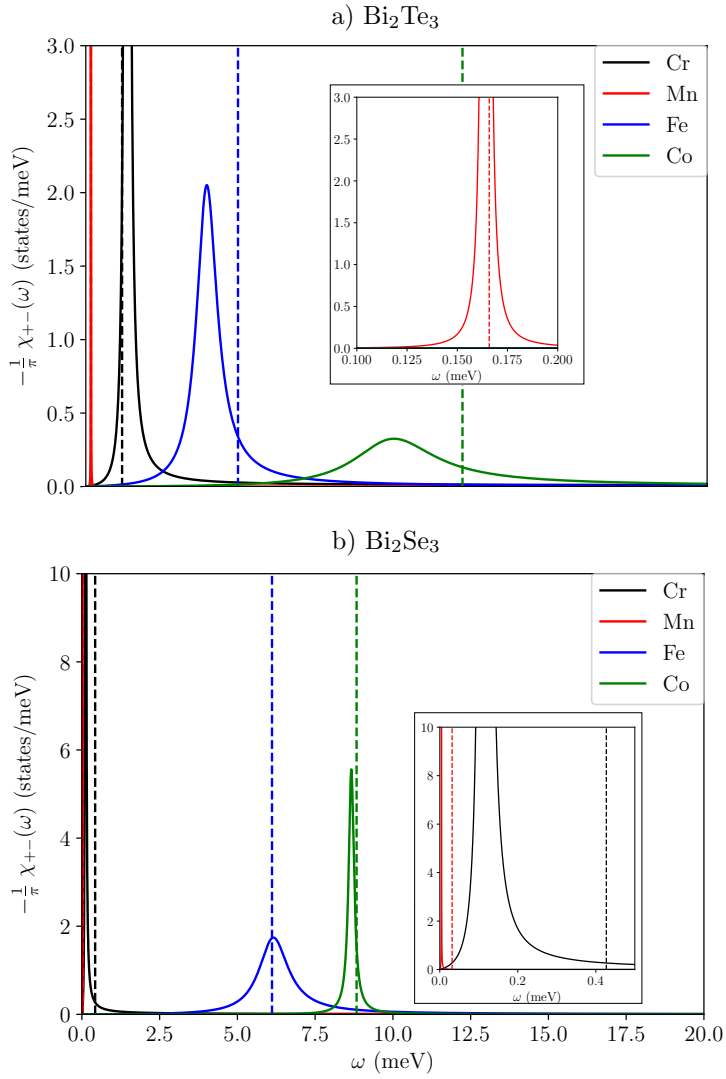

Figure 4.17: a) Density of states of transverse spin excitations for $3d$ impurities embedded in Bi_2Te_3. It has a Lorentzian form with a resonance located at the excitation energies of the system (in the meV range). The dashed lines represent the position of the resonance without the dynamical corrections from Eq. (4.38). b) Same as in a) but for a Bi_2Se_3 surface, where Mn, Cr and Co present sharper resonances compared to the Bi_2Te_3 case.

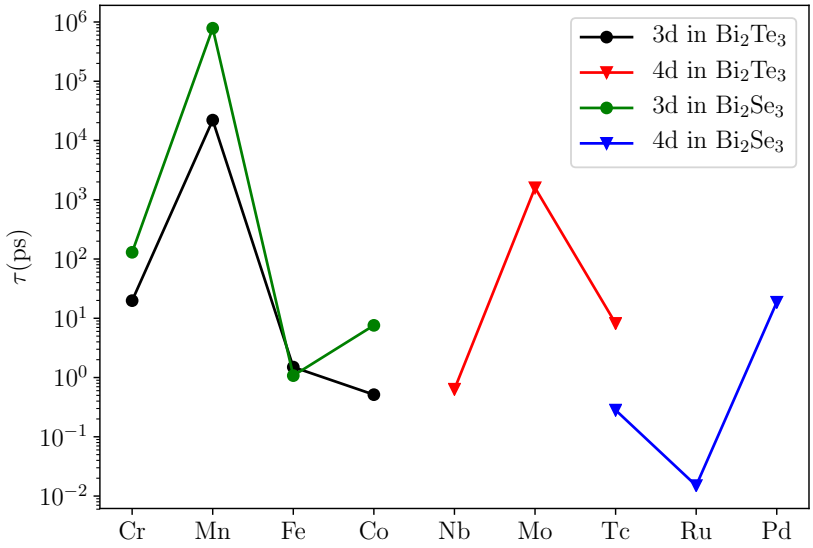

Figure 4.18: Summary of the lifetimes of the spin excitations for $3d$ and $4d$ impurities embedded in Bi_2Te_3 and Bi_2Se_3. A logarithmic scale is used for a better comparison between the lifetimes. For Mn very high lifetimes are observed, reaching microseconds in the Bi_2Se_3 case.

Element	$M_s(\mu_B)$	$\mathcal{G}^s_\parallel$	$\mathcal{G}^a_\perp$	$\mathcal{I}^s_\parallel$	$\mathcal{I}^a_\perp$	$\mathcal{K}_{\text{Susc}}$	$\omega^{\text{NI}}_{\text{max}}$	$\frac{\omega_c}{\omega^{\text{NI}}_{\text{max}}}$
Nb (Bi_2Te_3)	1.097	0.053	-0.087	0.004	0.002	4.091	16.313	1.3
Mo (Bi_2Te_3)	2.678	0.000	0.096	0.000	0.000	0.417	0.568	394
Tc (Bi_2Te_3)	2.493	0.172	0.099	-0.003	0.001	0.353	0.509	62
Tc (Bi_2Se_3)	2.534	0.512	0.081	-0.018	0.006	3.845	5.073	0.8
Ru (Bi_2Se_3)	0.564	0.852	-0.396	-0.039	0.003	-8.178	55.490	0.1
Pd (Bi_2Se_3)	0.578	0.094	1.824	-0.004	0.000	-0.431	1.055	414

Table 4.10: LLG parameters for $4d$ impurities embedded in Bi_2Te_3 and in Bi_2Se_3 obtained from fitting the magnetic susceptibility computed using TD-DFT. M_s is the spin moment, $\mathcal{G}^s_\parallel$ and $\mathcal{G}^a_\perp$ are the transversal components of the damping tensor, $\mathcal{I}^s_\parallel$ and $\mathcal{I}^a_\perp$ are the transversal components of the nutation tensor, they are given in meV^{-1}. $\mathcal{K}_{\text{Susc}}$ is the MAE obtained from the magnetic susceptibility. $\omega^{\text{NI}}_{\text{max}}$ is the resonance frequency without including nutation (in meV) and the ratio $\frac{\omega_c}{\omega^{\text{NI}}_{\text{max}}}$ informs us about the relevance of the nutation.

value obtained using Eq. (4.40), where the nutation is not included. We conclude that the nutation has an important impact on the Nb impurities in Bi_2Te_3 leading to a repositioning of the resonance frequency.

4.7.4 Spin excitations of $3d$ and $4d$ impurities in Bi_2Se_3

We now investigate the impact of the substrate on the spin excitation spectrum of $3d$ and $4d$ impurities. Once more the Bi_2Te_3 surface is exchanged with Bi_2Se_3 and we consider the same setup as in Sec. 4.3.1. We show the LLG parameters for $3d$ in Bi_2Se_3 in Table 4.9. The damping parameters $\mathcal{G}^s_\parallel$ and $\mathcal{G}^a_\perp$ follow a similar trend compared to the Bi_2Te_3 case for Cr, Mn and Fe. However, $\mathcal{G}^s_\parallel$ is one order of magnitude smaller compared to the Bi_2Te_3 case for Co. This can be observed in the spin excitation spectrum shown in Fig. 4.17b, where Co exhibits a much sharper peak compared to the Bi_2Te_3 case with a higher lifetime for the spin excitation (see Fig. 4.18). We notice that Cr has a resonance located at lower frequency compared to the Bi_2Te_3 case. Mn is not observed on the plot since its resonance is located almost at zero frequency. The nutation has no impact on the resonance frequency of Cr, Mn and Fe but affects the one of Co causing a reduction from 8.83 meV without nutation to 8.65 meV when it is included. Overall the spin dynamics of $3d$ adatoms in Bi_2Se_3 is similar to the Bi_2Te_3 with noticeable differences for Co impurities.

The LLG parameters for the $4d$ elements were obtained as well. They are given in Table 4.10, where we notice an increase of the damping $\mathcal{G}^s_\parallel$ for Tc which can be explained by the increase of the majority LDOS at ε_F as seen in Fig. 4.6b compared to the Bi_2Te_3 case. Ru has a very large damping with a very flat resonance (short lifetime for the excitation as shown in Fig. 4.18) in contrast to Tc and Pd as seen in Fig. 4.19b. Pd has smaller damping compared to Tc and Ru with a sharper resonance. The nutation has a negligible impact on Pd since $\frac{\omega_c}{\omega^{\text{NI}}_{\text{max}}} \gg 1$, while it has an small impact for Tc since it shifts $\omega^{\text{NI}}_{\text{max}} = 5.07$ meV to $\omega_{\text{max}} = 4.70$ meV when the nutation is included. Finally, Ru is the extreme limit where the nutation leads to a dramatic shift in ω_{max}, indeed without nutation we obtain $\omega^{\text{NI}}_{\text{max}} = 55.49$ meV, while when including it one gets $\omega_{\text{max}} = 25.52$ meV.

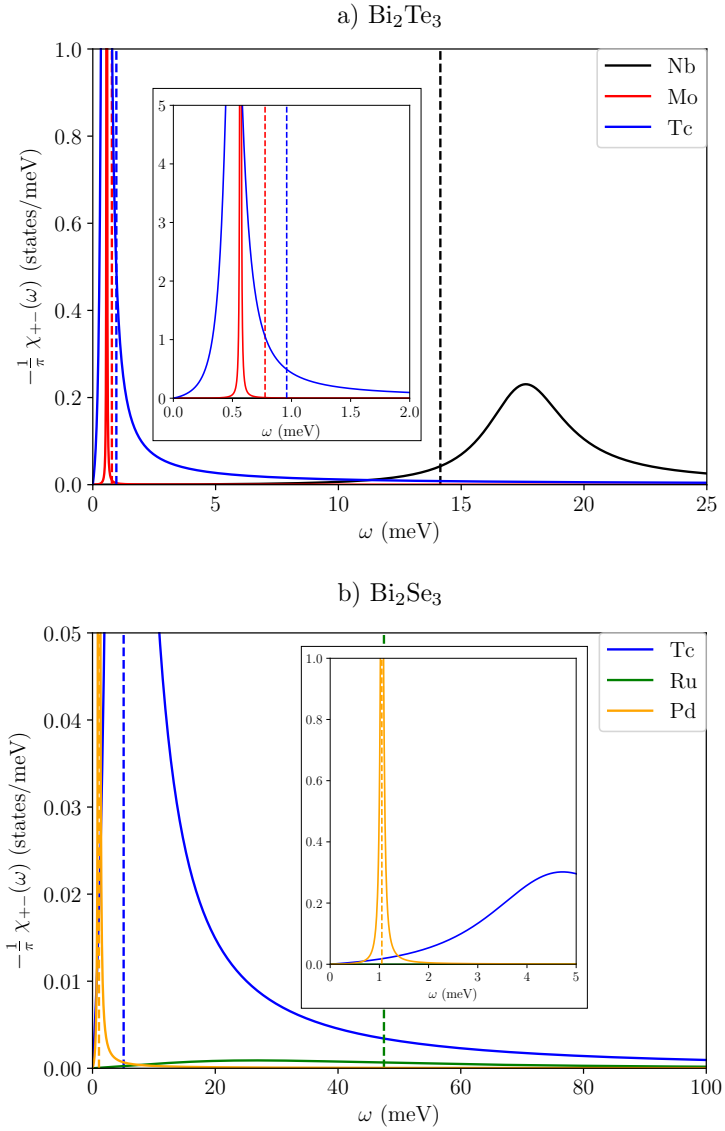

Figure 4.19: a) Density of states of transverse spin excitations for $4d$ impurities embedded in Bi_2Te_3. It has a Lorentzian form with a resonance located at the excitation energies of the system (in the meV range). The dashed lines represent the position of the resonance without the dynamical corrections from Eq. (4.38). b) Same as in a) but for a Bi_2Se_3 surface, where Tc has a higher resonance frequency compared to the Bi_2Se_3 case.

We do not show the spin excitation spectrum or the LLG parameters for Nb and Mo since for these elements at low frequency (meV range) the non linear orders in frequency of the Taylor expansion for the KS susceptibility are large, therefore, the second order expansion used in these calculations (see Sec. 2.6.3) is not accurate enough to capture the proper frequency dependency of the dynamical magnetic susceptibility.

4.7.5 Impact of the surface state on spin excitations of $3d$ and $4d$ impurities in Bi_2Te_3

Here the surface state contribution to the transversal spin excitations of $3d$ and $4d$ impurities in Bi_2Te_3 is investigated. It can be identified by comparing the LLG parameters obtained when the impurities are embedded in the bulk to the ones calculated for the surface case. Therefore, we show a comparison in Table 4.11 for the $3d$ impurities. We used the subscript "s" for surface quantities and "b" for bulk quantities. $\mathcal{G}_{\parallel}^{s}$ decreased when moving from surface to bulk for Cr and Fe, this can be explained by the following: in the bulk the hybridization is reduced due to the absence of the surface states, which reduces the LDOS at ε_{F} as shown in Fig. 4.8 when comparing the LDOS of Cr embedded in bulk and at the surface. However, Co is an exception since $\mathcal{G}_{\parallel}^{s}$ increased in the bulk case, which is counter intuitive since in absence of the surface state, one expects less coupling to host electrons. This can be understood when comparing the LDOS obtained for the bulk and surface cases. Indeed, the minority-spin LDOS at ε_{F} is almost unchanged when going from the surface to the bulk, while in the majority-spin channel the in-gap state is shifted upwards, closer to ε_{F}. Thus, $n^{\uparrow}(\varepsilon)$ increases and leads to a higher $\mathcal{G}_{\parallel}^{s}$ in the bulk for Co. $\mathcal{G}_{\perp}^{a}$, which expresses the renormalization of γ, follows a similar trend as the surface case, with the exception of Co once more where $\gamma_{\mathrm{eff}} > 2$ in contrast to what is observed in the surface case. The nutation is small for Cr, Mn and Fe and noticeable for Co since it renormalizes $\omega_{\mathrm{max}}^{\mathrm{NI}}$ from 4.24 meV without nutation to $\omega_{\mathrm{max}} = 4.68$ meV with nutation. A similar comparison is done for $4d$ impurities and shown in Table 4.12. The damping parameter $\mathcal{G}_{\parallel}^{s}$ increased for Nb and Mo in bulk. Analogously to the Co case, this can also be attributed to a shift of the in-gap state towards ε_{F}, now in the minority-spin channel, leading to an increase of the LDOS at ε_{F}. The nutation is negligible for Mo and Tc similarly to the surface case and noticeable for Nb since it leads to a shift of $\omega_{\mathrm{max}}^{\mathrm{NI}} = 5.07$ meV without the contribution of the nutation to $\omega_{\mathrm{max}} = 5.43$ meV when including it.

In summary, the surface state affects considerably the spin dynamics of $3d$ and $4d$ impurities in Bi_2Te_3 especially the damping and in some cases such as Co the nutation as well.

4.7.6 Transversal zero-point spin-fluctuations of $3d$ and $4d$ impurities in Bi_2Te_3 and Bi_2Se_3

Experimentally, when observed with X-ray magnetic circular dichroism (XMCD) or ISTS, $3d$ adatoms have a substantial MAE in the meV range [27, 208, 201]. However, the same elements display a paramagnetic signal when measured with spin-polarized scanning tunneling microscopy (SP-STM), *i.e.* the magnetic stability is destroyed locally [209, 150, 210]. For Ru and Rh impurities deposited on Ag(001) surface, even in presence of a

Element	$M_{\mathrm{s}}(\mu_{\mathrm{B}})$	$\mathcal{G}_{\parallel}^{s}$	$\mathcal{G}_{\perp}^{a}$	$\mathcal{I}_{\parallel}^{s}$	$\mathcal{I}_{\perp}^{a}$	$\mathcal{K}_{\mathrm{Susc}}$	$\omega_{\mathrm{max}}^{\mathrm{NI}}$	$\frac{\omega_{\mathrm{c}}}{\omega_{\mathrm{max}}^{\mathrm{NI}}}$
$\mathrm{Cr_s}$	3.844	0.018	-0.245	0.003	0.002	0.959	1.322	58
$\mathrm{Cr_b}$	3.823	0.004	-0.215	0.000	0.000	-0.824	1.090	302
$\mathrm{Mn_s}$	4.412	0.000	0.109	0.000	0.000	-0.201	0.164	20921
$\mathrm{Mn_b}$	4.335	0.000	0.118	0.000	0.000	-0.216	0.178	4816
$\mathrm{Fe_s}$	3.395	0.143	0.286	-0.002	-0.002	4.302	3.917	34
$\mathrm{Fe_b}$	3.294	0.045	0.234	0.004	0.002	3.055	3.004	19
$\mathrm{Co_s}$	2.109	0.164	0.274	0.000	-0.004	-6.725	9.926	27
$\mathrm{Co_b}$	1.977	0.307	-0.011	-0.011	0.005	-2.168	4.237	0.2

Table 4.11: Comparison between the LLG parameters for $3d$ impurities embedded in $\mathrm{Bi_2Te_3}$ a bulk Bi site (b) and in the first subsurface Bi layer (s). The parameters are obtained from fitting the magnetic susceptibility computed using TD-DFT. M_{s} is the spin moment, $\mathcal{G}_{\parallel}^{s}$ and $\mathcal{G}_{\perp}^{a}$ are the transversal components of the damping tensor, $\mathcal{I}_{\parallel}^{s}$ and $\mathcal{I}_{\perp}^{a}$ are the transversal components of the nutation tensor, they are given in meV^{-1}. $\mathcal{K}_{\mathrm{Susc}}$ is the MAE obtained from the magnetic susceptibility. $\omega_{\mathrm{max}}^{\mathrm{NI}}$ is the resonance frequency without including nutation (in meV) and the ratio $\frac{\omega_{\mathrm{c}}}{\omega_{\mathrm{max}}^{\mathrm{NI}}}$ informs us about the relevance of the nutation.

Element	$M_{\mathrm{s}}(\mu_{\mathrm{B}})$	$\mathcal{G}_{\parallel}^{s}$	$\mathcal{G}_{\perp}^{a}$	$\mathcal{I}_{\parallel}^{s}$	$\mathcal{I}_{\perp}^{a}$	$\mathcal{K}_{\mathrm{Susc}}$	$\omega_{\mathrm{max}}^{\mathrm{NI}}$	$\frac{\omega_{\mathrm{c}}}{\omega_{\mathrm{max}}^{\mathrm{NI}}}$
$\mathrm{Nb_s}$	1.097	0.053	-0.087	0.004	0.002	4.091	16.313	1.3
$\mathrm{Nb_b}$	0.740	0.314	0.049	0.005	-0.001	1.028	5.074	2
$\mathrm{Mo_s}$	2.678	0.000	0.096	0.000	0.000	0.417	0.568	394
$\mathrm{Mo_b}$	2.527	0.012	0.151	0.000	0.000	0.454	0.624	518
$\mathrm{Tc_s}$	2.493	0.172	0.099	-0.003	0.001	0.353	0.509	62
$\mathrm{Tc_b}$	2.057	0.059	0.072	0.006	0.002	0.755	1.368	9

Table 4.12: Comparison between the LLG parameters for $4d$ impurities embedded in $\mathrm{Bi_2Te_3}$ a bulk Bi site (b) and in the first subsurface Bi layer (s). The parameters are obtained from fitting the magnetic susceptibility computed using TD-DFT. M_{s} is the spin moment, $\mathcal{G}_{\parallel}^{s}$ and $\mathcal{G}_{\perp}^{a}$ are the transversal components of the damping tensor, $\mathcal{I}_{\parallel}^{s}$ and $\mathcal{I}_{\perp}^{a}$ are the transversal components of the nutation tensor, they are given in meV^{-1}. $\mathcal{K}_{\mathrm{Susc}}$ is the MAE obtained from the magnetic susceptibility. $\omega_{\mathrm{max}}^{\mathrm{NI}}$ is the resonance frequency without including nutation (in meV) and the ratio $\frac{\omega_{\mathrm{c}}}{\omega_{\mathrm{max}}^{\mathrm{NI}}}$ informs us about the relevance of the nutation.

static magnetic field in an XMCD experiment, no magnetic response is observed [211]. Recently, a breakthrough has been made by Natterer et *al.* [212]: They used SP-STM and showed that a Ho atom deposited on MgO/Ag(100) surface can retain its magnetic information over several hours (magnetic remanence). To explain the contradictions between large MAE and the presence of fluctuations, Azpiroz et *al.* evaluated zero-point spin-fluctuations (ZPSF) of $3d$ and $4d$ adatoms deposited on Cu(111) and Ag(001) surfaces [42]. They found them to be large and of the order of the spin moments. These fluctuations are related to the Heisenberg uncertainty principle and can be used to ascertain the stability of a magnetic moment. Indeed, large ZPSF impact the magnetic anisotropy energy by effectively reducing it by a large magnitude. This provides a possible explanation for the paramagnetic behavior of the adatoms.

The knowledge of the dynamical magnetic susceptibility $\chi_{\alpha\beta}(\omega)$ gives access to ZPSF, as discussed in Sec. 2.6.5. Here, we focus on the transversal fluctuations since the longitudinal ones are found to be one order of magnitude smaller for the systems investigated so far [42]. The amplitude of the transversal ZPSF $\xi_\perp^2$ is related to the transversal magnetic susceptibility $\chi_\perp(\omega) = \chi_{xx}(\omega) + \chi_{yy}(\omega)$ via:

$$\xi_\perp^2 = -\frac{1}{\pi}\int_0^{+\infty} \mathrm{d}\omega\, \mathrm{Im}\chi_\perp(\omega) \quad . \tag{4.41}$$

This relation, as discussed in Sec. 2.6.5, demonstrates that electron hole excitations, MAE and other mechanisms and interactions among different degrees of freedom will shape the magnitude and the behavior of the ZPSF. We consider the same setup as in Sec. 4.3.1 and focus on the ZPSF of $3d$ and $4d$ elements in Bi_2Te_3 and Bi_2Se_3. In Fig. 4.20a, we compare the mean value of the transverse ZPSF $\xi_\perp = \sqrt{\xi_\perp^2}$ to the spin moments. The ZPSF are rather large, reaching $\xi_\perp \sim 2.4\,\mu_\mathrm{B}$ for Cr in Bi_2Te_3, while the smallest value is obtained for Mn in Bi_2Se_3 where $\xi_\perp \sim 0.5\,\mu_\mathrm{B}$. We also notice that for Cr and Co $\xi_\perp \sim \frac{2M_\mathrm{s}}{3}$ and $\xi_\perp \sim \frac{M_\mathrm{s}}{2}$ for Fe. As observed in Ref. [42], the fluctuations follow the same trend than the spin moments with a maximum at half band filling. Mn impurities in both hosts are the only exceptions with a clear decrease of the ZPSF. Using the LLG model (Sec. 2.6.4, Ref. [42]), it was found that $\frac{\xi_\perp}{M_\mathrm{s}} \sim \frac{1}{\sqrt{M_\mathrm{s}}}$: Although the fluctuations increase with the magnetic moment, their relative value decreases. This means that the larger the moment is, the closer it is to a classical behavior. Moreover, a reduction of the electron-hole excitations due to a decrease of the resonance width leads to smaller fluctuations. These two conditions (larger moment and small width) are fulfilled for Mn in Bi_2Se_3. As discussed in Sec. 4.7.5, the lifetime of the spin excitations and the amount of electron-hole excitations are shaped by the existence of in-gap states and their intensity at ε_F. Mn in Bi_2Se_3 is the only element with no in-gap state close to ε_F, leading to the lowest amount of electron-hole excitations and a lifetime of the excitations reaching microseconds, as shown in Fig. 4.18.

The ZPSF for $4d$ elements in Bi_2Te_3 are depicted in Fig. 4.20b. The highest amount of ZPSF is obtained for Tc with $\xi_\perp \sim 1.9\,\mu_\mathrm{B}$. For Nb the ZPSF are larger than M_s, while for Mo and Tc, $\xi_\perp > \frac{M_\mathrm{s}}{2}$. Fig. 4.20b shows the ZPSF for $4d$ elements in Bi_2Se_3 as well. Once more the Tc impurity displays the largest amount of fluctuations with $\xi_\perp \sim 1.6\,\mu_\mathrm{B}$; lower values are observed for Ru and Pd with $\xi_\perp \sim 0.3\,\mu_\mathrm{B}$ and $\xi_\perp \sim 0.5\,\mu_\mathrm{B}$, respectively. Furthermore, we notice that for the $4d$ elements $\xi_\perp \propto \sqrt{M_\mathrm{s}}$ and that the spin-fluctuations

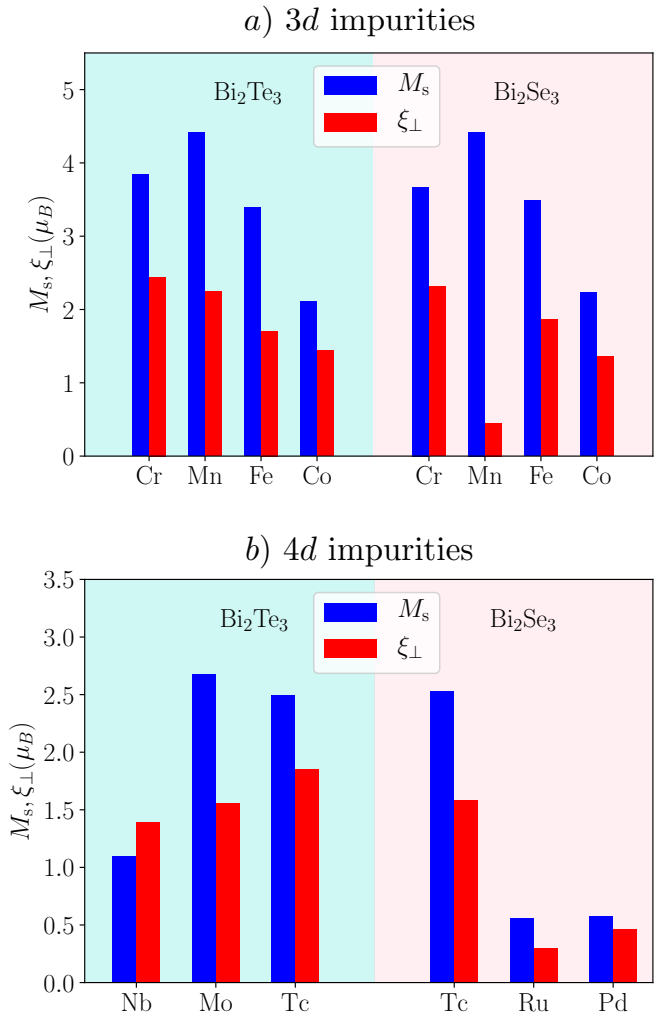

Figure 4.20: Mean value of the transversal ZPSF $\xi_\perp$ and spin moment M_s of (a) $3d$ and (b) $4d$ impurities embedded in Bi_2Te_3 and Bi_2Se_3. The transversal ZPSF are of the same order of magnitude as M_s. The ratio between $\xi_\perp$ and M_s is larger for the $4d$ elements compared to the $3d$ ones.

Element	$M^{\mathrm{s}}(\mu_{\mathrm{B}})$	$\xi_{\perp}$	$\mathcal{K}_{\mathrm{Susc}}$	$\mathcal{K}_{\mathrm{sf}}$	$\frac{\mathcal{K}_{\mathrm{Susc}}-\mathcal{K}_{\mathrm{sf}}}{\mathcal{K}_{\mathrm{Susc}}}$
Cr (Bi_2Te_3)	3.844	2.442	0.959	0.316	67%
Cr (Bi_2Se_3)	3.671	2.315	0.088	0.029	66%
Mn (Bi_2Te_3)	4.412	2.245	-0.201	-0.098	51%
Mn (Bi_2Se_3)	4.421	0.453	0.005	0.005	3%
Fe (Bi_2Te_3)	3.395	1.706	4.302	2.137	50%
Fe (Bi_2Se_3)	3.482	1.859	6.018	2.739	54%
Co (Bi_2Te_3)	2.109	1.436	-6.725	-1.872	72%
Co (Bi_2Se_3)	2.231	1.354	-5.894	-2.143	63%

Table 4.13: Comparison between the MAE obtained from the static magnetic susceptibility with and without including the contributions of the ZPSF for $3d$ elements embedded in Bi_2Te_3 and in Bi_2Se_3. The MAE of Co is the most affected with a reduction of ~ 4.8 meV.

to magnetization ratio ($\frac{\xi_{\perp}}{M_{\mathrm{s}}}$) is larger in comparison with the $3d$ elements. Similar results were obtained for $3d$ and $4d$ adatoms on Ag(100) in Ref. [42]. The presence of such large ZPSF — in the order of magnitude of the spin moments — are capable of altering their properties such as the MAE. This is addressed in the next section.

4.7.7 Renormalization of the MAE from the ZPSF

Here, we focus on the impact of the ZPSF on the magnetic anisotropy of the impurities. Since the ZPSF make the spin moment deviate from its equilibrium orientation (easy axis), they cause a reduction of the MAE. The renormalized value of the MAE $\mathcal{K}_{\mathrm{sf}}$ was derived in Sec. 2.6.6 within the spin fluctuation theory of Moriya and reads:

$$\mathcal{K}_{\mathrm{sf}} = \mathcal{K}_{\mathrm{Susc}} \left(1 - \frac{3\xi_{\perp}^2}{M_{\mathrm{s}}^2 + 2\xi_{\perp}^2} \right) \quad . \tag{4.42}$$

We use the MAE $\mathcal{K}_{\mathrm{Susc}}$ extracted from the magnetic susceptibility that is also used to compute the fluctuations. Depending on the values of $\xi_{\perp}$ and M_{s}, the MAE can be considerably altered by the ZPSF. We show, in Table 4.13, a comparison between the MAE obtained with and without the ZPSF contribution for $3d$ impurities embedded in Bi_2Te_3 and Bi_2Se_3. For the Bi_2Te_3 case, the large amount of ZPSF affects considerably the MAE of Cr, Mn and Fe, despite the large values of their spin moments. The MAE of Co is the most affected one, with a reduction of ~ 4.8 meV (72%) due to the large ZPSF combined with a relatively small spin moment (the smallest spin moment for the considered $3d$ elements). For the Bi_2Se_3 case, the MAE of Cr is small but still affected by the fluctuations. The MAE of Mn is very weak and is unaffected since the ZPSF are one order of magnitude smaller than the spin moment. The MAE of Fe and Co is considerably affected, with a reduction of ~ 3.5 meV.

Finally, we investigated the impact of the ZPSF on the MAE of $4d$ elements embedded in Bi_2Te_3 and Bi_2Se_3. The obtained results are shown in Table 4.14. In the Bi_2Te_3 host, the most affected element is Nb, where the MAE switches sign due to large fluctuations and a rather small magnetic moment $M_{\mathrm{s}} = 1.1\ \mu_{\mathrm{B}}$. The MAE of Tc and Mo is small,

Element	$M^{\mathrm{s}}(\mu_{\mathrm{B}})$	$\xi_{\perp}$	$\mathcal{K}_{\mathrm{Susc}}$	$\mathcal{K}_{\mathrm{sf}}$	$\frac{\mathcal{K}_{\mathrm{Susc}}-\mathcal{K}_{\mathrm{sf}}}{\mathcal{K}_{\mathrm{Susc}}}$
Nb (Bi_2Te_3)	1.097	1.395	4.090	-0.595	114%
Mo (Bi_2Te_3)	2.678	1.557	0.417	0.165	60%
Tc (Bi_2Te_3)	2.493	1.858	0.353	0.074	78%
Tc (Bi_2Se_3)	2.534	1.581	3.847	1.322	65%
Ru (Bi_2Se_3)	0.564	0.296	-8.189	-3.827	53%
Pd (Bi_2Se_3)	0.578	0.468	-0.431	-0.064	85%

Table 4.14: Comparison between the MAE obtained from the static magnetic susceptibility with and without including the contributions of the ZPSF for $4d$ elements embedded in Bi_2Te_3 and Bi_2Se_3. The MAE of Nb is the most affected with a reduction of ~ 4.7 meV due to ZPSF larger than the spin moment.

while their spin moment is twice the value obtained for Nb, resulting in a MAE that is less affected by the ZPSF. For the Bi_2Se_3 case, the reduction of the MAE for Tc is ~ 2.5 meV; Ru has a small spin moment and $\xi_{\perp} \sim \frac{M_{\mathrm{s}}}{2}$. Due to its large MAE, any small change in the quantity between parenthesis in Eq. (4.42) results in a considerable reduction of $\mathcal{K}_{\mathrm{sf}}$. Thus, for Ru the MAE diminishes by ~ 4.3 meV. Pd has also a small spin moment, with a weak MAE that is considerably altered by the ZPSF and $\xi_{\perp} \sim \frac{3M_{\mathrm{s}}}{4}$.

In Ref. [42], Azpiroz et *al.* calculated the renormalization of the MAE of $3d$ and $4d$ adatoms deposited on Cu(111) and Ag(001) surfaces due to ZPSF. They found that the fluctuations could change the direction of the easy axis (*i.e.* the sign of the MAE) in some cases, such as Co and Ru impurities deposited on a Cu(111) surface. The MAE for other elements like Fe, Mo and Tc was also reduced considerably. From our results, we find that there is a drastic impact on the MAE as well. The most altered element by the ZPSF is the Nb impurity embedded in Bi_2Te_3 for which the sign of the MAE also changes. Clearly, on the investigated topological insulators, the magnetic moments are more stable than the ones so far investigated on metals. However, the presence of in-gap states leads to higher fluctuations, which may destabilize the magnetic moments. Using the argument given in Ref. [81, 16] stating that a gap opening occurs when the magnetic moment points along the z-direction, we find that Co ($\mathcal{K}_{\mathrm{sf}} < 0$) is the most susceptible element to create a gap in Bi_2Te_3, while in the Bi_2Se_3 case, both Co and Ru would create a gap. However, these elements lead to an in-gap state filling locally the band gap.

4.8 Summary and outlook

In this chapter, we employed the KKR Green function method in real space to investigate $3d$ and $4d$ impurities embedded at a Bi site in Bi_2Te_3 and Bi_2Se_3 thin films and bulk. For both hosts, we found that the considered $3d$ impurities (Cr, Mn, Fe and Co) are all donors of electrons. For the $4d$ impurities which are more sensitive to their surroundings, we considered the following elements: Nb, Mo, Tc, Ru, Rh and Pd. All these impurities donate electrons as well. In the Bi_2Se_3 thin film, only Rh was found to be paramagnetic, while in the Bi_2Te_3 host, Ru and Pd are also paramagnetic. The electronic structure of some $3d$ and

$4d$ elements displayed in-gap states in the bulk band gap. They appear when the d peak is close to the bulk band edge. We showed from first principles and using a simple Anderson model that they arise solely from the hybridization with the bulk bands. Furthermore, we investigated the MAE for all the considered impurities. We demonstrated that for elements with a high occupation at the Fermi energy, such as Fe or Co, the magnetic force theorem breaks down. Reliable values of the MAE can only be obtained near self-consistency using linear response, for example.

We then computed the magnetic excitation spectra for the $3d$ and $4d$ adatoms. They display sharper resonances compared to the case where the same elements are embedded in a metallic environment. This is due to a lower hybridization and damping, resulting in higher lifetimes for the spin excitations (such as Mn for example). In addition to the damping, we also studied the nutation of the magnetization due to inertial effects. We showed that this contribution is important for some elements, such as Nb in Bi_2Te_3, where it leads to a noticeable shift in the resonance frequency. Finally, the magnetic susceptibility was used to compute the transversal ZPSF, which were found to be highly important. They can reach the same order of magnitude as the spin moments. We also found that such important ZPSF cause a reduction of the MAE — they can even lead to a sign change of the MAE for a Nb impurity in Bi_2Te_3.

The results set fourth in this chapter show that the magnetic doping of topological insulators results in a plethora of interesting effects. However, several aspects are left to be uncovered, such as the magnetic properties and dynamics of magnetic nanoclusters or full magnetic layers deposited on topological insulators. Furthermore, the dynamical magnetic susceptibility can be used to compute the electron-magnon self energies and provide access to the ISTS spectrum.

Chapter 5

Magnetic Skyrmions

Skyrmions were introduced in nuclear physics by Tony Skyrme [213]. They are topologically protected particle-like solutions for a system of interacting pions. In magnetism, Skyrmions are particle-like swirling chiral spin textures [68], which can be stabilized by the spin-orbit interaction. They are topologically protected because they cannot be continuously transformed to a different magnetic state (for example a ferromagnet). Recently, they raised a lot of interest due to their potential usage in spintronics [214, 69]. Magnetic Skyrmions and the topological surface states of a topological insulator discussed in the previous chapter are not foreign to each other, in the sense that both are topologically protected. This protection for topological surface states is reflected in an integer Chern number as discussed previously. Analogously, the topological protection in magnetic Skyrmions results in an integer topological charge or winding number. From the technological perspective, the ideal Skyrmions carrying spin information in a device should be individual Skyrmions (not a lattice of Skyrmions) with sub-10 nm size [69]. We address in this chapter the electronic structure of small magnetic Skyrmions (sizes < 3 nm) with the goal of understanding their fundamental electronic and magnetic properties in order to find new ways of detecting them by electrical or optical means.

This chapter is structured as follows: First, we introduce the basic notions about magnetic Skyrmions such as the topological charge or winding number. Second, we present simulations from first principles calculations of magnetic Skyrmions in a thin film constituted of a magnetic bilayer (Pd/Fe) deposited on the Ir(111) surface which is a heavy metal substrate with a strong spin-orbit interaction. Third, we establish the concept of tunneling spin-mixing magnetoresistance (TXMR) observed in the density of states of the Fe layer from first principles calculations and from the model perspective. We propose to use the TXMR effect for the all-electrical detection of Skyrmions in devices. Then, we discuss the presence of a chiral orbital magnetization (COM), which develops into a topological orbital magnetization (TOM) in large magnetic Skyrmions in Pd/Fe/Ir(111). The COM was already discussed in Sec. 3.9.6 in the context of magnetic nanostructures with a chiral spin texture. Finally, we establish a connection between the topological charge and the TOM in the limit of slowly varying magnetic textures.

The results on the TXMR presented in this chapter were published in Ref. [215]. Our main contribution to the paper consisted in uncovering the TXMR mechanism using multiple scattering theory and the Alexander-Anderson model. Part of the results on the chiral orbital magnetization were also published in Ref. [67]. In this paper, we performed the ab initio calculations for the density of states calculations which allowed a mapping into the tight-binding model used to compute the COM's. Moreover, we uncovered the COM's from first-principles calculations on realistic sub-5 nm Skyrmions.

5.1 Introduction to magnetic Skyrmions

Magnetic Skyrmions are observed in a wide variety of magnetic materials in bulk [70, 71, 216] and on surfaces (thin films) [72, 217]. An example of such a spin texture is depicted in Fig. 5.1, where the spin magnetic moments rotate smoothly from the Skyrmion core to point in the opposite direction at the edges. Skyrmions have been extensively investigated due to their possible use in the field of spintronics [214]. The current densities needed to move them are orders of magnitude smaller compared to conventional domain walls [75, 76]. Another appealing aspect of magnetic Skyrmions is their robustness against external perturbations thanks to their topological protection [218, 219]. A measure of the topological character of a magnetic Skyrmion is the so-called topological charge or winding number, which measures the number of times the magnetization rotates when the magnetic moments of the Skyrmion are mapped onto a sphere [220]:

$$\mathcal{Q} = \frac{1}{4\pi} \int \mathrm{d}\vec{r}\ \vec{e}_M \cdot \left(\frac{\partial \vec{e}_M}{\partial x} \times \frac{\partial \vec{e}_M}{\partial y} \right) \quad . \tag{5.1}$$

$\vec{e}_M$ is a unit vector which points in direction of the spin magnetic moment $\vec{M}$, and the integral is performed over the area containing the Skyrmion. For magnetic Skyrmions $\mathcal{Q}$ is an integer number. More precisely, for the chiral Skyrmions shown in Fig. 5.1 where the ferromagnetic background is anti-parallel to the z-axis, $\mathcal{Q} = 1$. The integrand in Eq. (5.1) represents the emergent field induced by the spin texture [220]. Due to this emergent field, when electrons flow through a Skyrmionic spin texture, they experience a topological Hall effect which deflects the electrons generating a transverse current [77]. The key ingredient for the stabilization of the chiral Skyrmions shown in Fig. 5.1 is the Dzyaloshinskii-Moriya (DM) interaction [51, 50, 58] discussed in detail in chapter 3. It arises in magnets with inversion symmetry breaking and in the presence of the spin-orbit interaction (SOI), for example in magnetic thin layers on top of heavy metals. The DM interaction favors non-collinear spin textures as seen in Eq. (3.42) and dictates the direction of rotation of the magnetic moments. The competition of the DM interaction, the isotropic exchange (first term in Eq. (3.42)) and external magnetic fields or magnetic anisotropy leads to the formation of magnetic Skyrmions.

One of the first experimental observations of magnetic Skyrmions in thin films on heavy metal substrates was done in Ref. [72] using spin-polarized STM (SP-STM) combined with first principles calculations for an Fe layer deposited on Ir(111) surface. However, Fe/Ir(111) is not an appealing system since it is challenging to change its rather stable topological state, which is the ground state [217]. In order to have individual Skyrmions,

one can add a monolayer of Pd on Fe/Ir(111) so as to change the ground state to a spin spiral state. When a magnetic field of $\sim$ 1 Tesla is applied a Skyrmion lattice is stabilized [73]. For higher field intensities, a phase with isolated sub-5 nm Skyrmions can be obtained [217].

5.2 Magnetic Skyrmions in Pd/Fe/Ir(111)

Here, we address the previously mentioned appealing case of a Pd layer deposited on a monolayer of Fe which is grown on an Ir(111) surface [215] considering an fcc-stacking. The presence of a heavy substrate such as Ir provides a strong SOI, which combined with the breaking of inversion symmetry at the interface gives rise to a non-vanishing DM interaction within the Fe layer [51, 50]. The competition between the ferromagnetic isotropic exchange interaction J and the DM interaction D determines the size and the chirality of the Skyrmion. For a certain range of applied magnetic field strengths, it has been experimentally shown that for Pd/Fe/Ir(111), Skyrmions with a diameter $D_{\text{sky}} \approx 1 - 5$ nm can be stabilized [221].

To model this system from first principles, we used the relativistic Korringa-Kohn-Rostoker Green function method with a full-potential treatment [96]. With this approach we can embed a Skyrmion, considered as a defect, into a ferromagnetic host. The magnetic Skyrmions, were modeled in the following way: first a self consistent calculation of the periodic ferromagnetic Pd/Fe/Ir(111) host system was performed. Afterwards, a real space cluster is created, in which the spin moment of a single Fe atom is reversed with respect to the ferromagnetic background. Using the embedding technique then the magnetic moments in a certain area (depending on the size of the Skyrmion) are allowed to relax, whilst the rest are kept fixed. The Skyrmion profile is obtained self-consistently, and the contribution of the ferromagnetic background is included by the host Green function.

Three different Skyrmions sizes were considered [215]: Skyrmions containing 19, 37 and 71 Fe atoms. The Skyrmion spin structures obtained self-consistently are shown in Fig. 5.1. For all the three different sizes, the spin moment rotates form the core to edges while its amplitude remains constant $M \simeq 2.7\,\mu_{\text{B}}$. The Skyrmion profiles (cut in the radial direction) show that the rotation angles between two magnetic moments $\mathrm{d}\theta_{ij}$ strongly depends on the Skyrmion size. Nevertheless, the non-collinearity is always higher near the Skyrmion core for the sizes considered, and this leads to a lot of interesting features in the electronic structure, some of which will be described in the next sections.

5.3 Tunneling spin-mixing magnetoresistance

The detection of magnetic Skyrmions is paramount for any potential application, specially in the of case of Skyrmions at the nano-scale, such as the ones present in Pd/Fe/Ir (111). Hence, a method with high spatial resolution, such as the Scanning Tunneling Microscopy (STM) would be ideal. Using a spin-polarized tip to detect non-collinear spin textures is possible [72]. However, the technology involving the manufacturing and use of a spin-polarized electrode is not necessarily straightforward. In this section, we describe the detection of non-collinear spin structures such as Skyrmions using a non-magnetic tip.

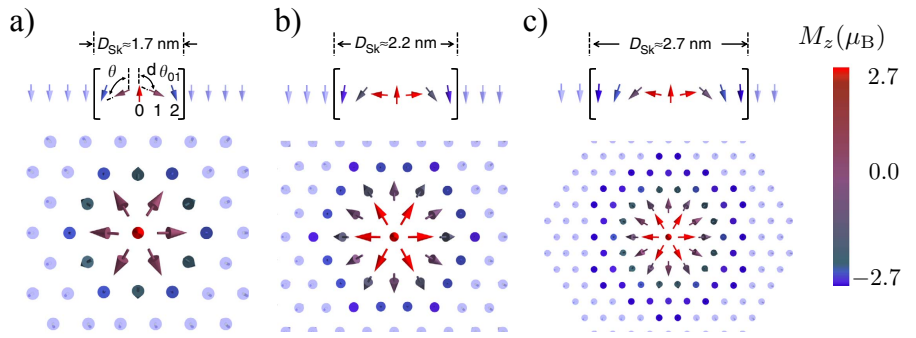

Figure 5.1: Spin texture of magnetic Skyrmions of different sizes, containing: a) 19 Fe atoms, b) 37 Fe atoms and c) 71 Fe atoms from Fe layer of Pd/Fe/Ir(111). The spin moments rotate smoothly from the center to the edges to point in the opposite direction. The light blue cones represent the ferromagnetic background in which the Skyrmion is embedded. The magnetic moments induced in the surrounding Pd and Ir atoms are not shown. This figure was taken from Ref. [215].

In other words, we propose to use an all-electrical detection scheme, which in principle is not limited to electrodes used in STM. This is achieved by using the tunneling spin-mixing magnetoresistance (TXMR), which we recently discovered [215]. This effect was also observed experimentally [222].

In the Tersoff-Hamann model [223], the differential conductance $\frac{\mathrm{d}I}{\mathrm{d}V}$ is related to the local density of states (LDOS) of the surface via:

$$\frac{\mathrm{d}I}{\mathrm{d}V} \propto n_{\mathrm{S}}(\vec{r}_{\mathrm{tip}}, \varepsilon_{\mathrm{F}} + eV)\, n_{\mathrm{T}} \quad , \tag{5.2}$$

where $n_{\mathrm{S}}(\vec{r}_{\mathrm{tip}}, \varepsilon_{\mathrm{F}} + eV)$ is the LDOS of the surface at the position of the tip, $\vec{r}_{\mathrm{tip}}$, and at an energy $\varepsilon_{\mathrm{F}} + eV$, where ε_{F} is the Fermi energy, when using a bias voltage V. The tip is considered as a geometrical point within this model and its LDOS n_{T} is a constant. Due to the large SOI in the Ir substrate, the orientation of the spin moment has an influence on the LDOS. We found that other mechanisms such as non-collinear magnetism can have an impact on the LDOS. Thus, we distinguish in the following two different possible mechanisms:

The first mechanism consists of the so-called tunneling anisotropic magnetoresistance (TAMR), where the LDOS depends on the polar angle θ_i between the spin magnetic moment $\vec{M}_i$ and the z-axis which is perpendicular to the surface. TAMR was discussed for Fe thin films on W(110) in Ref. [224], where they measured different scanning tunneling spectroscopy (STS) signals with a nonmagnetic tip for magnetic domains and domain walls, in which the spin structures rotate continuously into the opposite direction compared to the previous magnetic domain. TAMR is an effect induced by a spin rotation with respect to the z-axis in presence of the SOI, similarly to the anisotropic magnetoresistance discussed in Sec. 3.8.6.

In the second mechanism a mixing between the majority and minority spin channels occurs due to the non-collinearity among the magnetic moments. This effect depends then

on the relative angle $\mathrm{d}\theta_{ij} = \theta_i - \theta_j$ between different magnetic moments $\vec{M}_i$ and $\vec{M}_j$. It can be present even in absence of the SOI. This mechanism can be used as a local probe for the magnetization in complex magnetic textures such as Skyrmions since it relates the LDOS to $\mathrm{d}\theta_{ij}$. In some cases it is possible to separate the contributions of the TAMR and the contribution due to the non-collinearity to the STS signal. As an example, we consider a homogeneous spin spiral, the angle between each magnetic moment $\vec{M}_i$ and its neighbors $\vec{M}_j$ is always the same $\mathrm{d}\theta_{ij} = \mathrm{d}\theta$, thus, the non-collinearity contribution is the same for all the atoms contained in the spin spiral, while, the TAMR depends on the direction of each magnetic moment $\vec{M}_i$ with respect to the surface normal and leads to a different STS signal. Both the TAMR and the non-collinear (NC) contribution can subsumed as TXMR.

The TXMR is linked to the LDOS of the substrate. We show in Fig. 5.2a the LDOS for the minority (full lines) and majority spin channels (dashed lines) of the Fe atoms (constituting the Skyrmion shown in Fig. 5.1b). Note that the majority and minority spin channels are defined according to the local spin frame of reference for every Fe atom. Fig 5.2a shows the LDOS for different Fe atoms, labeled from (0-3) depending on their location with respect to the Skyrmion core (see Fig. 5.2c), as well as the LDOS on the ferromagnetic (FM) background, *i.e.* away from the Skyrmion (see Fig. 5.2c). The resonant states located between $0.5 - 1.0$ eV above ε_F represent the minority spin d-band of the Fe atoms, where we can clearly see an increase of the splitting of the $3d$-peaks when moving from the central Fe atom (Fe 0) antiferromagnetically coupled to its nearest neighbors towards the Skyrmion edges (Fe 3) coupled rather ferromagnetically as shown in Fig. 5.2c. The splitting between the two peaks is around 0.8 eV in the ferromagnetic background and changes as a function of the site (angle), which leads to the TXMR effect. Similar splittings are observed in majority d-band of the Fe atoms located at -1.0 eV, but the effect is smaller compared to the minority spin channel.

The d-peaks in the minority spin channel of the Fe layer hybridize with the sp-states present in the Pd layer. The d_{z^2} component from the Fe hybridizes the most and leads to Fe-Pd-spd_{z^2} hybrid states, which we call Pd-d_{z^2} states. They are localized in the Pd layer with a resonance around $\varepsilon \sim 0.4$ eV as shown in Fig. 5.2b. This Pd-d_{z^2} states of the surface Pd layer have the adequate orbital symmetry to decay into the vacuum and affect considerably the LDOS as displayed in Fig. 5.2b. The vacuum LDOS can be measured experimentally using all-electrical STS measurements. Furthermore, the splittings of the resonances of the LDOS as a function of the magnetic moments orientation propagate to the vacuum. The TXMR is measured in the vacuum layer and it can be defined at each site $\vec{r}$ as:

$$\mathrm{TXMR}(\vec{r}) = \frac{\mathrm{LDOS}^{\mathrm{vac}}_{\mathrm{FM}}(\vec{r}) - \mathrm{LDOS}^{\mathrm{vac}}_{\mathrm{Sky}}(\vec{r})}{\mathrm{LDOS}^{\mathrm{vac}}_{\mathrm{FM}}(\vec{r})} \times 100\% \quad . \tag{5.3}$$

$\mathrm{LDOS}^{\mathrm{vac}}_{\mathrm{FM}}$ is the LDOS in the vacuum above the ferromagnetic background away from the Skyrmion, while $\mathrm{LDOS}^{\mathrm{vac}}_{\mathrm{Sky}}(\vec{r})$ is the LDOS in the vacuum above a site located at position $\vec{r}$. In an STS measurement, one can select an energy window for which the TXMR is large. We show in Ref. [215] that for $\varepsilon \sim 0.5$ eV above ε_F, TXMR can reach 40% when the SOI is turned off and decreases to 20% in presence of the SOI. In other words, SOI can reduce the efficiency of the effect.

To understand the occurrence of these splittings within the LDOS of the Fe atoms and their relation to the non-collinearity of the magnetic moments and to the presence

of the SOI, we derive in the following an analytical expression connecting the LDOS to the opening angles between to magnetic moments $\mathrm{d}\theta_{ij}$ using multiple scattering theory. We then address the energy-dependence of these splittings using the Alexander-Anderson model [225] generalized to include non-collinear magnetism.

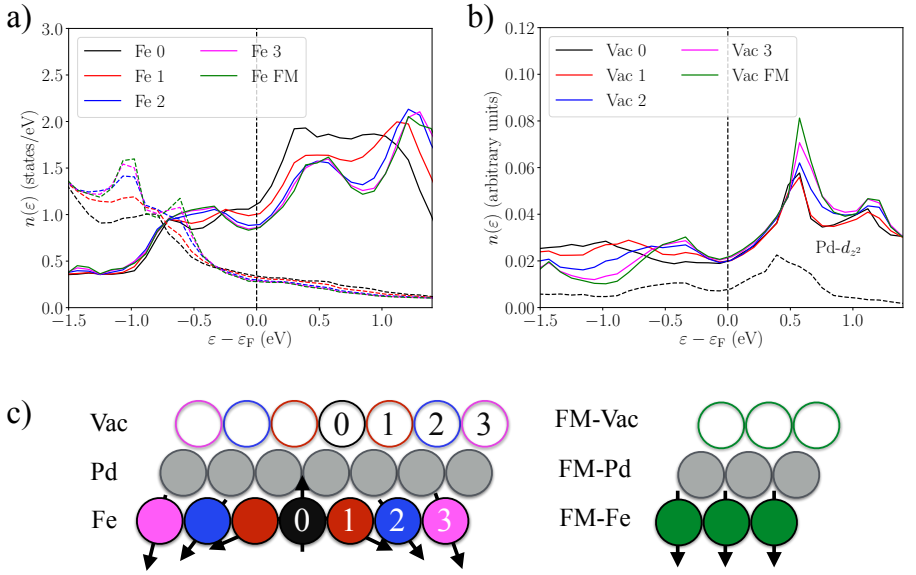

Figure 5.2: a) LDOS for the minority spin channel (full lines) and majority spin channel (dashed lines) of Fe atoms with magnetic moments pointing in different directions along the Skyrmion radius (see Fig. 5.1b). There is an increase of the splitting of the $3d$-peaks when moving from Fe-0 towards Fe-3. b) The change of the LDOS of the Fe atoms leads to a change in the LDOS of the vacuum layer through the hybridization with the Pd states. The dark dashed line represents the Pd-d_{z^2} state in the ferromagnetic configuration. c) On the left side view of the Pd/Fe/Ir(111) slab displaying the Skyrmion profiles and indicating the labeling of the Fe atoms from the center to the edges. On the right side we show the Pd/Fe/Ir(111) slab in the ferromagnetic configuration. The temperature broadening used here is smaller than the one used in Ref. [215].

5.3.1 TXMR from multiple scattering theory

We now use multiple scattering theory (see Sec. 2.4) to derive analytically the angular dependence of the TXMR according to the orientation of the magnetic moments [215]. We must compute the change in the LDOS, $\Delta n(\vec{r}, \varepsilon)$, at a position, $\vec{r}$, due to a change in the magnetic moment orientation. $\Delta n(\vec{r}, \varepsilon)$ can be decomposed into two contributions: the first one is due to the TAMR induced by the SOI and the second contribution is caused by the non-collinearity among the spin magnetic moments. The angular dependence of $\Delta n(\vec{r}, \varepsilon)$ due to the SOI is already known in the literature [224, 226, 227] and it can be

written as:

$$\Delta n(\vec{r}_i, \varepsilon) = N(\vec{r}_i, \varepsilon)\, \sin^2 \theta_i \quad , \tag{5.4}$$

where $N(r_i, \varepsilon)$ is a function that depends on the site position, $\vec{r}_i$, and the energy ε. θ_i is the polar angle of the spin magnetic moment $\vec{M}_i$ at site i. Eq. (5.4) shows that the TAMR effect is proportional to $\sin^2 \theta_i$ reminiscent of the magnetocrystalline anisotropy shown in Eq. (2.86). On the other hand, in the absence of the spin-orbit interaction $\Delta n(\vec{r}, \varepsilon)$ can be related to the Green function via (see Sec. 2.3.1):

$$\Delta n(\vec{r}_i, \varepsilon) = -\frac{1}{\pi} \operatorname{Im} \operatorname{Tr} \left(\boldsymbol{G}_{ii}^{\mathrm{NC}}(\varepsilon) - \boldsymbol{G}_{ii}^{\mathrm{FM}}(\varepsilon) \right) \quad . \tag{5.5}$$

$\boldsymbol{G}_{ii}^{\mathrm{NC}}(\varepsilon)$ is the Green function of the non-collinear state at site i, while $\boldsymbol{G}_{ii}^{\mathrm{FM}}(\varepsilon)$ is the Green of the ferromagnetic state (where the spin moments are oriented along the z-direction) at site i. The bold symbols indicate that the Green function has the spin structure indicated in Eq. (2.28). $\boldsymbol{G}_{ii}^{\mathrm{NC}}(\varepsilon)$ and $\boldsymbol{G}_{ii}^{\mathrm{FM}}(\varepsilon)$ are related to each other via the following Dyson equation:

$$\boldsymbol{G}_{ii}^{\mathrm{NC}}(\varepsilon) = \boldsymbol{G}_{ii}^{\mathrm{FM}}(\varepsilon) + \sum_j \boldsymbol{G}_{ij}^{\mathrm{FM}}(\varepsilon)\, \Delta \boldsymbol{V}_j\, \boldsymbol{G}_{ji}^{\mathrm{NC}}(\varepsilon) \quad , \tag{5.6}$$

and,

$$\Delta \boldsymbol{V}_i = \frac{V_i^{\uparrow\uparrow} - V_i^{\downarrow\downarrow}}{2} (\vec{\boldsymbol{\sigma}} \cdot \vec{e}_{M_i} - \boldsymbol{\sigma_z}) \quad . \tag{5.7}$$

Assuming that the nonmagnetic part of the potential (*i.e.* $\frac{V_i^{\uparrow\uparrow} + V_i^{\downarrow\downarrow}}{2}$) and the length of the magnetic part (*i.e.* $\frac{V_i^{\uparrow\uparrow} - V_i^{\downarrow\downarrow}}{2}$) remain unchanged when going from the ferromagnetic configuration to the non-collinear one, $\Delta \boldsymbol{V}_i$ describes the change of the potential upon rotation of the magnetic moments. $\vec{\boldsymbol{\sigma}}$ is the Pauli vector defined Sec. 2.2.2 and $\vec{e}_{M_i}$ is a unit vector pointing in the direction of $\vec{M}_i$. We now perform an expansion of Eq. (5.6) into Born series to second order in $\Delta \boldsymbol{V}_i$ and obtain:

$$\begin{aligned} \boldsymbol{G}_{ii}^{\mathrm{NC}}(\varepsilon) = \boldsymbol{G}_{ii}^{\mathrm{FM}}(\varepsilon) &+ \sum_j \boldsymbol{G}_{ij}^{\mathrm{FM}}(\varepsilon)\, \Delta \boldsymbol{V}_j\, \boldsymbol{G}_{ji}^{\mathrm{FM}}(\varepsilon) \\ &+ \sum_{jk} \boldsymbol{G}_{ij}^{\mathrm{FM}}(\varepsilon)\, \Delta \boldsymbol{V}_j\, \boldsymbol{G}_{jk}^{\mathrm{FM}}(\varepsilon)\, \Delta \boldsymbol{V}_k\, \boldsymbol{G}_{ki}^{\mathrm{FM}}(\varepsilon) + \ldots \quad . \end{aligned} \tag{5.8}$$

By taking the trace over the spin degree of freedom and using basic properties of the Pauli matrices $\boldsymbol{\sigma}_i$, we can easily write:

$$\begin{aligned} \Delta n(\vec{r}_i, \varepsilon) \simeq &\sum_j C_1^{iji}(\varepsilon)\, (1 - e_{M_i}^z) \\ &+ \sum_{jk} C_2^{ijki}(\varepsilon)\, \left[(\vec{e}_{M_j} \cdot \vec{e}_{M_k}) - (e_{M_j}^z + e_{M_k}^z) + 1 \right] + \ldots \quad . \end{aligned} \tag{5.9}$$

Where $C_1^{iji}(\varepsilon)$ and $C_2^{ijki}(\varepsilon)$ are coefficients of first and second order given by a trace over the orbital component of products of $\boldsymbol{G}_{ij}^{\mathrm{FM}}(\varepsilon)$ and $\Delta \boldsymbol{V}_i$. The dot product in Eq. (5.9) shows explicitly that TXMR depends on the relative angle between the spin moments located at different sites j and k.

5.3.2 TXMR in the Alexander-Anderson model

In order to understand the splitting that occurs in the $3d$-peaks of the LDOS for the Fe atoms shown in Fig. 5.2a, we consider the Alexander-Anderson model [225]. It was originally made for two atomic sites with one orbital per site and spin splitted bands, this model allows both ferromagnetic and antiferromagnetic exchange mechanisms. We generalize the model for non-collinear systems to compute the LDOS $n(\vec{r}_i, \varepsilon)$. The magnetic moment on one atomic site is fixed while the second one is rotating. The aim is to compare the LDOS obtained within the model to the one computed from first principles shown in Fig. 5.2a.

Assuming that we have two Fe atoms located at the neighboring sites i and j with a single atomic orbital d_{z^2} centered on each site. The effect of the SOI interaction was already addressed in Ref. [228], thus, it is not included in the model. The hopping between the sites i and j is taken to be $t_{ij} = 0.4$ eV in order to fit the splitting obtained from first principles. Our focus is in understanding the spin-splitting observed in the minority spin channel. Thus, we neglect in practice the contribution of the majority spin channel, which is almost fully occupied. We consider the center of the minority spin channel located at $\varepsilon_i^{\downarrow\downarrow} = \varepsilon_j^{\downarrow\downarrow} = 0.4$ eV above ε_F. The broadening of the states is set to $\eta = 0.5$ eV to have a good agreement with the first principles results. First, we numerically calculate $\boldsymbol{G}_{ii}(\varepsilon)$:

$$\boldsymbol{G}_{ii}(\varepsilon + \mathrm{i}\eta) = \left[\frac{1}{\varepsilon - \underline{\boldsymbol{H}} + \mathrm{i}\eta}\right]_{ii}, \tag{5.10}$$

$\boldsymbol{G}_{ii}(\varepsilon + \mathrm{i}\eta)$ is the Green function at site i, where $\underline{\boldsymbol{H}}$ is the tight-binding Hamiltonian of the system, it is a matrix in spin space and atom index i. For a two sites model with ferromagnetically coupled moments on each site i and j, it reads:

$$\underline{\boldsymbol{H}} = \begin{pmatrix} \varepsilon_i^{\uparrow\uparrow} & 0 & t_{ij} & 0 \\ 0 & \varepsilon_i^{\downarrow\downarrow} & 0 & t_{ij} \\ t_{ij} & 0 & \varepsilon_j^{\uparrow\uparrow} & 0 \\ 0 & t_{ij} & 0 & \varepsilon_j^{\downarrow\downarrow} \end{pmatrix} \quad . \tag{5.11}$$

$\underline{\boldsymbol{H}}$ can be written in terms of site diagonal and non-diagonal blocks as:

$$\underline{\boldsymbol{H}} = \begin{pmatrix} \boldsymbol{H}_{ii} & \boldsymbol{H}_{ij} \\ \boldsymbol{H}_{ji} & \boldsymbol{H}_{jj} \end{pmatrix} \quad . \tag{5.12}$$

When considering that the spin moment at site j is rotating with an angle θ_j, the rotated Hamiltonian $\underline{\boldsymbol{H}}'$ is given by:

$$\underline{\boldsymbol{H}}' = \begin{pmatrix} \boldsymbol{H}_{ii} & \boldsymbol{H}_{ij} \\ \boldsymbol{H}_{ji} & \boldsymbol{H}'_{jj} \end{pmatrix} \quad \text{with} \quad \boldsymbol{H}'_{jj} = \boldsymbol{U}_j \boldsymbol{H}_{jj} \boldsymbol{U}_j^\dagger \quad . \tag{5.13}$$

Where $\boldsymbol{U}_j^\dagger = \cos\frac{\theta_j}{2}\mathbb{1} + \mathrm{i}\sin\frac{\theta_j}{2}\boldsymbol{\sigma}_y$ rotates the spin moment at a site j with an angle θ_j away from the z-axis. The LDOS on site i in presence of non-collinear magnetic moments is given in terms of $\boldsymbol{G}_{ii}(\varepsilon)$ as:

$$n(\vec{r}_i, \varepsilon) = -\frac{1}{\pi} \operatorname{Im} \operatorname{Tr}_\sigma \{\boldsymbol{G}_{ii}(\varepsilon)\} \quad . \tag{5.14}$$

We show in Fig. 5.3 the results obtained for $n(\vec{r}_i, \varepsilon)$ for five different orientations of the magnetic moment at site j. We see a splitting of the d-resonance in the LDOS for the minority spin channel while going from the antiferromagnetic (AFM) configuration to the ferromagnetic (FM) one, where we recover the behavior of the LDOS in the Alexander-Anderson model for FM and AFM configurations [225]. In the FM configuration the hybridization between the d_{z^2} orbitals of the two sites i and j, induces a splitting of the initial orbital into two states a bonding and anti-bonding states. The energy difference between these two states is $\sim 2\,t_{ij}$. For the antiferromagnetic configuration the minority and majority spin channel resonances repel each other [109]. This leads to an additional shift between the the two resonances given by $2\,t_{ij}^2/(\varepsilon_i^{\downarrow\downarrow} - \varepsilon_i^{\uparrow\uparrow})$. However, the shift is expected to be very small considering the large exchange splitting between the orbitals.

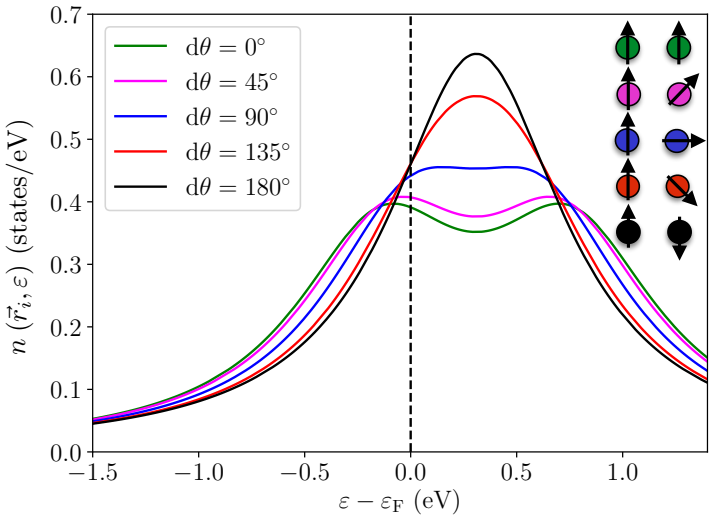

Figure 5.3: Local density of states in the generalized Alexander-Anderson model for an Fe at site i connected to an Fe atom at site j. The spin moment of the Fe atom at site j rotates from parallel to z direction (FM) to the opposite direction (AFM), five different orientations where considered. We see an apparent splitting of the single d -peak in the antiferromagnetic configuration into bonding and anti-bonding d-peaks in the ferromagnetic configuration.

5.4 Chiral orbital magnetization

Previously, we discussed the possibility of probing the spin texture of a magnetic Skyrmion using STM with a non-magnetic tip. The goal of this section is to address the possibility of using X-ray magnetic circular dichroism (XMCD) as a magnetic microscopy technique to detect Skyrmions. The XMCD sum rules [229, 208] give access to the net spin moment (M) and to the orbital moment (M^{orb}) individually. We will show in the following that with XMCD one can access two types of contributions to the orbital moments: one is

driven by the SOI and the other one is driven by the non-collinear alignments of the spin moment. The latter one can be used to discriminate Skyrmions with opposite topological charges ($\mathcal{Q}$) [67].

In order to understand the connection between non-collinear spin textures and orbital moments, we start from the isolated atom. The Hund's rules dictate the value of the orbital moments as a function of the atomic states filling. However, when an atom is introduced to a solid, it is subjected to an electrostatic field induced by the surrounding atoms. This field is known as the crystal field, which causes a quenching of the orbital moment. The orbital moment can be recovered if the SOI (discussed in Sec. 2.4.5) is strong enough to lift the orbital degeneracies.

An alternative way to lift the orbital degeneracies without the SOI is via non-collinear magnetism [67]. This was discussed in Sec. 3.9.6 in the context of magnetic impurities deposited on a two dimensional free electron gas. We found that, when the spin magnetic moments have a non-vanishing scalar chirality $\mathcal{C}_{ijk}$ defined by

$$\mathcal{C}_{ijk} = \vec{e}_{M_i} \cdot (\vec{e}_{M_j} \times \vec{e}_{M_k}) \quad , \tag{5.15}$$

we observe finite bound state currents (*i.e* a lifting of the orbital degeneracy). We also demonstrated within the model the relation between the induced orbital magnetization at a point, $\vec{r}$, in the electron gas, and the scalar chirality:

$$M_z^{\text{orb}}(\vec{r}) \approx \mathcal{F}(\vec{r})\, \mathcal{C}_{ijk} \quad , \tag{5.16}$$

where only the z-component of the orbital magnetization, $M_z^{\text{orb}}(\vec{r})$, is non-zero assuming that the electrons are confined in 2D. $\mathcal{F}(\vec{r})$ is an oscillatory function decaying with r (distance from the magnetic spin texture). A similar connection between the orbital magnetization and $\mathcal{C}_{ijk}$ for non-collinear magnetic systems without SOI exists. The first observation of a finite orbital magnetization without SOI was done in Ref. [230] for a magnetic vortex composed of Fe atoms, using first principles calculations. More recent investigations have been performed on periodic systems, for example a Mn monolayer deposited on a Cu(111) surface, where the magnetic ground state is an antiferromagnetic $3Q$ configuration, which displays a non-zero orbital magnetization without SOI, only relying on the chirality of the spin texture [231]. We refer to this orbital magnetization as chiral orbital magnetization (COM). Its connection to the scalar chirality makes the COM a local probe for the chirality of complex magnetic spin textures such as Skyrmions. Using a tight-binding model for magnetic Skyrmions parametrized from our first principles simulations of Pd/Fe/Ir(111), we computed the COM for different Skyrmion sizes up to ~ 8.0 nm wide and showed a clear connection between the COM and the Skyrmion emergent field which maps the local scalar spin chirality $\mathcal{C}_{ijk}$ [67].

5.4.1 Chiral orbital magnetization in Pd/Fe/Ir(111)

We now address the COM computed for magnetic Skyrmions found in Pd/Fe/Ir(111) using the KKR Green function method (see Sec. 2.4). First, the z-component for orbital magnetization (M_z^{orb}) in the Fe layer computed in presence of the SOI is shown in Fig. 5.4a. The orbital moment is parallel to the spin moment depicted in Fig. 5.1b. M_z^{orb} has a maximal amplitude at the edges or at the core of the Skyrmion, where the spin moments points

parallel or anti-parallel to the z-axis, respectively. We consider now the same system and turn-off the SOI, then compute the orbital magnetization. As predicted earlier [230, 67], we find a finite orbital magnetization shown in Fig. 5.4b. The latter one emerges solely from the non-collinearity between the spin moments (see Sec. 3.9.6). Therefore, it vanishes at the edges of the Skyrmion, where the magnetic moments are in a collinear configuration, and peaks at the Skyrmion center. The COM's are one order of magnitude smaller than the orbital moments obtained in presence of the SOI. The COM does not follow the spin moment but follows the scalar chirality and is highest in the non-collinear region (relevant part).

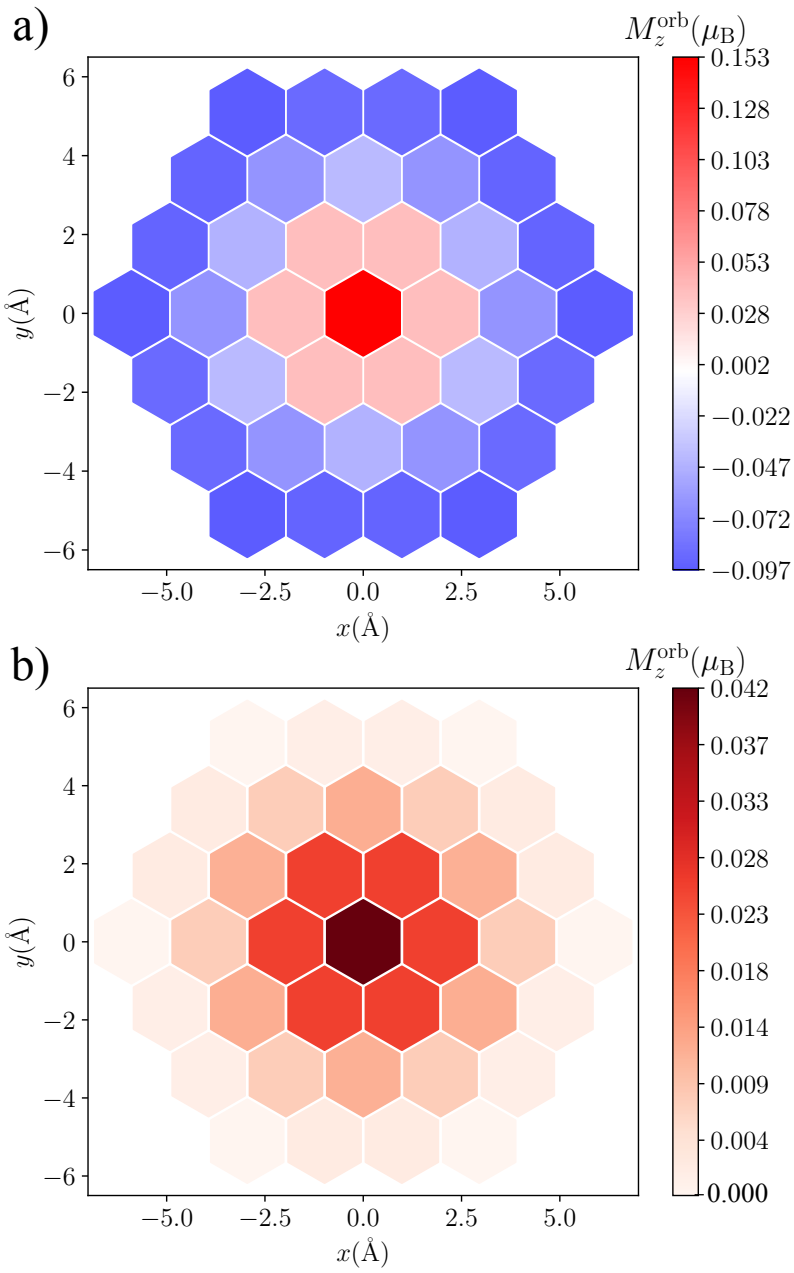

Figure 5.4: Map showing the distribution of the orbital magnetization on each Fe atom represented by a hexagon for the Skyrmion depicted in Fig. 5.1b in Pd/Fe/Ir(111). a) Orbital magnetization for the Skyrmion in presence of SOI and b) without SOI.

We then analyzed the dependence of the orbital magnetization regarding the size of the Skyrmions. We considered the three different sizes shown in Fig. 5.1 containing 19, 37 and 71 Fe atoms, respectively. First in presence of the SOI (blue curve in Fig. 5.5), there is an increase of the orbital magnetization when the Skyrmion size increases. This can be explained in the following way: when the number of Fe atoms increases, the system is provided with more rather ferromagnetically aligned Fe atoms, the orbital moments then add up because close to the edges they point in the same direction as shown in Fig. 5.4a. Second, in absence of the SOI for the COM (red curve in Fig. 5.5), we notice an increase of the COM of the Skyrmion. We also observe the same behavior within a tight binding model [67], where we found that the COM increases when increasing the size of the Skyrmion, reaching a constant value for Skyrmions with $D_{\text{sky}} \gtrsim 5.0$ nm as shown in Fig. 5.6a. Therefore, for large Skyrmions the COM is quantized by inheriting a topological nature, we call it a topological orbital magnetization (TOM). A quantization of the topological Hall conductivity of Skyrmions was also observed in Ref. [232].

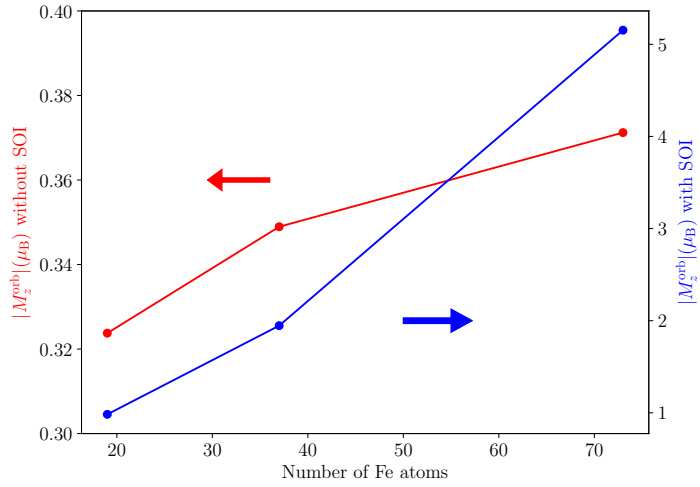

Figure 5.5: Evolution of the orbital magnetization as a function of the number of Fe atoms in the Skyrmion for three different sizes (19, 37 and 71 atoms). A comparison between the orbital magnetization with and without spin-orbit interaction is shown.

In order to detect the chiral contribution to orbital moment within XMCD, we suggest this experimental protocol: First, we consider Pd/Fe/Ir(111) which hosts magnetic Skyrmions and apply a strong external magnetic field driving the system into a ferromagnetic (FM) state. Second, using XMCD one can measure the net spin and orbital moments, $M(\text{FM})$ and $M^{\text{orb}}(\text{FM})$. In this ferromagnetic configuration the net orbital moment is driven by SOI and is proportional to $M(\text{FM})$, *i.e.* $M^{\text{orb}}(\text{FM}) = \alpha M(\text{FM})$ as discussed in Ref. [67]. When the intensity of the external magnetic field is reduced then Pd/Fe/Ir(111) enters into the Skyrmion (Sk) phase. Then, the net orbital moment for the Skyrmion is

given by $M^{\text{orb}}(\text{Sk}) = \alpha M(\text{Sk}) + M^{\text{orb}}(\text{COM})$, where $M^{\text{orb}}(\text{COM})$ is due to the chiral contribution. Finally, when assuming that the proportionality constant in the Skyrmion phase is the same as in the ferromagnetic one, then the chiral orbital magnetization ratio is given as:

$$\text{COMR} = \frac{M^{\text{orb}}(\text{Sky})}{M^{\text{orb}}(\text{FM})} - \frac{M^{\text{orb}}(\text{Sky})}{M^{\text{orb}}(\text{FM})} \simeq \frac{M^{\text{orb}}(\text{COM})}{M^{\text{orb}}(\text{FM})}. \tag{5.17}$$

where COMR is the COM ratio. For large Skyrmions, the COM ratio becomes a TOM ratio, which is found to be proportional to $\mathcal{Q}$ as shown in Fig. 5.6b.

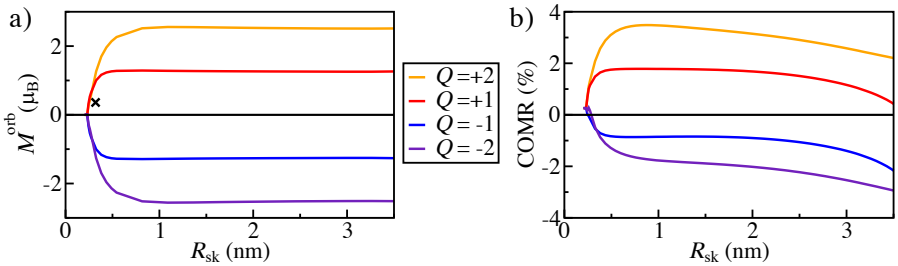

Figure 5.6: a) Net chiral orbital magnetization (COM) for Skyrmionic structures with different topological charges [67] without SOI. b) COM ratio in presence of the SOI for the same structures as in (a). The net COM obtained from our first principles simulations for the largest Skyrmion (Fig 5.1 .c) is indicated ($\times$) in (a). This figure was taken from Ref. [67]. Note that the convention defining the size of the Skyrmions has been changed with respect to the one used in Fig. 5.1.

5.4.2 Connection between TOM and topological charge

Here, we discuss the connection between the TOM and the topological charge. We have shown in Fig. 5.5 that the COM is increasing with the size of the Skyrmion. However, we have seen in Fig 5.6 that the COM is quantized for Skyrmions sizes $\gtrsim$ 5 nm . This can be understood by the following argument: The COM is proportional to the scalar chirality as shown previously in Eq. (5.16). Then, we consider the discretized version for the topological charge defined in Eq. (5.1). On a lattice $\mathcal{Q}$ is given as a sum over solid angles in each triangle obtained by triangulating the lattice [233]:

$$\mathcal{Q}_i = 2\,\tan^{-1}\left[\frac{\vec{e}_{M_j}\cdot(\vec{e}_{M_k}\times\vec{e}_{M_l})}{1+\vec{e}_{M_j}\cdot\vec{e}_{M_k}+\vec{e}_{M_j}\cdot\vec{e}_{M_l}+\vec{e}_{M_l}\cdot\vec{e}_{M_k}}\right] \quad . \tag{5.18}$$

$\mathcal{Q}_i$ is the solid angle formed by three spin moments located at sites $\{j,k,l\}$ defining the triangle i. For magnetic textures which are slowly changing in space, the term contained between brackets in Eq. (5.18) is small, thus, we can perform a Taylor expansion using $\tan^{-1}(x) \simeq x$ and obtain:

$$\mathcal{Q}_i \simeq 2\left[\frac{\vec{e}_{M_j}\cdot(\vec{e}_{M_k}\times\vec{e}_{M_l})}{1+\vec{e}_{M_j}\cdot\vec{e}_{M_k}+\vec{e}_{M_j}\cdot\vec{e}_{M_l}+\vec{e}_{M_l}\cdot\vec{e}_{M_k}}\right] \quad . \tag{5.19}$$

Always considering magnetic textures slowly varying in space, the angle between the magnetic moments is small, thus, $\vec{e}_{M_j} \cdot \vec{e}_{M_l} \simeq 1$ and the expression of $\mathcal{Q}_i$ simplifies even further:

$$\mathcal{Q}_i \simeq \frac{1}{2}\,\vec{e}_{M_j} \cdot (\vec{e}_{M_k} \times \vec{e}_{M_l}) \quad . \tag{5.20}$$

The topological charge is obtained by summing up the solid angles of all the triangles contained in the Skyrmion:

$$\mathcal{Q} = \frac{1}{4\pi} \sum_{\triangle_i} \mathcal{Q}_i \quad . \tag{5.21}$$

Using Eq. (5.20), Eq. (5.21) and Eq. (5.16), we establish a link between the topological charge and TOM of the Skyrmion $M^{\text{orb}}_{z,\text{Sky}}$:

$$M^{\text{orb}}_{z,\text{Sky}} \propto \mathcal{Q} \quad . \tag{5.22}$$

Considering that $\mathcal{Q}$ is quantized for Skyrmions, we conclude that for magnetic Skyrmions with a large a radius (*i.e.* magnetization slowly varying in space), the total TOM is also quantized. Here, we speculate that below 5 nm diameter higher order corrections to the COM become important. For instance, the five spin chirality discussed in Sec. 3.9.6 is the next term to consider. This implies the possibility of accessing high order spin chirality via the XMCD protocol, which we proposed.

5.5 Summary and outlook

In this chapter, we have studied the electronic structure and the orbital magnetization of single magnetic Skyrmions in Pd/Fe/Ir(111) from first principles. A multiple scattering expansion and a generalized Alexander-Anderson model were used to interpret the features observed in LDOS of the Fe layer. It was shown that Skyrmions could be detected electrically with a nonmagnetic tip. Indeed, the non-collinear magnetic texture of Skyrmions and the SOI cause a mixing between minority and majority LDOS resulting into the TXMR effect. Furthermore, we computed the orbital magnetization of the Skyrmions. When the SOI is turned-off, a non-vanishing orbital magnetization is still observed (COM), originating from the scalar chirality of the spin moments. For the considered Skyrmions sizes, we found that the total COM for the Skyrmion increases with the diameter. For large magnetic Skyrmions, this chiral contribution becomes a topological orbital magnetization (TOM) and is invariant under continuous deformations of the Skyrmion. We also suggested an experimental protocol that allows to access the sign and magnitude of the TOM using XMCD. Finally, we studied the connection between the TOM and the topological charge $\mathcal{Q}$ and found that the TOM is proportional to $\mathcal{Q}$ for large Skyrmions (*i.e.* when the angle between the spin moments is small).

The non-collinearity among the spin moments leads to several interesting effects similar to the ones originating from the SOI. This opens the route for the investigations of new effects such as: finite ground-state spin currents flowing through the Skyrmion without SOI, which might give rise to Dzyaloshinskii-Moriya-like interactions [57]. Furthermore, the dynamics of these topological spin textures under external time-dependent electric/magnetic fields, in the framework of TD-DFT, is also unknown and is worth investigating.

Chapter 6

Conclusions

This thesis covered a wide variety of topics all connected via the interplay between magnetism and spin-orbit interaction (SOI). The theoretical work done in this thesis can find potential applications in the field of spin-orbitronics. On the one hand, some problems were treated by means of a Rashba model, which incorporates SOI in a simple way allowing to track down its contribution to different quantities of interest such as magnetic interactions, residual resistivity, and orbital magnetization. On the other hand, we employed density functional theory (DFT) which provides an accurate description of the electronic structure of materials allowing to make quantitative predictions. Furthermore, to treat magnetic excitations from first principles, an extension of DFT to its time-dependent version was used (TD-DFT). The model approach and DFT are complementary since the former one allows to interpret and understand the predictions made using DFT.

The scattering theory for a two-dimensional electron gas offered the fundamental tool to explore the impact of SOI. Several lengthy and sometimes tedious analytical calculations have been carried out for a thorough understanding of the various investigated effects. The DFT approach in the framework of the Korringa-Kohn-Rostoker (KKR) Green function method required an analytical understanding as well. Moreover, a new interface between the KKR-impurity code and the KKR-susc code was implemented. These developments allowed the inclusion of the SOI starting from the host system, which is an essential feature for the investigated systems.

In the first part of the thesis, we have used the Rashba Hamiltonian to model the spin splitting of the energy bands observed at heavy metal surfaces. We used a real space embedding technique to incorporate impurities into the Rashba electron gas. First, a mapping into an extended Heisenberg model enabled the computation of the magnetic interactions. When employing the Ruderman-Kittel-Kasuya-Yosida (RKKY) approximation, analytical forms for the magnetic interaction tensor could be derived. These analytical forms were also used to connect the isotropic exchange interaction to the DM interaction. We also went beyond the RKKY approximation to rigorously include multiple scattering effects. This proved to be crucial for the determination of the magnetic interactions, which depend on the size and shape of the nanostructures. Second, we employed linear response

theory to derive the residual electrical resistivity tensor for a Rashba electron gas in presence of a single nonmagnetic/magnetic impurity. The impact of the SOI strength on the resistivity tensor was analyzed. For a general orientation of the magnetic moment of the impurity, a planar Hall effect (PHE) has been observed in the transversal response, while an anisotropic magnetoresistance (AMR) was found in the longitudinal part. Furthermore, phenomenological functional forms for the dependence of the resistivity tensor on the magnetization direction were derived. Third, we explored the orbital magnetization of Rashba electrons in presence of magnetic impurities. It was accessed through the ground state current density, which, in addition to the paramagnetic part, has a diamagnetic contribution from SOI. For trimer nanoclusters in absence of SOI, a non-vanishing contribution to the orbital magnetization was found (chiral orbital magnetization). We demonstrated that the latter one arises solely from the chirality of the spins structure.

Based on DFT and TD-DFT, we investigated in the second part of the thesis magnetic impurities embedded in topological insulators. We used DFT as implemented in the KKR Green function method, allowing efficient real space calculations. We investigated $3d$ and $4d$ transition metal impurities embedded in Bi_2Te_3, Bi_2Se_3 thin films and bulk. When the magnetic moments are oriented in the perpendicular direction with respect to the surface of the topological insulator, a gap opening at the Dirac point was predicted [81, 16]. However, an analysis of the local density of states shows that some $3d$ and $4d$ elements display very sharp features, which populate the bulk band gap. These features constitute in-gap states originating from the hybridization with the bulk bands. Furthermore, we computed the MAE for all the magnetic impurities. We highlighted the limitations of the magnetic force theorem. We showed that, upon rotation of the spin moment, if the electronic structure at the Fermi energy changes drastically, then the MAE obtained from band energy differences is not reliable. More elaborate schemes are required to obtain the MAE, which can be calculated using the torque method near self-consistency or linear response theory. We then computed the magnetic excitation spectrum of the impurities using linear response TD-DFT. The peaks observed in the dynamical magnetic susceptibility were rather sharp compared to the ones observed in metals. This was attributed to a lower hybridization with the topological insulator host states. The lifetimes of the transversal spin excitations are relatively large: the particular case of Mn in Bi_2Se_3 is rather astonishing, where the lifetime reached microseconds. Inertial effects were found to be important for some elements (such as Nb in Bi_2Te_3), leading to a repositioning of the excitation energies. Finally, the dynamical magnetic susceptibility was also used to compute zero-point spin-fluctuations, which were found to be important for some elements and could alter their magnetic properties. Indeed, we showed that zero-point spin-fluctuations can lead to sign change of the MAE for Nb in Bi_2Te_3.

In the third part of the thesis, we used the KKR Green function method to investigate the ground state properties and the electronic structure of magnetic Skyrmions, which represent topologically protected spin textures. We have shown that Skyrmions can be detected electrically due to the signature that the non-collinearity imprints in the local density of states, which we called tunneling spin mixing magnetoresistance. Furthermore, when SOI is turned off, a chiral orbital magnetization is observed in the spin texture. Once more, it arises from the non-collinearity among the spin moments. In the case of large magnetic Skyrmions where the spin magnetization rotates slowly in space, we show that the chiral

orbital magnetization is quantized by being proportional to the topological charge of the Skyrmion and becomes thereby a topological orbital magnetization. Finally, we suggested accessing the topological orbital moments experimentally using X-ray magnetic circular dichroism (XMCD) for the identification of the topological nature of complex magnetic textures by optical means.

To conclude our summary, we propose future interesting research directions beyond what has been investigated in this thesis. We suggest to use the Biot-Savart law to quantify the magnetic stray fields generated by the already investigated non-vanishing bound currents. This would provide means for detecting them experimentally. The computation of the residual resistivity tensor was so far performed using a model. It would be interesting to investigate it in the framework of the KKR Green function method for realistic materials to make quantitative comparisons with experiment. In addition to the resistivity tensor (charge response), one can explore the possibility of extracting the spin current response containing information on the spin currents generated when an external electric field is applied. This response might be substantial for magnetically doped topological insulators due to a huge charge-to-spin conversion ratio, which can be exploited in a spin-orbitronic device.

The TD-DFT work done in the thesis focused on the transversal spin response in presence of SOI, which can be used for the computation of the electron-magnon self-energy employing many-body perturbation theory. This self-energy can be used to renormalize the electronic structure. In this case, the anisotropy due to SOI would be included in the electronic structure and in the spin excitations, providing a complete picture and eventually explain the results obtained in inelastic scanning tunneling spectroscopy (ISTS). In addition, one can address the longitudinal response, which can be important in presence of perturbations altering the magnitude of the spin moment. Moreover, we always focused on the dynamics of the spin moment. However, for some elements such as Co in Bi_2Se_3, the orbital moment reaches 50% of the spin moment, motivating the computation of the orbital response function. Furthermore, the real space impurity clusters considered for our calculations include up to a few hundreds of atoms. An improvement of the parallelization scheme of the code would allow accessing larger nanostructures enabling the computation of the topological orbital magnetization for large Skyrmions, and the study of its robustness in presence of defects. Finally, the investigation of the dynamics of topological magnetic structures such as Skyrmions using TD-DFT constitutes a challenging task computationally. Alternatively one can also study Skyrmion dynamics in the time domain instead of the frequency domain. A deep understanding of the behavior of Skyrmions in presence of time-dependent external fields is required for any interesting technological applications.

Appendix A

Derivation of the t-matrix in the s-wave approximation

In this appendix, we derive the t-matrix in the s-wave approximation for magnetic adatoms deposited on a free two-dimensional (2D) electron gas without spin-orbit interaction (the Green function is diagonal in spin space). We start from the spin conserving Lippman-Schwinger equation for the electronic wave function in the cylindrical basis:

$$\varphi_{\varepsilon m\sigma}(\vec{r}) = \psi_{\varepsilon m\sigma}(\vec{r}) + \int d\vec{r}\,' d\vec{r}\,'' \, G^{\sigma\sigma}(\vec{r},\vec{r}\,',\varepsilon)\, t^{\sigma\sigma}(\vec{r}\,',\vec{r}\,'',\varepsilon)\, \psi_{\varepsilon m\sigma}(\vec{r}\,'') \quad , \tag{A.1}$$

where the 2D free electron wave function $\psi_{\varepsilon m\sigma}(\vec{r})$ and Green function $G^{\sigma\sigma}(\vec{r},\vec{r}\,',\varepsilon)$ are respectively given by:

$$\psi_{\varepsilon m\sigma}(\vec{r}) = e^{-\mathrm{i}\frac{(2m+1)}{4}\pi}\, J_m(kr)\, e^{\mathrm{i}m\phi} \tag{A.2}$$

$$G^{\sigma\sigma}(\vec{r},\vec{r}\,',\varepsilon) = \frac{1}{2\mathrm{i}} \sum_m H_m(kr)\, J_m^*(kr)\, e^{\mathrm{i}m(\phi-\phi')} \quad . \tag{A.3}$$

Since the Green function and the wave functions are expanded in the cylindrical basis, one also needs the expansion of the t-matrix in that basis. For a cylindrical scattering potential, the t-matrix reads:

$$t^{\sigma\sigma}(\vec{r},\vec{r}\,',\varepsilon) = \frac{1}{2\pi} \sum_m e^{\mathrm{i}m\phi}\, t_m^{\sigma\sigma}(r,r',\varepsilon)\, e^{-\mathrm{i}m\phi'} \quad . \tag{A.4}$$

After inserting Eq.(A.3) and Eq.(A.4) into Eq.(A.1) and performing the double integral over space, within the s-wave approximation $t^{\sigma\sigma}(r,r',\varepsilon) = t^{\sigma\sigma}(\varepsilon)\,\delta(r)\,\delta(r')$:

$$\varphi_{\varepsilon m\sigma}(\vec{r}) = \psi_{\varepsilon m\sigma}(\vec{r}) + 2\pi\, \frac{e^{-\mathrm{i}\frac{\pi}{4}}}{2\mathrm{i}}\, t_0^{\sigma\sigma}(\varepsilon)\, H_0(kr) \quad . \tag{A.5}$$

At large distance from the impurity, the scattered wave function $\varphi_{\varepsilon m\sigma}(\vec{r})$ can be written using the scattering phase shift $\delta_m^{\sigma\sigma}(\varepsilon)$ (see chapter 3):

$$\varphi_{\varepsilon m\sigma}(\vec{r}) = e^{2\mathrm{i}\delta_0^{\sigma\sigma}(\varepsilon)}\psi_{\varepsilon m\sigma}(\vec{r}) \quad . \tag{A.6}$$

By comparing Eq.(A.5) and Eq.(A.6) in the asymptotic limit using the following expansions:

$$\begin{aligned} J_0(kr) &= \frac{1}{\sqrt{2\pi kr}}\, e^{\mathrm{i}(kr-\frac{\pi}{4})} \quad , \\ H_0(kr) &= \sqrt{\frac{2}{\pi kr}}\, e^{\mathrm{i}(kr-\frac{\pi}{4})} \quad , \end{aligned} \tag{A.7}$$

we easily get the connection between the t-matrix and the scattering phase shift within the s-wave approximation:

$$t_0^{\sigma\sigma}(\varepsilon) = \frac{\mathrm{i}}{2\pi}(e^{2\mathrm{i}\delta_m^{\sigma\sigma}(\varepsilon)} - 1) \quad . \tag{A.8}$$

It can be also more convenient to define the t-matrix in the s-wave approximation without the cylindrical expansion as:

$$t^{\sigma\sigma}(\varepsilon) = \mathrm{i}\,(e^{2\mathrm{i}\delta_m^{\sigma\sigma}(\varepsilon)} - 1) \quad . \tag{A.9}$$

The 2D free electron Green function was defined in reduced units, it can be converted to the natural unit by multiplying it with $\frac{m^*}{\hbar^2}$, which leads to the final form of the t-matrix:

$$t^{\sigma\sigma}(\varepsilon) = \frac{\mathrm{i}\hbar^2}{m^*}\,(e^{2\mathrm{i}\delta_m^{\sigma\sigma}(\varepsilon)} - 1) \quad . \tag{A.10}$$

Appendix B

Extended Heisenberg model for a magnetic dimer

In this appendix, we derive the generalized Heisenberg Hamiltonian $H_m = \vec{e}_i \, \boldsymbol{J}_{ij} \, \vec{e}_j$, which was simplified to the form given by Eq. (3.42). For this purpose, we need to calculate the elements of the tensor of exchange interactions showing up in Eq. (3.40), *i.e.* $\mathrm{Tr}\,\{\boldsymbol{\sigma}_\alpha \, \boldsymbol{G}_{ij}(\varepsilon) \, \boldsymbol{\sigma}_\beta \, \boldsymbol{G}_{ji}(\varepsilon)\}$, considering that $\boldsymbol{G}_{ij}(\varepsilon)$ can be expressed in terms of G_D and G_ND (see Eq. (3.41)). This can be evaluated via the following trace (omitting the energy integration):

$$\begin{aligned} H_\mathrm{m} \propto \mathrm{Tr}\,[&(\vec{e}_i \cdot \vec{\boldsymbol{\sigma}})(G_\mathrm{D}\,\boldsymbol{\sigma}_0 - \mathrm{i}\,G_\mathrm{ND}(\cos\beta\,\boldsymbol{\sigma}_y - \sin\beta\,\boldsymbol{\sigma}_x)) \\ &\times (\vec{e}_j \cdot \vec{\boldsymbol{\sigma}})(G_\mathrm{D}\,\boldsymbol{\sigma}_0 + \mathrm{i}\,G_\mathrm{ND}(\cos\beta\,\boldsymbol{\sigma}_y - \sin\beta\,\boldsymbol{\sigma}_x))] \quad . \end{aligned} \tag{B.1}$$

Using the properties of the Pauli matrices, we know that for two vectors $\vec{A}$ and $\vec{B}$, the following relation holds: $(\vec{A}\cdot\vec{\boldsymbol{\sigma}})\,(\vec{B}\cdot\vec{\boldsymbol{\sigma}}) = (\vec{A}\cdot\vec{B})\,\boldsymbol{\sigma}_0 + \mathrm{i}\,(\vec{A}\times\vec{B})\cdot\vec{\boldsymbol{\sigma}}$, therefore, H_m can be written as:

$$\begin{aligned} H_\mathrm{m} \propto\; & 2\,\vec{e}_i\cdot\vec{e}_j\,(G_\mathrm{D}^2 - G_\mathrm{ND}^2) - 4\,(\vec{e}_i\times\vec{e}_j)_x\,\mathrm{i}\,G_\mathrm{D}\,G_\mathrm{ND}\,\sin\beta \\ & - 4\,(\vec{e}_i\times\vec{e}_j)_y\,G_\mathrm{D}\,G_\mathrm{ND}\,\cos\beta + 4\,e_i^y\,e_j^y\,G_\mathrm{ND}^2\,\cos^2\beta \\ & + 4\,e_i^x\,e_j^x\,G_\mathrm{ND}^2\,\sin^2\beta - 2\,(e_i^x\,e_j^y + e_i^y\,e_j^x)\,G_\mathrm{ND}^2\,\sin\beta\,\cos\beta \quad . \end{aligned} \tag{B.2}$$

The terms proportional to $e_i^x\,e_j^x$ and $e_i^y\,e_j^y$ will lead to the pseudo-dipolar like terms after performing the energy integration given in Eq. (3.49). The terms proportional to $(e_i^x\,e_j^y + e_i^y\,e_j^x)$ are called interface terms. We can combine both terms in a pseudo-dipolar Hamiltonian for the two-dimensional case;

$$H_\mathrm{psd} \propto I \sum_{i,j}[(\vec{e}_i\cdot\vec{e}_j) - (\vec{e}_i\cdot\vec{r}_{ij})(\vec{e}_j\cdot\vec{r}_{ij}) - e_i^z\,e_j^z] \quad . \tag{B.3}$$

$\vec{r}_{ij}$ is the vector connecting the impurities $\{i,j\}$. If we consider that the two magnetic impurities are along the x-axis then $\beta = 0$ and we get the expression below for the trace:

$$H_\mathrm{m} \propto 2\,(G_\mathrm{D}^2 - G_\mathrm{ND}^2)\,\vec{e}_i\cdot\vec{e}_j - 4\,G_\mathrm{D}\,G_\mathrm{ND}\,(\vec{e}_i\times\vec{e}_j)_y + 4\,G_\mathrm{ND}^2\,e_i^y\,e_j^y \quad , \tag{B.4}$$

which leads to the final form of the Hamiltonian given in Eq. (3.42), and to the identification of the different magnetic interaction terms as presented in Eqs. (3.46), (3.47), (3.49).

Appendix C

Asymptotic expansion of the Rashba Green function

In order to obtain the analytical forms of $J(r)$, $D(r)$ and $I(r)$ in the RKKY-approximation (Eqs. (3.46), (3.47), (3.49)), we evaluate the integrands needed in Eqs. (3.43), (3.44), (3.45) considering two regimes, positive or negative k_1. For $k_1 < 0$:

$$G_{\mathrm{D}}^2 = -\frac{(m^*)^2}{4\hbar^2(k_- + k_+)^2}\,[\,k_-^2\,H_0^{*2}(|k_-|r)+k_+^2\,H_0^2(k_+r)-2\,k_-k_+\,H_0^*(|k_-|r)\,H_0(k_+r)\,] \quad , \tag{C.1}$$

$$G_{\mathrm{ND}}^2 = -\frac{(m^*)^2}{4\hbar^2(k_- + k_+)^2}\,[\,k_-^2\,H_1^{*2}(|k_-|r)+k_+^2\,H_1^2(k_+r)-2\,k_-k_+\,H_1^*(|k_-|r)\,H_1(k_+r)\,] \quad , \tag{C.2}$$

and

$$G_{\mathrm{D}}\,G_{\mathrm{ND}} = -\frac{(m^*)^2}{4\hbar^2(k_- + k_+)^2}\,[\,-k_-^2\,H_0^*(|k_-|r)\,H_1^*(|k_-|r) + k_-k_+\,H_0^*(|k_-|r)\,H_1(k_+r) + k_-k_+\,H_1^*(|k_-|r)\,H_0(k_+r) - k_+^2\,H_1(k_+r)\,H_0(k_+r)\,] \quad . \tag{C.3}$$

In case $k_- > 0$:

$$G_{\mathrm{D}}^2 = -\frac{(m^*)^2}{4\hbar^2(k_- + k_+)^2}\,[\,k_-^2\,H_0^2(k_-r) + k_+^2\,H_0^2(k_+r) + 2k_-k_+\,H_0(k_-r)\,H_0(k_+r)\,] \quad , \tag{C.4}$$

$$G_{\mathrm{ND}}^2 = -\frac{(m^*)^2}{4\hbar^2(k_- + k_+)^2}\,[\,k_-^2\,H_1^2(k_-r)+k_+^2\,H_1^2(k_+r)-2k_-k_+\,H_1(k_-r)\,H_1(k_+r)\,] \quad , \tag{C.5}$$

and

$$G_{\rm D}\, G_{\rm ND} = -\frac{(m^*)^2}{4\hbar^2(k_- + k_+)^2}\,[\,k_-^2\, H_0(k_- r)\, H_1(k_- r) - k_- k_+\, H_0(k_- r)\, H_1(k_+ r) + k_- k_+\, H_1(k_- r) H_0(k_+ r) - k_+^2\, H_0(k_+ r)\, H_1(k_+ r)\,] \quad . \tag{C.6}$$

We use the asymptotic expansion for the Hankel functions for large distance ($r \to \infty$): $H_0(x) \simeq \sqrt{\frac{2}{\pi x}}\, e^{{\rm i}(x - \frac{\pi}{4})}$ and $H_1(x) \simeq \sqrt{\frac{2}{\pi x}}\, e^{{\rm i}(x - \frac{3\pi}{4})}$ which simplify the previous forms for negative $k_- < 0$ to:

$$G_{\rm D}^2 = \frac{{\rm i}(m^*)^2}{2\hbar^2(k_- + k_+)^2\pi r}\,[-|k_-|\, e^{-2{\rm i}|k_-|r} + k_+\, e^{2{\rm i}k_+ r} + 2{\rm i}\,\sqrt{|k_-|k_+}\, e^{{\rm i}(k_+ - |k_-|)r}\,] \quad , \tag{C.7}$$

$$G_{\rm ND}^2 = -\frac{{\rm i}(m^*)^2}{2\hbar^2(k_- + k_+)^2\pi r}\,[-|k_-|\, e^{-2{\rm i}|k_-|r} + k_+\, e^{2{\rm i}k_+ r} - 2{\rm i}\,\sqrt{|k_-|k_+}\, e^{{\rm i}(k_+ - |k_-|)r}\,] \quad , \tag{C.8}$$

and

$$G_{\rm D}\, G_{\rm ND} = \frac{(m^*)^2}{2\hbar^2(k_- + k_+)^2\pi r}\,[\,-|k_-|\, e^{-2{\rm i}|k_-|r} - k_+\, e^{2{\rm i}k_+ r}\,] \quad . \tag{C.9}$$

While a positive k_- leads to:

$$G_{\rm D}^2 = \frac{{\rm i}(m^*)^2}{2\hbar^2(k_- + k_+)^2\pi r}\,[\,k_-\, e^{2{\rm i}k_- r} + k_+\, e^{2{\rm i}k_+ r} + 2\sqrt{k_- k_+}\, e^{{\rm i}(k_- + k_+)r}\,] \quad , \tag{C.10}$$

$$G_{\rm ND}^2 = -\frac{{\rm i}(m^*)^2}{2\hbar^2(k_- + k_+)^2\pi r}\,[\,k_-\, e^{2{\rm i}k_- r} + k_+\, e^{2{\rm i}k_+ r} - 2\sqrt{k_- k_+}\, e^{{\rm i}(k_- + k_+)r}\,] \quad , \tag{C.11}$$

and

$$G_{\rm D}\, G_{\rm ND} = \frac{(m^*)^2}{2\hbar^2(k_- + k_+)^2\pi r}\,[\,k_-\, e^{2{\rm i}k_- r} - k_+\, e^{2{\rm i}k_+ r}\,] \quad . \tag{C.12}$$

From the expressions above we notice that contrary to the terms $(G_{\rm D}^2 - G_{\rm ND}^2)$ and $G_{\rm D}\, G_{\rm ND}$, $G_{\rm D}^2$ and $G_{\rm ND}^2$ behave differently in the first and second regime.

Appendix D

Evaluation of the momentum operator matrix elements

In this appendix we will calculate the matrix elements of the momentum operator between two quantum states $i = (\varepsilon, m, \alpha)$ and $j = (\varepsilon + \hbar\omega, m', \alpha')$ in the region where the scattered wave function can be expressed by the asymptotic form Eq. (3.63) and extract only the diverging terms $\sim 1/\omega$ in the limit $\omega \to 0$. In cylindrical coordinates the leading components of the momentum operator behaves at large distances as

$$\begin{aligned} \hat{v}_x &\sim \frac{\hbar}{\mathrm{i}m^*} \cos\phi \, \frac{\partial}{\partial r} + \frac{\hbar}{m^*} k_{\mathrm{so}} \, \sigma_y \\ \hat{v}_y &\sim \frac{\hbar}{\mathrm{i}m^*} \sin\phi \, \frac{\partial}{\partial r} - \frac{\hbar}{m^*} k_{\mathrm{so}} \, \sigma_x. \end{aligned} \tag{D.1}$$

With this representation of the momentum operators, we found that the diverging terms arise from the combinations

$$\left\langle \psi^{\mathrm{in,out}}_{\varepsilon+\hbar\omega,m',\alpha'} \middle| m^* \hat{v}_x \middle| \psi^{\mathrm{in,out}}_{\varepsilon,m,\alpha} \right\rangle \sim \frac{\hbar(\delta_{m',m+1} + \delta_{m',m-1})\delta_{\alpha\alpha'}}{2\mathrm{i}\Delta k} \frac{k_{\mathrm{M}}}{k_\alpha}, \tag{D.2}$$

where $\Delta k \equiv k_\alpha(\varepsilon + \hbar\omega) - k_\alpha(\varepsilon) \sim 2m^*\omega/k_{\mathrm{M}}(\varepsilon)$ is the same for both bands ($\alpha = \pm$).

By combining Eq. (3.63) and Eq. (D.2) we obtain the momentum matrix element in the limit of $\omega \to 0$,

$$\langle \varphi_j | \, m^* \hat{v}_x \, | \varphi_i \rangle \sim \frac{\hbar}{2\mathrm{i}\Delta k} \frac{k_{\mathrm{M}}}{\sqrt{k_\alpha k'_\alpha}} S^x(m\alpha, m'\alpha', \varepsilon), \tag{D.3}$$

where $S^x(m\alpha, m'\alpha', \varepsilon)$ is given by

$$\begin{aligned} S^x(m\alpha, m'\alpha', \varepsilon) = (\delta_{m\prime,m+1} + \delta_{m\prime,m-1})\delta_{\alpha\alpha'} \\ + \sum_{l\alpha''} C(m\alpha, l\alpha'') C^*(m'\alpha', l+1\alpha'') \\ + \sum_{l\alpha''} C(m\alpha, l\alpha'') C^*(m'\alpha', l-1\alpha''). \end{aligned} \tag{D.4}$$

Analogously, the matrix element for the y component of the momentum operator is given by

$$\langle\varphi_j|\, m^*\hat{v}_y\,|\varphi_i\rangle \sim \frac{-\hbar}{2\Delta k}\frac{k_{\mathrm{M}}}{\sqrt{k_\alpha k'_\alpha}} S^y(m\alpha, m'\alpha', \varepsilon), \tag{D.5}$$

with S^y defined by

$$\begin{aligned} S^y(m\alpha, m'\alpha', \varepsilon) = {} & (\delta_{m\prime,m+1} - \delta_{m\prime,m-1})\delta_{\alpha\alpha'} \\ & + \sum_{l\alpha''} C(m\alpha, l\alpha'')C^*(m'\alpha', l+1\alpha'') \\ & - \sum_{l\alpha''} C(m\alpha, l\alpha'')C^*(m'\alpha', l-1\alpha''). \end{aligned} \tag{D.6}$$

Appendix E

Phenomenological derivation of the functional forms

Here we derive phenomenologically the functional forms, which fit the computed longitudinal and transversal components of the residual resistivity tensor. The system of interest is an adatom with a tilted magnetic moment interacting with a gas of Rashba electrons. We assume a 2D current density flowing along the x-direction, J_x, that generates an electric field $\vec{E}$ (see Fig.E.1a). Before analyzing the general case of a tilted magnetic moment, let us recap what is expected when (i) the moment lies in-plane and (ii) the moment points out-of-plane. In case (i), we proceed as done by Thompson et al. [157] and consider the x-component of $\vec{E}$:

$$E_x^{(i)} = E_{\parallel} \cos\phi_{\vec{\mathrm{M}}} + E_{\perp} \sin\phi_{\vec{\mathrm{M}}} \quad , \tag{E.1}$$

where $E_{\parallel}$ and $E_{\perp}$ are the components of the electric field parallel and perpendicular to the projection of the unit vector of the magnetic moment, $\hat{e}_{\vec{\mathrm{M}}}$, lying in the (xy) plane (the surface plane) as depicted in Fig.E.1b. In terms of the current density and resistivity, the previous equation is then rewritten considering the parallel and perpendicular projection of the 2D current density on the direction of the magnetic moment:

$$E_x^{(i)} = J_{\parallel}\, \rho_{\parallel} \cos\phi_{\vec{\mathrm{M}}} + J_{\perp}\, \rho_{\perp} \sin\phi_{\vec{\mathrm{M}}} \quad , \tag{E.2}$$

as function of the azimuthal angle $\phi_{\vec{\mathrm{M}}}$. Also, knowing that $J_{\parallel} = J\cos\phi_{\vec{\mathrm{M}}}\,; J_{\perp} = J\sin\phi_{\vec{\mathrm{M}}}$ (see Fig.E.1b) leads to:

$$E_x^{(i)} = J\,(\rho_{\parallel}\cos^2\phi_{\vec{\mathrm{M}}} + \rho_{\perp}\sin^2\phi_{\vec{\mathrm{M}}}) \quad . \tag{E.3}$$

Here, though, we give this expression in terms of the unit vector, $\hat{e}_{\vec{\mathrm{M}}}$, defining the orientation of the moment:

$$E_x^{(i)} = J\,\left(\rho_{\parallel}(\hat{e}_{\vec{\mathrm{M}}}\cdot\hat{e}_x)^2 + \rho_{\perp}(\hat{e}_{\vec{\mathrm{M}}}\cdot\hat{e}_y)^2\right) \quad . \tag{E.4}$$

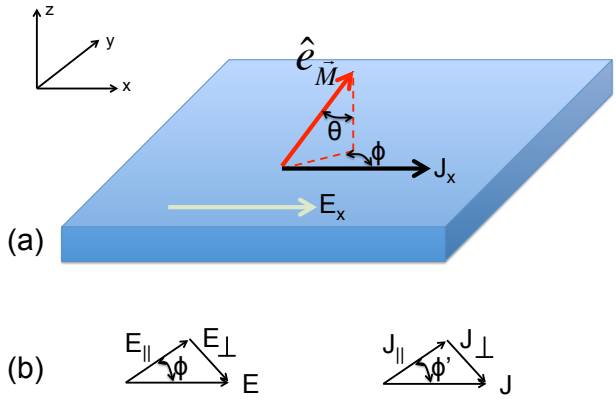

Figure E.1: (a) Geometry of the system considered: a magnetic moment rotated by a polar angle θ and azimuthal angle ϕ. The current density J is related to the electric field E via the resistivity. (b) Decomposition of the electric field and the current density parallel and perpendicular to the in-plane projection of the unit vector of the magnetic moment $\hat{e}_{\vec{\mathrm{M}}}$.

Our proposal is that in the general case of a tilted magnetic moment, the previous two equations involving $\hat{e}_{\vec{\mathrm{M}}} \cdot \hat{e}_{x/y}$ holds. However, there is a missing contribution from the out-of-plane component of the magnetic moment. In the extreme case (ii), *i.e.* magnetic moment out-of-plane, we have:

$$E_x^{(ii)} = \rho^{(ii)}\, J \tag{E.5}$$

and a simple generalization leads to:

$$E_x^{(ii)} = \rho^{(ii)} J (\hat{e}_{\vec{\mathrm{M}}} \cdot \hat{e}_z)^2 \quad . \tag{E.6}$$

As deduced from our numerical investigation, $\rho_{\parallel} = \rho^{(ii)}$ (see Fig.3.13a). This can be explained from Fig.3.12b for $\vec{\mathrm{M}} \parallel z$ and Fig.3.12c for $\vec{\mathrm{M}} \parallel x$, where the allowed scattering processes are the same except for the interband scattering which flips the spin but does not change the direction of $\vec{k}$. The latter affects only the spin part of the response function, not the residual resistivity (charge part) that we compute. Therefore we get the same residual resistivity for $\vec{\mathrm{M}} \parallel z$ and $\vec{\mathrm{M}} \parallel x$. Now we can add up both contributions (i) and (ii) and find:

$$E_x = J \left(\rho_{\parallel}\, \hat{e}_{\vec{\mathrm{M}}} \cdot (\hat{e}_x + \hat{e}_z)^2 \right) + \rho_{\perp} \left(\hat{e}_{\vec{\mathrm{M}}} \cdot \hat{e}_y \right)^2 \big) \quad , \tag{E.7}$$

which simplifies into:

$$E_x = J \left(\rho_{\parallel} + (\rho_{\perp} - \rho_{\parallel}) \sin^2 \phi_{\vec{\mathrm{M}}} \sin^2 \theta_{\vec{\mathrm{M}}} \right) \quad . \tag{E.8}$$

A similar approach can be used to derive the functional forms for the transversal part

of the residual resistivity tensor. Here we address the y-component of $\vec{E}$ and again after starting from the form of Thompson et al.[157] for the case (i):

$$E_y^{(i)} = E_{\parallel} \sin\phi_{\vec{\mathrm{M}}} - E_{\perp} \cos\phi_{\vec{\mathrm{M}}} \quad , \tag{E.9}$$

we end up with

$$E_y^{(i)} = J\left(\rho_{\parallel}(\hat{e}_{\vec{\mathrm{M}}} \cdot \hat{e}_y)^2 - \rho_{\perp}(\hat{e}_{\vec{\mathrm{M}}} \cdot \hat{e}_x)^2\right) \quad . \tag{E.10}$$

Since there is no transversal resistivity in the case (ii), the contribution $E_y^{(ii)}$ vanishes and we find:

$$E_y = J(\rho_{\perp} - \rho_{\parallel}) \cos\phi_{\vec{\mathrm{M}}} \sin\phi_{\vec{\mathrm{M}}} \sin^2\theta_{\vec{\mathrm{M}}} \quad . \tag{E.11}$$

Appendix F

Derivation of the current operator

In this appendix, we provide the details of the derivation for current operator defined in Eq. (3.110) starting from the time-dependent Schrödinger equation for the electronic wave function $\psi(\vec{r},t)$:

$$\frac{\partial\psi(\vec{r},t)}{\partial t} = \frac{1}{\mathrm{i}\hbar}\boldsymbol{H}_{\mathrm{R}}\,\psi(\vec{r},t) \quad , \tag{F.1}$$

and for the hand left side,

$$\frac{\partial\psi^{\dagger}(\vec{r},t)}{\partial t} = -\frac{1}{\mathrm{i}\hbar}\boldsymbol{H}_{\mathrm{R}}^{\dagger}\,\psi^{\dagger}(\vec{r},t) \quad . \tag{F.2}$$

The previous equations can be used to determine the time evolution of the electron density $n(\vec{r},t) = |\psi(\vec{r},t)|^2$:

$$\begin{aligned}\frac{\partial n(\vec{r},t)}{\partial t} &= \frac{\partial\psi^{\dagger}(\vec{r},t)}{\partial t}\,\psi(\vec{r},t) + \psi^{\dagger}(\vec{r},t)\,\frac{\partial\psi(\vec{r},t)}{\partial t} \quad , \\ &= -\frac{1}{\mathrm{i}\hbar}\boldsymbol{H}_{\mathrm{R}}^{\dagger}\,\psi^{\dagger}(\vec{r},t)\,\psi(\vec{r},t) + \psi^{\dagger}(\vec{r},t)\frac{1}{\mathrm{i}\hbar}\boldsymbol{H}_{\mathrm{R}}\,\psi(\vec{r},t) \quad .\end{aligned} \tag{F.3}$$

As reminder, we recall the expressions of the Rashba Hamiltonian $\boldsymbol{H}_{\mathrm{R}}$ and spin-orbit gauge field $\vec{\boldsymbol{A}}_{\mathrm{so}}$:

$$\begin{cases}\boldsymbol{H}_{\mathrm{R}} = \frac{1}{2m^*}\left(\vec{p} - \frac{e}{c}\vec{\boldsymbol{A}}_{\mathrm{so}}\right)^2 - V_{\mathrm{so}} \quad , \\ \vec{\boldsymbol{A}}_{\mathrm{so}} = \frac{m^* c\,\alpha_{\mathrm{so}}}{e\hbar}\,(-\boldsymbol{\sigma}_y, \boldsymbol{\sigma}_x) \quad .\end{cases} \tag{F.4}$$

$V_{\mathrm{so}} = \frac{m^*\alpha_{\mathrm{so}}^2}{\hbar^2}$ is a constant which does not contribute to the current density. In the following for simplicity we will drop the arguments of $\psi(\vec{r},t)$ and replace $\boldsymbol{H}_{\mathrm{R}}$ with its definition Eq. (F.3), thus, we obtain:

$$\frac{\partial n(\vec{r},t)}{\partial t} = \frac{1}{2\mathrm{i}m^*\hbar}\Big[(\psi^{\dagger}(\vec{p} - \frac{e}{c}\vec{\boldsymbol{A}}_{\mathrm{so}})^2\psi) - ((\vec{p} - \frac{e}{c}\vec{\boldsymbol{A}}_{\mathrm{so}})^2\psi)^{\dagger}\,\psi)\Big] \quad . \tag{F.5}$$

Since $\left[\vec{p}, \vec{\boldsymbol{A}}_{\rm so}\right] = 0$ and the terms $\propto \vec{\boldsymbol{A}}_{\rm so}^{\,2}$ vanish, Eq. (F.5) simply reads:

$$\frac{\partial n(\vec{r},t)}{\partial t} = \frac{1}{2\mathrm{i}m^*\hbar}\Big[(\psi^\dagger \vec{p}^{\,2}\psi - (\vec{p}^{\,2}\psi)^\dagger\,\psi) - \frac{2e}{c}(\psi^\dagger \vec{\boldsymbol{A}}_{\rm so}\vec{p}\,\psi - (\vec{p}\psi)^\dagger \vec{\boldsymbol{A}}_{\rm so}\,\psi)\Big], \tag{F.6}$$

In the position representation the momentum operator is defined as $\vec{p} = -i\hbar\vec{\nabla}$, therefore, the first order time derivative of the particle density $\rho(\vec{r},t)$ can be written as:

$$\frac{\partial n(\vec{r},t)}{\partial t} = -\frac{\hbar}{2\mathrm{i}m^*}\Big[(\psi^\dagger \vec{\nabla}^{\,2}\psi - (\vec{\nabla}^{\,2}\psi)^\dagger\,\psi)\Big] + \frac{e}{m^*c}\Big[(\psi^\dagger \vec{\boldsymbol{A}}_{\rm so}\vec{\nabla}\,\psi + (\vec{\nabla}\psi)^\dagger \vec{\boldsymbol{A}}_{\rm so}\,\psi)\Big] \quad . \tag{F.7}$$

Considering that:

$$\begin{aligned} \vec{\nabla}(\psi^\dagger\,\psi) &= \psi^\dagger\vec{\nabla}\,\psi + (\vec{\nabla}\psi)^\dagger\,\psi \quad , \\ \vec{\nabla}\cdot(\psi^\dagger\vec{\nabla}\psi - (\vec{\nabla}\psi^\dagger)\psi) &= \psi^\dagger\vec{\nabla}^{\,2}\psi - (\vec{\nabla}^{\,2}\psi)^\dagger\,\psi \quad . \end{aligned} \tag{F.8}$$

Thus,

$$\frac{\partial n(\vec{r},t)}{\partial t} = -\frac{\hbar}{2\mathrm{i}m^*}\Big[\vec{\nabla}\cdot(\psi^\dagger\vec{\nabla}\psi - (\vec{\nabla}\psi^\dagger)\psi)\Big] + \frac{e}{m^*c}\vec{\nabla}\cdot(\psi^\dagger \vec{\boldsymbol{A}}_{\rm so}\,\psi) \quad . \tag{F.9}$$

By comparing the previous equation with Eq. (3.102) we identify the current density:

$$\vec{j}(\vec{r}) = \frac{\hbar}{2\mathrm{i}m^*}(\psi^\dagger\vec{\nabla}\psi - (\vec{\nabla}\psi^\dagger)\psi) - \frac{e}{m^*c}(\psi^\dagger\vec{\mathbf{A}}_{\rm so}\,\psi) \tag{F.10}$$

Since we want to compute the ground state current induced by magnetic impurities deposited on a Rashba electron gas, we now derive an expression for the current density relying on the Green function of the system. The contribution to the ground state current density from each state ψ_n is given by:

$$\vec{j}_n(\vec{r}) = \frac{\hbar}{2\mathrm{i}m^*}(\psi_n^\dagger\vec{\nabla}\psi_n - (\vec{\nabla}\psi_n^\dagger)\psi_n) - \frac{e}{m^*c}(\psi_n^\dagger \vec{\boldsymbol{A}}_{\rm so}\,\psi_n) \quad . \tag{F.11}$$

The total current density at $T = 0$ K is:

$$\vec{j}(\vec{r}) = \sum_n \frac{\hbar}{2\mathrm{i}m^*}(\psi_n^\dagger\vec{\nabla}\psi_n - (\vec{\nabla}\psi_n^\dagger)\psi_n) - \frac{e}{m^*c}(\psi_n^\dagger\vec{\mathbf{A}}_{\rm so}\,\psi_n) \quad , \tag{F.12}$$

$N_{\rm occ}$ is the number of occupied states

$$\vec{j}(\vec{r}) = \sum_n \int^{\varepsilon_{\rm F}} \mathrm{d}\varepsilon\,\delta(\varepsilon - \varepsilon_n + \mathrm{i}0^+)\left[\frac{\hbar}{2\mathrm{i}m^*}(\psi_n^\dagger\vec{\nabla}\psi_n - (\vec{\nabla}\psi_n^\dagger)\psi_n) - \frac{e}{m^*c}(\psi_n^\dagger \vec{\boldsymbol{A}}_{\rm so}\,\psi_n)\right] \quad . \tag{F.13}$$

Using the following identities:

$$\begin{aligned} \delta(\varepsilon - \varepsilon_n + \mathrm{i}0^+) &= -\frac{1}{\pi}\,\mathrm{Im}\,\frac{1}{\varepsilon - \varepsilon_n + \mathrm{i}0^+} \quad , \\ \frac{1}{2\mathrm{i}}(\psi_n^\dagger\vec{\nabla}\psi_n - (\vec{\nabla}\psi_n^\dagger)\psi_n) &= \mathrm{Im}\,\psi_n^\dagger\vec{\nabla}\psi_n \quad . \end{aligned} \tag{F.14}$$

The current density can re-expressed as:

$$\begin{aligned}\vec{j}(\vec{r}) = &-\frac{1}{\pi}\,\mathrm{Im}\int^{\varepsilon_\mathrm{F}}\mathrm{d}\varepsilon\Big[\frac{\hbar}{2\mathrm{i}m^*}\sum_n\frac{\psi_n^\dagger\vec{\nabla}\psi_n-(\vec{\nabla}\psi_n^\dagger)\psi_n}{\varepsilon-\varepsilon_n+\mathrm{i}0^+}\\ &-\frac{e}{m^*c}\sum_n\frac{\psi_n^\dagger\vec{\boldsymbol{A}}_\mathrm{so}\,\psi_n}{\varepsilon-\varepsilon_n+\mathrm{i}0^+}\Big]\quad .\end{aligned}\tag{F.15}$$

We recall that the spectral representation of the Green function is:

$$\boldsymbol{G}(\vec{r},\vec{r}\,',\varepsilon+\mathrm{i}0^+)=\sum_n\frac{\psi_n(\vec{r})\,\psi_n^\dagger(\vec{r}\,')}{\varepsilon-\varepsilon_n+\mathrm{i}0^+}\quad .\tag{F.16}$$

We arrive at the final form of the current density in terms of the Green function:

$$\begin{aligned}\vec{j}(\vec{r}) = &-\frac{1}{\pi}\,\mathrm{Im}\int^{\varepsilon_\mathrm{F}}\mathrm{d}\varepsilon\,\mathrm{Tr}_\sigma\Big[\frac{\hbar}{2\mathrm{i}m^*}\lim_{\vec{r}\,'\to\vec{r}}(\vec{\nabla}_{\vec{r}}-\vec{\nabla}_{\vec{r}\,'})\,\boldsymbol{G}(\vec{r},\vec{r}\,',\varepsilon)\\ &-\frac{e}{m^*c}\lim_{\vec{r}\,'\to\vec{r}}\vec{\boldsymbol{A}}_\mathrm{so}\,\boldsymbol{G}(\vec{r},\vec{r}\,',\varepsilon)\Big]\quad .\end{aligned}\tag{F.17}$$

From the previous equation, the current operator is simply defined as:

$$\hat{\vec{j}}=\frac{\hbar}{2\mathrm{i}m^*}\lim_{\vec{r}\,'\to\vec{r}}(\vec{\nabla}_{\vec{r}}-\vec{\nabla}_{\vec{r}\,'})-\frac{e}{m^*c}\lim_{\vec{r}\,'\to\vec{r}}\vec{\boldsymbol{A}}_\mathrm{so}\quad .\tag{F.18}$$

Bibliography

[1] M. N. Baibich, J. M. Broto, A. Fert, F. Nguyen Van Dau, F. Petroff, P. Etienne, G. Creuzet, A. Friederich, and J. Chazelas. Giant magnetoresistance of (001)Fe/(001)Cr magnetic superlattices. *Phys. Rev. Lett.*, 61:2472–2475, Nov 1988.

[2] G. Binasch, P. Grünberg, F. Saurenbach, and W. Zinn. Enhanced magnetoresistance in layered magnetic structures with antiferromagnetic interlayer exchange. *Phys. Rev. B*, 39:4828–4830, Mar 1989.

[3] Y. Shiroishi, K. Fukuda, I. Tagawa, H. Iwasaki, S. Takenoiri, H. Tanaka, H. Mutoh, and N. Yoshikawa. Future options for HDD storage. *IEEE Transactions on Magnetics*, 45(10):3816–3822, 2009.

[4] R. Jansen. Silicon spintronics. *Nature Materials*, 11(5):400–408, 2012.

[5] D. E. Nikonov, G. I. Bourianoff, and Paolo A. Gargini. Power dissipation in spintronic devices out of thermodynamic equilibrium. *Journal of Superconductivity and Novel Magnetism*, 19(6):497–513, Aug 2006.

[6] D. E. Nikonov and G. I. Bourianoff. Operation and modeling of semiconductor spintronics computing devices. *Journal of Superconductivity and Novel Magnetism*, 21(8):479, Oct 2008.

[7] B. A. Bernevig and S. C. Zhang. Toward dissipationless spin transport in semiconductors. *IBM journal of research and development*, 50(1):141–148, 2006.

[8] J. E. Hirsch. Spin Hall effect. *Phys. Rev. Lett.*, 83:1834–1837, Aug 1999.

[9] J. Sinova, D. Culcer, Q. Niu, N. A. Sinitsyn, T. Jungwirth, and A. H. MacDonald. Universal intrinsic spin Hall effect. *Phys. Rev. Lett.*, 92:126603, Mar 2004.

[10] J. Schliemann and D. Loss. Dissipation effects in spin-Hall transport of electrons and holes. *Phys. Rev. B*, 69:165315, Apr 2004.

[11] Y. K. Kato, R. C. Myers, A. C. Gossard, and D. D. Awschalom. Observation of the spin Hall effect in semiconductors. *Science*, 306(5703):1910–1913, 2004.

[12] M. König, S. Wiedmann, C. Brüne, A. Roth, H. Buhmann, L. W. Molenkamp, X. L. Qi, and S. C. Zhang. Quantum spin Hall insulator state in HgTe quantum wells. *Science*, 318(5851):766–770, 2007.

[13] D. Hsieh, D. Qian, L. Wray, Y. Q. Xia, Y. S. Hor, R. J. Cava, and M. Z. Hasan. A topological Dirac insulator in a quantum spin Hall phase (experimental realization of a 3D topological insulator). *Nature*, 452:970, 2008.

[14] C. L. Kane and E. J. Mele. Quantum spin Hall effect in graphene. *Phys. Rev. Lett.*, 95:226801, Nov 2005.

[15] M. Berry. Quantal phase factors accompanying adiabatic changes. *Proceedings of the Royal Society of London A: Mathematical, Physical and Engineering Sciences*, 392(1802):45–57, 1984.

[16] M. Z. Hasan and C. L. Kane. Colloquium. *Rev. Mod. Phys.*, 82:3045–3067, Nov 2010.

[17] H. Suzuura and T. Ando. Crossover from symplectic to orthogonal class in a two-dimensional honeycomb lattice. *Phys. Rev. Lett.*, 89:266603, Dec 2002.

[18] M. X. Wang, P. Li, J. P. Xu, Z. L. Liu, J. F. Ge, G. Y. Wang, X. Yang, Z. A. Xu, S. H. Ji, C. L. Gao, D. Qian, W. Luo, C. Liu, and J. F. Jia. Interface structure of a topological insulator/superconductor heterostructure. *New Journal of Physics*, 16(12):123043, 2014.

[19] C. H. Li, O. M. J. van't Erve, J. T. Robinson, Y. Liu, L. Li, and B. T. Jonker. Electrical detection of charge-current-induced spin polarization due to spin-momentum locking in Bi_2Se_3. *Nature nanotechnology*, 9(3):218–224, 2014.

[20] Y. Fan, P. Upadhyaya, X. Kou, M. Lang, S. Takei, Z. Wang, J. Tang, L. He, L. T. Chang, M. Montazeri, et al. Magnetization switching through giant spin-orbit torque in a magnetically doped topological insulator heterostructure. *Nature materials*, 13(7):699–704, 2014.

[21] C. Z. Chang, J. Zhang, X. Feng, J. Shen, Z. Zhang, M. Guo, K. Li, Y. Ou, P. Wei, L. L. Wang, Z. Q. Ji, Y. Feng, S. Ji, X. Chen, J. Jia, X. Dai, Z. Fang, S. C. Zhang, K. He, Y. Wang, L. Lu, X. C. Ma, and Q. Xue. Experimental observation of the quantum anomalous Hall effect in a magnetic topological insulator. *Science*, 340(6129):167–170, 2013.

[22] S. Y. Xu, M. Neupane, C. Liu, D. Zhang, A. Richardella, L. A. Wray, N. Alidoust, M. Leandersson, T. Balasubramanian, J. Sánchez-Barriga, O. Rader, G. Landolt, B. Slomski, J. Hugo Dil, J. Osterwalder, T. R. Chang, H. T. Jeng, H. Lin, A. Bansil, N. Samarth, and M. Z. Hasan. Hedgehog spin texture and Berry's phase tuning in a magnetic topological insulator. *Nat Phys*, 8(8):616–622, Aug 2012.

[23] L. A. Wray, S. Y. Xu, Y. Xia, D. Hsieh, A. V. Fedorov, Y. S. Hor, R. J. Cava, A. Bansil, H. Lin, and M. Z. Hasan. A topological insulator surface under strong Coulomb, magnetic and disorder perturbations. *Nat Phys*, 7(1):32–37, Jan 2011.

[24] I. Lee, C. K. Kim, J. Lee, S. J. L. Billinge, R. Zhong, J. A. Schneeloch, T. Liu, T. Valla, J. M. Tranquada, G. Gu, and J. C. S. Davis. Imaging Dirac-mass disorder from magnetic dopant atoms in the ferromagnetic topological insulator $Cr_x(Bi_{0.1}Sb_{0.9})_{2-x}Te3$. *Proceedings of the National Academy of Sciences*, 112(5):1316–1321, 2015.

[25] M. R. Scholz, J. Sánchez-Barriga, D. Marchenko, A. Varykhalov, A. Volykhov, L. V. Yashina, and O. Rader. Tolerance of topological surface states towards magnetic moments: Fe on Bi_2Se_3. *Phys. Rev. Lett.*, 108:256810, Jun 2012.

[26] T. Valla, Z. H. Pan, D. Gardner, Y. S. Lee, and S. Chu. Photoemission spectroscopy of magnetic and nonmagnetic impurities on the surface of the Bi_2Se_3 topological insulator. *Phys. Rev. Lett.*, 108:117601, Mar 2012.

[27] J. Honolka, A. A. Khajetoorians, V. Sessi, T. O. Wehling, S. Stepanow, J. L. Mi, B. B. Iversen, T. Schlenk, J. Wiebe, N. B. Brookes, A. I. Lichtenstein, Ph. Hofmann, K. Kern, and R. Wiesendanger. In-plane magnetic anisotropy of Fe atoms on Bi_2Se_3(111). *Phys. Rev. Lett.*, 108:256811, Jun 2012.

[28] T. Schlenk, M. Bianchi, M. Koleini, A. Eich, O. Pietzsch, T. O. Wehling, T. Frauenheim, A. Balatsky, J. L. Mi, B. B. Iversen, J. Wiebe, A. A. Khajetoorians, Ph. Hofmann, and R. Wiesendanger. Controllable Magnetic Doping of the Surface State of a Topological Insulator. *Phys. Rev. Lett.*, 110:126804, Mar 2013.

[29] P. Sessi, F. Reis, T. Bathon, K. A. Kokh, O. E. Tereshchenko, and M. Bode. Signatures of Dirac Fermion-mediated magnetic order. *Nature communications*, 5:5349, Oct 2014. Article.

[30] R. R. Biswas and A. V. Balatsky. Impurity-induced states on the surface of three-dimensional topological insulators. *Phys. Rev. B*, 81:233405, Jun 2010.

[31] J. Sánchez-Barriga, A. Varykhalov, G. Springholz, H. Steiner, R. Kirchschlager, G. Bauer, O. Caha, E. Schierle, E. Weschke, A. A. Ünal, et al. Nonmagnetic band gap at the Dirac point of the magnetic topological insulator $(Bi_{1-x}Mn_x)_2Se3$. *Nature communications*, 7:10559, 2016.

[32] P. Sessi, R. R. Biswas, T. Bathon, O. Storz, S. Wilfert, A. Barla, K. A. Kokh, O. E. Tereshchenko, K. Fauth, M. Bode, et al. Dual nature of magnetic dopants and competing trends in topological insulators. *Nature communications*, 7, 2016.

[33] T. Eelbo, M. Sikora, G. Bihlmayer, M. Dobrzański, A. Kozłowski, I. Miotkowski, and R. Wiesendanger. Co atoms on Bi_2Se_3 revealing a coverage dependent spin reorientation transition. *New Journal of Physics*, 15(11):113026, 2013.

[34] F. Yang, Y. R. Song, H. Li, K. F. Zhang, X. Yao, C. Liu, D. Qian, C. L. Gao, and J. F. Jia. Identifying magnetic anisotropy of the topological surface state of $Ci_{0.05}Sb_{1.95}Te_3$ with spin-polarized STM. *Phys. Rev. Lett.*, 111:176802, Oct 2013.

[35] T. Eelbo, M. Waśniowska, M. Sikora, M. Dobrzański, A. Kozłowski, A. Pulkin, G. Autès, I. Miotkowski, O. V. Yazyev, and R. Wiesendanger. Strong out-of-plane magnetic anisotropy of fe adatoms on Bi_2Te_3. *Phys. Rev. B*, 89:104424, Mar 2014.

[36] L. Chotorlishvili, A. Ernst, V. K. Dugaev, A. Komnik, M. G. Vergniory, E. V. Chulkov, and J. Berakdar. Magnetic fluctuations in topological insulators with ordered magnetic adatoms: Cr on Bi_2Te_3 from first principles. *Phys. Rev. B*, 89:075103, Feb 2014.

[37] A. A. Khajetoorians, S. Lounis, B. Chilian, A. T. Costa, L. Zhou, D. L. Mills, J. Wiebe, and R. Wiesendanger. Itinerant nature of atom-magnetization excitation by tunneling electrons. *Phys. Rev. Lett.*, 106:037205, Jan 2011.

[38] D. L. Mills and P. Lederer. Dynamical properties of magnetic impurities in transition metals. *Phys. Rev.*, 160:590–599, Aug 1967.

[39] R. B. Muniz and D. L. Mills. Local spin dynamics of magnetic moments on metal surfaces. *Phys. Rev. B*, 68:224414, Dec 2003.

[40] S. Lounis, A. T. Costa, R. B. Muniz, and D. L. Mills. Dynamical magnetic excitations of nanostructures from first principles. *Phys. Rev. Lett.*, 105:187205, Oct 2010.

[41] M. dos Santos Dias, B. Schweflinghaus, S. Blügel, and S. Lounis. Relativistic dynamical spin excitations of magnetic adatoms. *Phys. Rev. B*, 91:075405, Feb 2015.

[42] J. Ibaẽz Azpiroz, M. dos Santos Dias, S. Blügel, and S. Lounis. Zero-point spin-fluctuations of single adatoms. *Nano Letters*, 16(7):4305–4311, 2016. PMID: 27248465.

[43] G. Dresselhaus. Spin-orbit coupling effects in Zinc Blende structures. *Phys. Rev.*, 100:580–586, Oct 1955.

[44] E. I. Rashba. *Sov. Phys. Solid State*, 2:1109, 1960.

[45] A. Manchon, H. C. Koo, J. Nitta, S. M. Frolov, and R. A. Duine. New perspectives for Rashba spin-orbit coupling. *Nature materials*, 14(9):871–882, 2015.

[46] I. Gierz, T. Suzuki, E. Frantzeskakis, S. Pons, S. Ostanin, A. Ernst, J. Henk, M. Grioni, K. Kern, and C. R. Ast. Silicon surface with giant spin splitting. *Phys. Rev. Lett.*, 103:046803, Jul 2009.

[47] S. LaShell, B. A. McDougall, and E. Jensen. Spin splitting of an Au(111) surface state band observed with angle resolved photoelectron spectroscopy. *Phys. Rev. Lett.*, 77:3419–3422, Oct 1996.

[48] G. Nicolay, F. Reinert, S. Hüfner, and P. Blaha. Spin-orbit splitting of the L-gap surface state on Au(111) and Ag(111). *Phys. Rev. B*, 65:033407, Dec 2001.

[49] A. Tamai, W. Meevasana, P. D. C. King, C. W. Nicholson, A. de la Torre, E. Rozbicki, and F. Baumberger. Spin-orbit splitting of the Shockley surface state on Cu(111). *Phys. Rev. B*, 87:075113, Feb 2013.

[50] T. Moriya. Anisotropic superexchange interaction and weak ferromagnetism. *Phys. Rev.*, 120:91, 1960.

[51] I. E. Dzyaloshinskii. Thermodynamic theory of weak ferromagnetism in antiferromagnetic substances. *Sov. Phys. JETP*, 5:1259, 1957.

[52] M. Bode, M. Heide, K. von Bergmann, P. Ferriani, S. Heinze, G. Bilhmayer, A. Kubetzka, O. Pietzsch, S. Blügel, and R. Wiesendanger. Chiral magnetic order at surfaces driven by inversion asymmetry. *Nature*, 447:190–193, 2007.

[53] P. Ferriani, K. von Bergmann, E. Y. Vedmedenko, S. Heinze, M. Bode, M. Heide, G. Bihlmayer, S. Blügel, and R. Wiesendanger. Atomic-scale spin spiral with a unique rotational sense: Mn monolayer on W(001). *Phys. Rev. Lett.*, 101:027201, Jul 2008.

[54] B. Santos, J. M. Puerta, J. I. Cerda, R. Stumpf, K. von Bergmann, R. Wiesendanger, M. Bode, K. F. McCarty, and J. de la Figuera. Structure and magnetism of ultra-thin Chromium layers on W(110). *New Journal of Physics*, 10(1):013005, 2008.

[55] B. Schweflinghaus, B. Zimmermann, M. Heide, G. Bihlmayer, and S. Blügel. Role of Dzyaloshinskii-Moriya interaction for magnetism in transition-metal chains at Pt step edges. *Phys. Rev. B*, 94:024403, Jul 2016.

[56] M. Menzel, Y. Mokrousov, R. Wieser, J. E. Bickel, E. Vedmedenko, S. Blügel, S. Heinze, K. von Bergmann, A. Kubetzka, and R. Wiesendanger. Information transfer by vector spin chirality in finite magnetic chains. *Phys. Rev. Lett.*, 108:197204, May 2012.

[57] T. Kikuchi, T. Koretsune, R. Arita, and G. Tatara. Dzyaloshinskii-Moriya interaction as a consequence of a Doppler shift due to spin-orbit-induced intrinsic spin current. *Phys. Rev. Lett.*, 116:247201, Jun 2016.

[58] A. Fert and P. M. Levy. Role of anisotropic exchange interactions in determining the properties of spin-glasses. *Phys. Rev. Lett.*, 44:1538–1541, 1980.

[59] D. A. Smith. New mechanisms for magnetic anisotropy in localised S-state moment materials. *J. Magn. Magn. Mater.*, 1:214–225, 1976.

[60] M. A. Ruderman and C. Kittel. Indirect exchange coupling of nuclear magnetic moments by conduction electrons. *Phys. Rev.*, 96:99–102, Oct 1954.

[61] T. Kasuya. A theory of metallic ferro- and antiferromagnetism on Zener's model. *Progress of Theoretical Physics*, 16(1):45–57, 1956.

[62] K. Yosida. Magnetic properties of Cu-Mn alloys. *Phys. Rev.*, 106:893–898, Jun 1957.

[63] A. A. Khajetoorians, M. Steinbrecher, M. Ternes, M. Bouhassoune, M. dos Santos Dias, S. Lounis, J. Wiebe, and R. Wiesendanger. Tailoring the chiral magnetic interaction between two individual atoms. *Nature Communications*, 7:10620, February 2016.

[64] N. Nagaosa, J. Sinova, S. Onoda, A. H. MacDonald, and N. P. Ong. Anomalous hall effect. *Rev. Mod. Phys.*, 82:1539–1592, May 2010.

[65] K. M. Seemann, F. Freimuth, H. Zhang, S. Blügel, Y. Mokrousov, D. E. Bürgler, and C. M. Schneider. Origin of the planar Hall effect in nanocrystalline $Co_{60}Fe_{20}B_{20}$. *Phys. Rev. Lett.*, 107:086603, Aug 2011.

[66] J. Bouaziz, S. Lounis, S. Blügel, and H. Ishida. Microscopic theory of the residual surface resistivity of Rashba electrons. *Phys. Rev. B*, 94:045433, Jul 2016.

[67] M. dos Santos Dias, J. Bouaziz, M. Bouhassoune, S. Blügel, and S. Lounis. Chirality-driven orbital magnetic moments as a new probe for topological magnetic structures. *Nature communications*, 7:13613, 2016.

[68] A. Bogdanov and A. Hubert. Thermodynamically stable magnetic vortex states in magnetic crystals. *Journal of Magnetism and Magnetic Materials*, 138(3):255 – 269, 1994.

[69] A. Fert, N. Reyren, and V. Cros. Magnetic skyrmions: advances in physics and potential applications. *Nature Reviews Materials*, 2:17031, 2017.

[70] S. Mühlbauer, B. Binz, F. Jonietz, C. Pfleiderer, A. Rosch, A. Neubauer, R. Georgii, and P. Böni. Skyrmion lattice in a chiral magnet. *Science*, 323(5916):915–919, 2009.

[71] C. Pappas, E. Lelièvre-Berna, P. Falus, P. M. Bentley, E. Moskvin, S. Grigoriev, P. Fouquet, and B. Farago. Chiral paramagnetic skyrmion-like phase in MnSi. *Phys. Rev. Lett.*, 102:197202, May 2009.

[72] S. Heinze, K. Von Bergmann, M. Menzel, J. Brede, A. Kubetzka, R. Wiesendanger, G. Bihlmayer, and S. Blügel. Spontaneous atomic-scale magnetic skyrmion lattice in two dimensions. *Nature Physics*, 7(9):713, 2011.

[73] B. Dupé, M. Hoffmann, C. Paillard, and S. Heinze. Tailoring magnetic skyrmions in ultra-thin transition metal films. *Nature communications*, 5:4030, 2014.

[74] S. Rohart, J. Miltat, and A. Thiaville. Path to collapse for an isolated Néel skyrmion. *Phys. Rev. B*, 93:214412, Jun 2016.

[75] F. Jonietz, S. Mühlbauer, C. Pfleiderer, A. Neubauer, W. Münzer, A. Bauer, T. Adams, R. Georgii, P. Böni, R.A. Duine, et al. Spin transfer torques in MnSi at ultralow current densities. *Science*, 330(6011):1648–1651, 2010.

[76] X.Z. Yu, N. Kanazawa, W.Z. Zhang, T. Nagai, T. Hara, K. Kimoto, Y. Matsui, Y. Onose, and Y. Tokura. Skyrmion flow near room temperature in an ultralow current density. *Nature communications*, 3:988, 2012.

[77] K. Everschor-Sitte and M. Sitte. Real-space Berry phases: Skyrmion soccer (invited). *Journal of Applied Physics*, 115(17):172602, 2014.

[78] A. Neubauer, C. Pfleiderer, B. Binz, A. Rosch, R. Ritz, P. G. Niklowitz, and P. Böni. Topological Hall effect in the a phase of MnSi. *Phys. Rev. Lett.*, 102:186602, May 2009.

[79] T. Schulz, R. Ritz, A. Bauer, M. Halder, M. Wagner, C. Franz, C. Pfleiderer, K. Everschor, M. Garst, and A. Rosch. Emergent electrodynamics of skyrmions in a chiral magnet. *Nature Physics*, 8(4):301–304, 2012.

[80] A.I. Liechtenstein, M.I. Katsnelson, V.P. Antropov, and V.A. Gubanov. Local spin density functional approach to the theory of exchange interactions in ferromagnetic metals and alloys. *Journal of Magnetism and Magnetic Materials*, 67(1):65 – 74, 1987.

[81] Q. Liu, C. X. Liu, C. Xu, X. L. Qi, and S. C. Zhang. Magnetic impurities on the surface of a topological insulator. *Phys. Rev. Lett.*, 102:156603, Apr 2009.

[82] M. Born and J. R. Oppenheimer. On the quantum theory of molecules. *Ann. Physik*, 84(457):36, 1927.

[83] P. Hohenberg and W. Kohn. Inhomogeneous electron gas. *Phys. Rev.*, 136:B864–B871, Nov 1964.

[84] W. Kohn and L. J. Sham. Self-consistent equations including exchange and correlation effects. *Phys. Rev.*, 140:A1133–A1138, Nov 1965.

[85] J. Korringa. On the calculation of the energy of a Bloch wave in a metal. *Physica*, 13:392, 1947.

[86] W. Kohn and N. Rostoker. Solution of the Schrödinger equation in periodic lattices with an application to metallic Lithium. *Phys. Rev.*, 94:1111–1120, Jun 1954.

[87] T. H. Dupree. Electron scattering in a crystal lattice. *Annals of Physics*, 15(1):63–78, 1961.

[88] P. A. M. Dirac. Note on exchange phenomena in the thomas atom. *Mathematical Proceedings of the Cambridge Philosophical Society*, 26:376–385, 1930.

[89] G. Ortiz and P. Ballone. Correlation energy, structure factor, radial distribution function, and momentum distribution of the spin-polarized uniform electron gas. *Phys. Rev. B*, 50:1391–1405, Jul 1994.

[90] R. O. Jones. Density functional theory: Its origins, rise to prominence, and future. *Rev. Mod. Phys.*, 87:897–923, Aug 2015.

[91] S. H. Vosko, L. Wilk, and M. Nusair. Accurate spin-dependent electron liquid correlation energies for local spin density calculations: a critical analysis. *Canadian Journal of Physics*, 58(8):1200–1211, 1980.

[92] U. von Barth and L. Hedin. A local exchange-correlation potential for the spin polarized case. i. *Journal of Physics C: Solid State Physics*, 5(13):1629, 1972.

[93] E. N. Economou. Green's functions in quantum physics. *Springer-Verlag*, 2006.

[94] A. Gonis and W. H. Butler. Multiple scattering in solids. *Springer-Verlag*, 2000.

[95] J. Zabloudil, R. Hammerling, L. Szunyogh, and P.Weinberger. Electron scattering in solid matter. *Springer-Verlag*, 2005.

[96] D. S. G. Bauer. Development of a relativistic full-potential first-principles multiple scattering Green function method applied to complex magnetic textures of nano structures at surfaces. *Forschungszentrum Jülich*, 2014.

[97] K. Wildberger, P. Lang, R. Zeller, and P. H. Dederichs. Fermi-Dirac distribution in ab initio Green's-function calculations. *Phys. Rev. B*, 52:11502–11508, Oct 1995.

[98] R. Zeller, P. H. Dederichs, B. Újfalussy, L. Szunyogh, and P. Weinberger. Theory and convergence properties of the screened Korringa-Kohn-Rostoker method. *Phys. Rev. B*, 52:8807–8812, Sep 1995.

[99] P. Rakyta, B. Ujfalussy, and L. Szunyogh. Band bending at the surface of Bi_2Se_3 studied from first principles. *New Journal of Physics*, 17(12):123011, 2015.

[100] P. Lloyd and P.V. Smith. Multiple scattering theory in condensed materials. *Advances in Physics*, 21(89):69–142, 1972.

[101] R. Zeller. Improving the charge density normalization in Korringa-Kohn-Rostoker Green-function calculations. *Journal of Physics: Condensed Matter*, 20(3):035220, 2008.

[102] P. Strange. Relativistic quantum mechanics: With applications in condensed matter and atomic physics. 1998.

[103] S. Heers. Effect of spin-orbit scattering on transport properties of low-dimensional dilute alloys. *Forschungszentrum Jülich*, 2011.

[104] B. J. Schweflinghaus. First-principles investigation of inelastic magnetic excitations in nanostructures deposited on surfaces. *Forschungszentrum Jülich*, 2015.

[105] X. Wang, R. Wu, D. S. Wang, and A. J. Freeman. Torque method for the theoretical determination of magnetocrystalline anisotropy. *Phys. Rev. B*, 54:61–64, Jul 1996.

[106] R. C. O'handley. *Modern magnetic materials: principles and applications*. Wiley, 2000.

[107] P. Bruno. Tight-binding approach to the orbital magnetic moment and magnetocrystalline anisotropy of transition-metal monolayers. *Phys. Rev. B*, 39:865–868, Jan 1989.

[108] G. van der Laan. Microscopic origin of magnetocrystalline anisotropy in transition metal thin films. *Journal of Physics: Condensed Matter*, 10(14):3239, 1998.

[109] A. Oswald, R. Zeller, P. J. Braspenning, and P. H. Dederichs. Interaction of magnetic impurities in Cu and Ag. *Journal of Physics F: Metal Physics*, 15(1):193, 1985.

[110] A.I. Liechtenstein, M.I. Katsnelson, V.P. Antropov, and V.A. Gubanov. Local spin density functional approach to the theory of exchange interactions in ferromagnetic metals and alloys. *Journal of Magnetism and Magnetic Materials*, 67(1):65 – 74, 1987.

[111] G. H. O. Daalderop, P. J. Kelly, and M. F. H. Schuurmans. First-principles calculation of the magnetocrystalline anisotropy energy of Iron, Cobalt, and Nickel. *Phys. Rev. B*, 41:11919–11937, Jun 1990.

[112] M. Bouhassoune, M. dos Santos Dias, B. Zimmermann, P. H. Dederichs, and S. Lounis. RKKY-like contributions to the magnetic anisotropy energy: $3d$ adatoms on Pt(111) surface. *Phys. Rev. B*, 94:125402, Sep 2016.

[113] E. Runge and E. K. U. Gross. Density-functional theory for time-dependent systems. *Phys. Rev. Lett.*, 52:997–1000, Mar 1984.

[114] T. L. Gilbert. A phenomenological theory of damping in ferromagnetic materials. *IEEE Transactions on Magnetics*, 40(6):3443–3449, Nov 2004.

[115] S. Bhattacharjee, L. Nordström, and J. Fransson. Atomistic spin dynamic method with both damping and moment of inertia effects included from first principles. *Phys. Rev. Lett.*, 108:057204, Jan 2012.

[116] H. B. Callen and T. A. Welton. Irreversibility and generalized noise. *Phys. Rev.*, 83:34–40, Jul 1951.

[117] T. Moriya. Spin fluctuations in itinerant electron magnetism. *Springer-Verlag*, 1985.

[118] P. Mohn. Magnetism in the solid state. *Springer-Verlag*, 2003.

[119] F. Reinert, G. Nicolay, S. Schmidt, D. Ehm, and S. Hüfner. Direct measurements of the L-gap surface states on the (111) face of noble metals by photoelectron spectroscopy. *Phys. Rev. B*, 63:115415, Mar 2001.

[120] A. M. Shikin, A. A. Rybkina, A. S. Korshunov, Y. B. Kudasov, N. V. Frolova, A. G. Rybkin, D. Marchenko, J. Sánchez-Barriga, A. Varykhalov, and O. Rader. Induced Rashba splitting of electronic states in monolayers of Au, Cu on a W(110) substrate. *New Journal of Physics*, 15(9):095005, 2013.

[121] C. R. Ast, J. Henk, A. Ernst, L. Moreschini, M. C. Falub, D. Pacilé, P. Bruno, K. Kern, and M. Grioni. Giant spin splitting through surface alloying. *Phys. Rev. Lett.*, 98:186807, May 2007.

[122] H. J. Elmers, R. Wallauer, M. Liebmann, J. Kellner, M. Morgenstern, R. N. Wang, J. E. Boschker, R. Calarco, J. Sánchez-Barriga, O. Rader, D. Kutnyakhov, S. V. Chernov, K. Medjanik, C. Tusche, M. Ellguth, H. Volfova, St. Borek, J. Braun, J. Minár, H. Ebert, and G. Schönhense. Spin mapping of surface and bulk Rashba states in ferroelectric α-GeTe(111) films. *Phys. Rev. B*, 94:201403, Nov 2016.

[123] M. Liebmann, C. Rinaldi, D. D. Sante, J. Kellner, C. Pauly, R.N. Wang, J. E. Boschker, A. Giussani, S. Bertoli, M. Cantoni, L. Baldrati, M. Asa, I. Vobornik, G. Panaccione, D. Marchenko, J. Sánchez-Barriga, O. Rader, R. Calarco, S. Picozzi, R. Bertacco, and M. Morgenstern. Giant Rashba-type spin splitting in ferroelectric GeTe(111). *Advanced Materials*, 28(3):560–565, 2016.

[124] J. Friedel. Metallic alloys. *Il Nuovo Cimento (1955-1965)*, 7(2):287–311, 1958.

[125] L. Petersen and P. Hedegård. A simple tight-binding model of spin–orbit splitting of sp-derived surface states. *Surface Science*, 459(1–2):49 – 56, 2000.

[126] S. Lounis, A. Bringer, and S. Blügel. Magnetic adatom induced skyrmion-like spin texture in surface electron waves. *Phys. Rev. Lett.*, 108:207202, May 2012.

[127] K. M. Seemann, Y. Mokrousov, A. Aziz, J. Miguel, F. Kronast, W. Kuch, M. G. Blamire, A. T. Hindmarch, B. J. Hickey, I. Souza, and C. H. Marrows. Spin-orbit strength driven crossover between intrinsic and extrinsic mechanisms of the anomalous Hall effect in the epitaxial L_{10}-ordered ferromagnets FePd and FePt. *Phys. Rev. Lett.*, 104:076402, Feb 2010.

[128] J. Bouaziz, M. dos Santos Dias, A. Ziane, M. Benakki, S. Blügel, and S. Lounis. Chiral magnetism of magnetic adatoms generated by Rashba electrons. *New Journal of Physics*, 19(2):023010, 2017.

[129] J. Bouaziz, M. dos Santos Dias, F. S. M. Guimarães, S. Blügel, and S. Lounis. Impurity-induced orbital magnetization in a rashba electron gas. *Phys. Rev. B*, 98:125420, Sep 2018.

[130] E.I. Rashba Y.A. Bychkov. *J. Phys. C: Solid State Phys*, 17:6039, 1984.

[131] G. A. Fiete and E. J. Heller. *Colloquium* : Theory of quantum corrals and quantum mirages. *Rev. Mod. Phys.*, 75:933–948, Jul 2003.

[132] S. Crampin, M. H. Boon, and J. E. Inglesfield. Influence of bulk states on laterally confined surface state electrons. *Phys. Rev. Lett.*, 73:1015–1018, Aug 1994.

[133] S. Crampin and O. R. Bryant. Fully three-dimensional scattering calculations of standing electron waves in quantum nanostructures: The importance of quasiparticle interactions. *Phys. Rev. B*, 54:R17367–R17370, Dec 1996.

[134] H. K. Harbury and W. Porod. Elastic scattering theory for electronic waves in quantum corrals. *Phys. Rev. B*, 53:15455–15458, Jun 1996.

[135] Lutz C. P. Eigler D. M. Crommie, M. F. Imaging standing waves in a two-dimensional electron gas. *Nature*, 363, Jun 1993.

[136] Y. Hasegawa and Ph. Avouris. Direct observation of standing wave formation at surface steps using scanning tunneling spectroscopy. *Phys. Rev. Lett.*, 71:1071–1074, Aug 1993.

[137] M. F. Crommie, C. P. Lutz, and D. M. Eigler. Confinement of electrons to quantum corrals on a metal surface. *Science*, 262(5131):218–220, 1993.

[138] Crommie M. F. Lutz C. P. Eigler D. M. Heller, E. J. Scattering and absorption of surface electron waves in quantum corrals. *Nature*, 369, 1994.

[139] S. Mankovsky, S. Bornemann, J. Minár, S. Polesya, H. Ebert, J. B. Staunton, and A. I. Lichtenstein. Effects of spin-orbit coupling on the spin structure of deposited transition-metal clusters. *Phys. Rev. B*, 80:014422, Jul 2009.

[140] A. Antal, B. Lazarovits, L. Udvardi, L. Szunyogh, B. Újfalussy, and P. Weinberger. First-principles calculations of spin interactions and the magnetic ground states of Cr trimers on Au(111). *Phys. Rev. B*, 77:174429, May 2008.

[141] L. Zhou, J. Wiebe, S. Lounis, E. Vedmedenko, F. Meier, S. Blügel, P. H. Dederichs, and R. Wiesendanger. Strength and directionality of surface Ruderman–Kittel–Kasuya–Yosida interaction mapped on the atomic scale. *Nat. Phys.*, 6:187–191, 2010.

[142] A. A. Khajetoorians, J. Wiebe, B. Chilian, S. Lounis, S. Blügel, and R. Wiesendanger. Atom-by-atom engineering and magnetometry of tailored nanomagnets. *Nat. Phys.*, 8:497–503, 2012.

[143] H. Prüser, P. E. Dargel, M. Bouhassoune, Ulbrich R. G., T. Pruschke, S. Lounis, and M. Wenderoth. Interplay between the Kondo effect and the Ruderman–Kittel-Kasuya–Yosida interaction. *Nature Communications*, 5:5417, 2014.

[144] H. Ebert and S. Mankovsky. Anisotropic exchange coupling in diluted magnetic semiconductors: *Ab initio* spin-density functional theory. *Phys. Rev. B*, 79:045209, Jan 2009.

[145] L. Udvardi, L. Szunyogh, K. Palotás, and P. Weinberger. First-principles relativistic study of spin waves in thin magnetic films. *Phys. Rev. B*, 68:104436, Sep 2003.

[146] H. Imamura, P. Bruno, and Y. Utsumi. Twisted exchange interaction between localized spins embedded in a one- or two-dimensional electron gas with Rashba spin-orbit coupling. *Phys. Rev. B*, 69:121303, Mar 2004.

[147] J. D. Walls and E. J. Heller. Spin-orbit coupling induced interference in quantum corrals. *Nano Letters*, 7(11):3377–3382, 2007.

[148] K. W. Kim, H. W. Lee, K. J. Lee, and M. D. Stiles. Chirality from interfacial spin-orbit coupling effects in magnetic bilayers. *Phys. Rev. Lett.*, 111:216601, Nov 2013.

[149] O. Sipr, S. Mankovsky, S. Polesya, S. Bornemann, J. Minár, and H. Ebert. Illustrative view on the magnetocrystalline anisotropy of adatoms and monolayers. *Phys. Rev. B*, 93:174409, May 2016.

[150] A. A. Khajetoorians, J. Wiebe, B. Chilian, S. Lounis, S. Blügel, and R. Wiesendanger. Atom-by-atom engineering and magnetometry of tailored nanomagnets. *Nature Physics*, 8(6):497, 2012.

[151] A. Antal, B. Lazarovits, L. Udvardi, L. Szunyogh, B. Újfalussy, and P. Weinberger. First-principles calculations of spin interactions and the magnetic ground states of Cr trimers on Au(111). *Phys. Rev. B*, 77:174429, May 2008.

[152] S. Lounis. Non-collinear magnetism induced by frustration in transition-metal nanostructures deposited on surfaces. *Journal of Physics: Condensed Matter*, 26(27):273201, 2014.

[153] W. Thomson. On the electro-dynamic qualities of metals:–effects of magnetization on the electric conductivity of Nickel and of Iron. *Proc. R. Soc. Lond.*, 8:546–550, 1856.

[154] K. L. Yau and J. T. H. Chang. The planar Hall effect in thin foils of Ni-Fe alloy. *Journal of Physics F: Metal Physics*, 1(1):38, 1971.

[155] J. D. Walls, J. Huang, R. M. Westervelt, and E. J. Heller. Multiple-scattering theory for two-dimensional electron gases in the presence of spin-orbit coupling. *Phys. Rev. B*, 73:035325, Jan 2006.

[156] H. Ishida. Microscopic theory of surface resistivity. *Phys. Rev. B*, 52:10819–10822, Oct 1995.

[157] D. Thompson, L. Romankiw, and A. Mayadas. Thin film magnetoresistors in memory, storage, and related applications. *IEEE Transactions on Magnetics*, 11(4):1039–1050, Jul 1975.

[158] M. Trushin, K. Výborný, P. Moraczewski, A. A. Kovalev, J. Schliemann, and T. Jungwirth. Anisotropic magnetoresistance of spin-orbit coupled carriers scattered from polarized magnetic impurities. *Phys. Rev. B*, 80:134405, Oct 2009.

[159] D. Xiao, M. C. Chang, and Q. Niu. Berry phase effects on electronic properties. *Rev. Mod. Phys.*, 82:1959–2007, Jul 2010.

[160] C. N. Yang and R. L. Mills. Conservation of isotopic spin and isotopic gauge invariance. *Phys. Rev.*, 96:191–195, Oct 1954.

[161] N. Hatano, R. Shirasaki, and H. Nakamura. Non-abelian gauge field theory of the spin-orbit interaction and a perfect spin filter. *Phys. Rev. A*, 75:032107, Mar 2007.

[162] S.H. Chen and C. R. Chang. Non-abelian spin-orbit gauge: Persistent spin helix and quantum square ring. *Phys. Rev. B*, 77:045324, Jan 2008.

[163] B. Berche and E. Medina. Classical Yang-Mills theory in condensed matter physics. *European Journal of Physics*, 34(1):161, 2013.

[164] S. S. Pershoguba, K. Björnson, A. M. Black-Schaffer, and A. V. Balatsky. Currents induced by magnetic impurities in superconductors with spin-orbit coupling. *Phys. Rev. Lett.*, 115:116602, Sep 2015.

[165] T. Thonhauser. Theory of orbital magnetization in solids. *International Journal of Modern Physics B*, 25(11):1429–1458, 2011.

[166] G. Tatara and N. Garcia. Quantum toys for quantum computing: Persistent currents controlled by the spin Josephson effect. *Phys. Rev. Lett.*, 91:076806, Aug 2003.

[167] L. Fu. Hexagonal warping effects in the surface states of the topological insulator Bi_2Te_3. *Phys. Rev. Lett.*, 103:266801, Dec 2009.

[168] A. Soumyanarayanan and J. E. Hoffman. Momentum-resolved STM studies of Rashba-split surface states on the topological semimetal Sb. *Journal of Electron Spectroscopy and Related Phenomena*, 201:66 – 73, 2015.

[169] I. Garate and M. Franz. Inverse spin-galvanic effect in the interface between a topological insulator and a ferromagnet. *Phys. Rev. Lett.*, 104:146802, Apr 2010.

[170] L. Fu and C. L. Kane. Probing neutral Majorana Fermion edge modes with charge transport. *Phys. Rev. Lett.*, 102:216403, May 2009.

[171] W. K. Tse and A. H. MacDonald. Giant magneto-optical Kerr effect and universal Faraday effect in thin-film topological insulators. *Phys. Rev. Lett.*, 105:057401, Jul 2010.

[172] J. Bouaziz, M. dos Santos Dias, J. Ibañez Azpiroz, and S. Lounis. Ab initio investigation of impurity-induced in-gap states in Bi_2Te_3 and Bi_2Se_3. *Phys. Rev. B*, 98:035119, Jul 2018.

[173] J. Bouaziz, M. dos Santos Dias, F. Souza Mendes Guimarães, and S. Lounis. Spin dynamics of $3d$ and $4d$ impurities embedded in prototypical topological insulators. *Phys. Rev. Materials*, 3:054201, May 2019.

[174] K. von Klitzing. The quantized Hall effect. *Rev. Mod. Phys.*, 58:519–531, Jul 1986.

[175] B. A. Bernevig and S. C. Zhang. Quantum spin Hall effect. *Phys. Rev. Lett.*, 96:106802, Mar 2006.

[176] H. Zhang, C. X. Liu, X. L. Qi, X. Dai, Z. Fang, and S.C. Zhang. Topological insulators in Bi_2Te_3 ,Bi_2Se_3 and Sb_2Te_3 with a single Dirac cone on the surface. *Nature physics*, 5(6):438, 2009.

[177] Y. L. Chen, J. H. Chu, J. G. Analytis, Z. K. Liu, K. Igarashi, H. H. Kuo, X. L. Qi, S. K. Mo, R. G. Moore, D. H. Lu, M. Hashimoto, T. Sasagawa, S. C. Zhang, I. R. Fisher, Z. Hussain, and Z. X. Shen. Massive Dirac Fermion on the surface of a magnetically doped topological insulator. *Science*, 329(5992):659–662, 2010.

[178] Y. S. Hor, A. Richardella, P. Roushan, Y. Xia, J. G. Checkelsky, A. Yazdani, M. Z. Hasan, N. P. Ong, and R. J. Cava. p-type Bi_2Te_3 for topological insulator and low-temperature thermoelectric applications. *Phys. Rev. B*, 79:195208, May 2009.

[179] F. D. M. Haldane. Model for a quantum Hall effect without Landau levels: Condensed-matter realization of the "parity anomaly". *Phys. Rev. Lett.*, 61:2015–2018, Oct 1988.

[180] D. J. Thouless, M. Kohmoto, M. P. Nightingale, and M. den Nijs. Quantized Hall conductance in a two-dimensional periodic potential. *Phys. Rev. Lett.*, 49:405–408, Aug 1982.

[181] D. N. Sheng, Z. Y. Weng, L. Sheng, and F. D. M. Haldane. Quantum spin-Hall effect and topologically invariant Chern numbers. *Phys. Rev. Lett.*, 97:036808, Jul 2006.

[182] R. B. Laughlin. Quantized Hall conductivity in two dimensions. *Phys. Rev. B*, 23:5632–5633, May 1981.

[183] W. Zhang, R. Y., H. J. Zhang, X. Dai, and Z. Fang. First-principles studies of the three-dimensional strong topological insulators Bi_2Te_3 ,Bi_2Se_3 and Sb_2Te_3. *New Journal of Physics*, 12(6):065013, 2010.

[184] Y. Ando. Topological insulator materials. *Journal of the Physical Society of Japan*, 82(10):102001, 2013.

[185] H. Ebert, D. Ködderitzsch, and J. Minár. Calculating condensed matter properties using the KKR-Green's function method-recent developments and applications. *Reports on Progress in Physics*, 74(9):096501, 2011.

[186] L. Fu and C. L. Kane. Topological insulators with inversion symmetry. *Phys. Rev. B*, 76:045302, Jul 2007.

[187] A. Pertsova and C. M. Canali. Probing the wavefunction of the surface states in Bi_2Se_3 topological insulator: a realistic tight-binding approach. *New Journal of Physics*, 16(6):063022, 2014.

[188] A. M. Black-Schaffer, A. V. Balatsky, and J. Fransson. Filling of magnetic-impurity-induced gap in topological insulators by potential scattering. *Phys. Rev. B*, 91:201411, May 2015.

[189] D. West, Y. Y. Sun, S. B. Zhang, T. Zhang, Xucun Ma, P. Cheng, Y. Y. Zhang, X. Chen, J. F. Jia, and Q. K. Xue. Identification of magnetic dopants on the surfaces of topological insulators: Experiment and theory for Fe on Bi_2Se_3(111). *Phys. Rev. B*, 85:081305, Feb 2012.

[190] L. B. Abdalla, L. Seixas, T. M. Schmidt, R. H. Miwa, and A. Fazzio. Topological insulator Bi_2Se_3(111) surface doped with transition metals: An ab initio investigation. *Phys. Rev. B*, 88:045312, Jul 2013.

[191] J. F. Janak. Uniform susceptibilities of metallic elements. *Phys. Rev. B*, 16:255–262, Jul 1977.

[192] L. Limot, E. Pehlke, J. Kröger, and R. Berndt. Surface-state localization at adatoms. *Phys. Rev. Lett.*, 94:036805, Jan 2005.

[193] S. Lounis, P. Mavropoulos, P. H. Dederichs, and S. Blügel. Surface-state scattering by adatoms on noble metals: Ab initio calculations using the Korringa-Kohn-Rostoker Green function method. *Phys. Rev. B*, 73:195421, May 2006.

[194] Š. Pick, V. S. Stepanyuk, A. N. Baranov, W. Hergert, and P. Bruno. Effect of atomic relaxations on magnetic properties of adatoms and small clusters. *Phys. Rev. B*, 68:104410, Sep 2003.

[195] P. Bruno. Exchange interaction parameters and adiabatic spin-wave spectra of ferromagnets: A "renormalized magnetic force theorem". *Phys. Rev. Lett.*, 90:087205, Feb 2003.

[196] F. S. M. Guimarães, M. dos Santos Dias, B. Schweflinghaus, and S. Lounis. Engineering elliptical spin-excitations by complex anisotropy fields in Fe adatoms and dimers on Cu(111). *Phys. Rev. B*, 96:144401, Oct 2017.

[197] A. A. Khajetoorians, B. Chilian, J. Wiebe, S. Schuwalow, F. Lechermann, and R. Wiesendanger. Detecting excitation and magnetization of individual dopants in a semiconductor. *Nature*, 467(7319):1084–1087, 2010.

[198] A. J. Heinrich, J. A. Gupta, C. P. Lutz, and D. M. Eigler. Single-atom spin-flip spectroscopy. *Science*, 306(5695):466–469, 2004.

[199] N. Lorente and J. P. Gauyacq. Efficient spin transitions in inelastic electron tunneling spectroscopy. *Phys. Rev. Lett.*, 103:176601, Oct 2009.

[200] S. Loth, K. Von Bergmann, M. Ternes, A. F Otte, C. P. Lutz, and A. J. Heinrich. Controlling the state of quantum spins with electric currents. *Nature Physics*, 6(5):340–344, 2010.

[201] C. F. Hirjibehedin, C. P. Lutz, and A. J. Heinrich. Spin coupling in engineered atomic structures. *Science*, 312(5776):1021–1024, 2006.

[202] C. F. Hirjibehedin, C. Y. Lin, A. F. Otte, M. Ternes, C. P. Lutz, B. A. Jones, and A. J. Heinrich. Large magnetic anisotropy of a single atomic spin embedded in a surface molecular network. *Science*, 317(5842):1199–1203, 2007.

[203] T. Balashov, T. Schuh, A. F. Takács, A. Ernst, S. Ostanin, J. Henk, I. Mertig, P. Bruno, T. Miyamachi, S. Suga, and W. Wulfhekel. Magnetic anisotropy and magnetization dynamics of individual atoms and clusters of Fe and Co on Pt(111). *Phys. Rev. Lett.*, 102:257203, Jun 2009.

[204] A. A. Khajetoorians, T. Schlenk, B. Schweflinghaus, M. dos Santos Dias, M. Steinbrecher, M. Bouhassoune, S. Lounis, J. Wiebe, and R. Wiesendanger. Spin excitations of individual Fe atoms on Pt(111): Impact of the site-dependent giant substrate polarization. *Phys. Rev. Lett.*, 111:157204, Oct 2013.

[205] S. Lounis, A. T. Costa, R. B. Muniz, and D. L. Mills. Theory of local dynamical magnetic susceptibilities from the Korringa-Kohn-Rostoker Green function method. *Phys. Rev. B*, 83:035109, Jan 2011.

[206] S. Lounis, B. Schweflinghaus, M. dos Santos Dias, M. Bouhassoune, R. B. Muniz, and A. T. Costa. Theoretical probing of inelastic spin-excitations in adatoms on surfaces. *Surface Science*, 630(Supplement C):317 – 324, 2014.

[207] S. Lounis, M. dos Santos Dias, and B. Schweflinghaus. Transverse dynamical magnetic susceptibilities from regular static density functional theory: Evaluation of damping and g shifts of spin excitations. *Phys. Rev. B*, 91:104420, Mar 2015.

[208] P. Gambardella, S. Rusponi, M. Veronese, S. S. Dhesi, C. Grazioli, A. Dallmeyer, I. Cabria, R. Zeller, P. H. Dederichs, K. Kern, C. Carbone, and H. Brune. Giant magnetic anisotropy of single Cobalt atoms and nanoparticles. *Science*, 300(5622):1130–1133, 2003.

[209] F. Meier, L. Zhou, J. Wiebe, and R. Wiesendanger. Revealing magnetic interactions from single-atom magnetization curves. *Science*, 320(5872):82–86, 2008.

[210] L. Zhou, J. Wiebe, S. Lounis, E. Vedmedenko, F. Meier, S. Blügel, P. H. Dederichs, and R. Wiesendanger. Strength and directionality of surface Ruderman-Kittel-Kasuya-Yosida interaction mapped on the atomic scale. *Nature Physics*, 6(3):187, 2010.

[211] J. Honolka, K. Kuhnke, L. Vitali, A. Enders, K. Kern, S. Gardonio, C. Carbone, S. R. Krishnakumar, P. Bencok, S. Stepanow, and P. Gambardella. Absence of local magnetic moments in Ru and Rh impurities and clusters on Ag(100) and Pt(997). *Phys. Rev. B*, 76:144412, Oct 2007.

[212] F. D. Natterer, K. Yang, W. Paul, P. Willke, T. Choi, T. Greber, A. J. Heinrich, and C. P. Lutz. Reading and writing single-atom magnets. *Nature*, 543(7644):226–228, 2017.

[213] T. H. R. Skyrme. A unified field theory of mesons and baryons. *Nuclear Physics*, 31(Supplement C):556 – 569, 1962.

[214] A. Fert, V. Cros, and J. Sampaio. Skyrmions on the track. *Nature nanotechnology*, 8(3):152–156, 2013.

[215] D. M. Crum, M. Bouhassoune, J. Bouaziz, B. Schweflinghaus, S. Blügel, and S. Lounis. Perpendicular reading of single confined magnetic skyrmions. *Nature communications*, 6:8541, 2015.

[216] E. Moskvin, S. Grigoriev, V. Dyadkin, H. Eckerlebe, M. Baenitz, M. Schmidt, and H. Wilhelm. Complex chiral modulations in FeGe close to magnetic ordering. *Phys. Rev. Lett.*, 110:077207, Feb 2013.

[217] N. Romming, C. Hanneken, M. Menzel, J. E. Bickel, B. Wolter, K. von Bergmann, A. Kubetzka, and R. Wiesendanger. Writing and deleting single magnetic skyrmions. *Science*, 341(6146):636–639, 2013.

[218] A.N. Bogdanov and U.K. Rößler. Chiral symmetry breaking in magnetic thin films and multilayers. *Physical review letters*, 87(3):037203, 2001.

[219] A.B. Butenko, A.A. Leonov, U.K. Rößler, and A.N. Bogdanov. Stabilization of skyrmion textures by uniaxial distortions in noncentrosymmetric cubic helimagnets. *Physical Review B*, 82(5):052403, 2010.

[220] N. Nagaosa and Y. Tokura. Topological properties and dynamics of magnetic skyrmions. *Nature nanotechnology*, 8(12):899–911, 2013.

[221] N. Romming, A. Kubetzka, C. Hanneken, K. von Bergmann, and R. Wiesendanger. Field-dependent size and shape of single magnetic skyrmions. *Phys. Rev. Lett.*, 114:177203, May 2015.

[222] C. Hanneken, F. Otte, A. Kubetzka, B Dupé, N. Romming, K. Von Bergmann, R. Wiesendanger, and S. Heinze. Electrical detection of magnetic skyrmions by tunnelling non-collinear magnetoresistance. *Nature nanotechnology*, 10(12):1039–1042, 2015.

[223] J. Tersoff and D. R. Hamann. Theory and application for the scanning tunneling microscope. *Phys. Rev. Lett.*, 50:1998–2001, Jun 1983.

[224] M. Bode, S. Heinze, A. Kubetzka, O. Pietzsch, X. Nie, G. Bihlmayer, S. Blügel, and R. Wiesendanger. Magnetization-direction-dependent local electronic structure probed by scanning tunneling spectroscopy. *Phys. Rev. Lett.*, 89:237205, Nov 2002.

[225] S. Alexander and P. W. Anderson. Interaction between localized states in metals. *Phys. Rev.*, 133:A1594–A1603, Mar 1964.

[226] C. Gould, C. Rüster, T. Jungwirth, E. Girgis, G. M. Schott, R. Giraud, K. Brunner, G. Schmidt, and L. W. Molenkamp. Tunneling anisotropic magnetoresistance: A spin-valve-like tunnel magnetoresistance using a single magnetic layer. *Phys. Rev. Lett.*, 93:117203, Sep 2004.

[227] K. von Bergmann, M. Menzel, D. Serrate, Y. Yoshida, S. Schröder, P. Ferriani, A. Kubetzka, R. Wiesendanger, and S. Heinze. Tunneling anisotropic magnetoresistance on the atomic scale. *Phys. Rev. B*, 86:134422, Oct 2012.

[228] N. M. Caffrey, S. Schröder, P. Ferriani, and S. Heinze. Tunneling anisotropic magnetoresistance effect of single adatoms on a noncollinear magnetic surface. *Journal of Physics: Condensed Matter*, 26(39):394010, 2014.

[229] C. T. Chen, Y. U. Idzerda, H.-J. Lin, N. V. Smith, G. Meigs, E. Chaban, G. H. Ho, E. Pellegrin, and F. Sette. Experimental confirmation of the X-ray magnetic circular dichroism sum rules for Iron and Cobalt. *Phys. Rev. Lett.*, 75:152–155, Jul 1995.

[230] K. Nakamura, T. Ito, and A. J. Freeman. Curling spin density and orbital structures in a magnetic vortex core of an Fe quantum dot. *Phys. Rev. B*, 68:180404, Nov 2003.

[231] J.-P. Hanke, F. Freimuth, A. K. Nandy, H. Zhang, S. Blügel, and Y. Mokrousov. Role of Berry phase theory for describing orbital magnetism: From magnetic heterostructures to topological orbital ferromagnets. *Phys. Rev. B*, 94:121114, Sep 2016.

[232] B. Göbel, A. Mook, J. Henk, and I. Mertig. Unconventional topological Hall effect in skyrmion crystals caused by the topology of the lattice. *Phys. Rev. B*, 95:094413, Mar 2017.

[233] G. Yin, Y. Li, L. Kong, R. K. Lake, C. L. Chien, and J. Zang. Topological charge analysis of ultrafast single skyrmion creation. *Phys. Rev. B*, 93:174403, May 2016.

List of publications

Published:

[1] D. M. Crum, M. Bouhassoune, **J. Bouaziz**, B. Schweflinghaus, S. Blügel and S. Lounis. Perpendicular reading of single confined magnetic skyrmions. *Nature communications*, 6:8541, 2015.

[2] **J. Bouaziz**, S. Lounis, S. Blügel and H. Ishida. Microscopic theory of the residual surface resistivity of Rashba electrons. *Phys. Rev. B*, 94:045433, 2016.

[3] M. dos Santos Dias, **J. Bouaziz**, M. Bouhassoune, S. Blügel and S. Lounis. Chirality-driven orbital magnetic moments as a new probe for topological magnetic structures. *Nature communications*, 7:13613, 2016.

[4] **J. Bouaziz**, M. dos Santos Dias, A. Ziane, M. Benakki, S. Blügel and S. Lounis. Chiral magnetism of magnetic adatoms generated by Rashba electrons. *New Journal of Physics*, 19:023010, 2017.

[5] F. S. M. Guimarães, M. dos Santos Dias, **J. Bouaziz**, A. T. Costa, R. B. Muniz and S. Lounis. Dynamical amplification of magnetoresistances and Hall currents up to the THz regime. *Scientific Reports*, 7:3686, 2017.

[6] F. J. dos Santos, M. dos Santos Dias, F. S. M. Guimarães, **J. Bouaziz** and S. Lounis. Spin-resolved inelastic electron scattering by spin-waves in non-collinear magnets. *Phys. Rev. B*, 97:024431, 2018.

[7] **J. Bouaziz**, M. dos Santos Dias J. I. Azpiroz, and S. Lounis. Ab initio investigation of impurity-induced in-gap states in Bi_2Te_3 and Bi_2Se_3. *Phys. Rev. B*, 98:035119, 2018.

[8] I. L. Fernandes, **J. Bouaziz**, S. Blügel and S. Lounis. Universality of defect-skyrmion interaction profiles. *Nature communications*, 9:4395, 2018.

[9] **J. Bouaziz**, M. dos Santos Dias, F. S. M. Guimarães, S. Blügel and S. Lounis. Impurity-induced orbital magnetization in a Rashba electron gas. *Phys. Rev. B*, 98:125420, 2018.

[10] **J. Bouaziz**, M. d. S. Dias, F. S. M. Guimarães, and S. Lounis. Spin dynamics of $3d$ and $4d$ impurities embedded in prototypical topological insulators. *Phys. Rev. Materials*, 3: 054201, 2019.

[11] F. S. M. Guimarães , J. R. Suckert , J. Chico , **J. Bouaziz** , M. d. S. Dias and S.

Lounis. Comparative study of methodologies to compute the intrinsic Gilbert damping: interrelations, validity and physical consequences. *JPCM*, 31:255802, 2019.

[12] L. Schneider, M. Steinbrecher, L. Rózsa, **J. Bouaziz**, K. Palotás, M. d. S. Dias, S. Lounis, J. Wiebe and R. Wiesendanger. Magnetism and in-gap states of $3d$ transition metal atoms on superconducting Re. *npj Quantum Materials*, 4:42, 2019.

Submitted:
[13] S. Grytsiuk, J. P. Hanke, M. Hoffmann, **J. Bouaziz**, O. Gomonay, G. Bihlmayer, S. Lounis, Y. Mokrousov, and S. Blügel. Topological-chiral magnetic interactions driven by emergent orbital magnetism. *Nature Comm*, 2019.

[14] F. S. M. Guimarães, **J. Bouaziz**, M. d. S. Dias, and S. Lounis. AC spin-orbit torques and their associated effective fields. *Communications Physics*, 2019.

In preparation:
[15] **J. Bouaziz**, Filipe S. M. Guimarães and S. Lounis. Spin excitation renormalization of electron self-energies in presence of spin-orbit interaction.

[16] **J. Bouaziz**, Filipe S. M. Guimarães and S. Lounis. Magnetic fluctuations of $3d$ and $4d$ transition metal impurities in topological insulators.

[17] **J. Bouaziz**, H. Ishida, S. Blügel and S. Lounis. Electron-skyrmion scattering and emergent Hall effects.

List of Tables

List of Figures

Acknowledgments

The work presented in this thesis required guidance and support from several people. I am happy to acknowledge their help here.

First, I would like especially to thank my supervisor Prof. Dr. Samir Lounis for giving me the chance to work with him on various captivating topics ranging from analytical models to first-principles simulations. I highly benefited from his broad knowledge on many topics. He always took the time to answer my questions on many occasions. He made me believe in myself and that there was always a way to circumvent the problems encountered in practice.

I would like to thank Prof. Dr. Carsten Honerkamp for accepting to be the second referee of my thesis for the examination.

Moreover, I express my gratitude to Prof. Dr. Stefan Blügel for giving me the chance to write my thesis in his institute "Quantum Theory of Materials". It was always a pleasure to interact with him scientifically. His vast and diverse knowledge always helped me to grasp the big picture and put things in context. Talking to him was always very motivating to push forward and achieve more.

I am gratful to Prof. Hiroshi Ishida for hosting me during my stay at the Nihon university, and for teaching me many interesting things about electronic transport and scattering theory in two dimensions.

Many thanks go to Dr. Manuel dos Santos Dias and Dr. Filipe Guimarães for reading my thesis and fruitful discussions. I benefited from their theoretical knowledge as well as their expertise in scientific programming.

I would like to thank Dr. Jonathan Chico and Dr. Imara Lima Fernandes for reading my Skyrmion chapter. Moreover, I would like to thank Philipp Rüssmann for reading my chapter on topological insulators. I benefited a lot from his expertise on the Jülich-Münich KKR code and topological insulators.

I would like to thank Philipp Rüssmann and Marcel Bornemann for helping with the German bureaucracy. I also thank Dr. Nikolai Kiselev, Dr. Sergii Grytsiuk, Dr. Imara Lima Fernandes, Flaviano Santos, Dr. Mohammed Bouhassoune, Marta Gibertini, Dr. Guillaume Geranton and Dr. Julen Ibañez Azpiroz for the nice and fun atmosphere and for the social events they organized off work.

I would like to thank Mrs. Ute Winkler for helping me at multiple occasions in any administrative issue.

Last but not least, I would like to thank my family for the warm and kind support overseas. In particular, my parents for always being supportive.

Band / Volume 191
Absolute scale off-axis electron holography of thin dichalcogenide crystals at atomic resolution
F. Winkler (2019), xxiii, 187 pp
ISBN: 978-3-95806-383-9

Band / Volume 192
High-resolution genome and transcriptome analysis of *Gluconobacter oxydans* 621H and growth-improved strains by next-generation sequencing
A. Kranz (2019), III, 182 pp
ISBN: 978-3-95806-385-3

Band / Volume 193
Group IV (Si)GeSn Light Emission and Lasing Studies
D. Stange (2019), vi, 151 pp
ISBN: 978-3-95806-389-1

Band / Volume 194
Construction and analysis of a spatially organized cortical network model
J. Senk (2019), 245 pp
ISBN: 978-3-95806-390-7

Band / Volume 195
Large-scale Investigations of Non-trivial Magnetic Textures in Chiral Magnets with Density Functional Theory
M. Bornemann (2019), 143 pp
ISBN: 978-3-95806-394-5

Band / Volume 196
Neutron scattering
Experimental Manuals of the JCNS Laboratory Course held at Forschungszentrum Jülich and at the Heinz-Maier-Leibnitz Zentrum Garching
edited by T. Brückel, S. Förster, G. Roth, and R. Zorn (2019),
ca 150 pp
ISBN: 978-3-95806-406-5

Band / Volume 197
Topological transport in non-Abelian spin textures from first principles
P. M. Buhl (2019), vii, 158 pp
ISBN: 978-3-95806-408-9

Band / Volume 198
Shortcut to the carbon-efficient microbial production of chemical building blocks from lignocellulose-derived D-xylose
C. Brüsseler (2019), X, 62 pp
ISBN: 978-3-95806-409-6

Band / Volume 199
Regulation and assembly of the cytochrome *bc*$_1$-*aa*$_3$ supercomplex in *Corynebacterium glutamicum*
C.-F. Davoudi (2019), 135 pp
ISBN: 978-3-95806-416-4

Band / Volume 200
Variability and compensation in Alzheimer's disease across different neuronal network scales
C. Bachmann (2019), xvi, 165 pp
ISBN: 978-3-95806-420-1

Band / Volume 201
Crystal structures and vibrational properties of chalcogenides: the role of temperature and pressure
M. G. Herrmann (2019), xi, 156 pp
ISBN: 978-3-95806-421-8

Band / Volume 202
Current-induced magnetization switching in a model epitaxial Fe/Au bilayer
P. Gospodarič (2019), vi, 120, XXXVIII pp
ISBN: 978-3-95806-423-2

Band / Volume 203
Network architecture and heme-responsive gene regulation of the two-component systems HrrSA and ChrSA
M. Keppel (2019), IV, 169 pp
ISBN: 978-3-95806-427-0

Band / Volume 204
Spin-orbitronics at the nanoscale: From analytical models to real materials
J. Bouaziz (2019), 228 pp
ISBN: 978-3-95806-429-4

Weitere ***Schriften des Verlags im Forschungszentrum Jülich*** unter
http://wwwzb1.fz-juelich.de/verlagextern1/index.asp

Schlüsseltechnologien / Key Technologies
Band / Volume 204
ISBN 978-3-95806-429-4

Mitglied der Helmholtz-Gemeinschaft

JÜLICH
Forschungszentrum